Graphene Nanoplatelets Reinforced AA2024 Composite Fabricated using Laser Powder Bed Fusion

Mulla Ahmet Pekok

School of Engineering

Cardiff University

This thesis is submitted in fulfilment of the requirement of the degree

of

Doctor of Philosophy

September 2022

This research is dedicated to my wife who has always been supportive of me.

Acknowledgements

During my thesis research, I experienced the most challenging journey of my life as well as the most rewarding adventure. This adventure taught me the value of dealing with adversity. Therefore, I would like to express my endless gratitude to my wife, family, parents and supervisors who have always been there for me during these difficult times.

First and foremost, I want to express my gratitude to Prof. Rossitza Setchi and Dr Michael Ryan for providing me with this incredible chance to do this research. Their unwavering support and guidance in all conditions have been the most important aspect in completing this PhD. Aside from their tremendous support for my academic endeavours, I've always felt their presence by my side when I've been despondent or emotionally troubled. Furthermore, they gave me a great opportunity to meet valuable persons with whom they were in contact, which considerably aided the expansion of this research.

In this regard, I owe a debt of gratitude to Dr Franck Lacan, Prof. Quanquan Han and Dr Heng Gu who assisted me with my experimental work as well as provided feedback on the publications. Their contribution to my project is invaluable and irreplaceable. In addition, I would also want to express my gratitude to Mr Justin Merridew, Dr Emmanuel Brousseau, Dr Victoria Garcia Rocha, Dr Debajyoti Bhaduri, Dr Simon Hutt, and Prof. Dongdong Gu for their priceless contribution.

Finally, I would like to express my heartfelt gratitude to the ministry of national education of Turkiye for their financial support which helped me to focus on my project without having to worry about any financial issues.

Abstract

Aluminium is the third most abundant material in the Earth's crust and, along with its alloys, is essential in many engineering sectors, including aerospace, automotive, defence, marine, construction, and medicine, owing to its high damage tolerance, fatigue resistance, conductivity, corrosion resistance, and low density. Despite this, some mechanical properties of Aluminium and its alloys are still inadequate to satisfy increasing industrial demands. Consequently, reinforcing an element indicates that superior mechanical properties of the new composite may be achieved by embedding reinforcement materials into the metal matrix. In the circumstances, Laser Powder Bed Fusion (LPBF) offers significant benefits, including geometric freedom of geometrically complex items with high precision, rapid production, short fabrication lead-time and reasonable cost, when compared with traditional manufacturing techniques. However, the mechanical properties and microstructure of the new composite have not been fully explored, as their manufacturability using LPBF is extremely challenging. Hence, the current study addresses the knowledge gap by emphasizing the LPBF of Aluminium 2024 Alloy (AA2024) reinforced with Graphene Nanoplatelets (GNPs) synthesized using ball milling. This study aims to investigate the effect of GNPs-reinforced AA2024 composite under various Graphene (Gr) percentages using ball milling and LPBF.

The initial contribution of this research is the characterization of raw AA2024 which investigates the effect of laser power, hatch spacing and scanning speed on the mechanical and microstructural properties of as-fabricated AA2024 manufactured using LPBF. More importantly, this research aids in understanding the correlation between fabrication processing parameters and specimen

characteristics. Exploring the effect of adding GNPs to AA2024 on the mechanical and microstructural properties of both milled powder (by ball-milling) and as-fabricated specimens (by LPBF) is another novelty of this study. The results reveal that almost crack-free structures with high relative (99.9%) and Archimedes' densities (99.7%) have been achieved.

The second contribution of this study is to investigate the effect of various ball milling speeds and times on GNPs reinforced composite powder. Powder morphology, flowability and agglomeration have been investigated. The flowability model employing a Discrete Element Method (DEM) is the third contribution of this research. The model was created to predict the flowability of commonly used particles and most representative milled particles of real powder morphologies. The fourth contribution of this study is the effect of Gr concentration and scanning speed on the composites' wear performance, as well as their microstructural and mechanical properties.

The experimental findings demonstrate that a certain amount of Gr enhances its Ultimate Tensile Strength (UTS), crystallite sizes, microhardness, wear rate and friction coefficient by up to 7%, 37.6%, 45%, 50% and 56%, respectively. The addition of Gr, on the other hand, led to the formation of more porosity and cracks in the structure. The significant impact of a small amount of Gr on composite is demonstrated by the enhancement in UTS despite considerable porosity and crack development. The relationship between microstructure and composite mechanical properties is research's another novelty, which demonstrates the substantial contribution of a certain quantity of GNPs to the improvement of advanced composites' mechanical and microstructural properties. Hereby, complex cross-sectional regions (i.e., the reticular, triangular, wavy or honeycomb lattice geometries) that decrease the weight-strength relationship

may be produced using this advanced alloy with the LPBF technique. For applications where weight is crucially important, such as transportation vehicles, it is possible to build structures that are both strong and light with this alloy.

Table of Contents

List of Figures

List of Tables

List of Abbreviations

3D	Three-Dimensional
AA2024	Aluminium 2024 Alloy
AFM	Atomic Force Microscopy
AM	Additive Manufacturing
ANOVA	Analysis of Variance
ASTM	American Society for Testing and Materials
CAD	Computer Aid Design
CAM	Computer Aid Manufacturing
CNC	Computer Numerical Control
CNT	Carbon Nanotube
CW	Continuous-Wave
DEM	Discrete Element Method
Dv	Diameter of Volume
ED	Energy Density
EDS	Energy Dispersive X-ray Spectroscopy
FLG	Few-layer Graphene
GNP	Graphene Nanoplatelet
Gr	Graphene
GO	Graphene Oxide
HAZ	Heat-Affected Zone
HEBM	High-Energy Ball Milling

JKR	Johnson-Kendall-Roberts
LBM	Laser Beam Melting
LPBF	Laser Powder Bed Fusion
MMC	Metal Matrix Composite
MWCNT	Multi-Walled Carbon Nanotube
Nd:YAG	neodymium-doped crystal: yttrium aluminium garnet
OM	Optical Microscope
PCA	Process Control Agent
PSD	Particle Size Distribution
PSPD	Position Sensitive Photo Detector
PW	Pulsed-Wave
SEM	Scanning Electron Microscopy
SLM	Selective Laser Melting
SS	Sum of Squares
SSSS	Strongly Supersaturated Solid Solutions
S/N	Signal-to-Noise
UTS	Ultimate Tensile Strength
YS	Yield Strength
XRD	X-ray Diffraction

Nomenclature

A	Mechanical advantage of level arm
a	Contact radius
d_h	Hatch spacing
d_p	Point distance
d_s	Spot size
E*	Equivalent Young's modulus
F	Friction signal
F_{JKR}	Normal elastic contact forces
L	Sliding distance
M	Lateral voltage output
N	Normal load
P	Laser power
R*	Equivalent radius
t	Layer thickness
T_d	Laser delay time
T_e	Laser exposure time
V	Scan speed
v	Poisson's ratio
V_Δ	Volume of loss
W_Δ	Weight of loss
ρ	Density

α	Conversion factor
λ	Wavelength
Γ	Surface energy
γ	Interface surface energy
Y_R	Response
ω_r	Wear rate
μ	Friction coefficient

List of Publications

Journal Publications

[1] Mulla Ahmet Pekok, Rossitza Setchi, Michael Ryan, Quanquan Han and Dongdong Gu. “Effect of process parameters on the microstructure and mechanical properties of AA2024 fabricated using Laser Powder Bed Fusion.” *International Journal of Advanced Manufacturing Technology* 112 (2021): 175-192. DOI: 10.1007/s00170-020-06346-y

[2] Mulla Ahmet Pekok, Rossitza Setchi, Michael Ryan, Heng Gu, Quanquan Han, Dongdong Gu. “Al-Cu-Mg Alloy Powder Reinforced with Graphene Nanoplatelets: Morphology, Flowability and Discrete Element Simulation.” *Advanced Powder Technology [under review]*

[3] Mulla Ahmet Pekok, Rossitza Setchi, Michael Ryan, Emmanuel Brousseau, Dongdong Gu. “Graphene Nanoplatelets Reinforced Al-Cu-Mg Composite Fabricated using Laser Powder Bed Fusion: Microstructure, Mechanical Properties, and Wear Behaviour.” *Composites Part A [under review]*

Conference Publications

[1] Mulla Ahmet Pekok, Rossitza Setchi, Michael Ryan and Quanquan Han. “Effect of Milling Speed and Time on Graphene-Reinforced AA2024 Powder” Presented at: The 7th International Conference on Sustainable Design and Manufacturing (KES-SDM 2020) on *Smart Innovation, Systems and Technologies 200*, 9-11 September 2020, 215–225. DOI: 10.1007/978-981-15-8131-1_20.

1. Chapter: Introduction

1.1 Research Motivation

Aluminium (Al) and its alloys are extensively used as non-ferrous metals and outstandingly important for many engineering sectors including aerospace, automotive, marine, medicine, defence and construction, owing to their strength, damage tolerance, fatigue resistance, low-density, corrosion resistance, malleability, conductivity, low cost and recyclability for their applications (Chen et al. 2018). According to the international aluminium institute (Prosser et al. 2022), 996,241 thousand metric tonnes of Al has been globally produced between 2000 and 2021 (Figure 1.1). Additionally, the global production of primary Al is growing every year by approximately 6%. A global market price of the high-strength Al alloys, which could be extended to $55 Billion by 2023, demonstrates the enormous importance of Al and its alloys for engineering sectors (Wood 2018). However, the requirement for new materials or composites (which contain superior mechanical properties) gain importance associated with technological improvements and significant developments in material science (Brock 2001; Prasad and Wanhill 2017). Even while Al alloys such as Aluminium 2024 Alloy (AA2024) (with copper (Cu) as the primary alloying element and magnesium (Mg) as a secondary element) satisfy most of the engineering sectors' demands for improved damage tolerance, corrosion resistance, and low density, their poor tribological properties (such as low strength) need to be improved. One of the most efficient ways to increase the mechanical properties of the matrix material is to reinforce a relevant element.

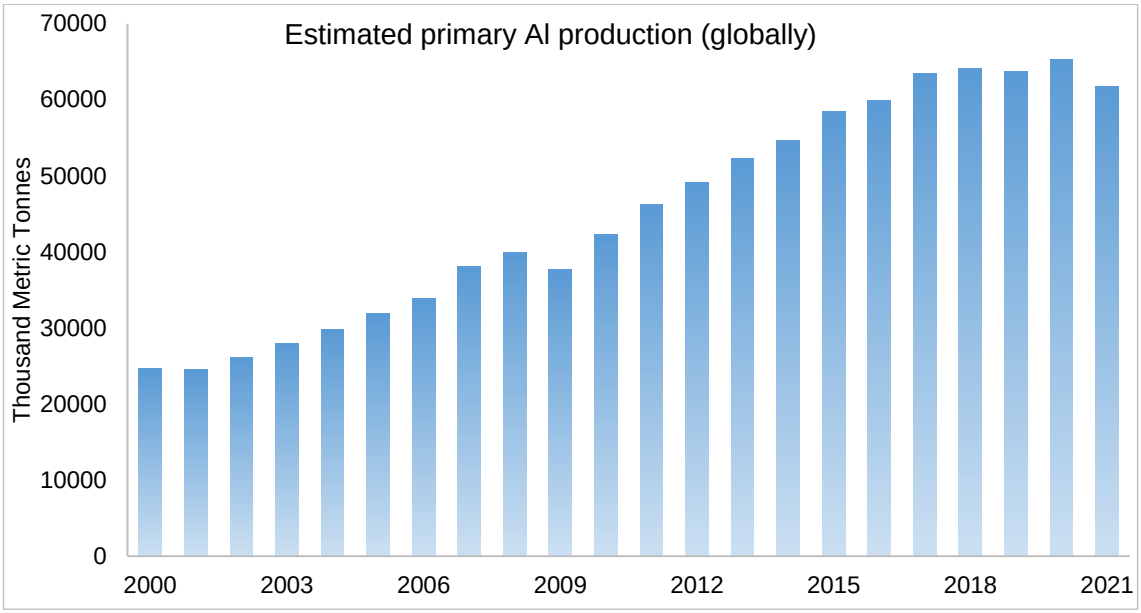

Figure 1.1: Estimated global data for primary Al production (Prosser et al. 2022).

Wide ranges of nanoparticles are used as reinforcement materials in order to improve the mechanical properties of pure Al and its alloys. The most common reinforcement materials used are ceramics, such as Aluminium Oxide (Al_2O_3), Titanium Diboride (TiB_2), Titanium Carbide (TiC), Silicon Carbide (SiC) and Boron Carbide (B_4C) (Shi and Wang 2020; Wang et al. 2020). In addition to these ceramics, carbon-based allotropes including Graphene (Gr) have attracted huge attention as a reinforcement element owing to their superior properties such as high elastic modulus (1 TPa), high mechanical strength (130 GPa), very good thermal (5300 W/mK) and electrical (6000 S/cm) conductivities (Saboori et al. 2018; Shi and Wang 2020). Furthermore, the strong carbon-to-carbon bonds allow Gr to improve the strength, thermal stability, and stiffness of the Metal Matrix Composites (MMCs) (Govindaraj et al. 2019).

Nevertheless, the milling technique and parameters play a crucial role in the as-fabricated parts in order to have a uniform distribution of Gr in composites without forming agglomerations (which is the main drawback of Gr) and achieve fully dense specimens (Ahmad et al. 2020). Ball milling (also known as mechanical

milling or mechanical alloying) is a dry powder processing technique for a small quantity of powder involving cold-welding, fracturing, diffusion and deformation of particles, owing to the repeatedly applied impact energy by the collision of the milling balls (Sopicka-lizer 2010; Gupta et al. 2017). More importantly, this technique (with unlimited milling and pause time combinations, different sizes of milling balls and large flexibility in milling atmosphere options) offers a wide range of solutions to achieve the desired powder morphology and reinforced particle distribution (Pourmand and Asgharzadeh 2020). With the aid of these parameters, requirements of powder size and morphology have to be thoroughly considered at this stage for post-processing techniques.

Because of the rapid fabrication of complicated geometries, short production lead times, environmentally friendly manufacturing, and inexpensive fabrication costs, Laser Powder Bed Fusion (LPBF) is gaining interest in many engineering sectors (Gu et al. 2015; Hu et al. 2018). This technique effectively combines several different manufacturing processes such as Computer Aided Design (CAD), Computer Aided Manufacturing (CAM) and Computer Numerical Control (CNC) in order to eliminate post-processing and accelerate the production rate (Wong and Hernandez 2012). Flowability, powder size and morphology, however, play a significant role in the LPBF process (Zhang et al. 2017; Han et al. 2019). Good flowability, spherical particle shapes and small powder size (1-100 μm) with a narrower Particle Size Distribution (PSD) range are required for LPBF in order to have a uniform and continuous layer (Han et al. 2016).

Various research about Gr and Al alloys in literature have been published using several approaches (i.e., hot-pressing and hot-rolling techniques), demonstrating that Gr has the capability of increasing some mechanical properties of as-

fabricated composites. However, GNPs reinforced AA2024 composite fabricated using the LPBF technique has not been uncovered, yet.

1.2 Research Aim and Objectives

The above studies illustrate that Gr nanoparticles can improve the mechanical properties of pure Al and its alloys when used in different milling and manufacturing techniques such as hot-rolling and hot-pressing. However, the impact of Gr on AA2024 manufactured using LPBF has yet to be determined. This study addresses the knowledge gap in this area by investigating the microstructural, mechanical properties and wear performance of Graphene Nanoplatelets (GNPs) reinforced AA2024 composite fabricated using LPBF. The focus of this work is to explore the effect of Gr concentration, milling and fabrication parameters on microstructure, microhardness, density, wear performance and tensile properties of the advanced composites. Hence, the main contribution of this research is developing an in-depth understanding of the relationship between the applied parameters and the obtained results, not only for raw AA2024 but also for Gr-reinforced composites which are extremely hard to study due to the extreme challenges (i.e., high crack susceptibility, reflectivity, accumulation and formation of Al_4C_3). More detailed information about the challenges is listed in the following chapter.

This aim will be achieved by addressing the following objectives:

1. To study the LPBF process of raw AA2024 in order to determine the optimum working parameters (i.e., laser power, scanning speed and hatch spacing) to fabricate nearly full dense specimens, investigate the microstructure (i.e., crystallite size, crack and porosity) and mechanical (i.e., UTS and

microhardness) properties of the as-fabricated specimens, and use the optimum parameters as a benchmark in all subsequent experiments.

2. To explore ball milling of advanced composite (GNPs/AA2024) powder in order to implement homogeneously dispersed Gr nanoparticles in the MMCs. One of the biggest challenges of Gr (which is agglomeration) as a reinforcement material has been studied. The flowability and compressibility of the advanced powder have been examined. Additionally, the Discrete Element Method (DEM) for flowability of the composite has contrasted with experimental work in order to demonstrate the effect of Gr in MMCs.
3. To study the LPBF process of the advanced composite in order to study the effect of the reinforced material on the composite. The different weight ratios of Gr (0.1, 0.2 and 0.5 wt.%) in the composite are prepared and fabricated using LPBF in order to find the optimum Gr percentage in the composite with regard to microstructural and mechanical properties (e.g., hardness, TS, wear behaviour). The best option among the applied parameters for the LPBF has been provided from the optimisation of raw AA2024. However, the scanning speed for the advanced composite was studied again.

1.3 Research Methodology

In order to accomplish the stated aim and objective above, the following methodology for the current research is employed.

- Renishaw AM250 metal Three-Dimensional (3D) printing system is used to conduct the experiments in this study. AA2024 powder (with -325 mesh size) was used to fabricate 6x6x7 mm^3 specimens. The three most effective parameters (laser power, hatch spacing and scanning speed) of the LPBF are selected to optimise the parameters.

- The ball milling technique is used to reinforce Gr to AA2024 because of the efficiency of the technique with regard to the homogeneity of the reinforced element in the MMCs. Another advantage of this technique is the availability of a wide range of processing parameters (i.e., milling/pause time, milling speed, Process Control Agent (PCA), weight ratio and size of milling balls). A small amount of powder is taken out at 0.5, 1, 2, 4, 8, 12 and 16 hr in order to see the morphological and microstructural evolution of powders.
- Milled powders under different weight ratios of GNPs (0.1, 0.2 and 0.5 wt.%) are used to fabricate cubic and tensile test specimens by a Renishaw AM250 LPBF system. The specimens were fabricated using various scanning speed parameters (from 195 to 727 mm/s). The other parameters (laser power and hatch spacing) are provided from previous experiments (raw AA2024). The schematic diagram of the composite (from powders to specimens) is shown in Figure 1.2. Mechanical and microstructural tests (which are also applied for raw AA2024 specimens) are investigated and compared with raw alloy. The ideal percentage of Gr in MMCs is determined.

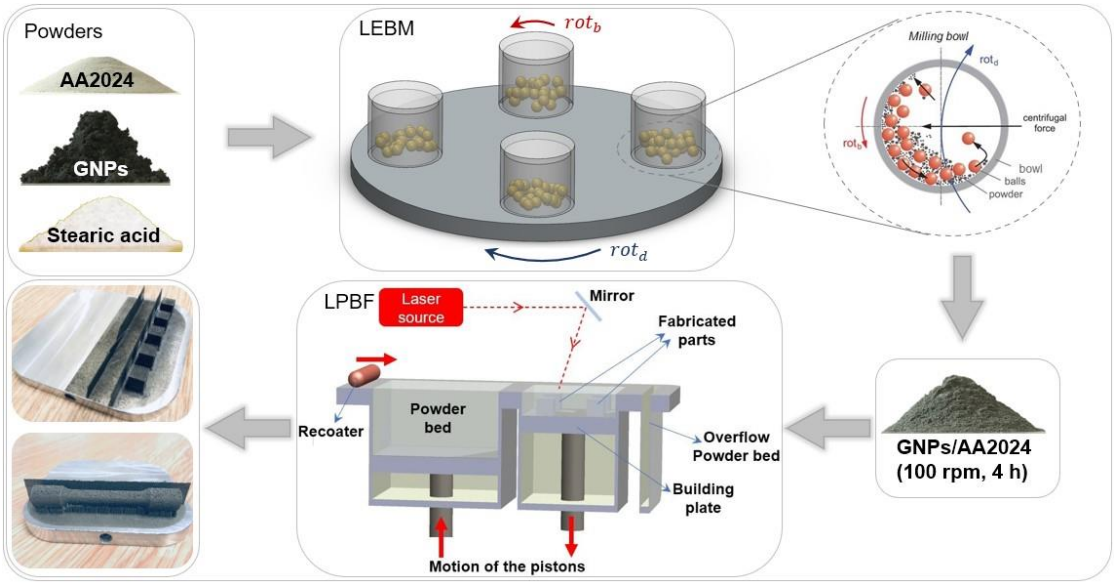

Figure 1.2: Schematic diagram of the fabrication steps from powder preparation to specimen buildings.

More detailed information about the methodology of the research is provided in Section 3.2.

1.4 The Organisation of the Thesis

Chapters in the present thesis are organised as listed below:

Chapter 1: In this chapter, the research motivation, aim and objectives, and methodology of the research are introduced.

Chapter 2: This chapter discusses the related studies in the literature that are relevant to the scope of this research. The role of the alloying elements of AA2024 is discussed. Then, studies about Gr (as a reinforcement material in pure elements), Al alloys and AA2024 are exemplified. Challenges of the alloy and Gr in composites are discussed. Additionally, ball milling and the LPBF process are briefly reviewed.

Chapter 3: In this chapter, as-received powder specifications and followed methodology are given. The methodology for each objective is represented in detail. Additionally, analysing and characterisation techniques of fabricated specimens and produced powders have been given in this chapter.

Chapter 4: The first objective of the thesis is addressed in this chapter. The effect of various energy densities (EDs) on the microstructure and mechanical properties of as-fabricated specimens (which were produced using LPBF) were investigated. The focus of this chapter is the mechanical and microstructural changes of the as-fabricated specimens produced under different processing parameters (i.e., laser power, scanning speed and hatch spacing). Thus, the contribution of this study is to increase an in-depth understanding of the relationship between ED, processing parameters, and the achieved results. The effects of these parameters on the microhardness, porosity, tensile strength (TS),

Archimedes' and relative densities are systematically analysed. Additionally, Analysis of Variance (ANOVA) is conducted using experimental results for porosity and microhardness.

Chapter 5: The second objective of the thesis is addressed in this chapter. The effect of milling speed and time are addressed in this chapter. First of all, the effect of milling speed (100 to 250 rpm) on GNPs-reinforced AA2024 is investigated by examining the PSD, the particle Diameter of Volume (Dv_{10}, Dv_{50} and Dv_{90}), and SEM images of the milled powder. Fast (250 rpm) and slow (100 rpm) milling speeds were examined after three milling times (0.5, 1 and 2 hr). Additionally, the effect of adding a PCA to the powder and milling balls is investigated. Secondly, the characteristic of the milled GNPs-reinforced composite under different milling times (0.5 to 16 hr) in terms of powder morphology, average grain size and flowability of the composite powder is investigated. Furthermore, the evolution of the microhardness of the milled powder by milling time was investigated. Moreover, a DEM of the milled powder without GNPs was investigated in order to estimate the repose angle for raw alloy and milled powders. Lastly, the effect of GNPs on repose angle is revealed with excluded GNPs particles in milled powder by contrasting the experimental and DEM simulation results. Exploring the characteristic of the milled powder is essential for understanding the suitability of the milled powder for the LPBF process.

Chapter 6: The third objective of this thesis is addressed in this chapter. In this chapter, advanced composites under the various percentage of Gr (0.1, 0.2 and 0.5 wt.%) are fabricated using LPBF. The effect of Gr concentration and scanning speed (195 to 727 mm/s) on the microstructural and mechanical properties of the composites have been investigated. Furthermore, a comparison of macroscale

(pin-on-disc test) and nanoscale (Atomic Force Microscopy (AFM) nano-scratching) wear performance of the composites is presented.

Chapter 7: The contributions, conclusion of this study and future work are highlighted in this chapter.

2. Chapter: Literature Review

This chapter reviews related studies regarding ball milling and LPBF of GNPs-reinforced advanced MMCs. This review is logically divided into six main parts. In the first part, Al and its alloy are reviewed. In addition, the microstructural and mechanical effects of alloying elements are presented. Additionally, challenges of the alloy (such as crack sensitivity and reflectivity) are highlighted. The second part discusses the effect of Gr as a reinforcement element. Studies about Gr-reinforced pure metals and Al alloys are listed. In the subsections, the advantages and challenges of Gr are reviewed. The third part of the chapter introduces the working principle of ball milling and discusses the effects of milling parameters. Eight different milling parameters and possible effects on processed powder are discussed. Similarly, the fourth part reviews the LPBF regarding typical process parameters. The parameters are classified into four categories (laser, scanning, external and powder related parameters). The most effective parameter from each section is criticised. Then, opportunities and potential applications of Gr-reinforced AA2024 are discussed with regard to the improved mechanical properties of the MMC after fabrication. Finally, the summary of this chapter is provided in the last section.

2.1. Aluminium and Its Alloys

2.1.1 Effect of Several Alloying Elements on Al

Al is a nonferrous metal and third ample material in the crust of the earth. The low density of Al (2.7 g/cm^3), which is almost three times lighter than steel (7.83 g/cm^3), makes it one of the most essential materials for global markets. Moreover,

Al has reasonable resistance to corrosion by water, a large variety of chemicals and physical agents, salt and so many other environmental factors due to the formation of self-protective oxide film (Davis 2001). Furthermore, Al and most of its alloys have high reflectivity, and electrical and thermal conductivity (Revie 2011). As shown in Table 2.1, primary components of Al alloys are Cu (series 2xxx), Mn (series 3xxx), Si (series 4xxx and 6xxx), Mg (series 5xxx), Zn (series 7xxx) and Li (series 8xxx).

Table 2.1: Series and the primary components of Al alloys (Davis 2001).

Alloy Series	Primary Components
1xxx	Al (99%)
2xxx	Cu (up to 6.3%)
3xxx	Mn (up to 1.5%)
4xxx	Si (up to 12.2%)
5xxx	Mg (up to 5.1%)
6xxx	Si (up to 1.4%)
7xxx	Zn (up to 11%)
8xxx	Li (up to 4.2%)

Table 2.2 and Table 2.3 show the chemical composition and some mechanical properties of the alloy (i.e., YS, Ultimate Tensile Strength (UTS), hardness and elongation) of the as-cast alloy based on different heat treatments (Khodir and Shibayanagi 2007; Revie 2011; Wang et al. 2018b). Despite the fact that Cu (as a principal element) has a dominant effect on the mechanical properties, the remaining elements (shown in Table 2.2) significantly influence the mechanical and microstructural characteristics of the alloy. In comparison to the as-fabricated alloy, heat treatment enhanced the mechanical properties of as-cast alloys. The improvement in YS and UTS can be attributed to the release of accumulated stress during heat treatment. Similarly, the hardness value increased owing to the smaller crystallite size as a result of heat treatments.

Table 2.2: The chemical composition of AA2024 (wt.%) (Revie and Uhlig 2008).

Alloy	Al	Cu	Mg	Mn	Si	Fe	Zn	Ti	Cr
AA2024	Bal.	4.35±0.55	1.5±0.3	0.6±0.3	<0.5	<0.5	<0.25	<0.15	<0.1

Table 2.3: Some mechanical properties of as-cast AA2024 (Khodir and Shibayanagi 2007; Revie 2011; Wang et al. 2018b).

Alloys	YS (MPa)	UTS (MPa)	Hardness (HV)	Elongation (%)
AA2024-T0	75	185	80	20
AA2024-T3	>295	>440	137	>15
AA2024-T4	325	470	137	17
AA2024-T6	>345	>427	135-145	>5

The alloying elements have a substantial effect on the microstructure and mechanical properties of the as-fabricated samples. Because Cu and Mg have a high percentage in the AA2024, they have a significant effect on the alloy. Notwithstanding, other elements also have a considerable effect on the alloy despite their limited quantity in composition. Effects of individual elements and co-elements are listed below.

i. **Copper (Cu) (4.35 wt.% ± 0.55) in Al:** Cu is the primary alloying element of 2 series of Al alloys and its weight ratio of it in alloys shows a variety between 2% and 6.5%. The addition of Cu (2-10 wt.%) to Al can influence the strength and hardness positively but decrease the elongation of the composite (Davis 2001; Prasad and Wanhill 2017). Cu reacts with Al and creates Al_2Cu formation in microstructure and the further incensement of Cu content causes to raise in the percentages of Al_2Cu (Shehadeh and Jalham 2016). Additionally, the strengthening of the alloy reaches a maximum value when Cu concentration is between 4 and 6% (Prasad and Wanhill 2017). Moreover, it has been reported that when the percentage of Cu is increased from 1.5 to 7.5 wt.%, TS (from 170 up to 410 MPa) and microhardness (from

54 up to 87 HV) improved on both heat-treated and non-heat-treated alloys (Shehadeh and Jalham 2016). Even though this alloy has poor corrosion resistance in comparison to the other Al alloys, commonly prefered for aircraft fuselage and wing skins, truck suspension parts, truck and aircraft wheels, and structural parts owing to the high strength-to-weight ratio at temperatures up to 150°C (Davis 2001). Several studies, on the other hand, focused on the Cu-GNP composite and reported significant improvement in hardness, UTS, YS and Young modulus about 50% (Dutkiewicz et al. 2015), 42.8% (Kim et al. 2014; Li et al. 2014), 114% (Chu and Jia 2014) and 61% (Tang et al. 2014) up to 8 vol% GNPs. Further increase in the volume of the GNP results in a reduction in the mechanical properties of the bulk composite owing to the agglomeration of reinforcement elements (Nieto et al. 2017).

ii. **Magnesium (Mg) (1.5 wt.% ± 0.3) in Al:** Mg is a secondary main element for 2 series of Al but the primary element of 5 and 6 series of Al-based on the weight ratio. Even though Mg is the secondary component of 2 series of Al, it consists of up to 4% of Mg in some alloys. Mg presence in Al-Cu alloys substantially increases both strength and ductility; however, manganese (Mn) shows an adverse effect on ductility compared to Mg (Prasad and Wanhill 2017). Si and Mg combine and form Mg_2Si which improves the strengthening of the alloy (Rana et al. 2012). Furthermore, the addition of 2% of Mg into Al improved hardness and TS by about 25% and 58% respectively (Girisha and Sharma 2012). Nonetheless, enhancing Mg from 0 to 2% and Cu from 4 to 6% improve the hardness of both cast and homogenized Al alloy (Nafsin and Rashed 2013). Furthermore, a tetragonal intermetallic Al_2Cu form was observed with the addition of Cu, and

orthorhombic intermetallic Al_2CuMg forms were detected with the further addition of Mg (Girisha and Sharma 2012). Additionally, a reduction in the grain size of casted material was determined due to the addition of Mg (Girisha and Sharma 2012). On the other hand, it has been observed that the overall mechanical properties of pure Mg were enhanced by the incorporation of GNPs using different manufacturing techniques (Chen et al. 2012; Rashad et al. 2014; Rashad et al. 2015). For instance, microhardness and UTS of the pure Mg were increased by 34% and 32% by adding 1% Al and 0.3% GNPs (Rashad et al. 2015).

iii. **Manganese (Mn) (0.6 wt.% ±0.3) in Al:** Manganese is the main element of 3 series of Al alloy. It has been reported that up to 0.6% of manganese in the compound for heat-treated and non-heat-treated alloys improves the TS from 70 to 410 MPa, and microhardness up to 87 HV (Shehadeh and Jalham 2016). On the other hand, manganese can improve corrosion resistance owing to the compound $MnAl_6$ and $(MnFe)Al_6$ forms (Revie and Uhlig 2008).

iv. **Others (<0.05 wt.%) in AA2024:** The alloy contains some elements less than 0.5% in the composition such as Iron (Fe), Chromium (Cr), Si, Titanium (Ti) and Zinc (Zn). However, they are very effective on the microstructure and mechanical properties of the content. On the other hand, the weight ratios of Fe and Si should be in balance in order to have FeSi intermetallic particles in the alloy. Surpassed Fe units create more Cu_2FeAl_7 that cause a dramatic loss of Cu and affect the strength and hardness detrimentally as mentioned above (Prasad and Wanhill 2017). Similarly, exceeded Si weight ratio in the composite can diminish the strength because Si also combines with Mg and forms Mg_2Si. Si is one of the remarkable examples of the significant effect of a small number of elements in alloy because of the fact

that the most critical range of Si on crack formation in the composition is between 0.17 and 0.8 wt.% (Prasad and Wanhill 2017). In opposition to the low percentage of Si, a particularly higher percentage of Si between 1.5 and 6% in Al alloy increases the TS from 120 to 150 MPa, and fluidity is also enhanced in consequence of the addition of Si, which decreases the melting point (Kumar et al. 2015). Contrary to Si, increased Fe element in Al-Si casting alloys despite low Si content can cause to increase in the porosity (Taylor 2004). The Fe weight ratio in AA2024 is under the Fe critical level calculation related to Si concentration $[Fe_{crit} \approx 0.075 \times (Si\ wt\%) - 0.05]$ (Taylor 2004).

2.1.2. Effect of Heat Treatment

Heat treatment is a post-processing procedure that involves heating and cooling on produced specimens in order to alter the combination of mechanical properties or microstructure without affecting physical shape. The heat treatment and cooling process of the metal resulted in phase transitions and structural alterations, which may change the mechanical properties and microstructure of specimens (Yahaya et al. 2020). Depending on the treatment process (i.e., T3, T4 and T6, especially for AA2024), several heat treatment cycles (such as different configurations of temperatures and times) may be utilised.

Some unique peculiarities that come with LPBF (for instance; high cooling rate, heating and cooling cycle on the solidified metal, remelting (or re-solidification) of previous layers due to the overlapping) cause additional residual stresses, epitaxial growth on the underlying layers and development of Strongly Supersaturated Solid Solutions (SSSS) (Fiocchi et al. 2021). Thermal treatments might be one of the other potential solutions to release these stresses in the manufactured specimens in addition to the processing parameter optimisation.

Typical heat treatment involves three stages including solution heat treatment, quenching and age hardening (Sjölander and Seifeddine 2010). The initial stage involves a relatively high temperature (around 500°C) to dissolve Cu and Mg-rich particles that were produced during the solidification of the LPBF process in order to achieve a high and homogeneous concentration of the alloying elements in a solid solution (Sjölander and Seifeddine 2010). Then, in order to create a solid solution that is supersaturated with solute atoms and vacancies, the quenching stage is often carried out at room temperature. Finally, the age hardening stage can be performed at either room temperature (natural ageing) or a reheating temperature (artificial ageing, for instance, 150-210°C for 2-5 hours) to produce precipitation from the SSSS (Sjölander and Seifeddine 2010; Yahaya et al. 2020).

The Al-Cu-Mg alloys exhibit a considerable improvement in strength following heat treatment owing to the production of nm-sized “S phase” of Al_2CuMg precipitates and “θ' phase” of $CuAl_2$ during age hardening with reheating (Schuster et al. 2021; Kumar et al. 2022). Mg provides a major contribution to the specimen's strengthening at this point because of the acceleration of Al-Cu alloys' natural ageing. When the mass ratio of Cu to Mg is greater than 2, and Mg to Si is greater than 1.7, the "S" phase is generated (Rahmati et al. 2021). The AA2024 alloy provides both conditions. Additionally, when the Mg to Si mass ratio of Al-Cu-Mg alloy is close to 1.7, the principal strengthening precipitates are Mg_2Si and Al_2Cu (Majimel et al. 2004).

On the other hand, all phases formed during the solidification of the LPBF process do not easily dissolve in structure as β-Mg_2Si and θ- Al_2Cu. For instance, the phases containing Fe (i.e., π-$Al_8Mg_3FeSi_6$ and α-$Al_{15}(Fe,Mn)_3Si_2$) are hard to dissolve (Crowell and Shivkumar 1995; Moustafa et al. 2003). However, Mg and Cu containing phases have to dissolve in structure for the AA2024 alloy to reach

its full ageing capability. Undissolved Cu and Mg atoms during solution treatment and age hardening are not available to improve the strength via precipitation hardening (Sjölander and Seifeddine 2010).

2.1.3. Challenges of Fabricated AA2024 Samples using LPBF

There are some noticeable challenges in studying high-strength Al-Cu-Mg alloys such as reflectivity, flowability and metallurgical defects including cracks, oxidation and loss of alloying elements. The remaining sections of this part emphasize the mechanism of their formation, key affecting factors, and remedial measures for each of these issues.

a) Reflectivity

The powder's reflectivity is an important aspect when performing the AM process to create fully dense specimens. The high reflectivity of these elements (because of the high density of free electrons (Ion 2005)) also prevents absorption of the laser power, and therefore complete melting of the powder is restricted; it has been reported that Al can only absorb 7% of the laser energy at 1 µm wavelength (Gu et al. 2012). Si, however, can absorb 70% of the laser energy, which assists in melting the Al powder by transferring the absorbed energy into the Al (Sercombe and Li 2016). However, the Si percentage in the alloy is only 0.5 wt.%, which again limits the laser energy absorption. Consequently, processing with lower EDs can lead to an increase in the melt-pool viscosity, irregular surfaces, and unmelted powder particles; however, higher ED may create material stacking, which causes material bumps on the surface owing to the movement of the molten material from the centre to the back section of the melt-pool (Dadbakhsh et al. 2019). Moreover, excessive ED may lead to the formation of

surface balls, discontinuous scan tracks, and unsmooth surfaces due to the high evaporation of the elements (Dadbakhsh et al. 2019).

b) Flowability

Flowability of the powder for AM applications is vital to have well separated and uniform powder layer. Typically, aluminium has poor flowability. Low density and non-spherical form are two characteristics that contribute to the poor flow of aluminium powder (Sercombe and Li 2016). When spreading aluminium alloy powder in the LPBF process, poor fluidity of the aluminium alloy powders causes agglomeration, which reduces the layer quality and causes the powder layers to be irregular in thickness (Zhang et al. 2019). Additionally, powder features, including morphology, surface chemistry, packing density, hydroxides and oxygen concentration, have a big impact on flowability of a powder, causes numerous defects, and eventually result in low relative density and bad mechanical properties (Kotadia et al. 2021).

c) Metallurgical Defects

i. Porosity

The frequent types of porosities in LPBF produced are the porosities caused by insufficient melting (lack of fusion) energy, the trapping of gases in the melt-pool (gas porosity) and instabilities in the process parameters. (Olakanmi et al. 2015; Abdel-Aziem et al. 2022). Lack of fusion porosity is primarily triggered by improperly adjusted process parameters, including laser power, hatch spacing, scanning speed, layer thickness, laser wavelength and others. Due to insufficient dissipation of the laser ED, coherent bonding cannot be achieved at the top of the preceding layer, which results in a lack of fusion porosity (Olakanmi et al. 2015).

Another porosity formation during the LPBF process is entrapped gas bubbles in the interlayers. Small gas pores (below 5 µm in diameter) may develop as a result of moisture in the stock of powder and exceeded ED used. When the moisture reacts with aluminium to create Al_2O_3, the remaining hydrogen can be absorbed by the melted metal during the cooling time (Kotadia et al. 2021). Furthermore, inefficient process parameters cause additional entrapped gas bubbles in the melt-pool during the LPBF process. The capability of controlling the laser energy dissipation, solidification cracking, porosity, and solidified microstructure in the powder bed might be offered by PW laser systems (Olakanmi et al. 2015).

On the other hand, keyhole pores (>30 µm in diameter) with almost spherical shape are associated with the keyhole mode of melting, arising from intense ED (Kotadia et al. 2021; Abdel-Aziem et al. 2022). Extreme ED results in the vaporization of alloying elements (which have lower melting points) in the form of gas bubbles. These bubbles can be entrapped by laser beams and drawn to the bottom of the melt-pool by convective currents (Narasimharaju et al. 2022). Thereby, the gas bubbles cannot arise and escape from the melt-pool due to the rapid solidification rate. Correspondingly, excessive local ED is more likely to generate keyhole pores in certain parts of the specimens (i.e., border region and periphery of inner volume) The melt poles at border sides produce excessive heating owing to the low heat transfer of the powder at that region (Kotadia et al. 2021). Similarly, a higher local ED results from the laser's acceleration and deceleration during the switch in scan direction at the periphery region of inner volume (Kotadia et al. 2021). These porosities considerably reduce the fatigue performance of the produced specimens: however, it can be avoided by adjusting and optimising the energy input in the relevant locations.

Furthermore, conduction and keyhole mode melting are the two distinct operational melting modes that often exist in laser beam operations, depending on the applied ED. Heat conduction is the predominant heat transmission process when the power density drops below a specified threshold value, especially for determining the depth of the generated melt-pools, which causes conduction mode melting (Patel and Vlasea 2020). Melt-pools produced in conduction mode often have semi-circular cross sections. Additionally, the evaporation of metals during conduction mode melting is considered minimal due to low ED (Ion et al. 1992). The keyhole mode, however, may be appeared once the ED surpasses the threshold value, causing a deep and narrow vapour cavity to form in the melt-pool because the recoil momentum pressure (also known as recoil pressure) of the metal vapours is greater than the combined effects of surface tension and hydrostatic pressure (Li et al. 2022). The predominant mechanism of convective heat transport inside the melt-pool is thermo-capillary convection (also known as Bénard–Marangoni convection) (Rai et al. 2007).

ii. Cracking

Aluminium and its alloys manufactured by LPBF have a very high potential to crack. The heat-treatable 2 and 6 series of Al alloys are known to be more prone to solidification cracking during laser processing than work hardening 5 series of Al alloys (Olakanmi et al. 2015). The reason behind it could be explained by their high solidification temperature range, high coefficient of thermal expansion, residual stresses and significant solidification shrinkage of the alloys (Olakanmi et al. 2015). Liquation and solidification cracks can frequently occur in LPBF-produced parts, where they undergo a similar process to welding (Karg et al. 2014; Olakanmi et al. 2015). The presence of many alloying additions in heat-treatable alloys, which precipitate low melting point eutectic phases, has been

associated with liquation cracks (Cao et al. 2003). Liquation cracks may be prevented or minimised by reducing the dissipated ED.

The solidification cracks may develop when the welding is subjected to significant tensile stress during the solidification time. Additionally, the form of the solidifying ductility curve of material has been found to be correlated with the susceptibility to solidification cracks (Liu et al. 2006). It has been also demonstrated that the dendritic coherence temperature range and the amount of liquid present during freezing have a significant influence on the solidification cracking, metallurgically (Liu et al. 2006; Brandl et al. 2012). Cracking can be prevented by modifying the composition of the melt pool using alloying elements that have a narrower critical solidification range (Olakanmi et al. 2015).

Even though the protective inner gas (i.e., Argon and Nitrogen) in the building chamber is crucial in preventing oxide film cracking, there is always a potential that a small amount of undesired oxygen content may be present in the building chamber due to the invisible air filling among the powder particles which causes oxide film cracking (Narasimharaju et al. 2022). Furthermore, passive oxide films on powder surfaces can also increase crack formation. The addition of Mg and Si to Al alloys during the gas atomisation process might be expected to negatively alter the nature of the oxide film of the alloy (Olakanmi et al. 2015). Particularly, Mg and Si encourage the thin-layer production of spinel ($MgAl_2O_4$) and mullite (Al_2O_3 SiO_2), respectively (Olakanmi et al. 2015). Additionally, it has been reported that the stirring action of the laser beam and Marangoni flow cannot completely evaporate the micrometre range oxide layers (10-100 µm) of uneven geometry (Narasimharaju et al. 2022).

On the other hand, it has been also reported that crack initiation and propagation generally occur when the temperature gradients and residual stresses are high,

as the cooling rate of the melt-pool can reach 108 K/s (Zhang et al. 2017). These types of cracks are also called hot-tearing cracks or fatigue cracks. Figure 2.1 shows the relative crack sensitivity of the binary alloy (Al-Cu, Al-Mg and Al-Si) compositions. Al alloys with a Cu content below 5 wt.%, Mg content under 4 wt.% and Si content under 2 wt.% are most susceptible to relative cracking (Sampath 2009). The Al percentage in the binary alloy accounts for the balance of the alloying elements in each composition (Al-Cu, Al-Mg and Al-Si). The weight ratios of Cu (4.9 wt.%), Mg (1.8 wt.%), and Si (0.5 wt.%), therefore make AA2024 particularly challenging to process. Moreover, possible evaporation of the alloying elements (such as Mg, owing to the low boiling point) may cause the loss of the elements and bring the weight ratios closer to the peak points of the relative crack sensitivity curves (Mathers 2002), further increasing the relative crack sensitivity more for the AA2024. Consequently, the chemical composition of AA2024 (see Table 2.2) demonstrates that this alloy satisfies most of the conditions above to become a very critical alloy in terms of relative crack, and it explains the enormous gap of the alloy in the literature.

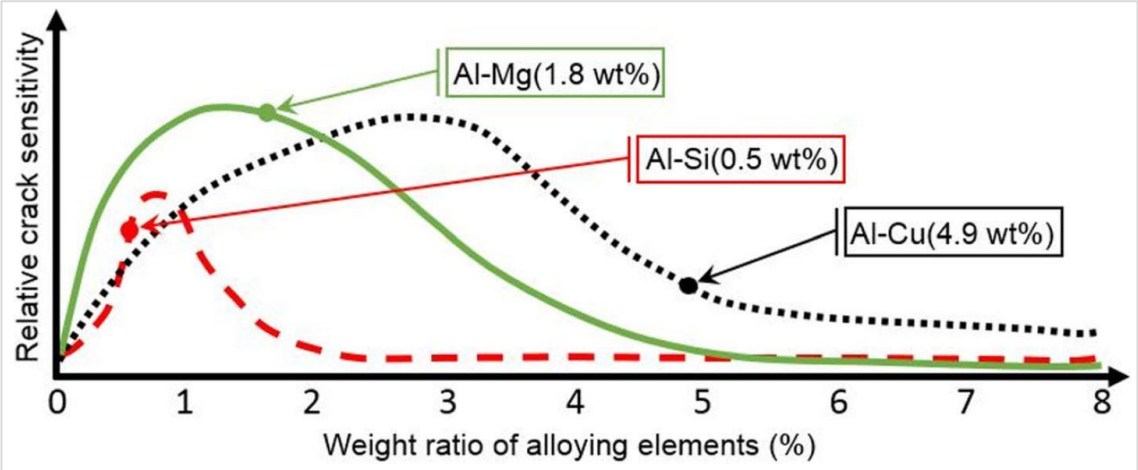

Figure 2.1: The effect of alloying elements on the relative crack sensitivity of the binary alloys (Mathers 2002; Sampath 2009; Galy et al. 2018)

d) Loss of Alloying Elements

When the surface temperature of the molten melt pool is higher than the boiling point of the alloying elements at very high laser fluences, vaporization occurs. Additionally, energy delivery systems (such as laser types) also have a big influence on the loss of alloying elements associated with ED (Pastor et al. 1999). The losses of alloying elements will unavoidably result in a divergence from the original alloy composition and alteration in performance due to the super-heated melt-pool. Hence, the microstructure and mechanical properties of the manufactured components may substantially vary as a result of the vaporization of volatile elements during LPBF. Loss of alloying elements results in microstructural defects such as keyholes, pores, spatters, voids, cracks, and unmelted tracks, thus lowering the mechanical performance of parts manufactured with LPBF (Narasimharaju et al. 2022). For instance, dissipation of elemental Mg from an Al alloy diminishes the stability of the scanning tracks, yield strength, elongation, formability, corrosion resistance, solidification cracking susceptibility and hardness as well as precipitation strengthening effect (Collur et al. 1987; Zhao and Debroy 2001; Zhang et al. 2019). Furthermore, the loss of Al alloying elements might also have a significant impact on the amount of non-spontaneously nucleated particles in the melt-pools, which is crucial for the development of columnar grains (Zhang et al. 2019). Despite the fact that the rate of evaporation rises with laser power, an alloying content may change at low laser powers because the melt-pool is small and has a high surface-to-volume ratio (Olakanmi et al. 2015; Abdel-Aziem et al. 2022). Additionally, solid solution strengthening of the post-processed specimens (especially simple T4, T5 and T6 post-heat treatment) predominantly comes from Mg, and the specimens can suffer from Mg evaporation (Rometsch et al. 2022). Since excessive Mg

evaporation is known to impact printability and lead to defect development at higher Mg concentrations, care must be taken to prevent Mg evaporation. To minimise or prevent alloying evaporation, laser processing parameters (especially laser power and scanning speed) can be varied to determine optimum parameters. Furthermore, it is also possible to utilize fluxing materials to compensate for the detrimental effect of an alloying element loss (Olakanmi et al. 2015).

2.2. Graphene (Gr)

Gr is considered a reinforcement material owing to its high strength, high Young's modulus, low specific gravity, chemical and mechanical compatibility with the matrix material, and high electrical and thermal conductivity as shown in Table 2.4 (Saboori et al. 2018). Particularly, low density and high strength are crucial attributes in the transportation industry (such as automotive and aerospace). Gr is a film or sheet of two-dimensional atomic carbon monolayer which is like a honeycomb structure. Even though Gr was first discovered and studied in 1947, it could not attract much attention until 2004. Gr was successfully synthesized in a lab and studied (Geim and Novoselov 2007).

Table 2.4: Properties of Gr

	Gr	Ref.
Density	1.05 g/cm^3	(Pourmand and Asgharzadeh 2020)
Surface area	2630 m^2/g	(Pourmand and Asgharzadeh 2020)
Melting point	5727 °C	(Pourmand and Asgharzadeh 2020)
YS	912 GPa	(Dorri Moghadam et al. 2015)
Young's modulus	500 – 1000 GPa	(Pourmand and Asgharzadeh 2020)
Tensile strength	101 – 130 GPa	(Dorri Moghadam et al. 2015)
Yield strength	912 GPa	(Dorri Moghadam et al. 2015)
Thermal conductivity	4840 – 5300 W/mK	(Pourmand and Asgharzadeh 2020)
Electrical conductivity	10^8 S/m	(Pourmand and Asgharzadeh 2020)

2.2.1. Studies about Gr as a Reinforcement Material

Most of the Gr reinforcement studies in the literature highlight that Gr has the capability to increase the mechanical properties of some pure elements and their alloys. Derivatives of Gr (i.e., GNPs, Carbon Nanotube (CNT) and Graphene-Oxide (GO)) and layers (e.g., single layer, few-layer and multilayer) of Gr have been studied under different mixing techniques (such as ultrasonic dispersion, novel powder mixture and ball milling) and manufacturing methods (i.e., hot pressing, laser sintering and LPBF) techniques. Effects of Gr on pure elements, and alloys including AA2024 have been depicted below.

i. Gr-Reinforced Elements

Studies with pure elements (such as Ti, Cu, nickel (Ni), Al and Mg) show the positive effect of Gr on a number of mechanical properties (see Table 2.5). The effect of different weight ratios on single-layer GO has been studied (Hu et al. 2016b). They used ultrasonic dispersion mixing and laser sintering techniques and achieved a 300% increase in the hardness of 2.5 wt.% GO reinforced pure Ti. Additionally, different percentages of GNPs-reinforced pure Ni are mixed by wet mixing technique and manufactured using laser sintering technique (Hu, et al., 2016). The hardness was improved by 175% when 5 wt.% Gr nanoplatelets were reinforced (Hu, et al., 2016). Similarly, the hardness of pure Al was improved by 75% when a 2.5 wt.% multi-layer Gr sheet was reinforced using planetary ball milling and laser printing technique (Hu et al. 2018). Another research shows that Gr nanosheets improve the hardness, UTS and elongation of the pure Cu element processed using HEBM and hot-press sintering technique (Yue et al. 2017). The strength and hardness of the composite were increased by 28% and 15% respectively by adding 0.5 wt.% Gr nanoplatelets (Yue et al. 2017). On the

other hand, liquid-based mixing of Mg, Al and Gr by hot-pressing technique results in progress on the UTS, YS and Young's modulus (Rashad et al. 2015). These elements (Al, Cu, Mg, Ti and Ni) are some alloying elements of AA2024 and demonstrate significant positive effects on mechanical properties with the addition of Gr and allotropes.

Table 2.5: Effect of Gr as a reinforcement material in pure elements.

Matrix	Reinforce.	Methods	Results	Ref.
Ti	● Single layer GO (1 / 2.5 / 5%)	● Ultrasonic dispersion ● Laser sintering process	● The hardness: 180 (raw), 630 (1), 742 (2.5%) and 509 HV (5%).	(Hu et al. 2016b)
Cu	● Gr nanosheets (0.5 / 1 / 2%)	● HEBM ● Hot-press sintering	● The hardness: 47 (raw), 53 (0.5%), 42 (1%) and 38 HV (2%). ● The UTSs: 185 (raw), 230 (0.5%), 135 (1%) and 110 Mpa (2%). ● The elongations: 21 (raw), 24 (0.5%) 11 (1%) and 8% (2%).	(Yue et al. 2017)
Ni	● GNPs (1 / 5 / 10%)	● Dispersing agent Polyvinyl alcohol in deionized water. ● Laser sintering	● The hardness: 220 (raw), 561.5 (1%), 605.2 (5%) and 519 HV (10%). ● The average modulus: 124.3 (raw), 201.3 Gpa (reinforced).	(Hu et al. 2016a)
Al	● Multi-layer Gr sheets (0.5 / 1 / 2.5%)	● Planetary ball milling ● Laser 3D printing	● The hardness: 38 (raw), 47.1 (0.5%), 49.6 (1%) and 66.6 HV (2.5%). ● Al_4C_3 improved the wettability. ● Higher Gr content increased the agglomeration and so reduced the hardness.	(Hu et al. 2018)
Mg	● Al (1%) ●GNPs (0.09 / 0.18 / 0.3%)	● Liquid-based mixing ● Hot-press sintering	● The UTSs: 186 (raw), 206 (0.09%), 223 (0.18%) and 246 Mpa (0.3%). ● The hardness: 41 (raw), 48 (0.09%), 51 (0.18%) and 55 HV (0.3%). ● The Young's modulus: 5.98 (raw), 13.4 (0.09%), 12.18 (0.18%) and 13.84 Gpa (0.3%).	(Rashad et al. 2015)

ii. Gr-Reinforced Al Alloys

The effects of Gr and allotropes on Al alloys including AA2024 by different milling techniques (i.e., planetary and HEBM) and different manufacturing methods (i.e., hot rolling and pressing) have been studied (see Table 2.6). HEBM and Selective Laser Melting (SLM) techniques were used in order to fabricate the GNPs-reinforced AlSi10Mg alloy specimens, and limited improvement on the UTS

(2.7%) and YS (5%) has been reported (Wang et al. 2018c). A similar study involving the same matrix material and Multi-Walled Carbon Nanotube (MWCNT) found that long milling time and the higher rotation speed of the milling container increase the agglomeration of advanced composite (Zhao et al. 2016). They also reported that laser power has in direct proportion to hardness and density. A remarkable rise in the YS of FLG-reinforced AA2024 composites up to 100% has been reported (Shin and Bae 2015). A similar study involving the same alloy has been conducted with FLG and CNTs, and the compressive YS of advanced composite improved between 130 to 230% regarding pressing temperatures (Shin et al. 2016). Besides, TS and YS of 2 series of Al alloy have been improved by adding Gr respectively 25% and 50% (Yan et al. 2014).

Table 2.6: Effect of Gr and derivatives as reinforcement materials on Al alloys

Alloys	Reinforce.	Methods	Results	Ref.
AlSi10Mg	● FLG (0.5%)	● HEBM ● SLM	● Porosity was increased by adding GNPs. ● The UTSs: 337 (raw) and 346 Mpa (0.5%). ● The Yss: 234 (raw), 246 Mpa (0.5%). ● The elongations: 3% (raw), 3.2% (0.5%).	(Wang et al. 2018c)
	● MWCNT (1%)	● Slurry ball milling ● SLM	● Long milling time and higher rotation speed increased the agglomeration. Best results were achieved from 100 rpm and 1 hr. ● The hardness: 100±5 (raw), 123±20 (1%). ● Higher laser power increased density and hardness.	(Zhao et al. 2016)
AA2024	● MWCNT (5%) ● FLG (0.5%)	● HEBM ● Hot pressing	Compressive YS*: ● (at 250°C) 60 (raw), 120 (Milled), 160 (5% MWCNT), 200 Mpa (0.5% FLG), ● (at 300°C) 50 (raw), 70 (Milled), 100 (5% MWCNT), 115 Mpa (0.5% FLG), ● (at 350°C) 35 (raw), 55 (Milled), 95 (5% MWCNT), 100 Mpa (0.5% FLG)	(Shin et al. 2016)
	● FLG (0.3 / 0.5 / 0.7%)	● HEBM ● Hot rolling	● The YS: 350 (raw), 480 (0.3%), 585 (0.5%), 700 Mpa (0.7%). ● The elongation at failure: 4%.	(Shin and Bae 2015)
2 series of Al alloy	● Gr (0.15 / 0.5%)	● Ball milling ● Hot-extrusion pressure	● The TS: 373 (raw), 400 (0.15%), 467 Mpa (0.5%). ● The YS: 214 (raw), 262 (0.15%), 319 Mpa (0.5%).	(Yan et al. 2014)

***** Compressive YS values are estimated from the YS figures.

2.2.2. Challenges of Gr Reinforcement

Owing to the exclusive properties of Gr (such as low density and high strength), it is a widely preferred reinforcement material. However, Gr has some serious drawbacks to overcome. One of the biggest disadvantages of using Gr as a reinforcement is poor dispersion caused by the strong interplanar Van der Waals interaction (Chen et al. 2018). Different methods (such as ball milling, flake powder metallurgy and molecular-level mixing) have been studied in order to eliminate agglomeration of Gr in advanced MMCs. It has been reported that ball milling can provide homogenous dispersion of Gr particles in a matrix (Pérez-Bustamante et al. 2015). However, the same research stated that further increasing of milling time by one hour negatively affected the Gr dispersion.

Additionally, Gr reacts with Al over 500°C and forms a brittle phase of aluminium carbide (Al_4C_3) (Huang et al. 2019). This inter-facial Al_4C_3 has a detrimental impact on the mechanical properties of as-fabricated specimens using AM technique (Su and Teng 2021). The Al_4C_3 is known to develop when carbonaceous nanomaterials, such as Gr, react with the Al matrix during the formation of composites or subsequent treatment at high temperatures for a prolonged time (Pourmand and Asgharzadeh 2020). The following interfacial reaction can occur between Al and Gr elements as:

$$4Al(s) + 3C(s) = Al_4C_3 \quad (2.1)$$

The Al_4C_3 phase predominantly forms at the edge of Gr because the rich carbon dangling bonds enable Gr edges to be more reactive and defective than its basal plane (Banhart et al. 2011). The structural integrity, size, and shape of graphene may be altered to efficiently control the formation of Al_4C_3. Additionally, PCA can be adopted to prevent the formation of Al_4C_3 during the milling stage of the metal

matrix and Gr. Due to effective PCA, Al alloy and Gr are prevented from having direct contact, and the interfacial reaction was transformed from Al_4C_3 and Al_2OC to Al_2O_3 (which has 30% better interface bonding between Al and Al_2O_3) (Su and Teng 2021).

The majority of investigations on Al-Gr composites show that, while adding Gr initially improves mechanical qualities, surpassing a specific level of Gr in the composite causes a reduction in mechanical properties especially strength (Güler and Bağcı 2020). However, a certain amount of Al_4C_3 may enhance the wettability, thus the mechanical strengthening of the fabricated specimen can be affected positively (Hu et al. 2018; Su and Teng 2021). The presence of a significant amount of Gr particles in composite increases the probability of agglomeration of Gr particles, and the formation of brittle Al_4C_3 in the structure that causing the failure of strength for excessive Gr percentages (Pourmand and Asgharzadeh 2020).

2.3. Ball Milling

Ball milling is a technique that can be used for various purposes such as particle size reduction, comminution and intermixing of multiple materials. Even though there are plenty of milling techniques (i.e., attrition, spex shaker, low energy and vibrator mixer), the most common technique for fast/slow speed milling of solid particles is planetary ball milling (Gupta et al. 2017). In this technique, the main disk comprises two or four milling bowls. Due to the high rotation speed, two or four of them should be filled out with the same amount of powder in order to keep the balance of the disk during the process.

2.3.1. Working Principle of Planetary Ball Milling

Most laboratory-scale planetary ball milling machines are capable of processing small-size feeding volumes for instance Pulverisette-5 (P5) has approximately 250 g feeding capacity for each bowl. Therefore, increasing rotation speed up to 1000 rpm provides high energy inside the milling bowls.

Rotation of disk ($\mathrm{rot_d}$, clockwise) and bowls ($\mathrm{rot_b}$, anticlockwise) have reversed directions around their centre points as can be seen from Figure 2.2. Due to the different rotation axes of the main disc and milling bowl, reverse rotation creates a 'D-shape' movement of balls inside the bowl under the influence of Coriolis and centrifugal forces of disk and bowl rotations. These forces help to increase the kinetic energy inside the bowl at the same time. Consequently, ball-to-ball and ball-to-wall high-impact energy effectively grind and blend the material which is placed in the milling bowls.

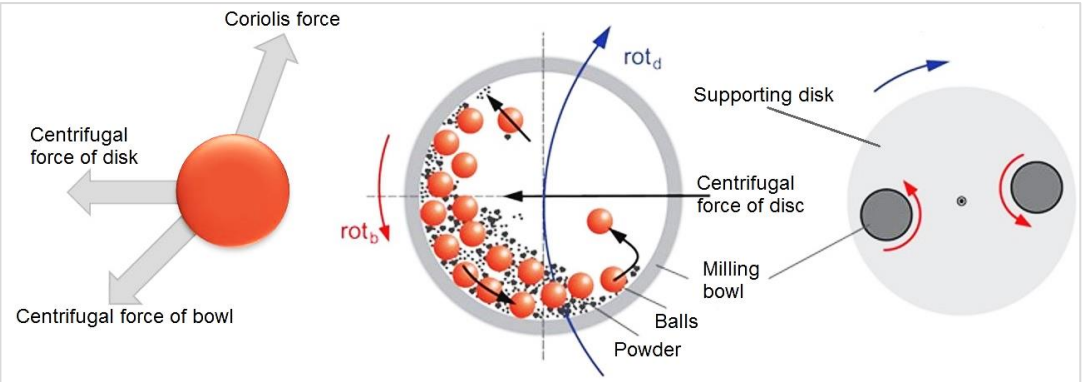

Figure 2.2: Working principle of ball milling (Wilkening et al. 2017).

2.3.2. Effect of Ball Milling Parameters

The mechanical milling process and parameters are essential in order to have homogeneously dispersed reinforcement material in advanced composites. Many internal and external determinants can affect the quality of the milled composite as shown in Figure 2.3.

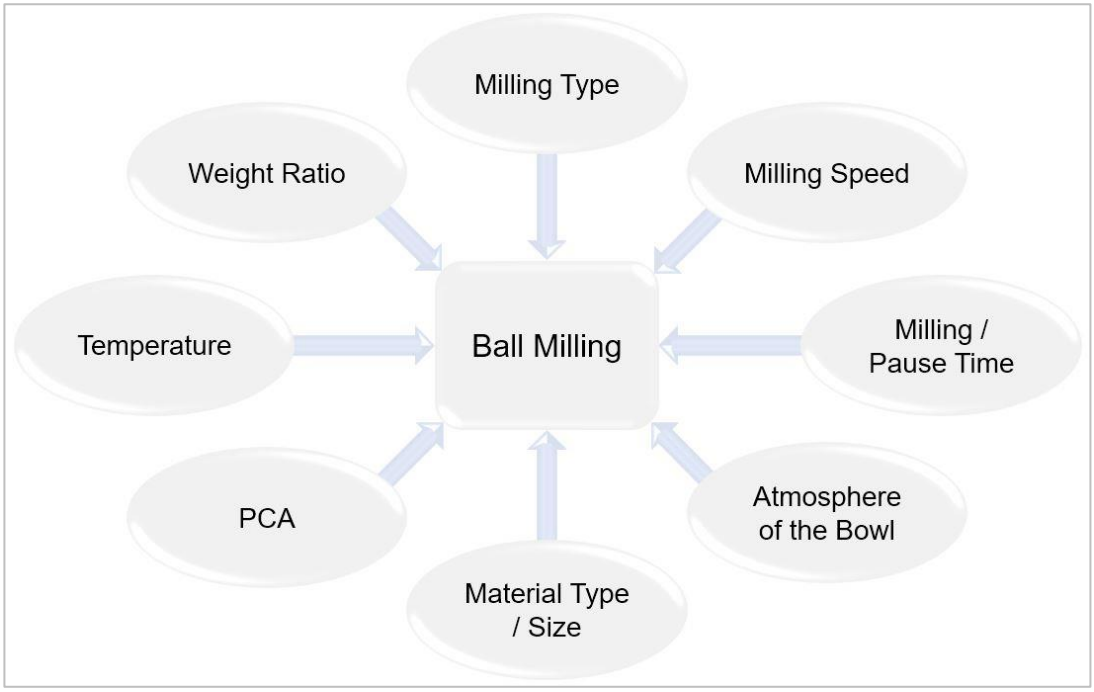

Figure 2.3: Ball milling parameters that affect the quality of milled composite.

i. **Milling type:** The selection of wet and dry milling based on reinforcements and matrix materials plays a vital role in order to achieve desired size reduction rate, size distribution, surface morphology, and degree of agglomeration (Jung et al. 2015).

ii. **Milling speed:** Planetary ball milling technique provides a wide range of milling speeds. This range both have the same benefits such as having high impact energy at high speed, and some drawbacks such as the high temperature at high velocity. Additionally, it has been reported that furthering the milling speed than a critical point can intensify the agglomeration of powder in the composite at the same time (Zakeri and Vakili-Ahrarirudi 2012). The optimum milling speed is changing for reinforcing elements and matrix.

iii. **Milling/pause time:** Other significant parameters, in which optimisation is highly required, are milling and pause time. The microhardness of TiC reinforced Al6005 was improved from 70 to 225 $HV_{0.01}$ by increasing the milling time up to 10 hr (Cabeza et al. 2017). However, longer milling time

caused to increase the contamination, temperature in milling bowls and undesirable phase transformation (Gupta et al. 2017). Pause time is effectively used to avoid high temperatures and cool the milling bowls and balls.

iv. **Atmosphere of the bowl:** The primary effect of the milling atmosphere is the chemical reaction of milled powder with atmosphere gas due to high impact energy. Correspondingly, Al is highly susceptible to contamination. Although argon gas is widely used for planetary ball milling, other gasses such as nitrogen, helium, hydrogen, ammonia, and vacuumed air are used, as well (Suryanarayana 2001; Gupta et al. 2017). The type of inner atmosphere affects the oxidation of powder and the nature of the final phase (Suryanarayana 2001).

v. **Material type/size:** The material type of milling bowls and balls are significant due to the fact that improper material choice of milling bowls and balls can cause contamination owing to the collision of balls to the inner wall of the bowl. Moreover, the powder cannot be milled unless the powder is harder than a milling ball or bowl. Hence, hard materials are chosen in general such as hardened steel, hardened chromium steel, tungsten carbide, stainless steel, tool steel, zirconia, and bearing steel (Suryanarayana 2001; Baláž 2008).

One of the factors to increase the impact forces which could be transferred to the powder is the selection of high-density and large balls. 10 mm diameter size of milling balls is commonly preferred for planetary ball milling (Gupta et al. 2017). Notwithstanding, different size of balls helps to randomize the track and roll along with the same size of milling balls following the regular path (Baláž 2008).

vi. **Process Control Agents (PCA):** Agents are preferred to reduce the cold welding between powder-to-powder, powder-to-ball and powder-to-wall. Three different phase forms (i.e., solid, liquid and gas) of agents have been used in literature. The most common agents are stearic acid, methanol, ethanol, argon, benzene, and hexane (Suryanarayana 2001). This wide range of agents demonstrates that the selection of appropriate agents depends on the chemical and thermal constancy of the agent and the cold welding characteristic of powder (Suryanarayana 2001).

vii. **Temperature:** Temperature is highly affected by other parameters such as milling types, speed, ball size, and weight ratio. Exceeding the tolerated temperature for powder can dramatically affect the formation of the powder phase. In order to avoid high temperatures inside the milling bowl, periodic pause times during the milling can prevent surpassing the critical temperature.

viii. **Weight ratio:** Higher ball-to-powder weight ratio can increase the collision impact energy transferred from ball-to-powder and reduce milling time. However, the high density of milling balls can increase the temperature which results in changing the structure of the powder. Even though a wide range of ratios from 1:1 to 220:1 has been studied, the most common ball-to-powder weight ratio of planetary ball milling is 10:1 (Suryanarayana 2001; Gupta et al. 2017).

2.4. Laser Powder Bed Fusion (LPBF)

In comparison to traditional manufacturing techniques, the layer-by-layer principle of AM provides significant opportunities, such as fast production of geometrically complex items with high precision, reasonable cost, flexible design,

and short fabrication lead-time (Jiang et al. 2018; Ngo et al. 2018; Niu et al. 2019; Jiang and Ma 2020). LPBF, in particular, can process a wide range of metals (i.e. Al, Fe, Ni, Ti and steel) and their alloys, with the aid of a combination of different technologies, such as CAD, CAM and CNC in one system (Wong and Hernandez 2012).

2.4.1. Working Principle of LPBF

The working principle of LPBF is illustrated in Figure 2.4. The process starts with a deposition of a thin layer of powder from a powder bed to build a chamber with the aid of a silicone recoater cord. Exceeded powders stored in overflow bed in order to recycle the powder for future usage. Then, the high-power laser beam applies to a selected area to melt the powder, with this procedure being repeated every layer till the desired component is constructed. The motions of the pistons and recoater during the fabrication are remarked with white arrows in Figure 2.4.

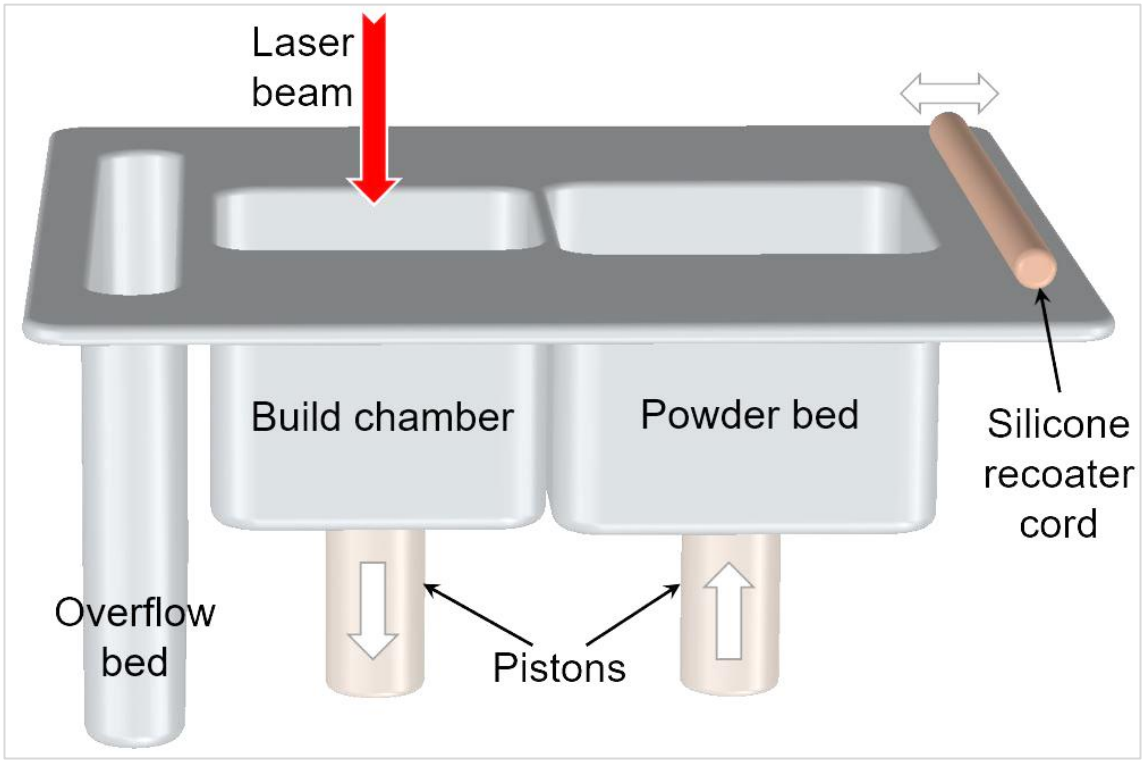

Figure 2.4: Schematic demonstration of the working principle of LPBF.

Different types of lasers are used in AM systems including CO_2, Nd:YAG (neodymium-doped crystal: yttrium aluminium garnet), disc laser, fibre laser, etc. (Gu et al. 2012). Even though, each laser has its own benefits, CO_2 and Nd:YAG lasers are common types of lasers for LPBF (Olakanmi et al. 2015). Due to several factors, the type of laser beam directly impacts the consolidation of powders (Gu et al. 2012). First, the absorption of powders is significantly influenced by the laser's wavelength. Second, the input laser energy density determines the active metallurgical mechanism for powder densification. The CO_2 laser is generally selected in LPBF energy delivery systems owing to its higher energy capacity (10.6 µm), greater efficiency, proven reliability and safety, as well as its lower cost per watt output (Williams 1997). Since the shorter wavelength (1.06 µm), Nd:YAG laser has a better absorptivity than the CO_2 laser, less energy is required to achieve the equivalent penetration depth and scanning speed with the Nd:YAG laser (Williams 1997). Furthermore, spectral radiation of the Nd:YAG laser is less reflective for the majority of metals and safer for unexpected accidents at a wavelength of 1.06 µm (Thompson et al. 2015). Consequently, In this research, Renishaw AM250 SLM machines (which use modulated Nd:YAG fibre laser) have been used. The temporal distribution of the available power must be taken into consideration as a crucial parameter as the laser beam is the heat source required to locally melt the single powder layer (Biffi et al. 2018). There are two types of laser beam emission modes in lase-based AM processes: Continuous-Wave (CW) and Pulsed-Wave (PW) (which is also called pulse-width-modulation) (Caprio et al. 2019). While CW lasers retain a fixed power value, PW lasers produce certain energy for a particular time with a duty cycle shown in Figure 2.5. According to application requirements, certain lasers are often unable to function in continuous mode, where they are designed to emit

high-energy pulses rather than an average continuous-wave output (Kumar et al. 2021). Hence, the necessity for PW lasers has grown in the additive manufacturing sector because microstructure printing capabilities are in higher demand (Demir et al. 2017; Kim et al. 2018). Additionally, PW lasers can be utilized with materials that have a higher melting temperature since they have a higher pulsed power output. Furthermore, PW lasers allow for more precise temperature control of the melt pool hence enhancing the surface finish of the generated components (Kumar et al. 2021).

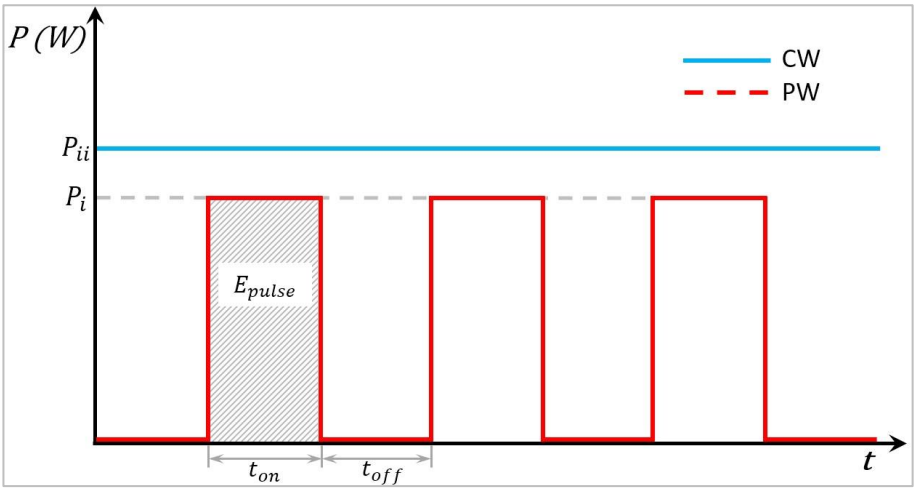

Figure 2.5 Temporal profile of heat source for CW and PW.

2.4.2. Effect of LPBF Parameters

Several LPBF parameters which affect the quality and quantity of the fabricated specimens are classified in Figure 2.6. In this subsection, the most effective parameters from each category are discussed below. In addition, ED which is the combination of these main parameters is discussed.

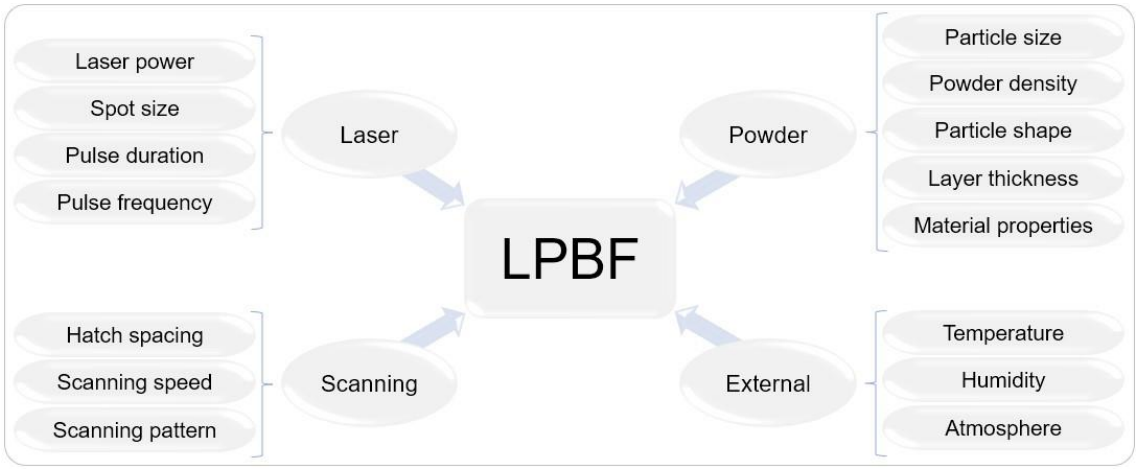

Figure 2.6: LPBF parameters that affect the quality of printed components (Niu et al. 2019).

i. **Laser power:** Laser power is one of the main parameters in the process. LPBF is generally required 50 to 400 W laser power depending on the powder (Kumar 2014). Lower laser energy than optimal energy level will decrease the part density and increase the number of defects as a result of incomplete melting; however, higher laser power than optimum level may create keyholes owing to the trapped metal vapour inside the melt-pools (Lathabai 2018).

ii. **Scanning speed:** Another significant process parameter of LPBF is scanning speed. Because scanning speed and ED have an inverse proportion, faster-scanning speed will reduce ED and part density due to insufficient melting. Nevertheless, the negative effect of faster scanning speed on the fabricated specimen could be compensated by increasing the laser power (Kumar 2014; Hanzl et al. 2015). In most of the studies, a slower scanning speed with higher laser power is preferred; however, over-sintering (which is caused by excessive ED) should be avoided (Varia and Goyal 2017).

iii. **Layer thickness:** This parameter is directly related to the production velocity and density of the fabricated parts. Higher layer thickness will

reduce the production time; however, higher ED may require the complete melting of the powder (Kumar 2014). Higher layer thickness with insufficient ED may lead to detachment of the layers for the reason that the melt-pool may not be deep enough to adhere the layers together (Varia and Goyal 2017).

iv. **Hatch spacing:** Hatch spacing is the space of the central points of two close hatch tracks. Overlapping of the laser during the scanning depends on the laser spot diameter and hatch spacing value. The distance between tracks influences the ED, directly. Hence, this parameter is strongly influential on the relative density of the fabricated parts (Shah and Dey 2019; Wu et al. 2020).

v. **The atmosphere of the chamber:** Used gas in the building chamber is essential for oxidation elimination (which is the main challenge of Al alloys) during the process. Oxidised Al powders may promote the formation of porosity (Aboulkhair et al. 2019). The argon is the most commonly used gas as a protective chamber atmosphere in LPBF.

vi. **Energy Density (ED):** ED is one of the most commonly used metrics to optimise process parameters (Aboulkhair et al. 2019). ED is directly related to mechanical and microstructural properties of the fabricated parts owing to the fact that the formulation of the ED contains the most significant parameters for LPBF (Olakanmi et al. 2015). In order to obtain crack and pore-free parts, ED optimisation should be carefully studied.

2.5. Opportunities and Potential Applications of the GNPs/AA2024

The outstanding properties of Gr-reinforced Al matrix composites are ideal for many engineering applications. With the accelerated development of the technology for Gr, the required demands from materials for some industrial applications can create an application area in order to replace Al-Gr nanocomposites which are designed for more strength, enhanced tribological characteristics and thermal constancy over conventional structural materials (Chen et al. 2018). Some opportunities and possible applications for Gr-reinforced AA2024 are listed below.

i. Landing gears and brakes of aerospace vehicles required excellent wear resistance, high strength, outstanding thermal conductivity, and low density (Pourmand and Asgharzadeh 2020). Studies about Gr/AA2024 composite (which is already discussed in section 2.2.1) prove that the composite can provide these extended properties for landing gears and brakes.

ii. The low coefficient of thermal expansion and elevated strength is highly recommended for the piston combustion face of diesel engines in order to diminish the emission at superior temperatures (Chen et al. 2018). Correspondingly, the high thermal conductivity of Gr aids to Gr/AA2024 composite to reduce the coefficient of thermal expansion and make this composite ideal for the piston combustion faces.

iii. Moreover, piston rings, gears and brake shoes necessitate excessive wear resistance, high strength and low density (Prasad and Asthana 2004), and can be fabricated using this advanced composite.

iv. The Gr/AA2024 composite is also an ideal candidate for the sports industry in order to manufacture lightweight bicycles, tennis rackets and so many others owing to the outstanding elastic modulus and low density of the advanced composite (Pourmand and Asgharzadeh 2020).

2.6. Summary

Numerous studies on Gr and Al alloys have been reported in the literature utilizing a variety of procedures (such as hot-rolling and hot-pressing techniques), proving that Gr has the capacity to increase some mechanical characteristics of as-fabricated composites. Nevertheless, the LPBF technique-fabricated GNPs reinforced AA2024 composite has not yet been identified. In this chapter, the literature studies on Gr and allotropes reinforced elements and alloys were covered, as well as the research gap on GNPs-reinforced AA2024 using LPBF. The first part focused on Al and its alloys. Individual effects of alloying elements of AA2024 are examined. According to the studies presented in this section, AA2024 specimens produced using LPBF are extremely sensitive to microcracks, defects, voids, and hot and cold cracks. Moreover, the high reflectivity of Al powders during LPBF demands a higher laser intensity to thoroughly melt the powder. Studies on Gr as a reinforcement element, as well as challenges (including, agglomeration and brittle phase of Al_4C_3 in composite), are presented in the second part. The majority of Gr reinforcement studies in the literature indicate that Gr and allotropes can improve the mechanical properties of MMCs including Al. In the meantime, agglomeration and final powder flowability become LPBF's most challenging problems. Following that, working principles and major process parameters of ball milling and LPBF were acknowledged. Major ball milling parameters for the output powder, as well as essential LPBF parameters

for the produced sample, have been identified. Finally, advantages, disadvantages, opportunities, challenges and possible applications for GNPs/AA2024 composite in the light of related studies in the literature are discussed. Overall, studies of Gr reinforced Al alloys in the literature show that Gr can enhance composite properties; however, milling and manufacturing processes are full of challenges for the novel composite. Besides, this chapter reveals that even though several Al alloys containing Gr have been investigated using a variety of manufacturing techniques, it is essential to fill the literature gap about Gr reinforced AA2024 using LPBF in order to uncover the effect of the weight ratio of Gr to mechanical properties and microstructure of the fabricated AA2024 sample using LPBF.

3. Chapter: Materials and Methodology

The material and methods used during the research were addressed in this chapter. The chapter is divided into four main sections. First of all, the used powders and specification methods are given in Section 3.1. Then, three main research methodologies (LPBF of as-received powder, ball milling and LPBF of advanced powder) in relation to the three objectives are represented in Section 3.2. After that, utilised characterisation tools and techniques were listed in Section 3.3 during the processing and analysing stages. Finally, a summary of the chapter is given in Section 3.4.

3.1. Powder Specification

This study used a commercial gas atomised AA2024 powder (-325 mesh) obtained from Carpenter Additive Technology Corporation (Philadelphia, USA). The gas atomization is currently the most common commercial manufacturing process for Al and its alloys, as the high solidification rate of gas atomization produces powders with good homogeneity and a fine structure (Yefimov 2019). The chemical composition of the powder is 4.9Cu-1.8Mg-0.9Mn-0.5Si-0.5Fe-bal.Al (wt.%), and the particle size range is between 2 and 86 µm, with an average particle size of 37.6 µm (see Figure 3.1a), obtained using a Malvern Mastersizer-3000 (Malvern, UK). Figure 3.1a shows the PSD with Dv_{10}, Dv_{50} and Dv_{90} which are particle diameters of the volume distribution of 10, 50 and 90%. Additionally, Figure 3.1b-c show an SEM image showing non-spherical as-received AA2024 powder and accumulated Gr nanosheets. Furthermore, the alloy had a 2.7 g/cm^3 relative density and melting point of 660°C.

On the other hand, GNPs (15 µm particle size, 50-80 m^2/g surface area), which were attained from Sigma-Aldrich Company Ltd. (Dorset, UK), had a 50-80 m^2/g surface area and a 3652°C melting point (see Figure 3.1c).

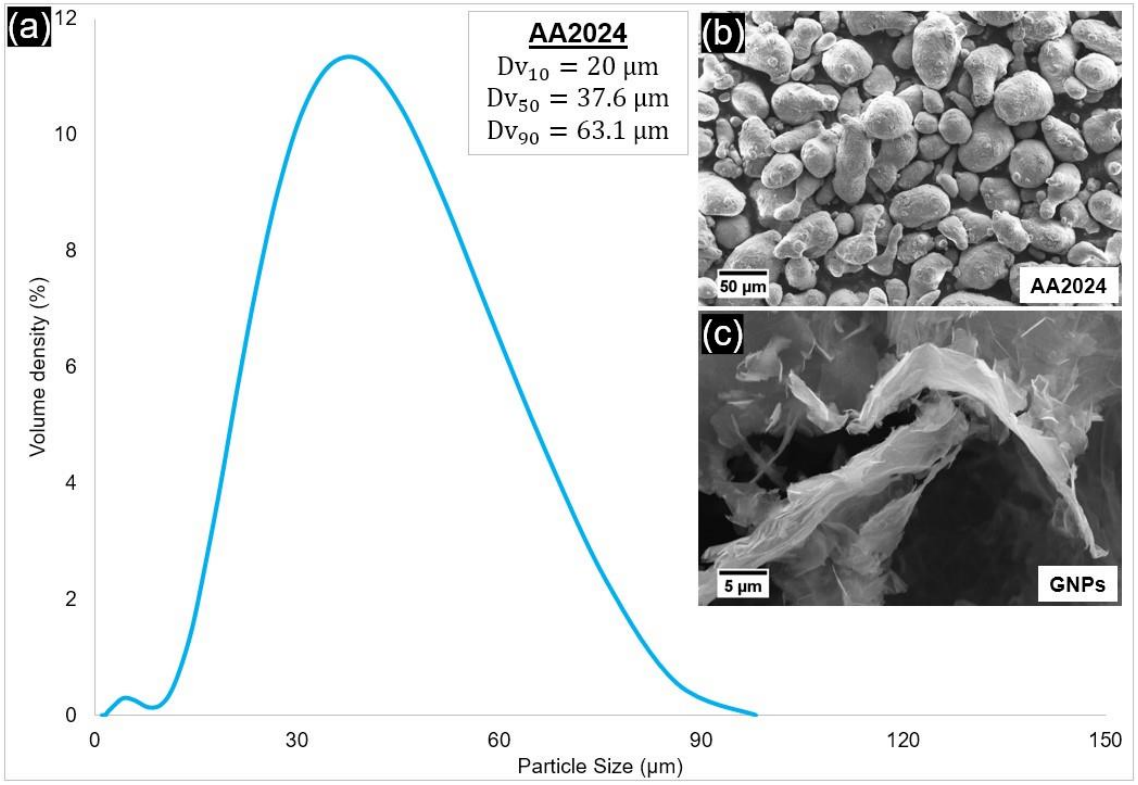

Figure 3.1: Showing (a) the particle size distribution of as-received AA2024 powder, (b) particle shape of AA2024 and (c) accumulated Gr nanosheets.

3.2. Research Methodology

The current research employs the following methods in three steps to achieve the above-mentioned purpose and objectives (Section 1.2).

(a) LPBF of as-received AA2024 Powder

In order to understand the influence of process parameters of LPBF, the most effective parameters are investigated in peer experiments. Peer experiments (laser power-scanning speed and hatch spacing-scanning speed) in this part are conducted in order to see the effect of the peer parameters. In Experiment 1, the laser power (from 100 to 200 W) and scanning speed (from 98 to 727 mm/s) parameters were varied in order to understand the effect of these parameters

(Table 3.1) on the properties of as-fabricated specimens. Laser powers below 100 W are not examined in this study, because this requires a slow-scanning speed to melt the powder completely and therefore increases the fabrication time and cost. The laser power chosen for producing the five specimens was therefore varied between 100 to 200 W (the highest laser power available from the LPBF machine). In order to see the impact of laser power in a trend line and cover the region between 100 and 200 W laser power uniformly, the middle laser power parameters (125, 150, and 175) have been chosen with equal distances. A similar approach has also been applied to select scanning speed parameters. The laser exposure time has varied between 100 and 800 µs. The middle points (400, 200, and 150 µs) have been positioned to mostly encircle the border point. The scanning speeds were chosen over a wide range in order to understand the effect of fast (727 mm/s) and slow (98 mm/s) scanning speeds under different laser power settings on the as-fabricated specimens. The hatch spacing (80 µm), point distance (80 µm), layer thickness (25 µm) and scanning strategy were kept constant during Experiment 1.

In Experiment 2, the hatch spacing, and scanning speed parameters varied from 40 to 100 µm and 98 to 727 mm/s respectively (Table 3.1), while the laser power (200 W), layer thickness (25 µm), and scanning strategy were kept constant. The hatch spacing values were chosen over a range that creates both laser spot overlapping (40 and 60 µm) and creates a gap between laser spots (80 and 100 µm), owing to the laser spot size (75 µm), in order to see the effect of the distance between spots on the microstructure of the as-fabricated specimens. The layer thickness was kept constant across both experiments due to the fact that using thinner layers can create voids on the deposited layer, and can cause a high percentage of the powder to be pushed out of the building zone; however, using

thicker layers may create short feeds, which can dramatically decrease the quality of the built part (Han et al. 2019). Similarly, the scanning strategy was kept constant across both experiments due to the small dimensions of the specimens. Although layer thickness and scanning strategy are important parameters for AM, these parameters have not been changed during these experiments in order to focus on the effect of the laser power, hatch spacing and scanning speed. A single specimen was produced for each unique pair of parameters. Forty 6x6x7 mm^3 specimens were produced in total (25 for Experiment 1, and 15 for Experiment 2), using a Renishaw AM-250 system (Gloucestershire, UK), which has a modulated ytterbium fibre laser with a wavelength (λ) of 1.071 μm. The diameter of the laser spot is 75 μm.

Table 3.1: LPBF process parameters for Experiments 1 and 2.

	Parameters	Value
Experiment 1	Laser power (W)	100 / 125 / 150 / 175 / 200
	Scanning speed (mm/s)	98 / 195 / 381 / 500 / 727
	Hatch spacing (μm)	80
Experiment 2	Laser power (W)	200
	Scanning speed (mm/s)	98 / 195 / 381 / 500 / 727
	Hatch spacing (μm)	40 / 60 / 80/ 100

Figure 3.2a shows a schematic diagram of the manufactured specimens; Figure 3.2b-c shows the working principle of the pulsed laser of LPBF and related parameters. A meander fill-hatch type scanning strategy was used to build the specimens, and the fill-hatch angle was rotated 67° at each layer, in order to achieve the highest distance between repetitions of the same layer angle (180 layers) (see Figure 3.2c). Thus, any possible cracks and defects in the neighbouring layers can be directed through different angles, which can increase the mechanical properties of manufactured specimens.

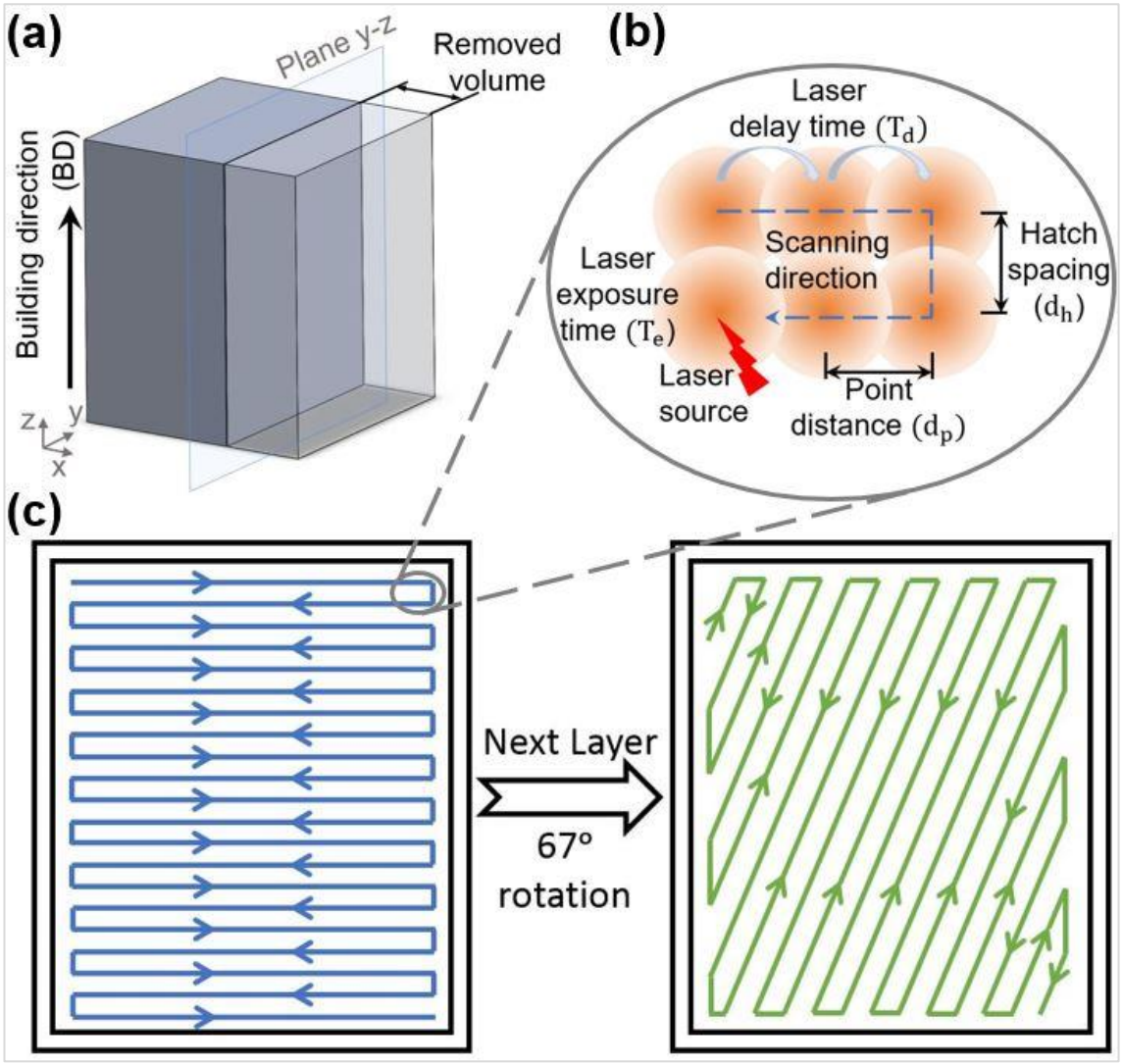

Figure 3.2: Schematic diagram of the specimen from cross-section view (a), working principle of the pulsed laser (b), laser scanning strategy of layers (c).

The laser scanning speed (V) was calculated using the below equation (obtained from Renishaw)

$$V = d_p/(T_e + T_d) \quad (3.1)$$

where d_p is the point distance, T_e (800, 400, 200, 150, 100 µs) is the laser exposure time at one point, and T_d is the laser delay time from one point to another. Laser delay time (10 µs) is a constant value for the machine.

The ED was calculated using the below equation (Malekipour and El-Mounayri 2018; Dadbakhsh et al. 2019):

$$ED = P/(V * d_h * t) \quad (3.2)$$

where P is the laser power (from 100 to 200 W), V is the scanning speed (from 98 to 727 mm/s), d_h is the hatch spacing (from 40 to 100 µm), and t is the layer thickness, set at a constant 25 µm in the present study. A wide range of EDs, from 69 to 2041J/mm^3 have been achieved by changing the laser power, hatch spacing and scanning speed parameters.

The EDs used in Experiments 1 and 2 are shown in Table 3.2. The values are calculated using Equation 3.2. Hatch spacing was kept constant at 80 µm during Experiment 1 and laser power was kept constant at 200 W in Experiment 2.

Table 3.2: ED (J/mm^3) of Experiments 1 and 2 calculated using Equation 3.2.

ED (J/mm^3)	Experiment 1					Experiment 2			
	P=100 W	P=125 W	P=150 W	P=175 W	P=200 W	d_h=40 µm	d_h=60 µm	d_h=80 µm	d_h=100 µm
V=98 mm/s	510	638	765	893	1020	2041	1361	1020	816
V=195 mm/s	256	321	385	449	513	1026	684	513	410
V=381 mm/s	131	164	197	230	262	525	350	262	210
V=500 mm/s	100	125	150	175	200	400	267	200	160
V=727 mm/s	69	86	103	120	138	275	183	138	110

Figure 3.3 shows the laser spot overlap for different hatch spacing parameters (isometric and top views). If the overlap is too large (i.e., d_h=40 µm), it will re-melt the previous melt-pool. If it is too small, or there is no overlap (i.e., d_h=100 µm), unmelted powder and porosity may occur, due to the high distance between each hatch line.

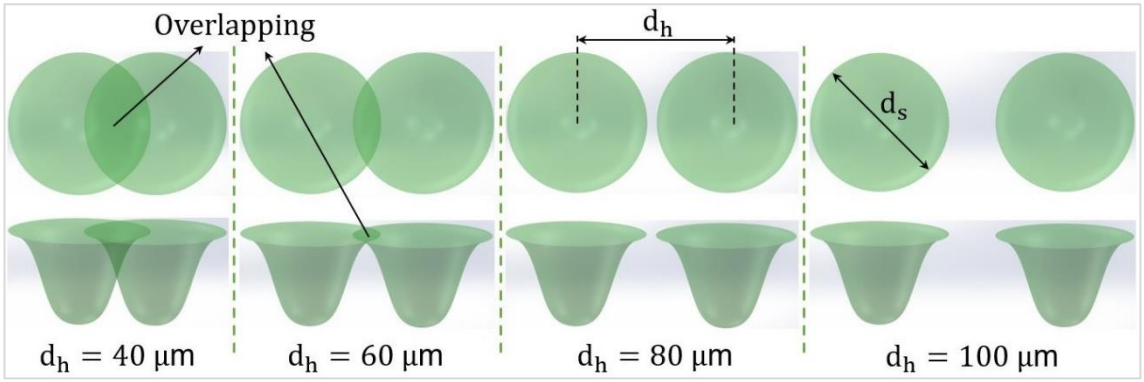

Figure 3.3: Schematic diagram of hatch distance (d_h) showing the isometric (3D Gaussian curve) and top view of the laser spot overlapping in the melt-pool based on spot size (d_s).

(b) Ball Milling of AA2024

The optimum milling time and speed for the advanced composite are employed after PSD, X-ray Diffraction (XRD), Scanning Electron Microscopy (SEM), Energy-Dispersive X-ray Spectroscopy (EDS), microhardness, powder flowability and compressibility results. In order to contrast the experimental results, DEM simulation was generated from real powder size and morphology. Un representing the Gr particles in DEM (owing to the difficulties of simulating nanoflake particles in the software) offered an understanding of the effect of Gr in composites.

In order to investigate the effect of milling time, a laboratory planetary ball milling machine (PULVERISETTE 5 classic line, Fritsch GmbH, Idar-Oberstein, Germany) was employed to mill the alloy with Gr under different milling times, ranging from 0.5 to 16 hr. Two milling bowls were placed opposite each other inside the milling machine in order to balance the centrifugal force. Each bowl was filled with 800 g milling balls and 80 g powder (including 77 g AA2024, 1.6 g stearic acid, and 0.8 g GNPs). The ball-to-powder weight ratio was adjusted as 10:1 during the experiment. The milling bowls were loaded with approximately 40 stainless steel balls with two different diameters (10 and 20 mm) and weights (4

and 32 g) in order to vary the impact energy. Additionally, It has also been reported that using a mix of big and small size balls while milling reduces the amount of cold welding and powder coating on the balls' surfaces (Takacs and Pardavi-Horvath 1994). Even though no precise reason for the enhanced yield under these conditions has been provided, it is plausible that the various-sized balls cause shearing forces that aid in the detachment of the powder from the balls' surface (Suryanarayana 2001). Stearic acid from 1 to 3% is commonly preferred for Al powders in literature studies and is reported as adequate to prevent the powder from contamination (Ramezani and Neitzert 2012). With the aid of a previous study (Pekok et al. 2021), stearic acid (2 wt.%) was used to create a thin film on milling balls as a PCA. Additionally, the milling bowls were filled with argon gas in order to protect the powder from oxidation.

Milling speed was kept constant at 100 rpm in light of the previous study (Pekok et al. 2021) in order to eliminate the immediate changing of the powder morphology to flat. Seven different milling times from 0.5 to 16 hr (see Table 3.3) have been used in experiments in order to determine the effect of milling time and therefore establish the optimum milling time for the composite. Additionally, 10 minutes of milling followed by 10 minutes of pause time was used in order to prevent the powder from reaching high temperatures during the milling process (pause time is not included in the milling times stated).

Table 3.3: The processing parameters for the seven samples of the advanced Gr/AA2024 composites.

Parameters	Values
Milling speed (rpm)	100
Total milling time (h)	0.5 / 1 / 2 / 4 / 8 / 12 / 16
Milling/pause time (min)	10 / 10
Ball-to-powder weight ratio	10:1

XRD and EDS analyses were conducted to determine phases formed during the ball milling process. A Siemens/Bruker D5000 X-ray powder diffraction machine was used with Cu K_α radiation (λ=0.15406 nm) at 40 kV and 30 mA settings. The start and stop angles were selected as 15° and 90° with a step size (°2Θ) of 0.02. The average crystallite size (D) was estimated as follows (Singh et al. 2019):

$$D = (K * \lambda)/(\beta * cos\,\theta) \quad (3.3)$$

where K is a Scherrer constant close to unity (0.9), β is the line broadening at full width at half maximum (FWHM) and Θ is the Bragg's angle.

(c) LPBF of GNPs/AA2024

Furthermore, an LPBF (Renishaw AM250 system (Gloucestershire, UK)) machine was used to fabricate cubic and tensile testing specimens for different percentages of the composites. Reduced build volume (with plate dimensions of 78x78 mm^2) was engaged in the machine to save power and time. Laser scanning speed varied between 195, 380, 500 and 727 mm/s. Laser power (200 W), layer thickness (25 µm) and hatch spacing (80 µm) were kept constant during the building.

Scanning speeds (V) were calculated using Equation 3.1 which point distance (d_p) selected 80 µm, the laser exposure time (T_e) varied as 400, 200, 150, and 100 µs, and the laser delay time (T_d) is considered as 10 µs (which is a constant value for the AM machine). The ASTM-E8 tensile testing standard with the layers perpendicular to the loading direction was used to produce tensile test specimens. The barriers next to the cubic and tensile specimens were designed to keep an adequate amount of powder in the operation region and reduce the negative effect of short feeding during the fabrication.

3.3. Characterisation

3.3.1. Fabrication Process

During the experiments, the chosen scanning direction for the specimen parts was from left to right (the opposite direction of the gas flow inside the build chamber), in order to prevent the negative effect of particles spattering from the previous part. The effect of the scan direction and build chamber gas flow on AlSi10Mg alloy specimens fabricated using LPBF was studied, and it is reported that scanning in the same direction as the gas flow (which carries spattered powder over to the following parts) inhibits the laser beam path, generates oscillations in the melt-pool, and embeds spatters inside the following melt-pools (Anwar and Pham 2017). Therefore, the second and fourth fabrication layers on the build plate were slightly shifted (5 cm) in the +X direction, in order to prevent the parts from short feeding and spatters from previous parts becoming embedded in them. Additionally, the specimens were fabricated on 2 mm supports, and the chamber was filled with argon gas in order to prevent the as-fabricated sample from oxidation during the building time.

3.3.2. Mounting and Grinding

The specimens were mounted into an electrically conductive resin (see Figure 3.4), with each specimen oriented so that the build direction was parallel to the analysing surface. First, six different Si carbide (SiC) grinding sandpapers (200, 400, 800, 1200, 2400 and 4000) were used to grind the hot-mounted specimens at a fast rotational speed (250 rpm) of the sanding disk. Then, 5 µm and 3 µm grain size polishing cloths with diamond suspension, and 0.1 µm grain size polishing cloths with Al oxide lubricant at a slow rotational speed (100 rpm) were used to polish the surface of the specimens which meteorological data obtained.

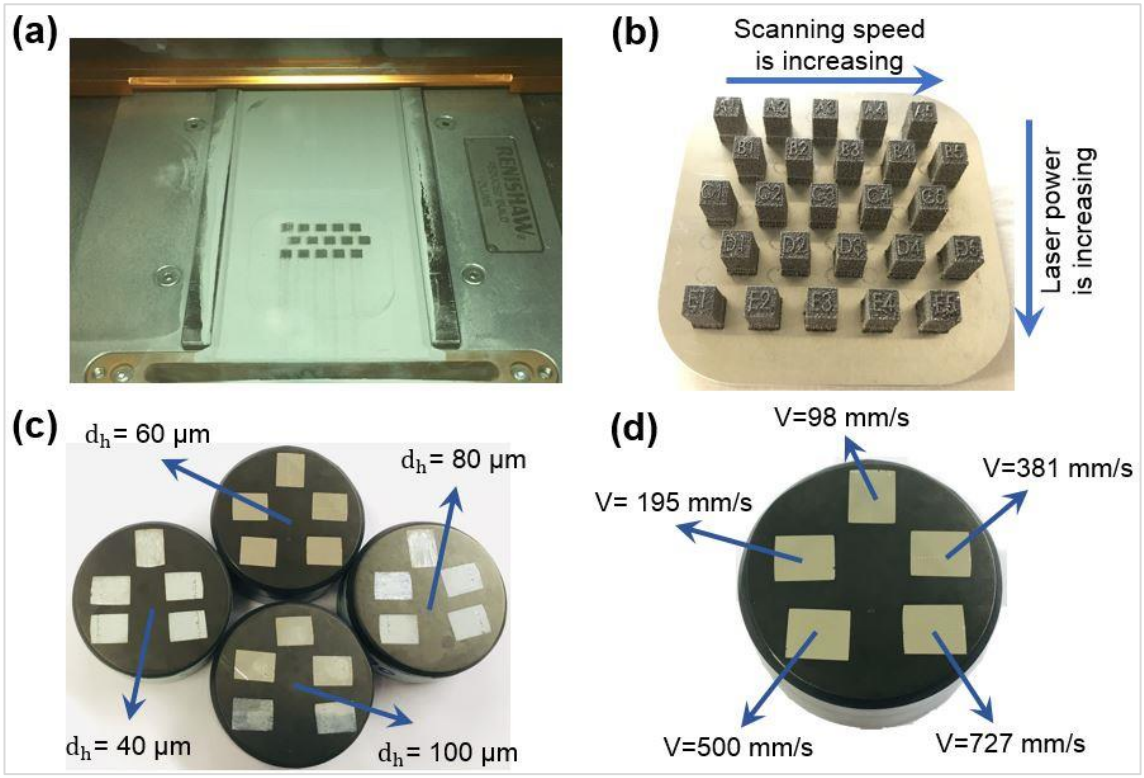

Figure 3.4: (a) The building pattern with specimens for Experiment 2 during fabrication, (b) specimens for Experiment 1 after fabrication; specimen holders with specimens of (c) different hatch spacings and (d) different scanning speeds.

3.3.3. Powder Preparation

There are numerous milling techniques available (e.g., attrition, Spex shaker, vibrator mixer). The ball milling technique is utilized in this study owing to the fact that this technique (with long milling time availability, different sizes of milling balls, and different milling atmosphere options) offers a wide range of solutions to achieve the desired powder morphology and reinforced particle distribution (Pourmand and Asgharzadeh 2020).

A laboratory planetary ball milling machine (PULVERISETTE 5 classic line, Fritsch GmbH, Idar-Oberstein, Germany) was employed to mill the alloy with Gr under different milling times, ranging from 0 to 16 h. The 0 h (zero hours) milling is representative of as-received powder without milling condition. Two milling bowls were placed opposite each other inside the milling machine in order to

balance the centrifugal force. Each bowl was filled with 800 g milling balls and 80 g powder (including 77 g AA2024, 1.6 g stearic acid, and 0.8 g GNPs). The ball-to-powder weight ratio was adjusted as 10:1 during the experiment. The milling bowls were loaded with approximately 40 stainless steel balls with two different diameters (10 and 20 mm) and weights (4 and 32 g) in order to vary and randomize the impact energy. It has also been reported that using a mix of big and small size balls while milling reduces the amount of cold welding and powder coating on the balls' surfaces (Takacs and Pardavi-Horvath 1994). Even though no precise reason for the enhanced yield under these conditions has been provided, it is plausible that the varied-sized balls cause shearing forces that aid in the detachment of the powder from the balls' surface (Suryanarayana 2001).

Atmospheric air was used inside the bowls during milling in order to prevent an exothermic reaction between the fresh Al surfaces and air when taking specimens at 0.5, 1 and 2 hr. However, the powder was stored in a glove box under argon gas to prevent further oxidation after the milling process is completed.

The working principle of ball milling is that the supporting disk (clockwise) and bowls (anticlockwise) turn in opposite directions around their own centre points. Due to the different rotational axes of the main disc and the milling bowls, reversed rotation creates a ‘D shape’ movement of balls inside the bowl under the influence of Coriolis and centrifugal forces of disk and bowl rotations. These forces help to increase the kinetic energy inside the bowls. Consequently, high-energy ball-to-ball and ball-to-wall impacts effectively grind and blend material which is placed in the grinding bowls.

Additionally, PCA inhibits contamination of the powder from milling materials by creating a thin layer on the milling balls and inner wall of the milling bowls (Nieto et al. 2017). Various studies have shown that when added in quantities of 1 to

5%, the PCA, stearic acid, covers the surface of the milling balls and the inside wall of the bowls preventing contamination from wearing of the stainless steel tools and cold welding (Suryanarayana 2001; Bartolucci et al. 2011; Li et al. 2015a). Moreover, the impact energy inside the milling bowl can be altered using different sizes of milling balls (Gotor et al. 2013; He et al. 2014). These parameters are directly related to the resulting powder morphology and the flowability of the powder produced, an understanding of which is essential for the 3D printing process.

3.3.4. Analysis

(a) Porosity and Density

The Archimedes' density (also known as bulk density) of the as-fabricated specimens was determined using a density determination kit, working according to Archimedes' principle, and the relative density was established using an OM by Nikon eclipse LV-100 (NY, USA). Then, a Nikon eclipse LV-100 (NY, USA) Optical Microscope (OM) was used to examine the surface, and ImageJ software was used to calculate the relative density of the specimens from the obtained OM images. Three different layers from the specimens were examined in order to obtain more accurate results. Keller's reagent (5 ml HNO3, 3 ml HCl, 2 ml HF, and 190 ml distilled water) as a metallographic etching compound was applied onto the specimen surface for 30 to 40 seconds in order to observe the microstructure of the as-fabricated specimens. Furthermore, theoretical density (ρ_t) was estimated using the mixing rule (Cree and Pugh 2010):

$$\rho_t = \rho_{Al} V_{Al} + \rho_{Gr} V_{Gr} \quad (3.4)$$

where ρ_{Al}, ρ_{Gr}, V_{Al} and V_{Gr} represent the density and volume fractions of Al and Gr, respectively. This equation gives accurate results for fully dense materials. For the present study, the density of the as-fabricated samples needs to be counted as:

$$\rho_t = (\rho_{Al}V_{Al} + \rho_{Gr}V_{Gr}) * (\rho_c/100) \quad (3.5)$$

where ρ_c represents the relative density of the fabricated composites obtained from OM images.

(b) Microhardness

A Nova 330/360 IMP Innovatest (Maastricht, Netherlands) hardness test machine was used to measure Vickers microhardness of the specimens under 200 g load and 10 seconds dwell time. A Zwick/Roell tensile tester with a strain rate of 0.001 mm/s was used to carry out the tensile tests, which were conducted at room temperature.

(c) Phase Identification

X-ray Differentiation (XRD) and Energy Dispersive X-Ray Spectroscopy (EDS) analysis were conducted to determine the phases formed during the ball milling process. A Siemens/Bruker D5000 X-ray powder diffraction machine (Billerica, MA) was used with Cu K_α radiation (λ=0.15406 nm) at 40 kV and 30 mA settings. The start and stop angles were selected as 15° and 90° with a step size (°2θ) of 0.02. The average crystallite size (D) was estimated as follows (Singh et al. 2019):

$$D = (K * \lambda)/(\beta * cos\,\theta) \quad (3.6)$$

where K is a Scherrer constant close to unity (0.9), β is the line broadening at full width at half maximum (FWHM) and θ is the Bragg's angle.

(d) Wear Performance

Rotating pin-on-disc wear tests have been conducted under 1 kg normal load, 25 rpm sliding speed, 30 min sliding time and 5 mm rotation diameter at room temperature and quiet place in order to eliminate the negative effect of temperature and vibration. Chrome-steel balls (3/8") were placed on the test pin.

The friction signals (F), recorded for each sample during the tests, were used to calculate the friction coefficients (μ) according to the ASTM D3702-94 standard:

$$\mu = F * A/N \tag{3.7}$$

where A denotes the mechanical advantage of the lever arm (approximately 0.6 for the present experiment), and N represents the normal load. Additionally, the wear rate (ω_r) of the specimens after the wear test was described as (Han et al. 2017b):

$$\omega_r = V_\Delta/N * L \tag{3.8}$$

where V_Δ and L represent the volume of loss and sliding distance, respectively. The volume of loss was determined by dividing the weight loss (W_Δ) by the density of the specimens as in the ASTM G99-95a standard. The wear test was repeated three times for each specimen to verify the results.

In order to measure the nano-wear behaviour of the samples, 10 scratches at 20 μm length under 10 μN normal force and 2 μm/s scratching speed were made on the sample surfaces using a commercial AFM (model XE-100 from Park Systems) mounted with a probe composed of a stainless steel cantilever and a

diamond tip (model DNISP from Bruker). The lateral output voltage signal of the PSPD detector built into the AFM instrument was used to detect the friction force of the AFM tip during the scratching time. Additionally, the lateral voltage output (M) (which was recorded by the position-sensitive detector of AFM) was used to calculate the friction coefficient (μ) as (Wang and Gee 2014):

$$\mu = \alpha * M/L \tag{3.9}$$

where α represents the conversion (calibration) factor. More details about the determination process of α may be found in the respective literature (Xie et al. 2012; Boland et al. 2018).

(e) Surface Roughness

Additionally, the surface roughness measurement was performed using an optical profilometer and the AFM instrument mounted with a contact mode probe (model CSG30 from NT-MDT) for both polished and as-fabricated composites.

(f) Tensile Testing

The uniaxial tensile tests were performed at room temperature using a Zwick/Roell tensile tester (Baden-Württemberg, Germany) with a strain rate of 0.001 mm/s. Due to the dimensional limitations of the reduced build volume plate in the vertical direction, the tensile test specimens were fabricated horizontally, according to the American Society for Testing and Materials (ASTM-E8) standard, with the layer perpendicular to the loading direction. Previous studies have reported that building direction does not strongly influence or have little effect on the mechanical properties of Al alloys (Read et al. 2015; Kimura and Nakamoto 2016; Ch et al. 2019; Hu et al. 2019). For instance, AlSi10Mg alloy specimens were fabricated in both horizontal and vertical directions using LPBF,

and it is reported that building direction does not strongly influence the creep and tensile properties of the alloy (Read et al. 2015). Similarly, it has been reported that the UTS results of the AlCu5MnCdVA alloy fabricated in both directions are nearly the same (Hu et al. 2019).

(g) Flowability and Compressibility Tests

Universally, the flow characteristic of a powder is measured by detecting the angle of repose of the deposited powder using a powder flowability measurement kit, with the powder flowing through a funnel onto a stage. The angle of repose can be explained as the angle which differentiates the transitions among the phases of the granular materials, and it is directly related to the resistance to movement, or inter-particulate friction, between particles (Amidon et al. 2017; Beakawi Al-Hashemi and Baghabra Al-Amoudi 2018), and is measured as the angle between the heaped cone of a free-standing powder and the horizontal plane (Amidon et al. 2017). DEM is a numerical technique for simulating the dynamic behaviour of a powder, and can also be used to calculate the angle of repose in relation to Newton’s law of motion (Chen et al. 2017; Lee et al. 2017). The interaction of powder-to-powder and powder-to-wall helps to understand powder's flowability prior to use in the AM process.

Figure 3.5 Powder flowability determination kit.

The apparent and tapped volumes of eight samples from as-received powder at each milling time (0.5 to 16 h) were measured to calculate the compaction characteristics of the composites. The tapped volume was obtained by tapping the powder 500 times while placed inside a 50 ml scaled cylinder tube. Measured volumes before tapping (apparent density) and after tapping (tapped density) were used to calculate Carr's Index (CI) and the Hausner Ratio (HR) using equations 6 and 7 (Emery et al. 2009; Goyal et al. 2015):

$$CI\ (\%) = 100 \times (\rho_t - \rho_a)/\rho_t \tag{3.10}$$

$$HR = \rho_a/\rho_t \tag{3.11}$$

where ρ_a and ρ_t are the apparent and tapped densities, respectively.

3.3.5. DEM Simulation Setup

Flowability tests were conducted using both DEM simulation and experimental work. The powder deposition model was designed using EDEM-5.0.0 (2019) simulation software. The model includes a powder tank, funnel, and floor (see

Error! Reference source not found.a). The funnel was designed according to t he ASTM-B213-13 standard. In order to estimate the angle of repose of the raw and milled powder, three different powder particle templates (see **Error! R eference source not found.**c) from the SEM images of real powder particles (see **Error! Reference source not found.**b) for each milling time were created u sing computer-aided design software (SolidWorks 2019). GNPs were not included in the DEM simulation, as it is not practical to model a nano-size thin layer with a large surface area (as found in Gr flakes) with spherical DEM cells without requiring enormous working time for each simulation. The simulation allows the flowability of the milled AA2024 powder without Gr to be calculated. Hereby, the difference between experimental work (with Gr) and simulation (without Gr) will allow the effect of Gr on the flowability of the milled powders to be examined.

Modelling particles at or below nano-scale is a significant challenge, owing to the limitations of computing power (Yeom et al. 2019). The simulations were produced using a computer of the following specification: Intel(R) Core(TM) i7-8665U CPU @ 1.90GHz 2.11 GHz, 16.0 GB Ram and 64-bit operating system. However, considerable computational time and high-performance computing may be required for some applications in order to simulate the size of the particles at the physical scale. A scaled-up of the powder size is commonly preferred to alleviate this computational burden (Radeke et al. 2010; Hassanpour et al. 2011; Thakur et al. 2016; Coetzee 2019; Yeom et al. 2019). Furthermore, full-scale modelling is impractical for DEM-based simulations when complicated powder morphologies (such as non-spherical AA2024 powders) are considered. Additionally, it has been stated that upscaling has no substantial effect on the results, and some coefficient of friction obtained from unscaled particles can be

used for upscaled particles in order to simulate the angle of repose precisely (Coetzee 2019). Furthermore, the contact sliding and rolling coefficients of friction for various particle sizes were investigated and reported that the angle of repose was independent of the particle diameter (Coetzee 2019). Therefore, micron-sized powders in the present study were scaled-up in order to reduce the excessive running time of a large number of simulations.

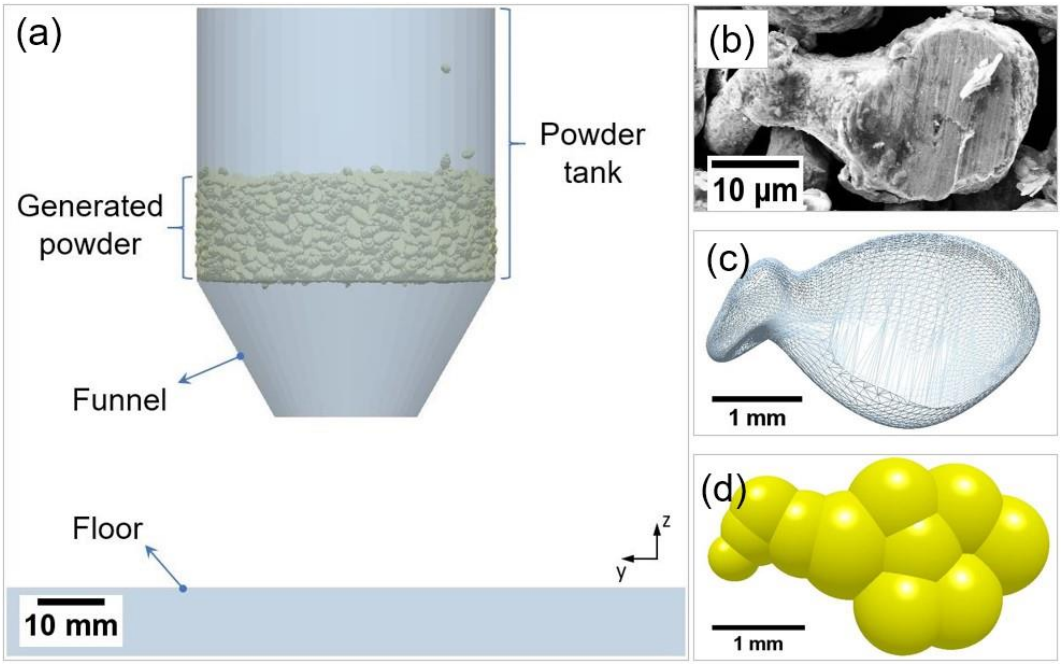

Fig. 3.6 Projection of (a) simulation model with an example of (b) SEM image of the 0.5 h milled powder, (c) created a 3D template based on the SEM images of the real powder and (d) created DEM particle with 11 spherical cells from the template.

Hertz–Mindlin with the Johnson-Kendall-Roberts (JKR) is a cohesive model which is also accounting the influence of Van der Waals forces (Lupo et al. 2021). According to the JKR model, the normal elastic contact force (F_{JKR}) is expressed with the interfacial surface energy (Γ) as follows (Lupo et al. 2021):

$$F_{JKR} = -4\sqrt{\pi\Gamma E^*}a^{\frac{3}{2}} + \frac{4E^*}{3R^*}a^3 \tag{3.12}$$

$$\Gamma = \gamma_1 + \gamma_2 - \gamma_{1,2} \tag{3.13}$$

where E^*, R^* and a are the equivalent Young's modulus, radius, and contact radius and γ_1, γ_2 and $\gamma_{1,2}$ are the surface energy of two spheres and interface surface energy, respectively. E^*, R^* can be defined as follows (Han et al. 2019):

$$\frac{1}{E^*} = \frac{1-{v_i}^2}{E_i} + \frac{1-{v_j}^2}{E_j} \quad (3.14)$$

$$\frac{1}{R^*} = \frac{1}{R_i} + \frac{1}{R_j} \quad (3.15)$$

where E_i, R_i, v_i and E_j, R_j, v_j are Young's modulus, radius, and Poisson's ratio of each spherical in contact, respectively.

Single spherical particle (Type 1a) and different combinations of several spherical particles (Type 1b-f) which are commonly used in literature were tested in order to contrast the common particles (Type 1) and SEM particles (Type 2) (see **Error! Reference source not found.**). In the beginning, combinations of different percentages (20, 30, 50, and 100%) of three particles (Type 2a-c) selected from SEM photos of as-received powder were compared in order to exhibit the effect of various percentages on the angle of repose. Additionally, three (Type 2a-c), six (Type 2a-f), and ten (Type 2a-j) different morphologies with equal percentages were analysed in order to determine the optimum number of different particle morphologies.

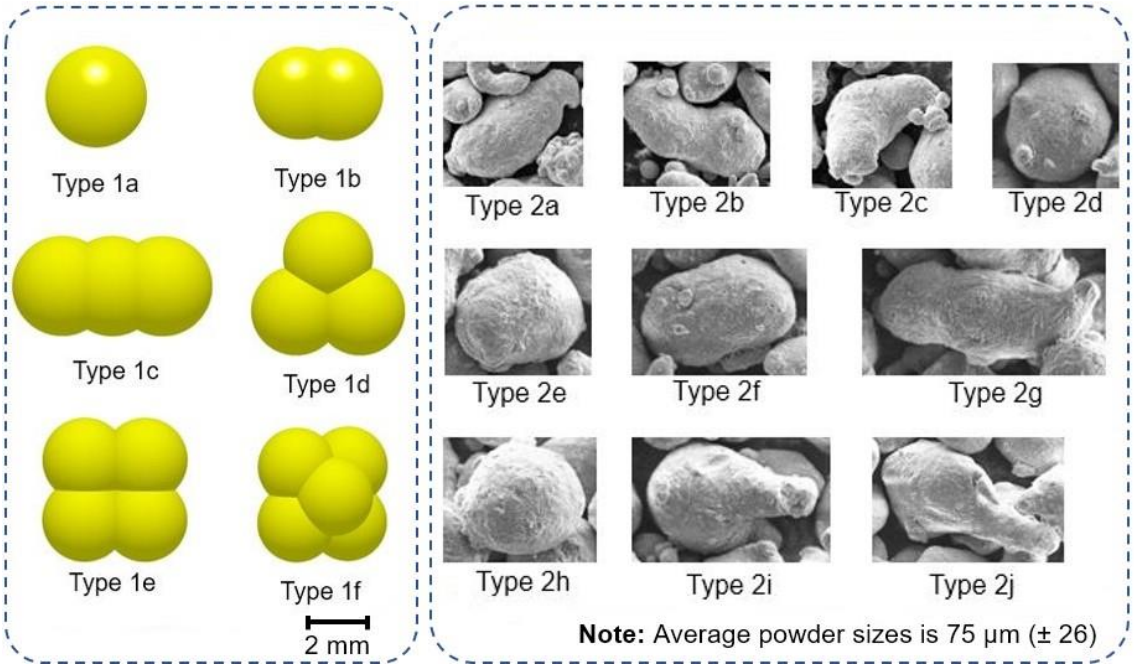

Fig. 3.7 Commonly used particle morphologies in literature (Type 1 series) and the most representative particles for SEM photos of the real powders (Type 2 series).

The three most representative particles for as-received powder at each milling time were selected based on visual observation of SEM images to create templates. Examples of these images are represented in the following section (see **Error! Reference source not found.** and **Error! Reference source not found.**) as an illustration. Based on the templates, DEM particles were formed using a combination of 5 to 42 spherical cells (see **Error! Reference source not found.**). Fewer spherical cells (5 to 14) are required for the alloys milled for up to 2 h, due to the dominant “round” particle shapes; however, a large number of cells (up to 42) were used to create milled particles over 4 h, because of the thin, flat particle shapes (see **Error! Reference source not found.**). Particle size distribution results from the experimental work were used to generate the powder's size in the powder pool of the simulations (see **Error! Reference source not found.**).

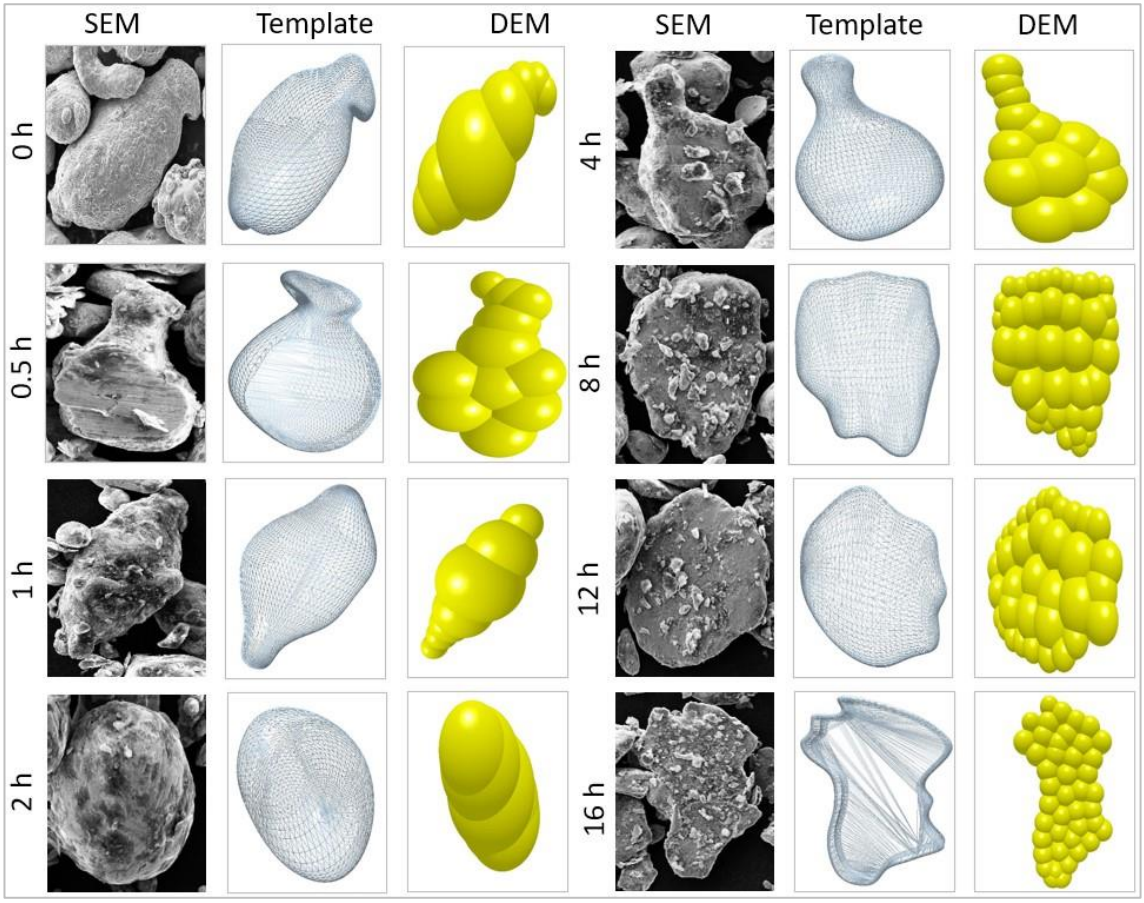

Fig. 3.8 Examples of created 3D particles showing the morphological evolution of particle shape from spherical to flat with increasing milling time.

The DEM parameters used are shown in **Error! Reference source not found.**. T he particle surface energy parameter for the as-received powder was optimised using the angle of repose of the as-received powder in the experimental work.

Table 3.4 The DEM parameters used in the flowability simulations.

Parameters	Value	Ref.
Poisson's ratio	0.33	(Gariépy et al. 2011)
Solid density	2768 kg/m^3	(Ruiz-Angulo and Hunt 2010)
Young's modulus	73.08 GPa	(Ruiz-Angulo and Hunt 2010)
Coefficient of restitution	0.8	(Ruiz-Angulo and Hunt 2010)
Coefficient of static friction	0.15	(Etsion and Amit 1993)
Coefficient of rolling friction	0.05	(Anthony Xavior et al. 2018)
Particle surface energy	1.4 mJ/m^2	(Determined)

For the experimental measurements, a protective cover for the flowability test kit, an airflow-free room and a silent workplace were selected to minimize the

influence of airflow and vibration on the experimental work. To achieve a more accurate outcome, the tests were performed three times for each powder. The angle was measured at both the right and left hillsides and the mean was taken for each deposited powder, in both the experiments and simulations. Experimental flowability tests were carried out according to the ASTM B213-13 standard, and each test was repeated three times for each powder milling time and conducted with approximately 20 g of powder. The angles of both hillsides (right and left) of the reposed powders were measured.

3.4. Summary

Used material and methodology significantly affect the quality of the fabricated specimens. Investigating the impact of an additional element and approach requires a methodical methodology. This chapter concentrated on the powder specification, technique, and characterization in order to achieve that. The as-received powder size distribution was discovered first. After that, the as-received powder was used to fabricate a wide range of specimens with different processing parameters. Mainly, ED is used to characterise and simplify the effect of three parameters on specimens. After that, ball milling and parameters were discussed. Then, the methodology of advanced powder fabrication using LPBF was demonstrated. Finally, preparation and measurement tools in order to characterise the fabricated specimens and powders were given in the last section. Additionally, DEM simulation setups for commonly used particles (Type-1) and SEM particles (Type-2) were illustrated.

4. Chapter: Optimisation of LPBF Parameters for As-received AA2024

The first objective of this thesis is addressed in this chapter. Wide ranges of processing parameters that are decided based on related studies are presented. The three most effective LPBF parameters (laser power, hatch spacing and scanning speed) are used to fabricate cubic specimens. The microstructure and mechanical properties of the as-fabricated specimens are analysed. The chapter is divided into four sections. First of all, the research hypothesis is presented in Section 3.1. Additionally, the results and discussion are provided in Sections 3.2 and 3.3, respectively. A wide range of characterisation techniques was used for the as-received alloy. Furthermore, ANOVA tests were applied to determine the significance of the process parameters and predict the influence of the middle points of the selected parameters. Finally, the summary of the chapter is given in Section 3.4.

4.1. Research Hypotheses

The following are the study's research hypotheses:

- Higher laser power (200 W) may result in better powder melting and thus higher relative density than lower laser power (100 W).
- The density of the as-fabricated specimens may be reduced if the hatch distance is exceeded or overlapped. Longer hatch distances may also increase the amount of unmelted powder in the structure.

- Faster scanning speeds may enhance the cooling rate, improving microhardness; nevertheless, the amount of unmelted powder in the structure might rise.

4.2. Results

4.2.1. Effect on Porosity

A Nikon eclipse LV-100 (NY, USA) OM (100x magnification) was used to determine the relative density of as-fabricated specimens based on the observed surface. More than twenty-five different OM images for each specimen (approximately 90% of the observed surface) were taken to calculate the relative density accurately. ImageJ software was used to calculate the porosity of the surfaces.

Figure 4.1 shows the relative porosity of as-fabricated specimens produced for Experiment 1 and the transition from high relative porosity to an almost crack and pore-free structure. Relative densities higher than 99.5% are highlighted inside the green discontinuous line, and relative densities lower than 97% are marked inside the red line. The main issues for the specimens inside the red line are poor wetting, large cracks and pores caused by incomplete fusion (also known as lack of fusion) (Malekipour and El-Mounayri 2018); however, small gas pores (a common phenomenon for LPBF, because of the dissolved gas between the powder particles (Zhang et al. 2019)) are the main problem for the specimens inside the green discontinuous line.

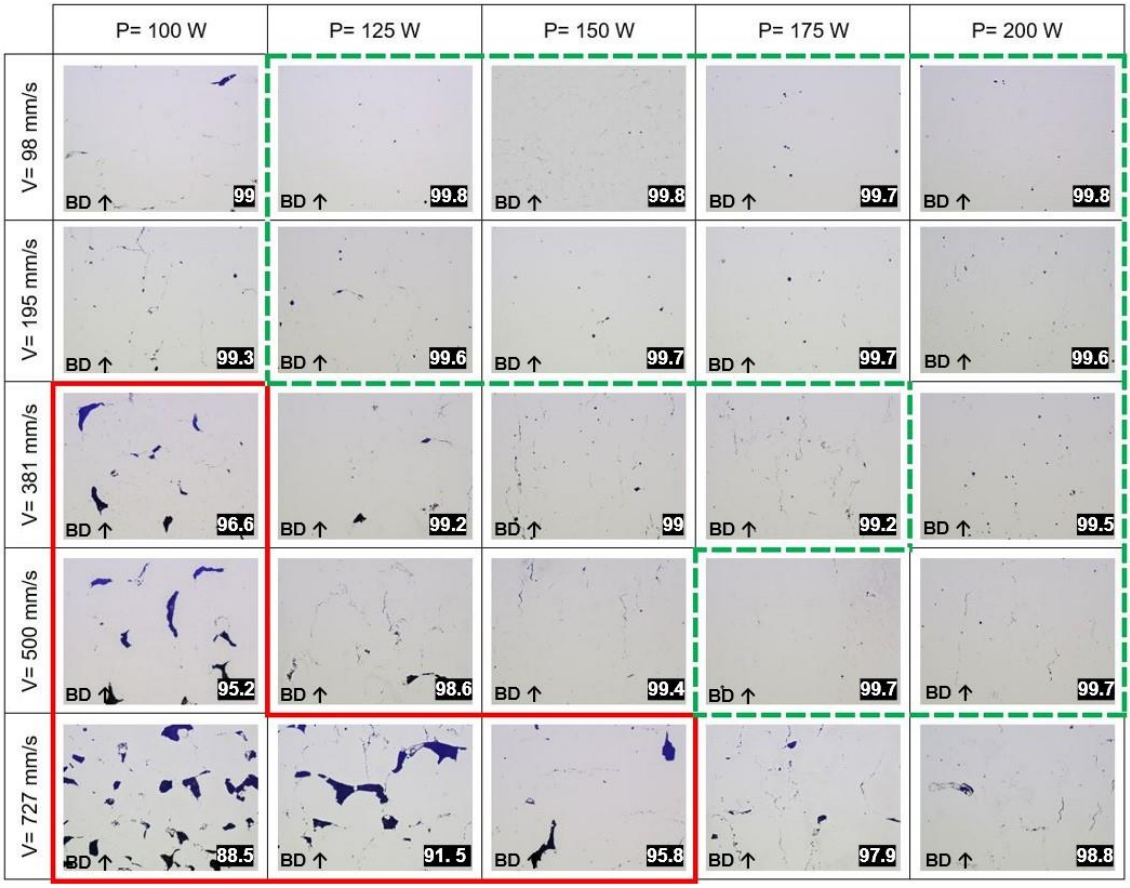

Figure 4.1: OM images of as-fabricated specimens from Experiment 1 showing the relative porosity plotted against laser power (100 to 200 W) and scanning speed (98 to 727 mm/s).

Figure 4.2 shows specimens produced for Experiment 2; the significant effect of varying the hatch spacing and scanning speed on relative porosity can be seen. Slower scanning speeds at 60 and 80 µm hatch space provide less relative porosity on the observed surface. Moreover, the surfaces with the lowest relative porosity were achieved from the slowest scanning speed and 80 µm hatch spacing. Porosities which are lower than 1% are shown inside a red line. Inside this region, small gas pores are the major issue. However, the major issues for the specimens outside the red line are incomplete fusion holes, sharp and hot cracks, un-melted powder and irregularly shaped pores. It has previously been reported that insufficient energy input during the LPBF process causes an increase in the discontinuous melt-pool and creates incomplete fusion holes (Zhang et al. 2017). The experimental density results show that the porosity is

significantly influenced by a variety of processing conditions. Despite the greatest densities (99.8%) being reached at 98 mm/s scanning speed, the high density (99.7%) was also attained with 500 mm/s scannings, 200 W laser power and 80 µm hatch spacing. Faster scanning speeds can significantly reduce the cost and time of production for industrial applications.

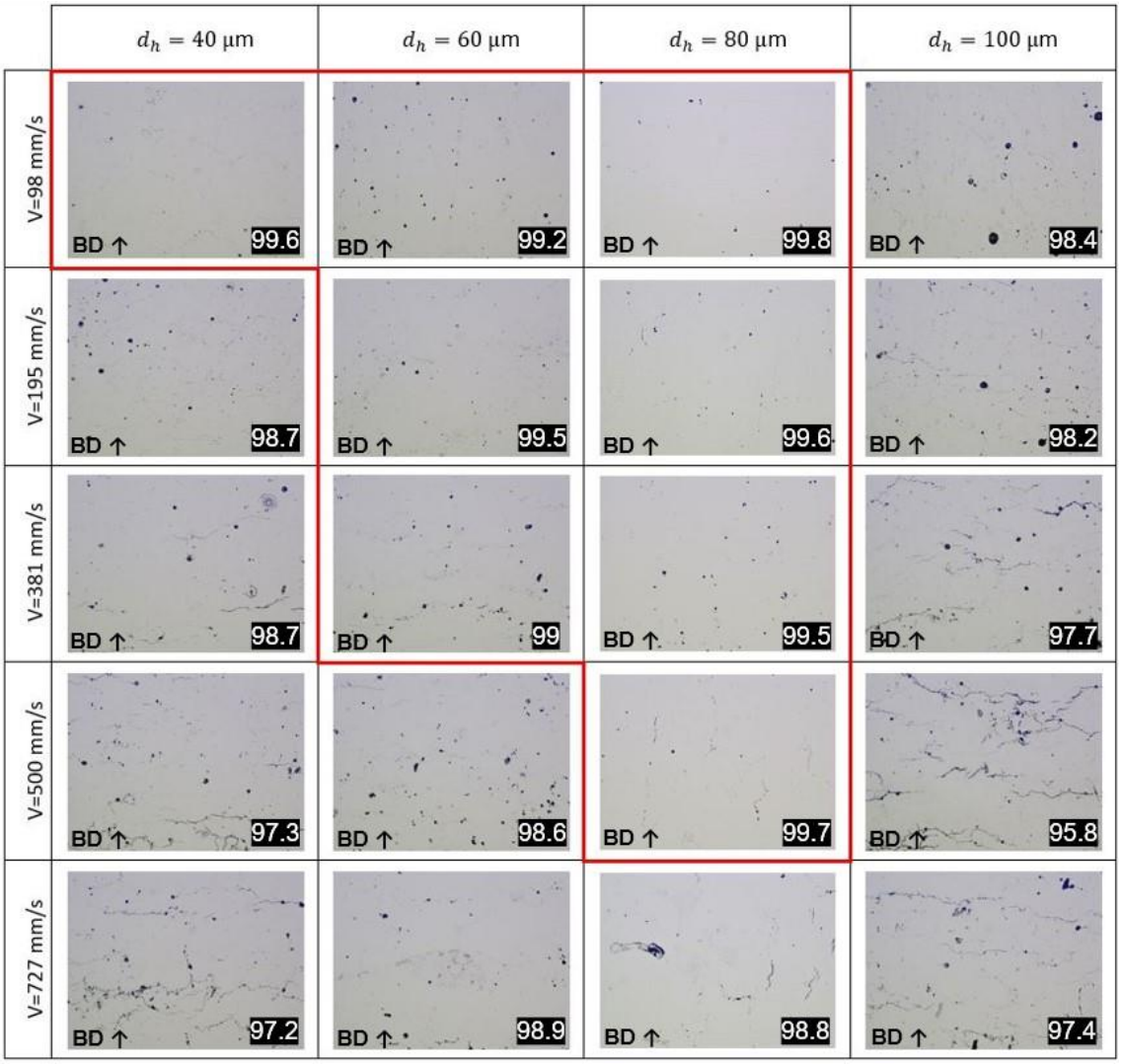

Figure 4.2: OM images of specimens from Experiment 2 showing the relative porosity of as-fabricated alloy plotted against hatch spacing (40 to 100 µm) and scanning speed (98 to 727 mm/s).

4.2.2. Relative and Archimedes' Densities

The results of Experiments 1 and 2, shown in Figure 4.3 and Figure 4.5, demonstrate that Archimedes' and relative densities are highly dependent on the laser power, scanning speed and hatch spacing parameters.

The effect of the ED on Archimedes' and relative densities is shown in Figure 4.3. In Experiment 1, the ED varied between 69 and 1020 (J/mm^3) with changes in laser power (from 100 to 200 W) and scanning speed (from 98 to 727 mm/s). The hatch spacing was kept constant at 80 µm in Experiment 1 in order to understand the effect of the laser power and hatch spacing on the Archimedes' and relative density. The highest relative density (99.9%) was achieved at an ED of 759 J/mm^3, and the lowest relative density (88.5%) was achieved at the lowest ED (69 J/mm^3). Additionally, the relative density becomes more stable when the ED is above 150 J/mm^3 and increases gradually. On the other hand, the highest Archimedes' density (99.5%) was achieved from the highest ED (1020 J/mm^3). A greater fluctuation in both the Archimedes' and relative densities were observed at low ED (see Figure 4.3).

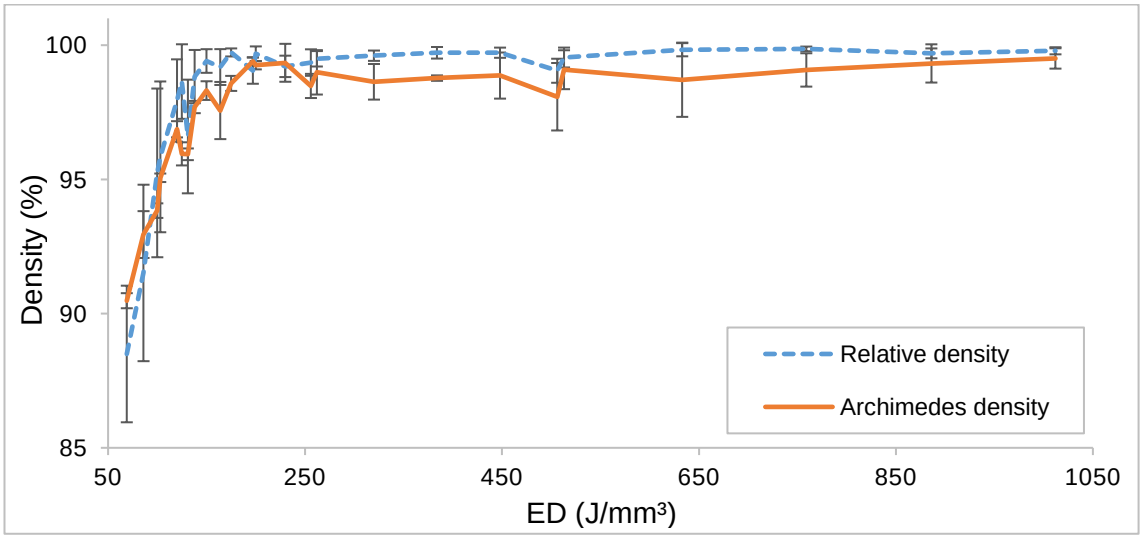

Figure 4.3: Archimedes' and relative densities of as-fabricated specimens in relation to ED (Experiment 1).

The effect of laser power and scanning speed on the relative and Archimedes' densities is given in Figure 4.4. Both densities show slow improvements at slow scanning speeds (98 and 195 mm/s); however, further increasing the scanning speed (381, 500 and 727 mm/s) results in dramatic changes in both densities. This reveals that processing with slow scanning speeds tolerates the negative effect of using low laser power.

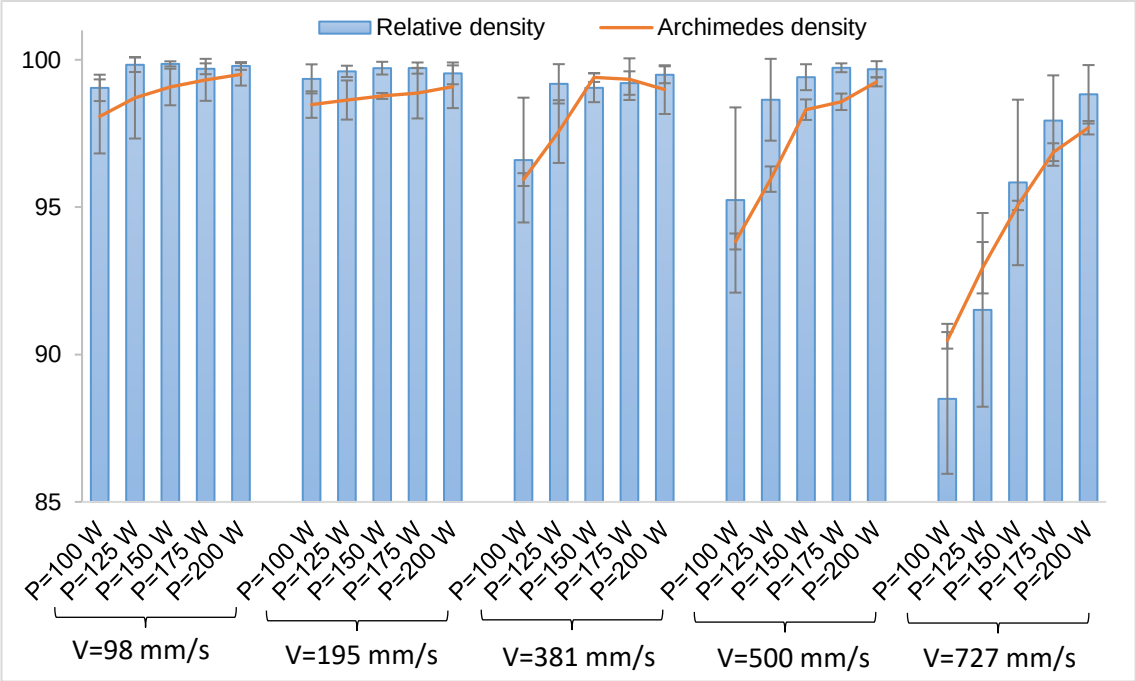

Figure 4.4: Archimedes' and relative densities of as-fabricated specimens in relation to laser power (P) and scanning speed (V) (Experiment 1).

In Experiment 2, ED varied between 110 and 2041 J/mm³ (which changes with varying hatch spacing from 40 to 100 µm and scanning speed from 98 to 727 mm/s). The laser power remains constant in Experiment 2, at 200 W. The Archimedes' and relative densities improve with increasing ED, up to 99.8% (see Figure 4.5). In this research, almost crack and pore-free structures (0.2% porosity, using a hatch spacing of 80 µm and scanning speed of 98 mm/s) have been achieved at high ED (1020 J/mm³). Moreover, Archimedes' density greater than 99% was achieved when the ED was over 684 J/mm³. The lowest Archimedes' density (97.4%) was obtained at the fastest scanning speed (727

mm/s), with 80 µm hatch spacing. The relative density shows greater fluctuation around Archimedes' density when the ED is under 410 J/mm³. However, the two sets of measurements become closer and more stable at the higher EDs, depicting that the layers of the specimens which are fabricated at high ED are more uniform.

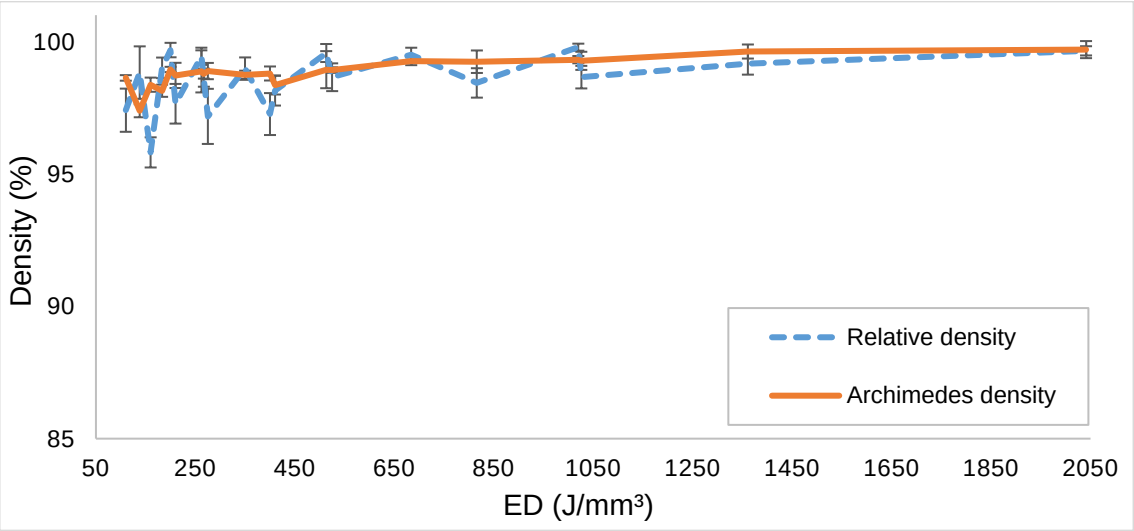

Figure 4.5: The Archimedes' and relative density of as-fabricated specimens in relation to the ED (Experiment 2).

The effect of hatch spacing and scanning speed on Archimedes' and relative densities is presented in Figure 4.6. The higher densities were achieved using hatch spacing values of 60 and 80 µm. Closer laser spots (i.e., 40 µm) and farther laser spots (i.e., 100 µm) than the laser focus diameter (75 µm) negatively affect the density of the as-fabricated specimen. Similar to the results of Experiment 1, slower scanning speeds tolerate the negative effect of the sub-optimal hatch spacings.

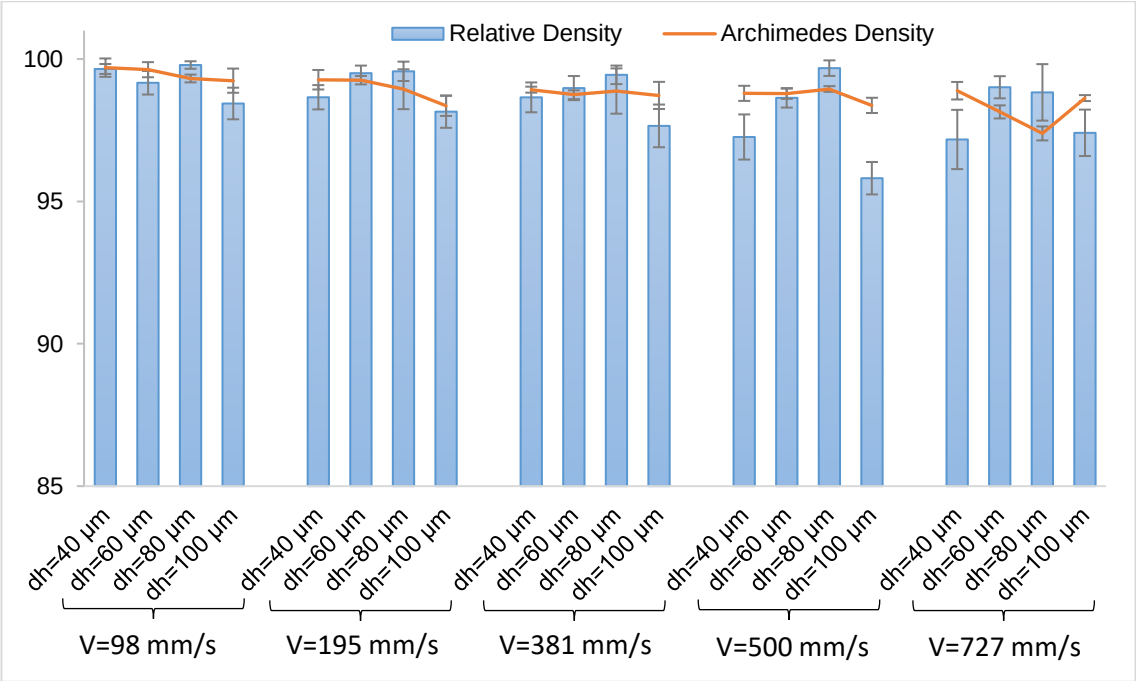

Figure 4.6: The Archimedes' and relative density of as-fabricated specimens in relation to the hatch spacing (d_h) and scanning speed (V) (Experiment 2).

4.2.3. Effect on Microstructure

EDS results, shown in Figure 4.7, show a uniform distribution of Al, Cu and Mg elements inside the fracture surface. The OM images in Figure 4.8 show the microstructure and melt-pool after etching, displayed from higher ED to lower ED. The melt-pool, Heat-Affected Zone (HAZ), dendrite orientation, cracks, porosities and microstructures of the post-processed specimens are shown. The chemical composition of the melted part and raw AA2024 powder shows an almost identical amount of Cu at the observed surface. However, even though medium laser power (150 W) was used, evaporation was observed for Mg, reducing from 1.8% to 1.4%, owing to the low boiling point of Mg (Mathers 2002). The EDS process could not detect the other alloying elements owing to the low weight ratio of the elements in the alloy. The build direction of the specimen is parallel to the observed surface. The OM images in Figure 4.8 show that coarse-grained microstructures are prevalent, owing to the high ED caused by high laser power (175 W) and slow scanning speed (195 mm/s) used to produce this specimen.

However, when the ED decreases with higher hatch spacing (100 µm) and scanning speed (727 mm/s), fine-grained microstructures become more apparent. Due to the fact that different EDs cause different thermal gradients and solidification rates in the melt-pool during the cooling, it is strongly influential on the microstructure (Maamoun et al. 2018). The coarse-grained microstructure at the melt-pool borders is more visible when manufactured with 60 µm hatch spacing, compared to 100 µm, even though the scanning speed and laser power are the same (see Figure 4.8h and Figure 4.8j). Examining the HAZ also shows the presence of some fine-grained microstructures, with gradients from fine-grained to coarse-grained microstructures. Moreover, solidification cracks (which is the foremost problem of the alloying elements for LPBF production) occur inside the melt-pool. It is also observed that the melt-pool depths of the specimens are non-uniform.

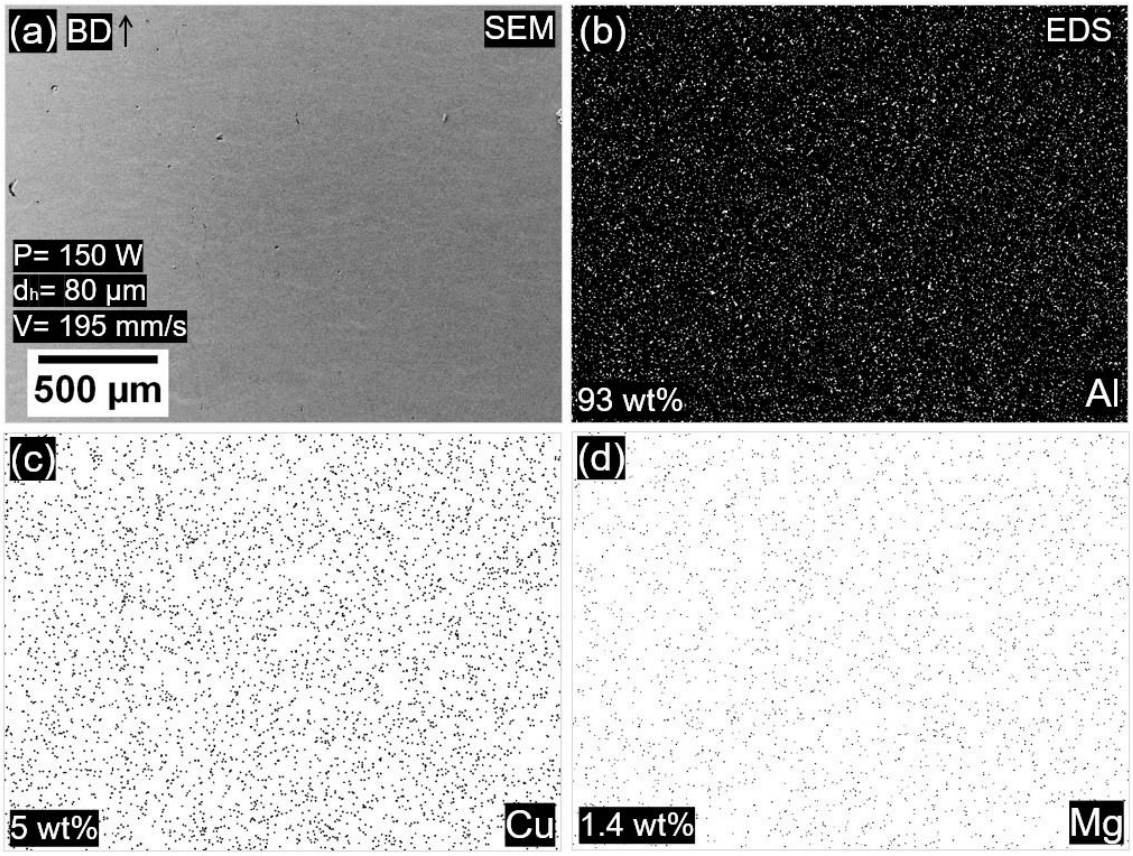

Figure 4.7 Showing the uniform distribution of Al, Cu, and Mg elements via EDS.

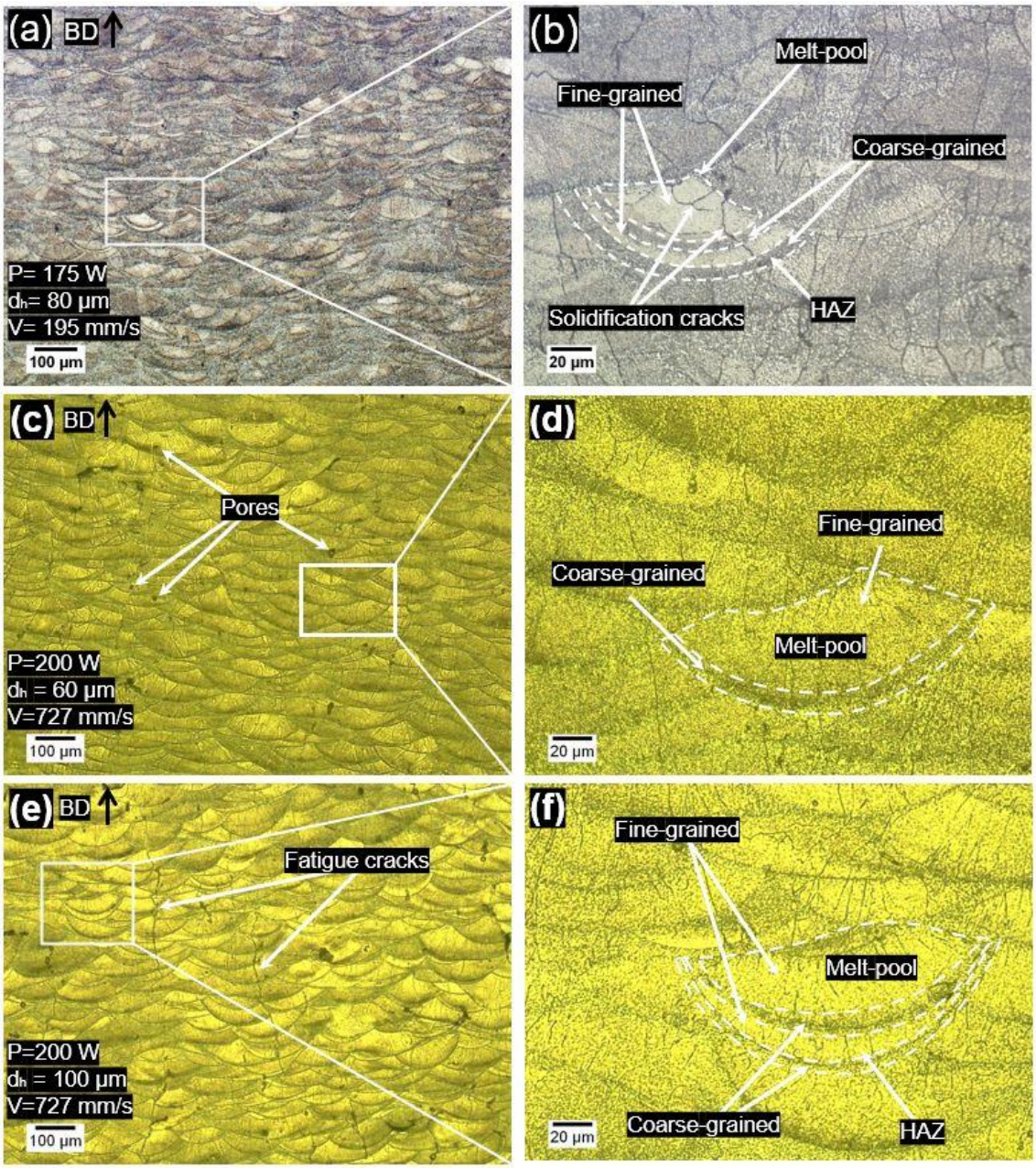

Figure 4.8: OM images showing the grain microstructure, cracks, pores and melt pool.

SEM images comparing three specimens produced with different laser power (125, 175 W and 200 W) and scanning speed (98, 381 and 500 mm/s) settings, at a constant hatch spacing (80 µm), are presented in Figure 4.9, showing the microstructure, melt-pool, solidification boundary, re-melt boundary and columnar dendrites of the as-fabricated specimens. Several micro-cracks, solidification cracking, micro-voids, small pores and cracks are shown in Figure 4.9. Moreover, Figure 4.9f shows that micro-cracks have grown throughout the melt-pool

boundary. In the same way, it has previously been reported that small amounts of unsolidified liquid between the melt-pool edges form films which keep the pools from bonding together in the final stage of solidification and eventuate in boundary cracks (Gu et al. 2018). Additionally, the dendrite orientation aligns towards the melt-pool centre.

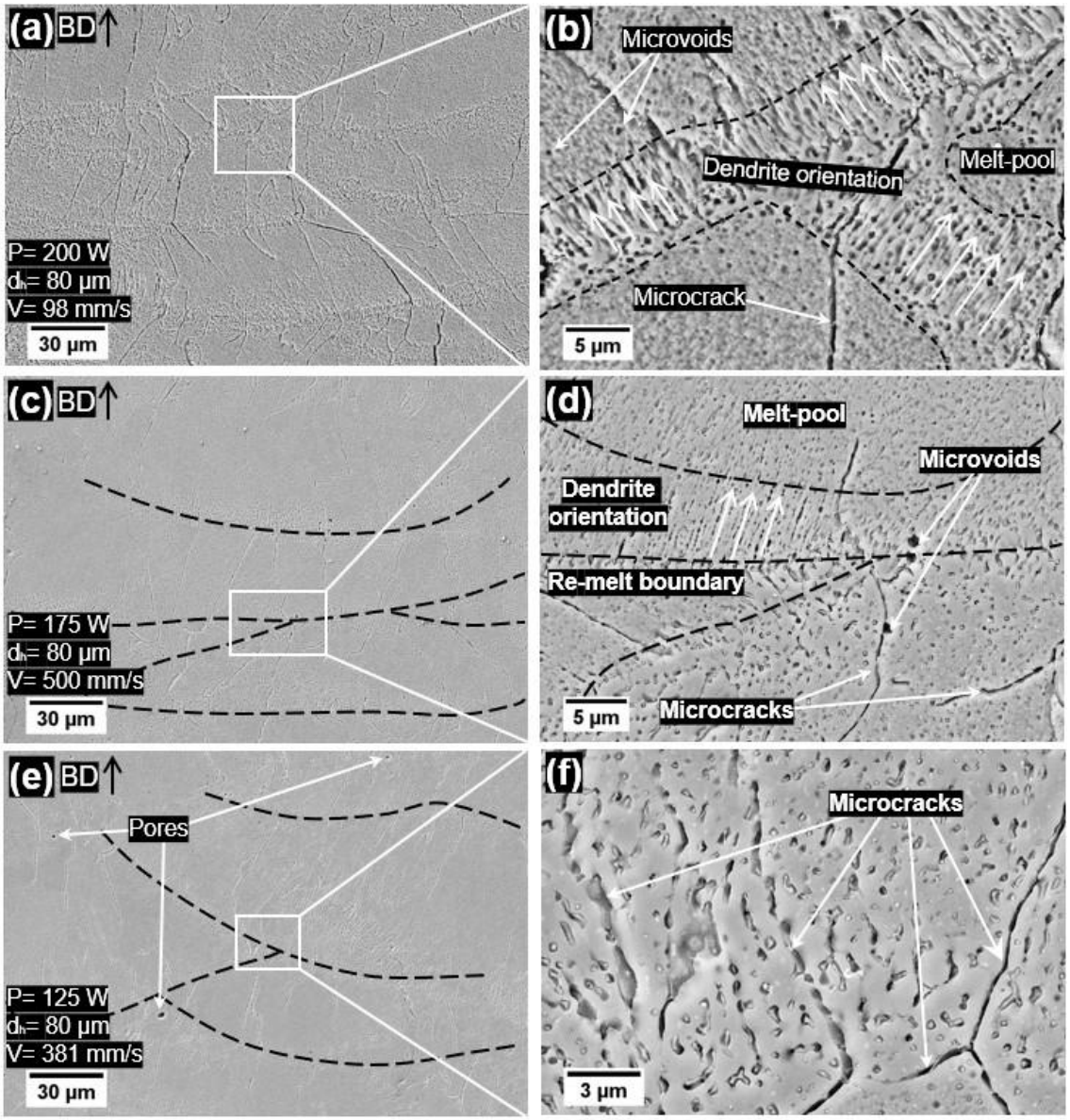

Figure 4.9: SEM images showing the microstructure, melt-pool, microcracks and columnar dendrites of the as-fabricated specimens.

Examples of specimens produced with low ED, owing to fast scanning speeds, are shown in Figure 4.10. Low ED, fast scanning speed, and incomplete fusion

cause unmelted powder and large cracks to form inside the structure, even though laser power is sufficiently high.

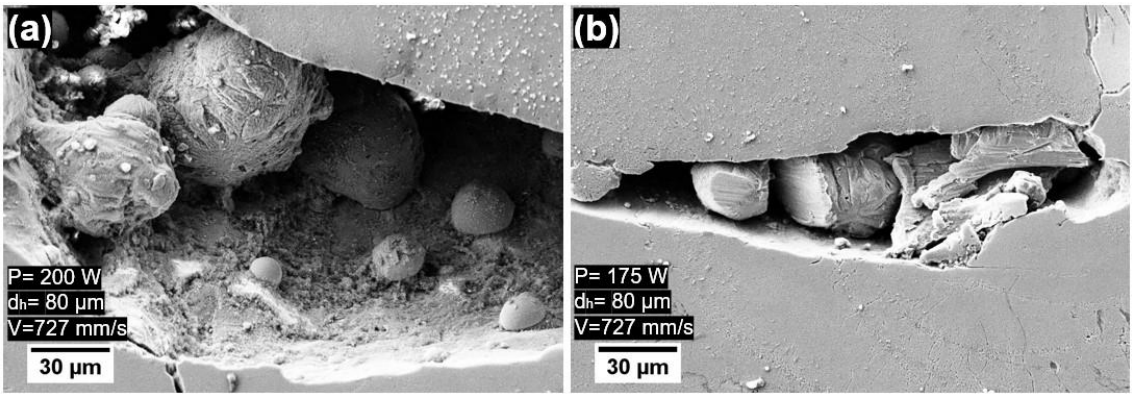

Figure 4.10: SEM images of unsuccessful fabrication showing (a) unmelted powders and (b) incomplete fusion defect owing to low ED.

4.2.4. Effect on Microhardness

Figure 4.11 and Figure 4.12 show that the microhardness and ED are inversely proportional. Increasing the ED results in a gradual reduction of microhardness. Figure 4.11 shows the effect of ED (in Experiment 1) on the Vickers microhardness under a 200g load ($HV_{0.2}$). With increasing ED, the microhardness gradually decreases, except for some small fluctuations. The highest microhardness (116 $HV_{0.2}$) was achieved from one of the lowest EDs (100 J/mm³), and the lowest microhardness (97.5 $HV_{0.2}$) was obtained from one of the highest EDs (759 J/mm³). Additionally, microhardness is inversely proportional to the relative and Archimedes' density results in Experiment 1, (see Figure 4.3). High densities were achieved at high EDs, which produces microhardness of a lower value. Moreover, the pattern of fluctuations in the results is identical to those seen in the results for Archimedes' and relative densities. At higher EDs, the fluctuations become smoother than at low EDs.

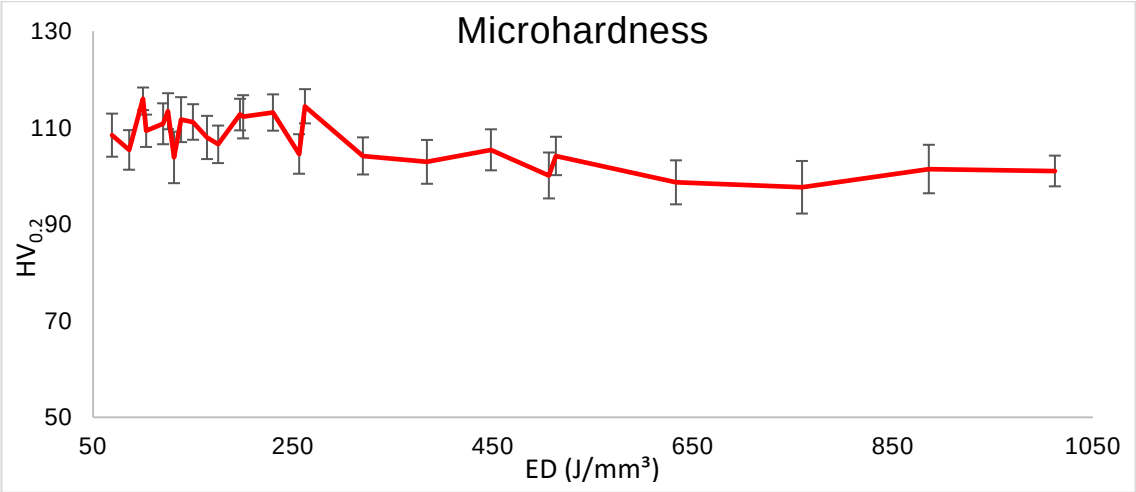

Figure 4.11: Vickers microhardness ($HV_{0.2}$) of as-fabricated specimens in relation to ED (Experiment 1).

Similar to Experiment 1 (Figure 4.11), the microhardness results of Experiment 2 also show fluctuations at low EDs (Figure 4.12). When the ED is increased, the microhardness becomes more stable, and the hardness progressively decreases. The highest microhardness obtained when varying the hatch spacing (115.5 $HV_{0.2}$) was obtained at the lowest ED. Similarly, the lowest microhardness (87.8 $HV_{0.2}$) is achieved at the highest ED. The pattern of fluctuation seen in Experiment 2 is identical to those seen in Experiment 1. Sharp fluctuations are apparent at low EDs and become smoother at higher EDs.

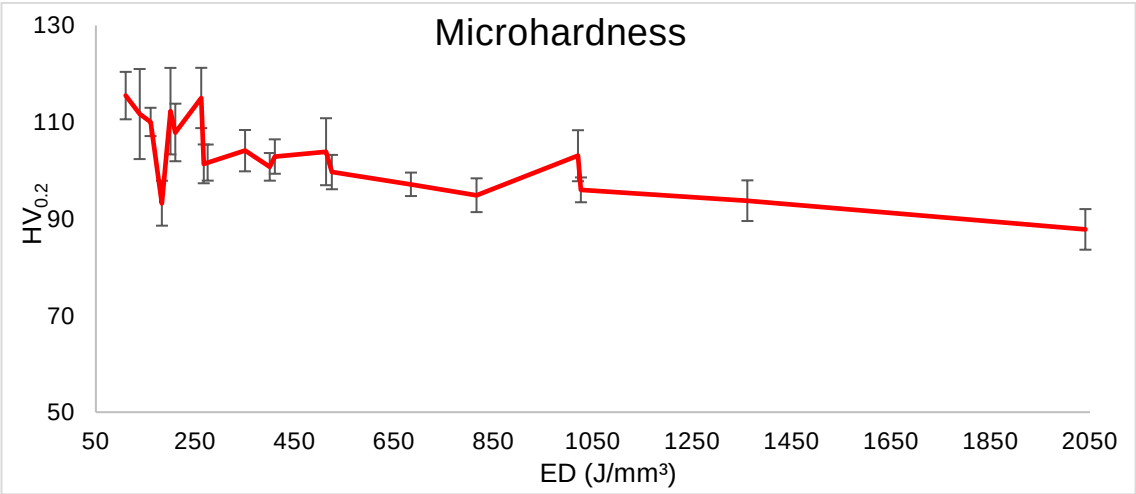

Figure 4.12: Vickers microhardness ($HV_{0.2}$) of as-fabricated specimens in relation to ED (Experiment 2).

The microhardness test indentation dimensions, depth and angle on the measured surface are depicted in Figure 4.13. Polished cross-section surfaces, which are parallel to the build direction of the specimens, were measured in order to examine the microhardness of different layers. The microhardness machine calculates the Vickers microhardness (HV) value below the equation (ASTM E92-16) (Broitman 2017):

$$HV = 1854.4 * P/(d_a)^2 \quad \textbf{(4.1)}$$

where P is the applied load (200 kgf) on test specimens and d_a is the arithmetic mean of d_1 and d_2 (Figure 4.13). During the experiment, d_1 and d_2 showed a variety between 54.12 and 65.5 μm.

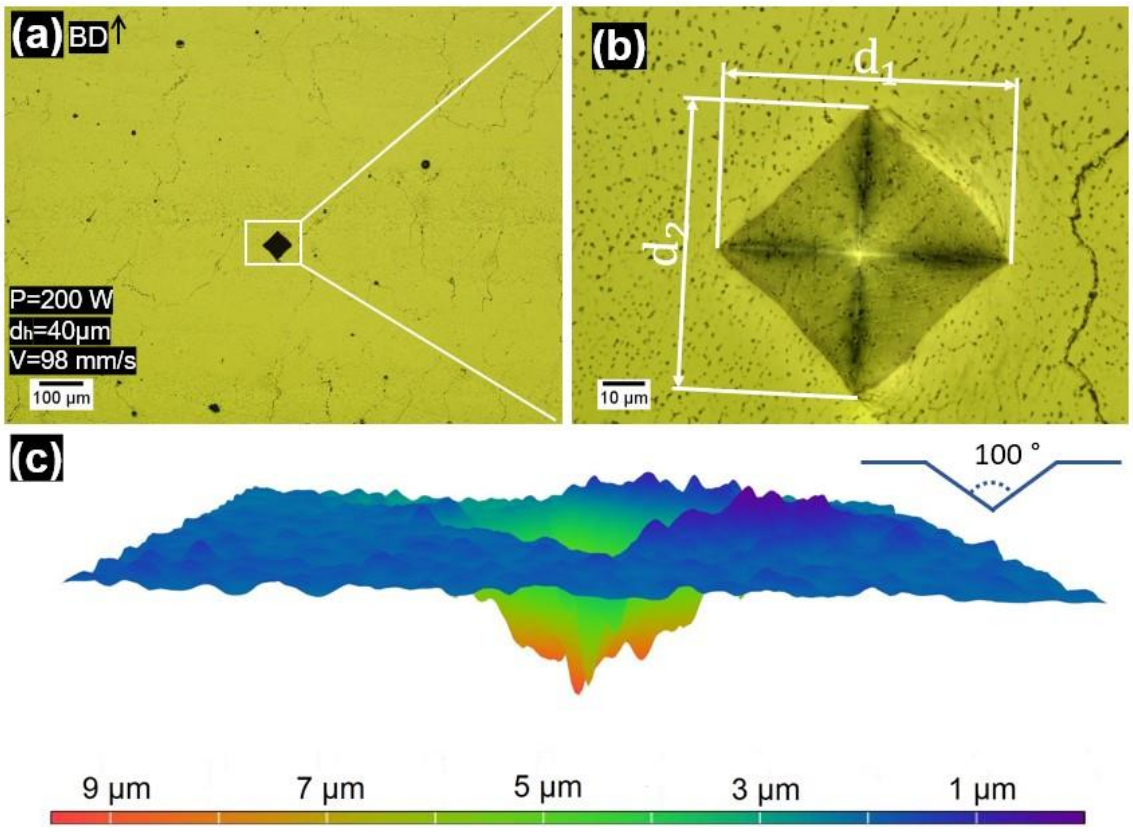

Figure 4.13: OM micrographs showing (a-b) microhardness indentation dimensions, (c) dept and angle of as-fabricated specimens.

4.2.5. Effect on Tensile Strength

The mechanical and microstructural properties of tensile test specimens are shown in Figure 4.14 and Figure ***4.15***. The UTS (145 MPa) and strain are shown in the stress-strain curves (Figure 4.14). Figure 4.14 shows that the tensile specimens fail before plastic deformation occurs, because of the brittle structure.

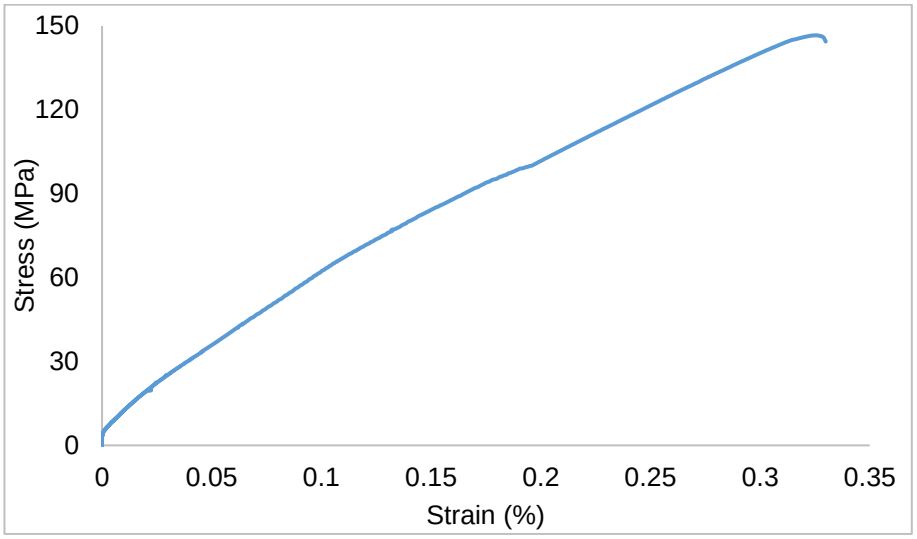

Figure 4.14: Strength vs strain curve of the as-fabricated specimen fabricated using 150 W laser power, 80 µm hatch spacing and 98 mm/s scanning speed showing the brittle failure of the specimens.

Further tensile test specimens were fabricated following the evaluation of Experiment 2. The optimum parameters (60 and 80 µm hatch spacing, with 98 mm/s scanning speed), were again chosen based on the highest relative and Archimedes' densities obtained from the cubic specimens. Figure 4.15 shows the tensile test results of the as-fabricated specimens (present study) and as-cast AA2024 (Zhang et al. 2016). It is seen from Figure 4.15 that the as-fabricated alloy specimens have approximately 20% less strength than the as-cast alloy.

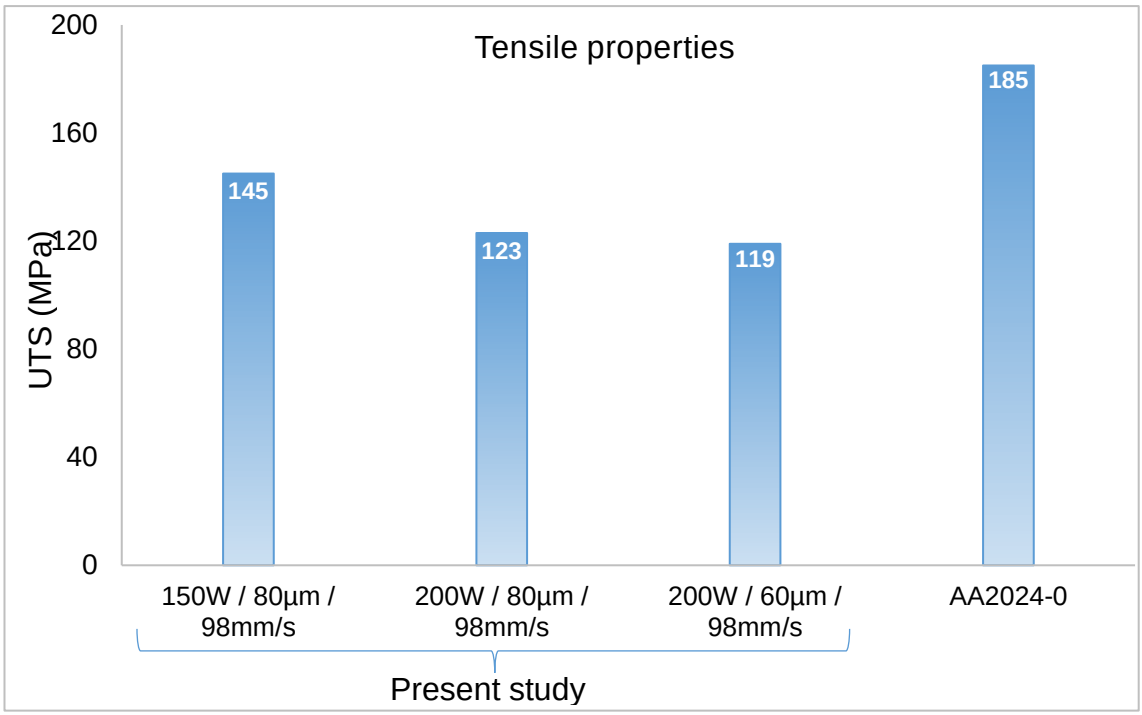

Figure 4.15: Tensile testing of as-fabricated AA2024 (fabricated using 60 and 80 µm hatch spacing and 98 mm/s scanning speed) in the present study and as-cast alloy in (Zhang et al. 2016) showing UTS.

Figure 4.16 indicates the dimensions and the fracture surface of the round tensile test specimens. The parameters, which achieved the highest relative density (99.9%) in Experiment 1 (with 150 W laser power, 80 µm hatch spacing, and 98 mm/s scanning speed) were used to fabricate the test specimens. Even though a relative density of 99.9% was achieved in the cubic specimens, the tensile test fracture surface has some unmelted powder holes, cracks, porosities and unmelted powder particles, which led to a brittle failure (Figure 4.16c-1,2,3). Furthermore, the crack initiation started from the site of unmelted powder particles and holes.

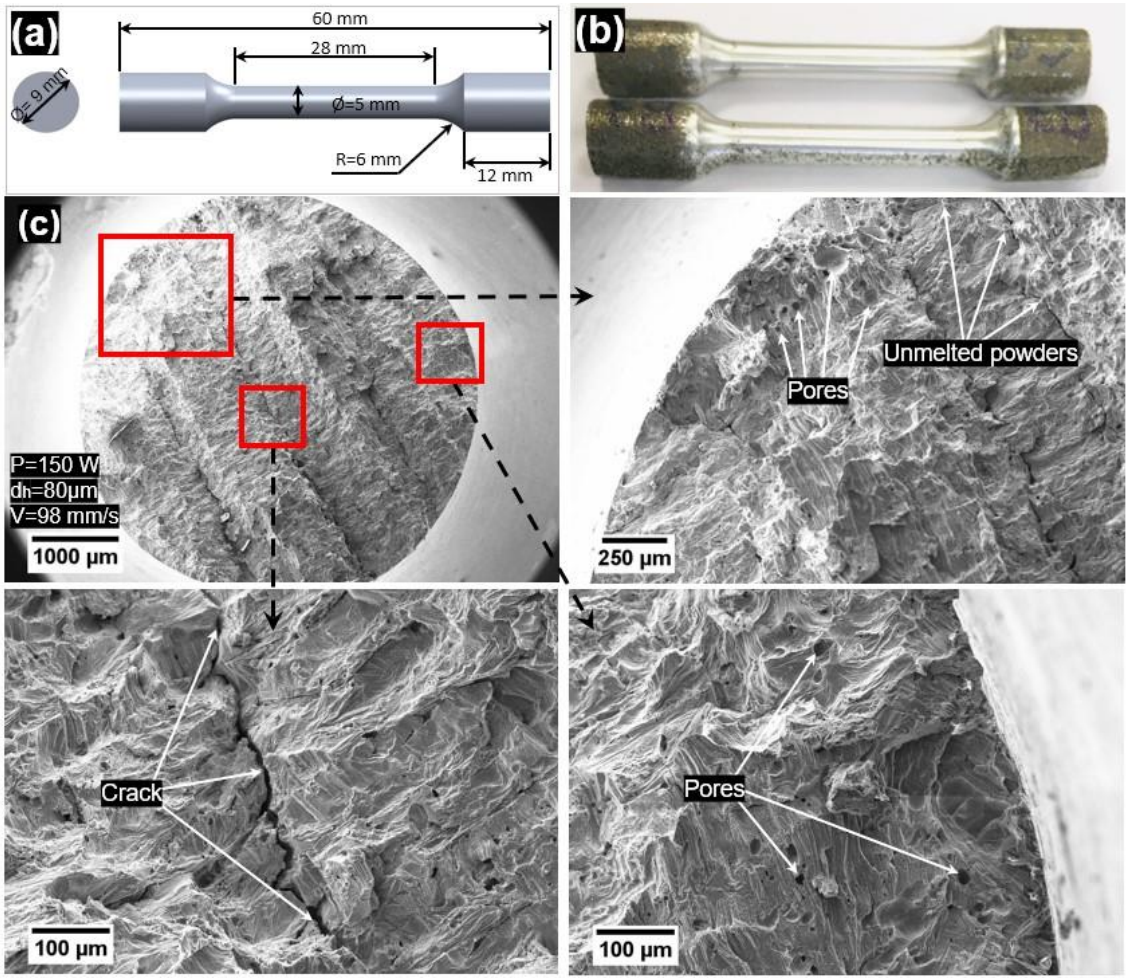

Figure 4.16: Dimensions of as-fabricated tensile testing specimens (a-b), and SEM images showing the fracture surface (c).

4.2.6. Statistical Analysis and ANOVA

ANOVA is a mathematical model to predict the porosity of the fabricated parts in relation to process parameters such as laser power, scanning speed and hatch spacing. This method has been studied to predict the effect and significance of processing parameters on the porosity of the different specimens (i.e., Ti6Al4V (Du et al. 2021), AA6082 (Ascari et al. 2012) and AlSi10Mg (Read et al. 2015) alloys) and fabrication techniques (i.e., SLM (Dutt et al. 2022) and direct energy deposition (Shim 2021)). In this study, Design-Expert 13 (Minneapolis, USA) calculation software was used to predict the density and microhardness. Three significant (laser power (P), hatch spacing (d_h) and scanning speed (V)) parameters were used as input factors, and three measured results

(microhardness, relative and Archimedes' densities) were used as outputs (Table 4.1). The second-order polynomial equation used in the calculation can be expressed to define the Response (Y_R) as follows (Read et al. 2015):

$$Y_R = b_0 + \sum b_i x_i + \sum b_{ii} {x_i}^2 + \sum b_{ij}(x_i x_j) \quad (4.2)$$

According to this equation, the open form of the response equation can be expressed as follows:

$$Y_R = b_0 + b_1(P) + b_2(V) + b_3(d_h) + b_4(PV) + b_5(Pd_h) + b_6(Vd_h) \quad (4.3)$$

where b_0 is the average response and b_1 to b_6 are model coefficients of process parameters. Additionally, the Signal-to-Noise (S/N) ratio can be calculated using the larger-the-better technique using the following equation (Dutt et al. 2022):

$$S/N = -10\, log(1/{Y_R}^2) \quad (4.4)$$

Table 4.1 Building parameter values, porosities and microhardness results of AA2024 fabricated using LPBF.

Run	Laser power (W)	Scanning speed (mm/s)	Hatch spacing (µm)	Relative density (%)	Archimedes' density (%)	Microhardness (HV)
1	100	98	80	99	98.08	100.1
2	100	195	80	99.3	98.48	104.55
3	100	381	80	96.6	95.94	103.87
4	100	500	80	95.2	93.84	115.99
5	100	727	80	88.5	90.48	108.47
6	125	98	80	99.8	98.71	98.67
7	125	195	80	99.6	98.64	104.14
8	125	381	80	99.2	97.56	107.97
9	125	500	80	98.6	95.95	113.41
10	125	727	80	91.5	92.95	105.39
11	150	98	80	99.8	99.08	97.66
12	150	195	80	99.7	98.77	102.92
13	150	381	80	99	99.4	112.71
14	150	500	80	99.4	98.31	111.18
15	150	727	80	95.8	95.06	109.36
16	175	98	80	99.7	99.32	101.43
17	175	195	80	99.7	98.87	105.41
18	175	381	80	99.2	99.34	113.14
19	175	500	80	99.7	98.57	106.55
20	175	727	80	97.9	96.87	110.81
21	200	98	80	99.8	99.5	101.03
22	200	195	80	99.6	99.08	104.14
23	200	381	80	99.5	98.99	114.43
24	200	500	80	99.7	99.25	112.26
25	200	727	80	98.8	97.69	111.67
26	200	98	40	99.6	99.7	87.8
27	200	195	40	98.7	99.27	95.98
28	200	381	40	98.7	98.92	99.66
29	200	500	40	97.3	98.8	100.74
30	200	727	40	97.2	98.89	101.62
31	200	98	60	99.2	99.63	93.74
32	200	195	60	99.5	99.26	97.12
33	200	381	60	99	98.75	104.09
34	200	500	60	98.6	98.78	101.36
35	200	727	60	98.9	98.14	93.22
36	200	98	100	98.4	99.24	94.87
37	200	195	100	98.2	98.35	102.87
38	200	381	100	97.7	98.72	107.86
39	200	500	100	95.8	98.37	110.03
40	200	727	100	97.4	98.63	115.48

Table 4.2 shows the result of the ANOVA statistical technique in relation to process parameters, density and microhardness. The total amount of data variation is represented as the Sum of Squares (SS). Based on the SS, F-value and p-value, the significance of parameters for densities can be listed as scanning speed, laser power and hatch spacing, respectively. However, the most significant parameter for microhardness is hatch spacing. The parameters are statistically significant at a 95% confidence level when the p-values are less than the significance threshold (0.05) (Modi and Sahu 2021). Additionally, the coefficient estimate shows the predicted change in reaction per unit change in factor value when all remaining factors are maintained constant. While R^2 and Adjusted R^2 exhibit substantial similarities, the Predicted R^2 and the Adjusted R^2 are in fair agreement with a difference of 9.6, 4.3 and 18%, respectively. A signal with an S/N ratio of 4 dB or above is considered to be satisfactory.

Table 4.2 Result of ANOVA for porosities and microhardness.

		SS	F-value	p-value	Coefficient Estimate	Error	R^2	Adjusted R^2	Predicted R^2	S/N Ratio
Relative density	P	0.0012	59.45	0.0001	0.0087	0.0011	0.8571	0.8202	0.7237	23.2
	d_h	0	0.8078	0.3757	-0.0012	0.0013				
	V	0.0021	105.76	0.0001	-0.0122	0.0012				
Archimedes' density	P	0.0012	211.78	0.0001	0.0088	0.0006	0.944	0.9296	0.8876	36.08
	d_h	0.000007	1.43	0.2409	-0.0008	0.0007				
	V	0.0013	242.56	0.0001	-0.0098	0.0006				
Microhardness	P	0	0.0966	0.758	-0.0012	0.0039	0.7727	0.714	0.5343	13.37
	d_h	0.007	29.91	0.0001	0.0252	0.0046				
	V	0.0045	19.49	0.0001	0.0181	0.0041				

Figure 4.17 to Figure 4.19 depict 2D contour plots and scatter diagrams of relative density, Archimedes' density and microhardness results of ANOVA, respectively. Based on the measured values, the ANOVA predicts the middle points of the

parameters. It is obvious in Figure 4.17a,b and Figure 4.18a,b that higher laser power values resulted in better density. However, better density results for hatch spacing values are accumulated between 60 to 80 µm (Figure 4.17b,c and Figure 4.18b,c). On the other hand, a comparison of measured and predicted density values is given in Figure 4.17d and Figure 4.18d. While Archimedes' density values are well predicted by ANOVA (Figure 4.18d), lower relative density values are predicted higher than measured values.

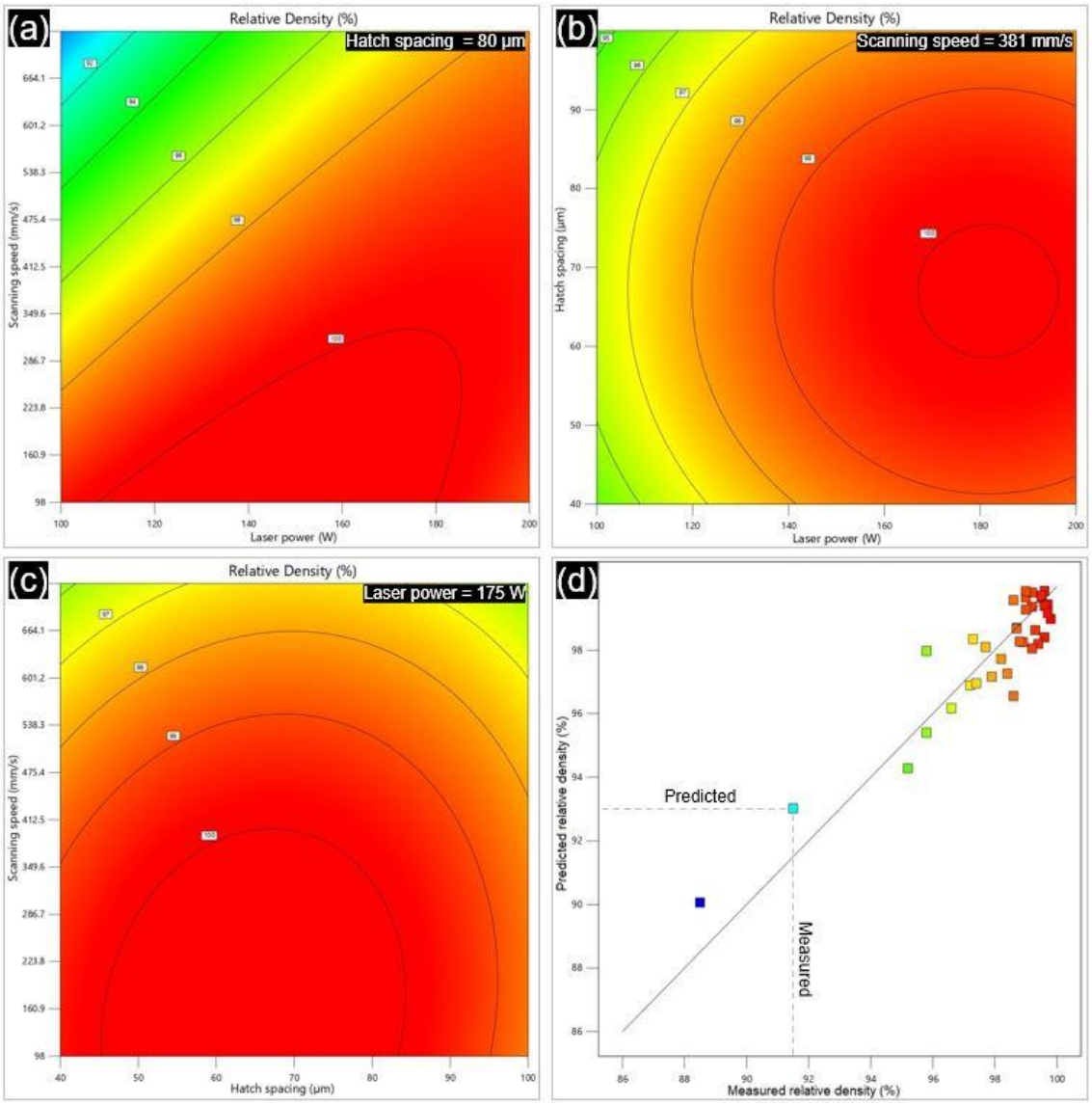

Figure 4.17 2D contour plots of relative density for (a) laser power-scanning speed, (b) laser power-hatch spacing, (c) hatch spacing-scanning speed, and (d) scatter diagram for measured and predicted relative density.

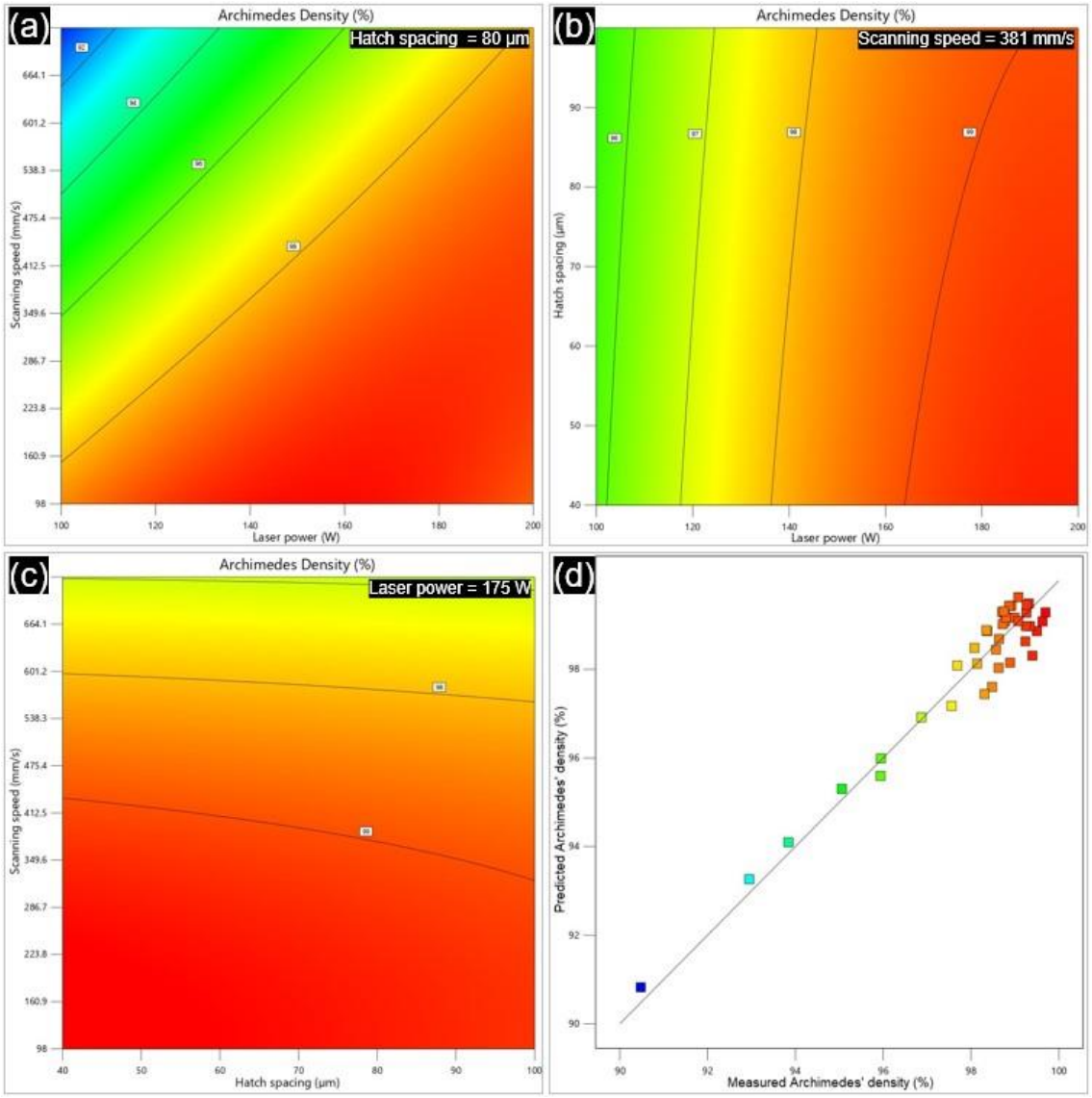

Figure 4.18 2D contour plots of Archimedes' density for (a) laser power-scanning speed, (b) laser power-hatch spacing, (c) hatch spacing-scanning speed, and (d) scatter diagram for measured and predicted Archimedes' density.

In comparison to densities, microhardness results indicate an inverse relation for processing parameters. Higher scanning speed and hatch spacing result in better microhardness value as discussed earlier (Figure 4.19a-c). However, the comparison of predicted and measured values is more separated than densities owing to the fluctuations in the measured microhardness results (Figure 4.19d).

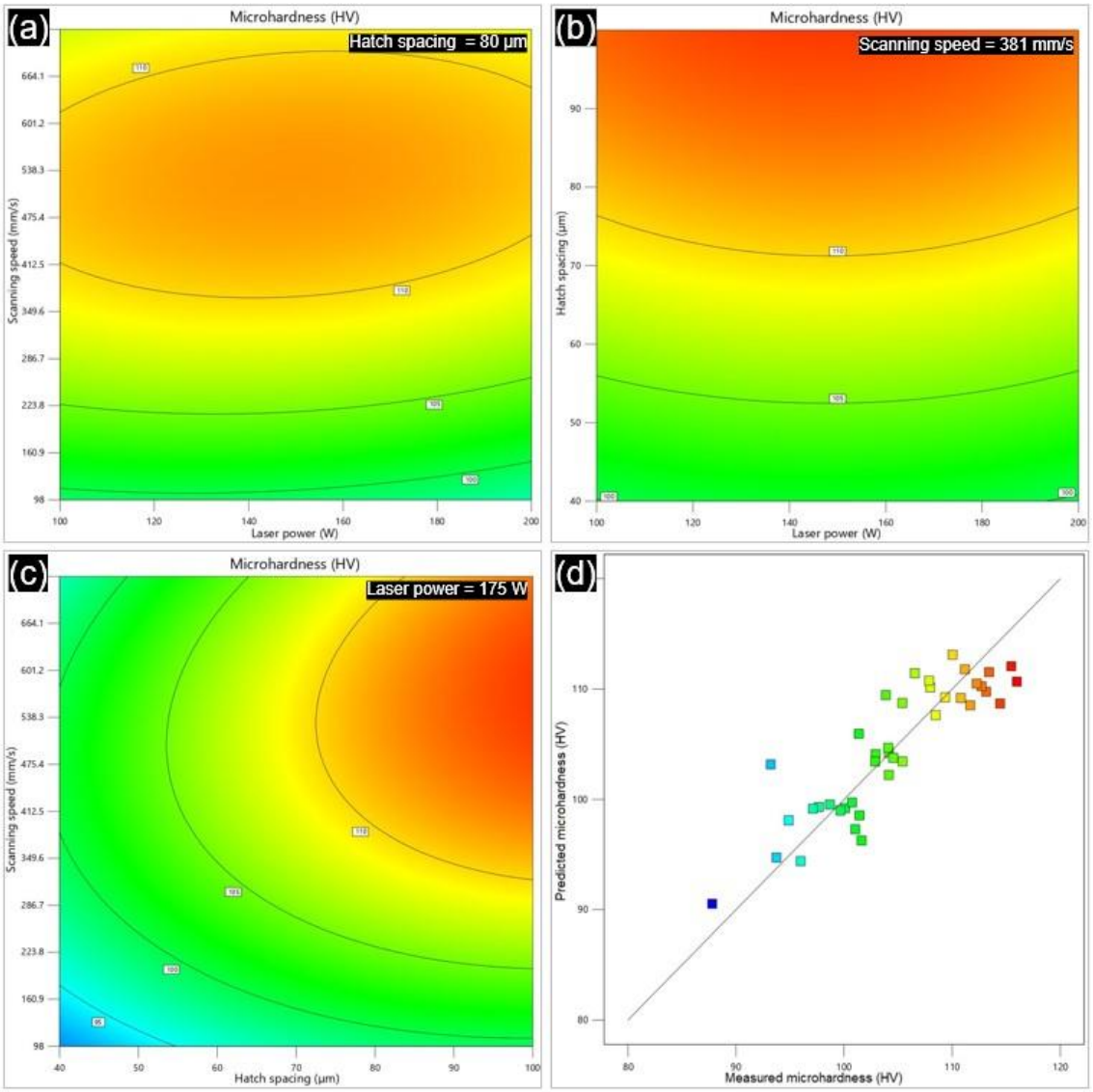

Figure 4.19 2D contour plots of microhardness for (a) laser power-scanning speed, (b) laser power-hatch spacing, (c) hatch spacing-scanning speed, and (d) scatter diagram for measured and predicted microhardness.

4.3. Discussion

The Archimedes' and relative densities of as-fabricated specimens are directly proportional to the ED used in manufacturing, due to the fact that high power, low hatch distance and slow scanning speed create a high melt-pool temperature. Additionally, the high temperature reduces the viscosity of the melted metal and results in better filling of the possible cracks or pores, which correlates with this result. Similarly, it has previously been observed that high ED results in a high level of liquid phase accompanied by a slow solidification time, which lowers the

viscosity of the liquid (Olakanmi 2013; Wang et al. 2018a). Thus, more neighbouring layers are positively affected, because the high ED will increase the number of penetrated layers. It was also reported that a high melt-pool temperature can decrease the surface tension and improve the wettability of the liquid metal as a result of the low cooling rate and better Marangoni flow (Olakanmi 2013). Moreover, both Archimedes' density and relative density have fluctuations at low ED, and the difference between the densities recorded with the two measurement methods at low ED is larger than at high ED. This is because low ED can cause large cracks to form in some layers, causing inconsistencies in the structure, and therefore variation in the measurements. On the other hand, using a slow-scanning speed can partially reduce the negative effect of the laser power and hatch spacing settings. This is because slower scanning speeds at constant laser power allow the powder to be melted more effectively than at faster scanning speeds, owing to the higher ED.

When examining the microstructure, coarse-grained microstructures have been observed at higher EDs, with lower EDs creating fine-grained microstructures. The reason for this difference is that higher ED increases the temperature of the melt-pool, thus decreasing the cooling rate. A slower cooling rate allows for more grain growth, increasing the coarse-grained microstructure formation (Mahamood et al. 2013). It has previously been observed that different solidification rates, created by using different hatch spacing parameters, can result in the formation of these different microstructures and that both fine-grained and coarse-grained microstructures can be found around the HAZ in a single specimen (Han and Jiao 2019). Furthermore, it has been reported that the cooling rate of solidification in the midpoint of the melt-pool is more rapid in comparison to the boundary regions (Han et al. 2017c). During the LPBF process, the laser is applied to one deposited

layer of powder, and the heat then transfers from the top to the bottom of the melt-pool. Owing to these temperature gradients, columnar grains can form during the solidification process, which then grow from the top to the bottom of the melt-pool (Zhang et al. 2016). It has also been reported that coarse-grained microstructures generally form at the bottom of the melt-pool, due to the thermal gradients and subsequent different solidification rates between the top and the bottom of the melt-pool (Wang et al. 2018b). The HAZ can also cause an accumulation of coarse-grained microstructures at the bottom region of the melt-pool (Wang et al. 2018b). Moreover, gradients from fine-grained to coarse-grained microstructures become more distinct at high EDs, owing to the high thermal gradient through the melt-pool. Hence, the boundaries of the different microstructures in the melt-pool become more obvious. Similarly, the slower cooling rate at the boundary regions of the melt-pool produces larger grains, which explains the coarse dendritic microstructure (Kalpakjian et al. 2014).

An inversely proportional relationship between the microhardness and ED has been determined in both experiments. This can be explained by the difference in the microstructure. High energy in the melt-pool area increases the solidification time, the temperature of melted material and the size of the melt-pool (Zhang et al. 2019). However, high temperatures also result in a slow cooling rate at the solidification interface, which generates a coarse-grained microstructure. Contrary to this, using a low ED increases the cooling rate and creates a fine-grained microstructure, which restricts the dislocation movement (Larimian et al. 2020). Due to this limited dislocation movement, the microhardness shows a gradual increase at low EDs. Similarly, low microhardness at high ED has been previously reported in another study (Lei et al. 2019). Microhardness of Sc and Zr modified Al7075 composite firstly increased and then decreased with

increasing ED owing to the grain size and chemical composition of the alloy. Additionally, it has been stated that the reduction of the Mg with increasing temperature of melt-pool and ED may reduce the microhardness of the as-fabricated specimens (Wei et al. 2017). A reduction in the weight ratio of Mg is also observed in the present study. The maximum microhardness achieved is approximately 45% higher than as-cast AA2024 but 17% lower than wrought AA2024-T6. However, LPBF provides 26% higher microhardness in comparison to the as-cast alloy, but 28% lower than wrought alloy at the optimum parameter (Table 4.3). The increase in microhardness, when compared to the as-cast alloy, may be due to the limitation of dislocation and movement by the fine-grained microstructures produced using LPBF (Yusuf et al. 2017); higher dislocation density restricts slip along the grain boundaries, restricting deformation and increasing the strength. It is also noted that, although the diagonal angle of the microhardness indentation tool is 136° the measured angle after the test is completed is 100° (see Figure 4.13c). This is because the as-fabricated specimen deforms elastically during the dwell time and retracts after the microhardness indentation tool is removed. Similarly, in another study, the diagonal angle of the indentation trace of the Vickers indentation tool on the observed surface of the Al(Si)-Cu-Co alloy after the load was measured as approximately 75° (Mukhopadhyay et al. 2001).

Table 4.3: Microhardness results of the alloy under different manufacturing methods.

Matrix	Microhardness (HV)	Method	Reference
AA2024	116 (Maximum)	LPBF	Present study
	101 (Optimum)	LPBF	
AA2024-0	80	As-cast	(Zhang et al. 2016)
AA2024-T6	135-145	Wrought	

The UTS of as-fabricated AA2024 produced using LPBF (145 MPa) in the present work is lower than as-cast AA2024 (185 MPa), as expected, because of the high relative crack sensitivity of the alloy during the welding process. Unmelted powder particles on the surface of the tensile specimens may also contribute to their brittleness. Comparably, the effect of specimen size on porosity of as-fabricated Al2618 (which has a similar weight ratio of alloying elements to AA2024), manufactured using LPBF may give an indication of the effect of the fabricated component size on priority (Koutny et al. 2018). It has been reported that when the fabricated specimen size is increased from 5x5x5 to 13x13x5 mm^3, the relative porosity dramatically increases from 0.03 to 5.95 % (Koutny et al. 2018). It has also been shown that, for as-fabricated Al2618 series alloys, different tensile test results were observed for different processing strategies (i.e., built on supports, built on the plate, meander, chessboard, hull and core) and different fabrication techniques (i.e., LPBF vs extruded material) (Koutny et al. 2018). It is discussed that, while defects in the structure are reduced substantially, the cracks on the interface are a major restriction in achieving a high mechanical strength for the alloy (Koutny et al. 2018). Hence, the high crack susceptibility of the alloy, especially for larger parts, makes the tensile test specimen more brittle.

In our study, even though a relative density of 99.9% was achieved in the cubic specimens when using the optimum parameters, unmelted powder holes, lack-of-fusion porosities and gas porosity have been observed on the fracture surface of the tensile test specimens (as shown in Figure 4.16). It has also been reported that higher laser energy, along with high scanning speed, causes an increase in the residual stress in both the x-direction and y-direction of the built specimen (Wang et al. 2018a). Hence, the mechanical properties of the as-fabricated tensile specimens may be affected dramatically. Another possible cause of the

low mechanical properties of the alloy may be an oxide film around the melt-pool. Difficulties in fabricating Al alloys using LPBF have been previously studied, and it has been reported that the formation of a thin oxide film happens around melt-pool, upper and lower surfaces in every layer, and cracks and pores are formed when several oxide films meet at one region (Louvis et al. 2011). It was concluded that the formation of the oxide film can be eliminated by producing a 100% dense part which is technically impossible for Al fabricated using LPBF.

The ANOVA test results represent that the parameters (laser power, hatch spacing and scanning speed) significantly affect the density of the as-fabricated parts based on the SS, F-value and p-value. Additionally, the ANOVA results show that hatch spacing is more significant on the density of the specimens than the other parameters. Furthermore, the value of R^2, predicted R^2 and the adjusted R^2 show similarities to each other suggesting that forty combinations using three parameters are adequate to predict the middle values of the parameters.

4.4. Summary

This study investigates the effect of laser power, hatch spacing and scanning speed on the mechanical properties and microstructure of as-fabricated AA2024 manufactured using LPBF. A wide range of EDs, which are obtained by varying the laser power (100, 125, 150, 175 and 200 W), scanning speed (98,195,381,500 and 727 mm/s) and hatch spacing (40, 60, 80 and 100 µm), are investigated for the processing of this alloy. Other parameters of the LPBF process were kept constant during the experimental work to allow comparisons. Archimedes' density, relative density, microhardness and TS were studied in order to determine the effect of varying ED. The following conclusions are drawn from the experimental results.

1) The highest relative density (99.9%) was achieved using a 98 mm/s scanning speed, 80 µm hatch spacing and 150 W laser power (rather than 200 W laser power, which produced a density of 99.8%). However, the highest Archimedes' density (99.7%) was achieved from the highest laser power (200 W) and the slowest scanning speed (98 mm/s) at a 40 µm hatch spacing.

2) The major phenomena when using EDs lower than 130 J/mm^3 are unmelted powder and large cracks forming inside the structure, due to incomplete fusion. The foremost issue for EDs higher than 300 J/mm^3 are microcracks and small gas pores (due to air remaining between the prepared powder particles), inside the melt-pool during the melting process.

3) Slower scanning speeds provide higher Archimedes' and relative densities at constant laser power and hatch spacing. The negative effect of low laser power may partially be eliminated by reducing the scanning speed.

4) Both Archimedes' and relative density results at higher EDs show similarities; however, high fluctuations were observed at lower EDs due to the nonuniform layers of the as-fabricated specimens, and the measurement technique for relative density, which utterly depends on the nature of the observed surface.

5) The highest microhardness (115.5 $HV_{0.2}$) was achieved from the lowest ED. Correlatively, the lowest microhardness was achieved from the highest ED. The reason for this inversely proportional relationship is that low ED provides low temperatures in the melt-pool, a high cooling rate, and produces a fine-grained microstructure, which restricts dislocation movement in the structure and hence increases the microhardness.

6) Tensile testing results and the analysis of the fracture surface reveal that solidification cracking plays a significant role in the strength of larger parts made from these alloys. The maximum UTS was measured as 145 MPa for the tensile test specimen manufactured with 150 W laser power and 98 mm/s scanning speed at 80 µm hatch spacing. SEM images show that unmelted powder is observed on the fracture surface of the tensile test specimen, contrary to the results obtained from the 6x6x7 mm^3 specimens. The crack initiation started from the edge of the tensile specimen on which unmelted powder occurred, due to the incomplete fusion.

Various processing parameters have a considerable impact on porosity and mechanical properties, according to the ANOVA and experimental data. The highest densities (99.7%) were attained with 500 mm/s scanning at 200 W laser power and 80 µm hatch spacing, despite the greatest densities (99.8%) being obtained at 98 mm/s scanning speed. For industrial applications, faster scanning speeds can dramatically reduce fabrication costs and time.

5. Chapter: Effect of Ball Milling Parameters on GNPs/AA2024 Powder

This chapter addresses the second research objective of this thesis. The effect of milling speeds and times on Gr-reinforced AA2024 composite are provided in this chapter. Additionally, the effect of PCA on MMC powder is examined with and without PCA. This chapter is mainly divided into four sections. First, the research methodology of the study is provided in Section 5.1. After that, the results are provided in Section 5.2. This result section is divided into two main parts. The first part studied the effect of high and low ball milling speed (Section 5.2.1). Additionally, powder morphology and agglomeration of the Gr in MMCs are also studied. In the second part of the result section, agglomeration of the GNPs in MMCs is investigated with regard to milling time (Section 5.2.2). DEM powders for each milling time were created using real powder from an experimental study. Both experimental and simulation results including PSD, microstructural characterisation and microhardness are provided in Section 5.2. Additionally, experimental and simulation flowability analysis results of powders are presented in this section. Finally, a discussion and summary of the chapter are given in Sections 5.3 and 5.4.

5.1. Research Hypotheses

The following are some of the research hypotheses:

- Due to the high impact energy, even short milling times may result in the powder being flattened instantly.

- Slow milling speed (100 rpm) might not embed the Gr particles inside the matrix material owing to the low impact energy.
- Due to the low impact energy, powder morphological differentiation may be slow at low milling speeds.
- Dispersion of the Gr particles might take time owing to the van der Waals forces between GNPs.

5.2. Results

5.2.1. Effect Of Milling Speed

5.2.1.1. Effect of PCA

The PCA was added into the milling bowl in order to prevent cold welding and the accumulation of the milled powder. A wide range of control agents have been examined in practice; however, different percentage of stearic acid in the milling bowl was extensively preferred due to the sufficiency of the acid to the welding and powder contamination (Han et al. 2017a; Yue et al. 2017). In the present study, raw Al alloy powder was tested with and without stearic acid (2 wt.%) for 15 minutes to examine the effect of the agent on the milled powder (Figure 5.1). During the milling process, the temperature inside the bowl increased to 70°C and the stearic acid, (which has a low melting point), melted and covered the surface of the bowls and the milling balls. Thus, the alloy powder was prevented from accumulating and sticking onto the ball surfaces during the milling (Figure 5.1b-d). Without PCA, the powder agglomerated and stuck onto both the milling balls and bowl surfaces (Figure 5.1a-c).

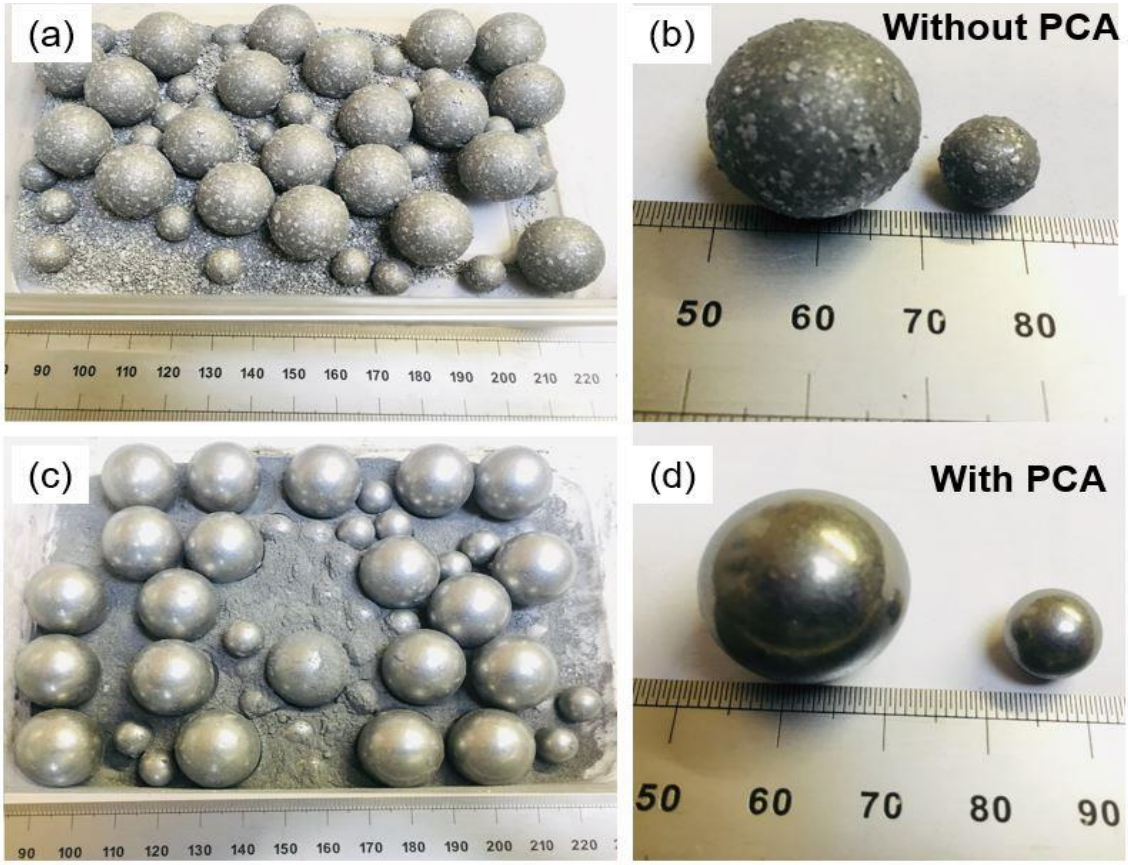

Figure 5.1: The milling balls and powder after 15 minutes of milling without (a-b) and with 2% of PCA (c-d).

5.2.1.2. The PSD of the MMC after Slow Milling Speed

The PSD and powder shapes for raw AA2024, Gr and milled powders are shown in Figure 5.2. The Al alloy powders are not spherical, and the median particle Dv_{50} of the alloy and Gr are 37.6 µm and 35.1 µm; however, Dv_{10} and Dv_{90} of the elements show big differences. The PSDs after milling at a slow speed (100 rpm) for short milling times (0.5, 1 and 2 hr) are also presented in Figure 5.2. The powder distribution is approximately between 10 µm to 70 µm for raw Al and between 5 µm to 150 µm for Gr before the milling process. However, the powder particle size for the milled MMC after 0.5 hr ranges between 5 µm to 110 µm, and bigger particles become more distinct. The reason for this is because a short milling time (0.5 hr) at 100 rpm agglomerates the powders. Moreover, the accumulated large Gr sheets are not sufficiently separated because of the low impact energy inside the milling bowl at the beginning of the process.

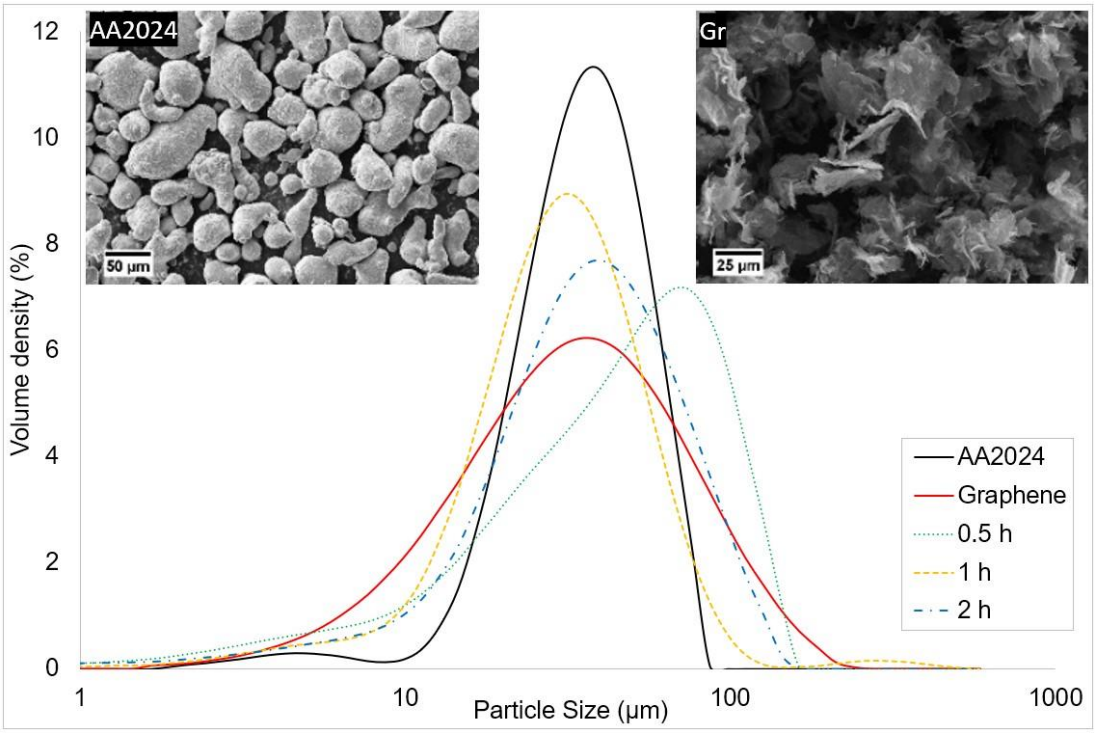

Figure 5.2: The powder shape and PSD of raw materials (AA2024 and Gr) and the milled powders after milling times of 0.5, 1, and 2 h at 100 rpm.

The particles Dv_{10}, Dv_{50} and Dv_{90} are shown in Figure 5.3. At the beginning from 0 to 0.5 hr milling time, Dv_{10} decreases, but Dv_{90} increases, due to the lower Dv_{10} and higher Dv_{90} of the Gr compared to the Al alloy. However, further milling causes a fluctuation in Dv_{50} and Dv_{90}. This may indicate the disintegration of Gr sheets first (1 hr milling), and then agglomeration of alloying powder and Gr (2 hr milling).

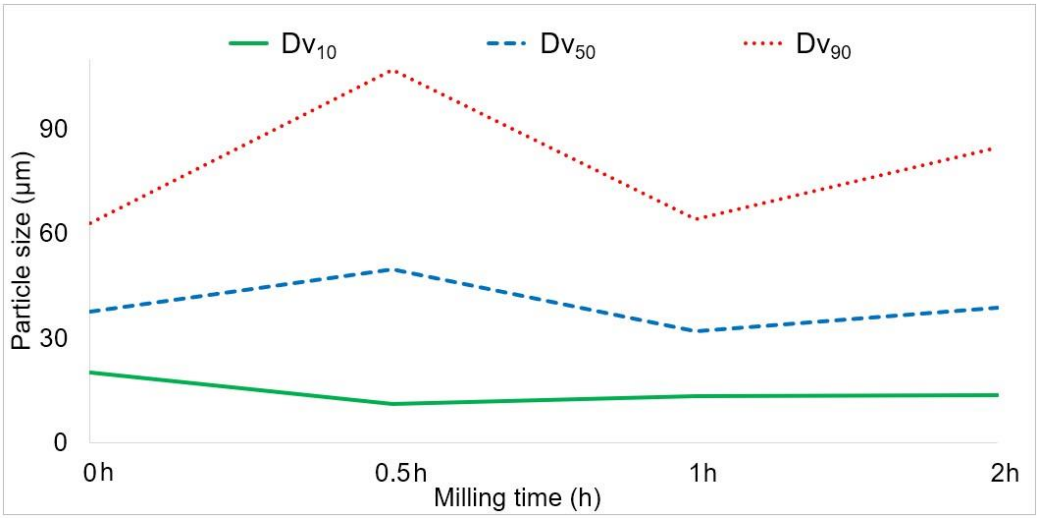

Figure 5.3: The particles Dv_{10}, Dv_{50} and Dv_{90} of the powder after milling times of 0, 0.5, 1, and 2 h at 100 rpm.

5.2.1.3. Gr Distribution in MMC after Slow Milling Speed

Figure 5.4 shows the SEM images of the milled MMC after different milling times (0.5, 1 and 2 hr) at 100 rpm. The shape of the alloy powder is not extensively changed and the Gr sheets, which are indicated in Figure 5.4, are not embedded inside the alloy powders due to the low impact energy. Moreover, agglomerated Gr sheets could not be dispersed in a short milling time (0.5 hr); nevertheless, further milling up to 2 hr has separated the sheets and distributed the Gr in the MMC more homogeneously than after a short milling time. Furthermore, even after 2 hr milling the powder shape is not dramatically changed; however, the Gr sheets are still not adhered to the Al alloy surface, owing to the low impact energy. On the other hand, some parts of the surface of the alloy powder have been coloured black by the Gr, which is made of a honeycomb shape of black carbon molecules.

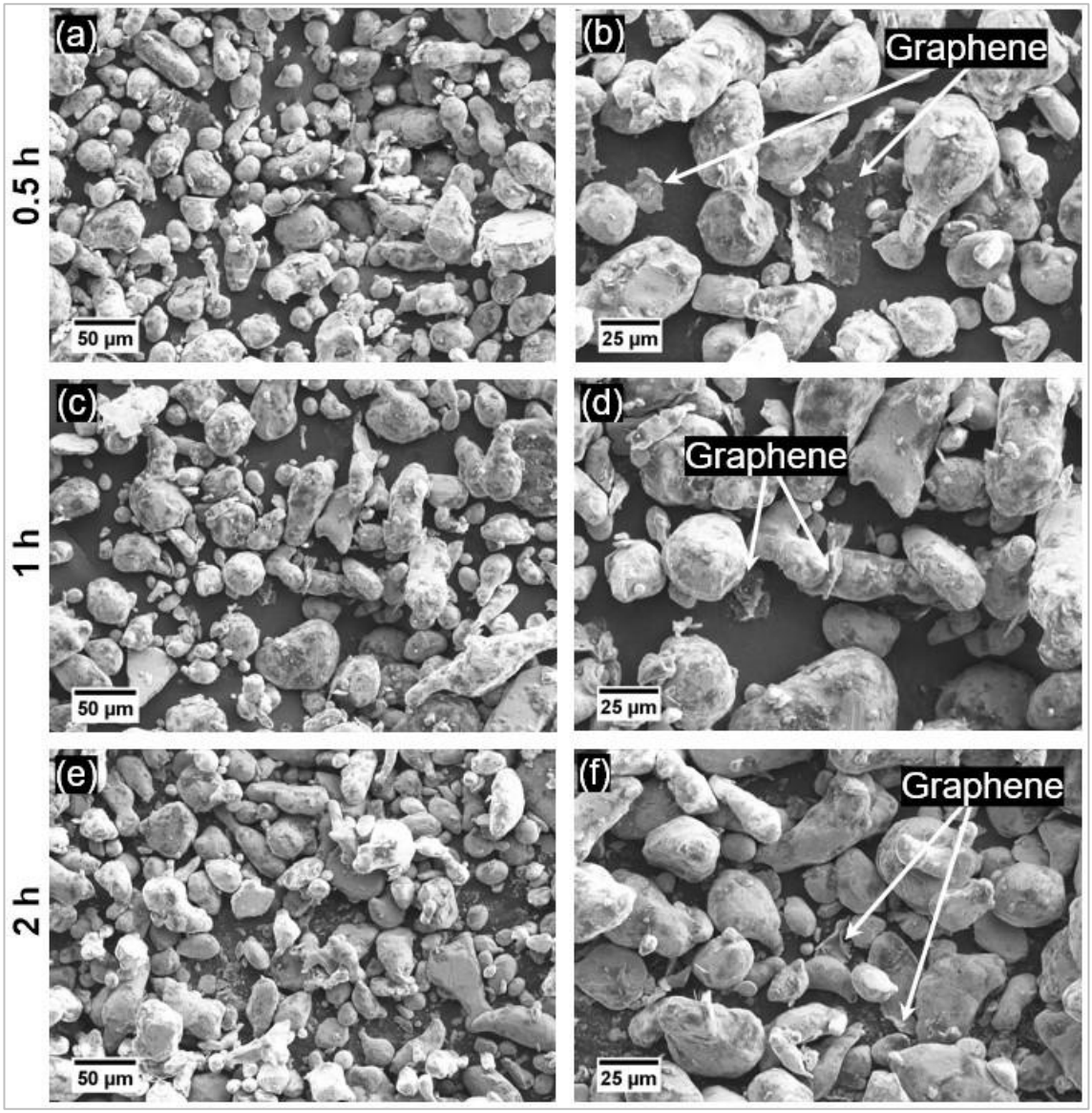

Figure 5.4: SEM images showing the distribution of the Gr sheets in MMC after the milling times of 0.5, 1, and 2 hr at 100 rpm.

5.2.1.4. The PSD of the MMC after Fast Milling Speed

The PSD of raw Al alloy, Gr and milled MMC after different milling times are shown in Figure 5.5. The volume of small particles less than 10 µm is dramatically increased using a faster milling speed (250 rpm) in comparison to the slow milling speed because high energy impacts crumble both the Al alloy and Gr particles. Additionally, the volume density of bigger particles greater than 100 µm is also enhanced using a faster milling speed, due to both the accumulation of the Al powder, and large agglomerations of Gr sheets.

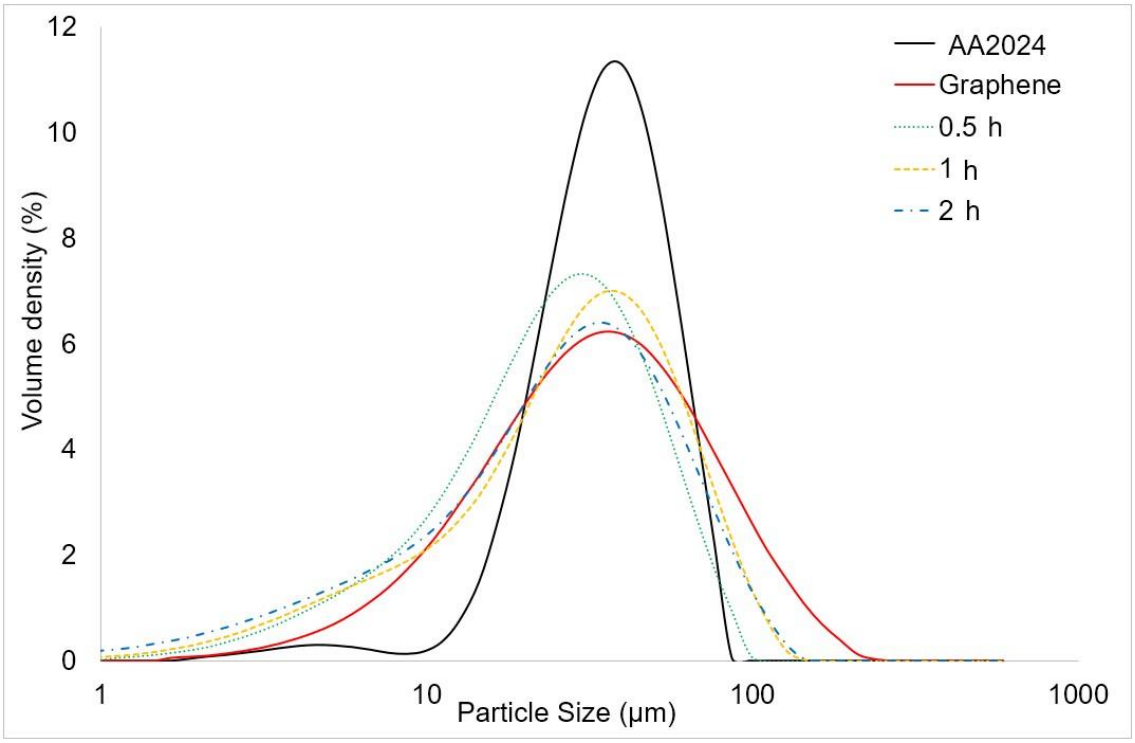

Figure 5.5: The PSD of raw materials (AA2024 and Gr) and the milled powders after the milling times of 0.5, 1, and 2 h at 250 rpm.

Figure 5.6 depicts the Dv_{10}, Dv_{50} and Dv_{90} of the MMC. Reinforcing Gr (which has a low Dv_{10} and high Dv_{90}) into Al alloy for 0.5 hr shows an identical effect as when using a slow milling speed. However, further milling time increases the particle size, owing to both accumulations of the elements and enlargement of the surface area of the powder with high impact energy. In order to achieve a constant deposited layer for the AM process, the volume of particles with a size above 90% should not be high, otherwise, larger particles may negatively affect the layer deposition process.

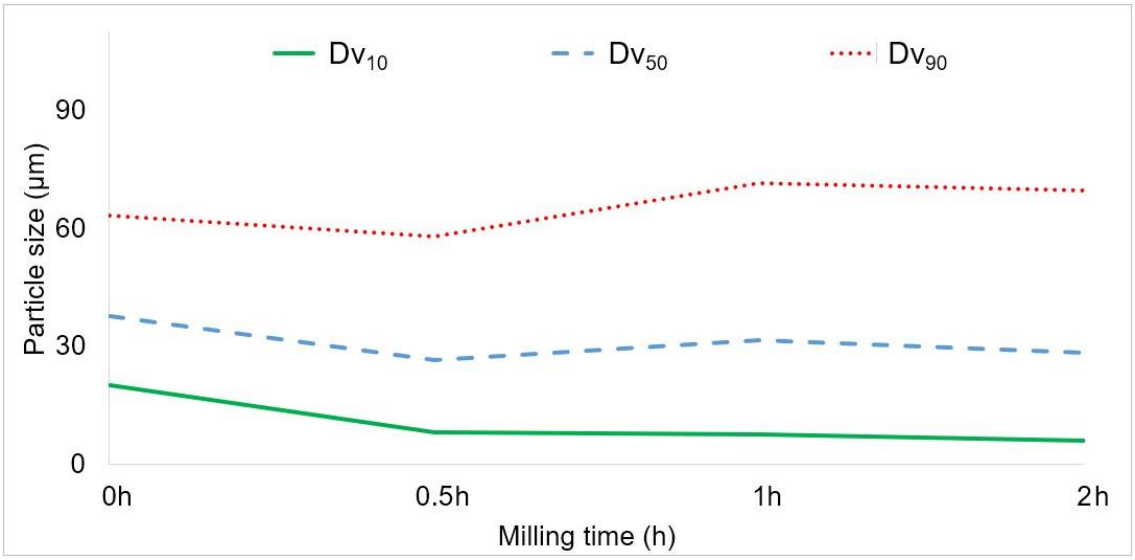

Figure 5.6. The particles Dv_{10}, Dv_{50} and Dv_{90} of the MMC after the milling times of 0, 0.5, 1, and 2 h at 250 rpm.

5.2.1.5. Gr Distribution in MMC after Fast Milling Speed

SEM images after different milling times at 250 rpm milling speed are shown in Figure 5.7. The Al alloy powder shape has been flattened by the high impact energy of milling balls. The Gr platelets have been crumbled into small pieces and stuck on the surface of the powder. Even though most of the Gr sheets have been dispersed, some accumulated Gr sheets remain visible inside the MMC. Hence, visual identification of Gr among the flattened powders is difficult. Additionally, flattened particles inside MMC become more distinct when the milling time is increased up to 2 hr (see Figure 5.7). On the other hand, the non-spherical form of the powder may negatively affect the deposition quality of the AM process.

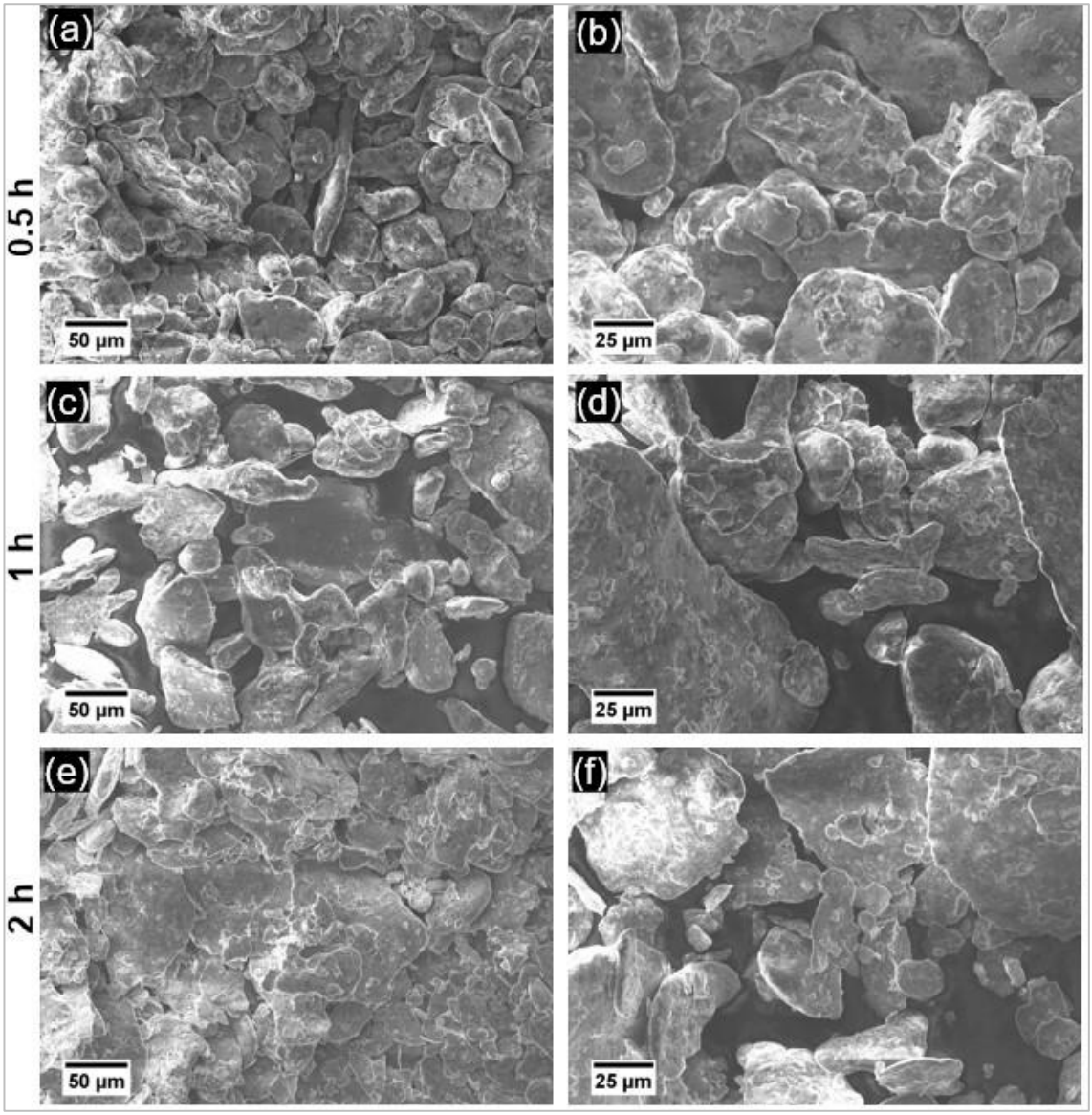

Figure 5.7: SEM images showing the distribution of the Gr sheets in MMC after the milling times of 0.5, 1 and 2 h at 250 rpm.

5.2.2. Effect of Milling Time

5.2.2.1. The PSD of the Composites

The PSD of milled composites under different milling times (from 0.5 to 16 hr) is shown in Figure 5.8 including median particle size and volume density of Dv_{50}. While median particle size progressively increases with regards to milling time, the volume density of the median particle shows a significant decrease after 4 hr milling. The rise in particle size can be explained by plastic deformation in the powder during milling (Fogagnolo et al. 2003). On the other hand, the volumes of

small and large particles tend to become closer to the median value (Dv_{50}), and the volume density increases from 6.3 to 8.1% with an increasing milling time from 0.5 to 4 hr. However, beyond 4 hr milling, the trend of particle sizes moving towards the median reverses, and Dv_{50} of the 16 hr milled powder is reduced to 5.75%. This sharp reduction in median volume density and larger median particles after 4 hr milled powder demonstrate that particle welding had initiated in this period. Moreover, the large surface area of the flattened particle also dominantly affects the particle size and volume density. It has been reported that laminar structures might cause fluctuation in the particle measurement owing to the angle between the laminar particle and the laser beam of the analyser (Fogagnolo et al. 2003). Therefore, accumulated and disintegrated Gr can also cause this fluctuation because of the large surface area of the GNPs. Furthermore, the progressive curve shifting of the Dv_{50} to right shows that welding occurs mostly at smaller particles, which tend to get larger particles due to the compressive force of the milling balls during milling (Benjamin 1976).

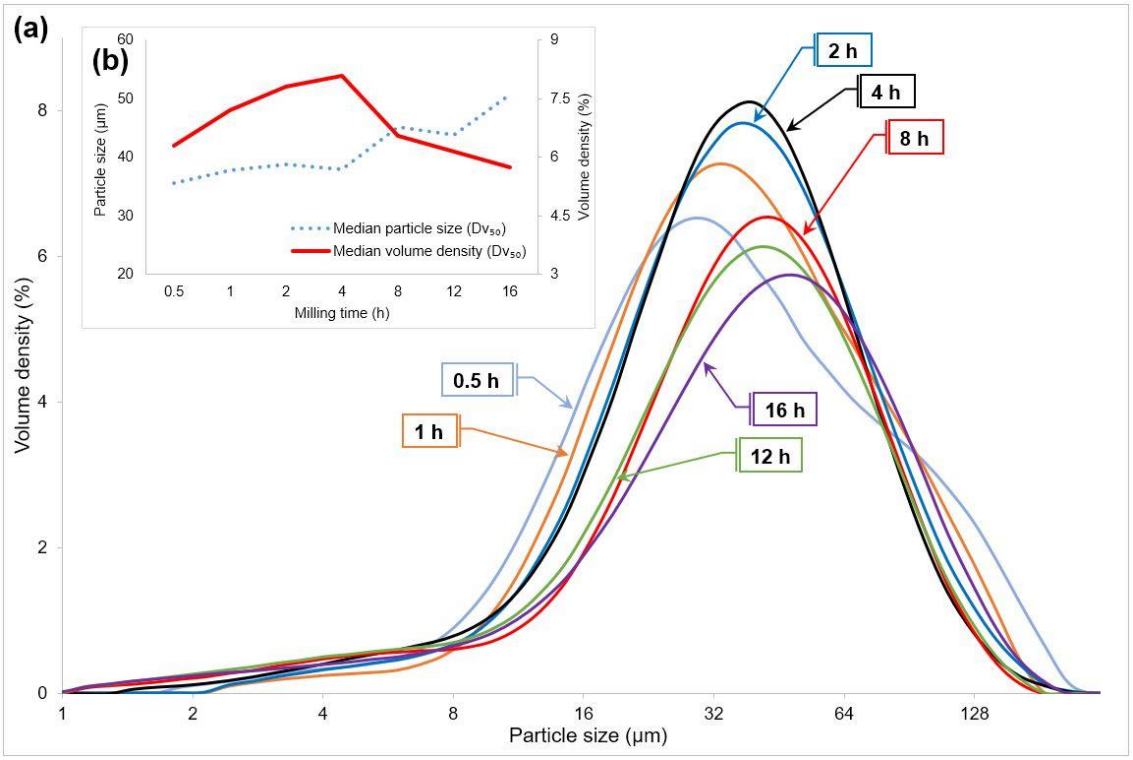

Figure 5.8: The PSD and median values of milled composites from 0.5 to 16 hr.

5.2.2.2. Microstructural Characterisation

The XRD pattern of the raw alloy, 4 hr and 16 hr milled composites in Figure 5.9 shows that the patterns are nearly identical. Raw alloy refers to the average crystallite size and lattice strain of the as-received powder in the case of an unreinforced alloy. The intensity of the 16 hr milled powder is contracted and broadened compared to the 4 hr milled composite and raw alloy. This broadening (which is also related to a reduction in the size of the coherent domain (Gusev et al. 2019)) is caused by the presence of a high density of dislocations and other crystalline defects during grinding (Wu et al. 2013). Additionally, this contraction substantiates the idea that crystallite density was enhanced with increasing milling time (Fathy et al. 2014). The average crystallite size of the alloy powder is estimated using Equation 1 as 35.75, 33.93, and 27.14 nm for the raw alloy, 4 and 16 hr milled powder, respectively. Five peaks of AA2024 were detected at two-theta of 38.5°, 44.7°, 65.1°, 78.2°, and 82.4°. Similarly, grain refinements from gas atomised raw alloy powder to milled powder for AA2124 and AA6005 alloys were observed because of the mechanical deformation in the milled powder particles (Eldesouky et al. 2014; Cabeza et al. 2017). Gr (or Carbon) and any other inter-metallic compound did not form in the XRD test due to the limitation of the X-ray Identify phases having a volume fraction of less than 2% (Cullity 2001; Ahamed and Senthilkumar 2010; Raviathul Basariya et al. 2014). Similarly, no other phases including alloying elements in both as-received and milled AA2024 powder have been observed in the literature studies (Tailor 2011; Mirzaei et al. 2015). The absence of carbon peaks might potentially be due to homogeneous dispersion of GNPs within the matrix, amorphization and unfavourable strain/GNPs effect which decreases the peak intensity of GNPs (Esawi et al. 2009; Raviathul Basariya et al. 2014).

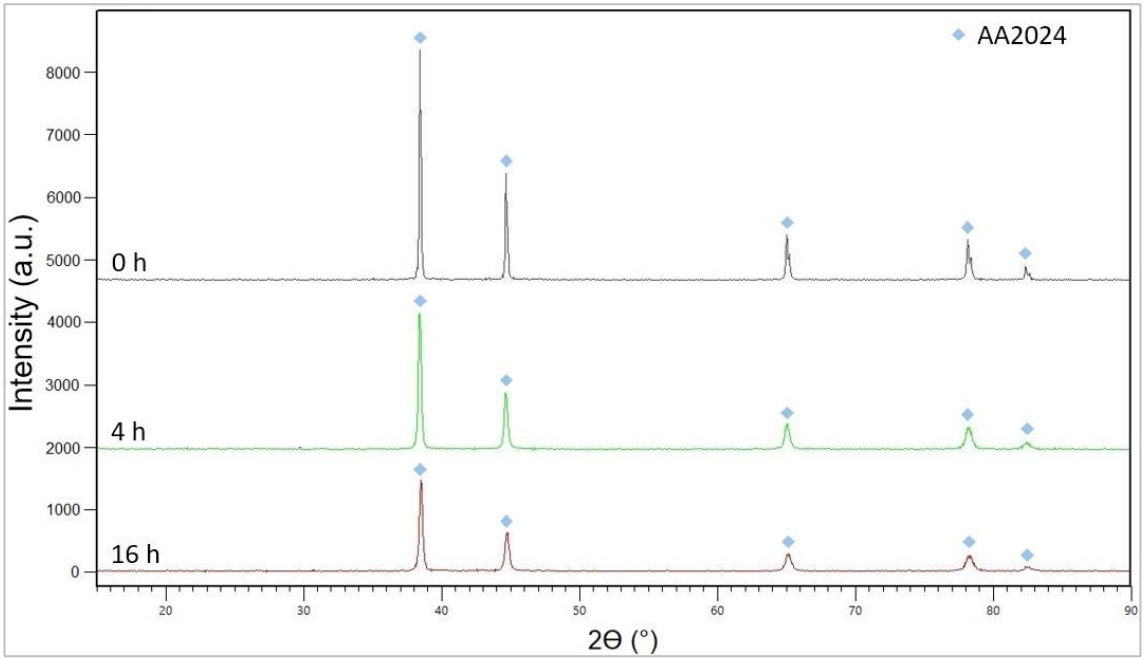

Figure 5.9: XRD patterns of raw alloy, 4 and 16 hr milled composites.

SEM, EDS, and map sum spectrum of 4 hr milled powder are shown in Figure 5.10. Reinforced GNPs (one of the carbon allotropes) and oxygen are represented as C and O under white background (see Figure 5.10e,f). EDS maps and X-ray spectrum of the cross-section region depict the existence of Carbon (as a representative of GNPs) in the 4 hr milled powder composite. Additionally, the homogeneous dispersion of the Gr is shown in Figure 5.10e. It has been stated that oxide film presented on the surface of the Al alloy powders is one of the biggest problems, and it is difficult to avoid or remove owing to the thermodynamic stability of Al sesquioxide (Olakanmi et al. 2015). Alloying elements that are present in quantities lower than 1 wt.% (Mn, Si, Fe, and Ti) are not detected because the elements' concentration is lower than the detector's threshold value. Additionally, Figure 5.10 corroborates that contamination from milling equipment (which is made of stainless steel) is not detected. One reason is that the contamination is lower than the threshold level of the detector; however, this also demonstrates that the weight ratio of the stearic acid (2 wt.%) in the bowl is adequate to cover the surface of the milling ball and interior wall of

the bowl and inhibit the contamination of worn iron elements during milling. Low milling speed which generates low impact energy inside the milling bowls is another important factor to inhibit the powder from contamination.

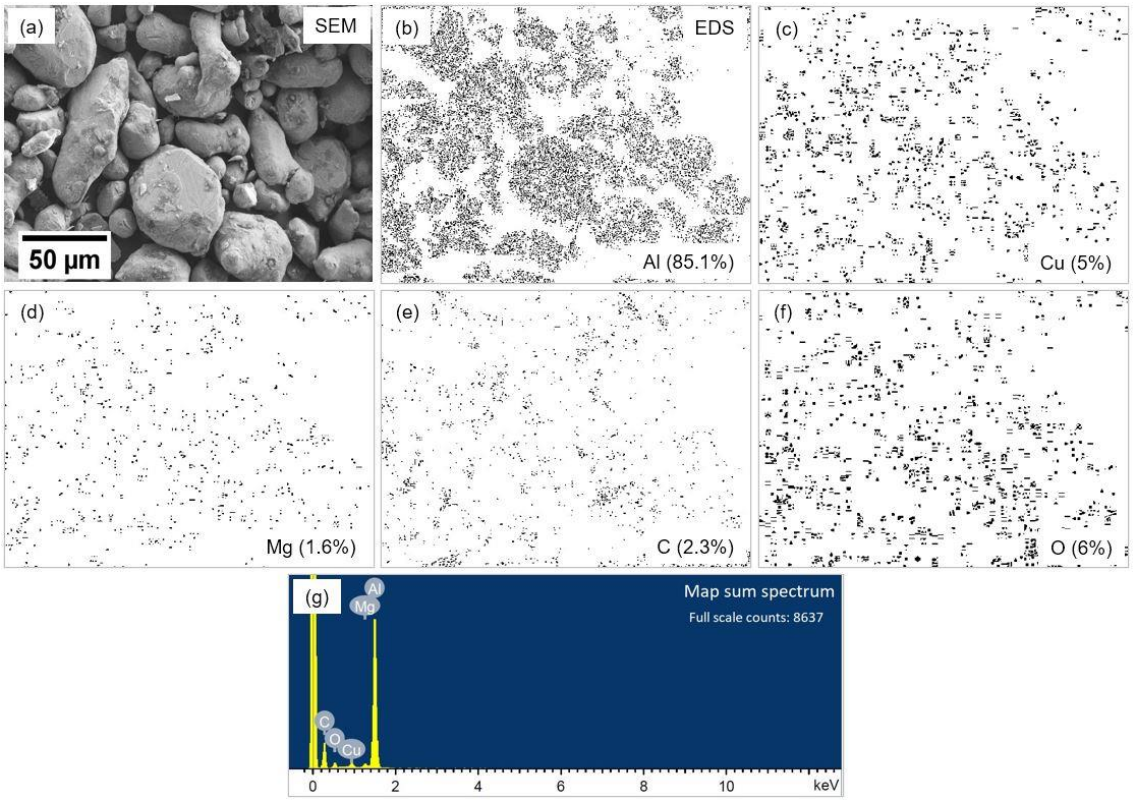

Figure 5.10: SEM images (a) and distribution of Al, Cu, Mg, C and O elements via EDS (b-f) and (g) map sum spectrum of 4 hr milled powder.

SEM images showing the effect of different milling times (from 0.5 to 16 hr) on the milled powder under the constant milling speed (100 rpm) are shown in Figure 5.11 and Figure 5.12. Agglomerated large GNPs (marked with arrows), apparent at 0.5 to 2 hr milling times, demonstrate that the distribution of agglomerated Gr flakes is insufficient. Moreover, Gr flakes did not adhere to the surface of Al powders. However, at 4 hr milling, GNPs are starting to disperse and adhere to the Al powder surface. It is important to note that powder morphology did not change significantly between 0.5 to 4 hr milling time because of the mild impact energy under low milling speeds. The other reason for the less plastically deformation on the powder is the protective role of the PCA. It has been noted

that stearic acid creates resistance against cold welding between particles and the accumulation of the particles by coating the particle's surface (Zhang et al. 1999). Additionally, the particle-to-milling-equipment fracture rate may increase with the addition of PCA, while the friction coefficient between the ball and the powder particle decreases (Nouri et al. 2010). Therefore, an adequate amount of PCA can prevent the powder from extensive plastic deformation at short milling times (Nouri et al. 2010). Gr provides an intrinsic tendency to form agglomeration due to the large specific surface area, strong Van der Waals attraction and π-π interaction of Gr (Hu et al. 2018). Short milling times promote the formation of agglomeration at the beginning, resulting in impact energy being used to dissolve the Gr particles first. Because of this reason, shorter milling times tend to result in less morphological difference.

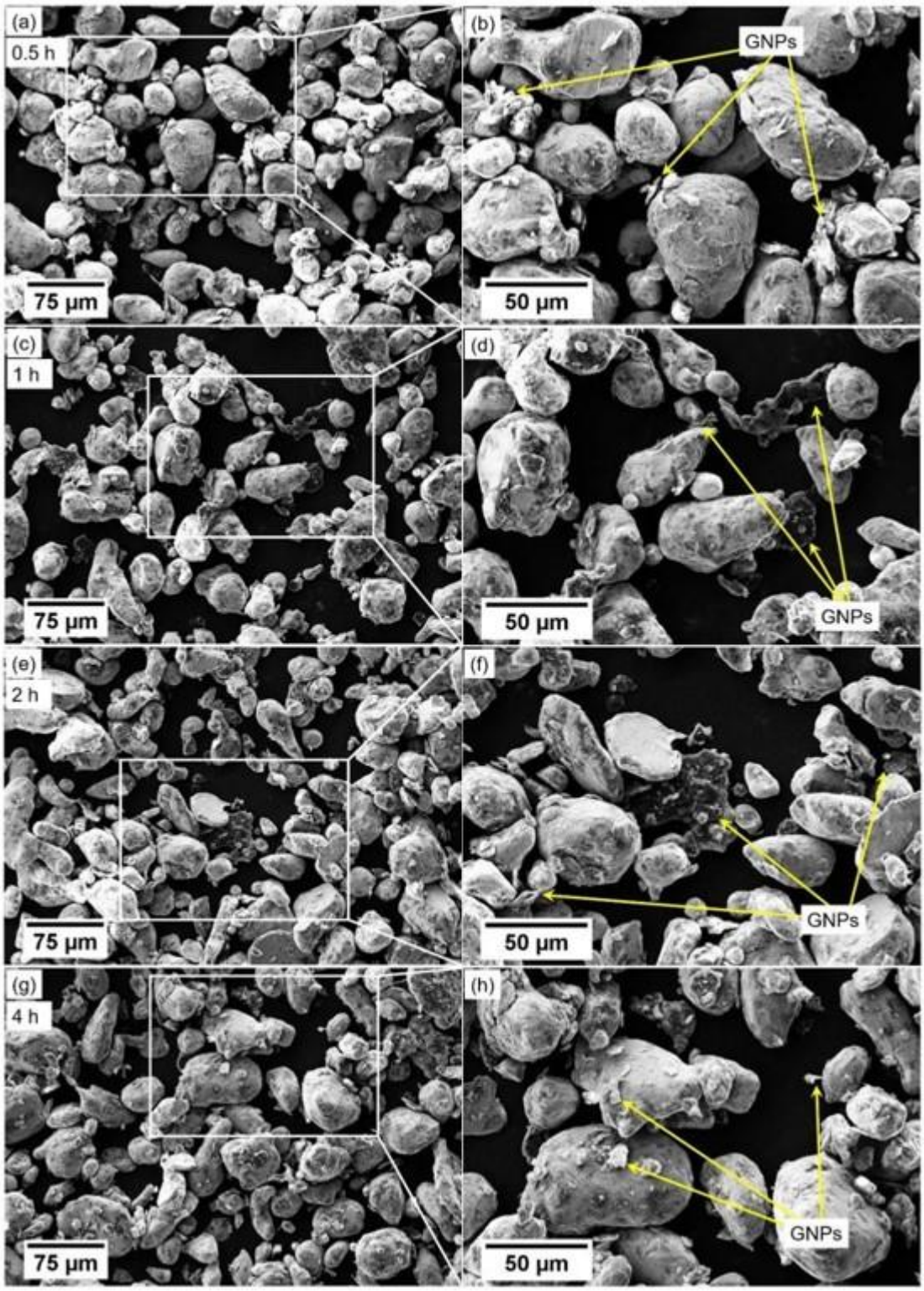

Figure 5.11: SEM images showing the morphological alteration of powders and the dispersion of agglomerated GNPs in the milled alloys from 0.5 to 4 hr.

Afterwards, long milling times from 8 to 16 hr visibly changed the powder morphology from nearly spherical to flat, as shown in Figure 5.12. The plastic deformation of the powder with a long milling time is becoming more obvious because of the continuously applied impact energy. Another reason for the more

flattened particle at longer milling time is that while PCA protects the powder against plastic deformation during short milling times (as stated above), the particles cannot tolerate continuous mechanical deformation due to the work-hardening effect (Nouri et al. 2010). The average thickness of the raw and milled powders is given in Figure 5.13. Over a hundred powders were processed from SEM images of the powder for each milling time. The thickness of the powder is measured and found to be decreasing gradually in direct proportion to milling time. The powder keeps flattening throughout the mechanical milling operation, but cold welding did not appear until the 16 hr. A similar evaluation of ball milling under low-speed ball milling has been observed for CNT-reinforced Al (Xu et al. 2017). Therefore, flat powder particles negatively affect powder flowability, and decent flowability is crucial for AM processes (Gu et al. 2012). In the following sections, the negative effect of flattened particles is analysed in detail in both experimental and DEM simulations. What's more, GNP particles were dispersed and adhered to the Al powder surfaces at increased milling times as shown with yellow arrows. The finest GNPs, homogeneous dispersion and best adherence of Gr flakes to the Al powder were obtained from 16 hr milled composite powder (see Figure 5.12f).

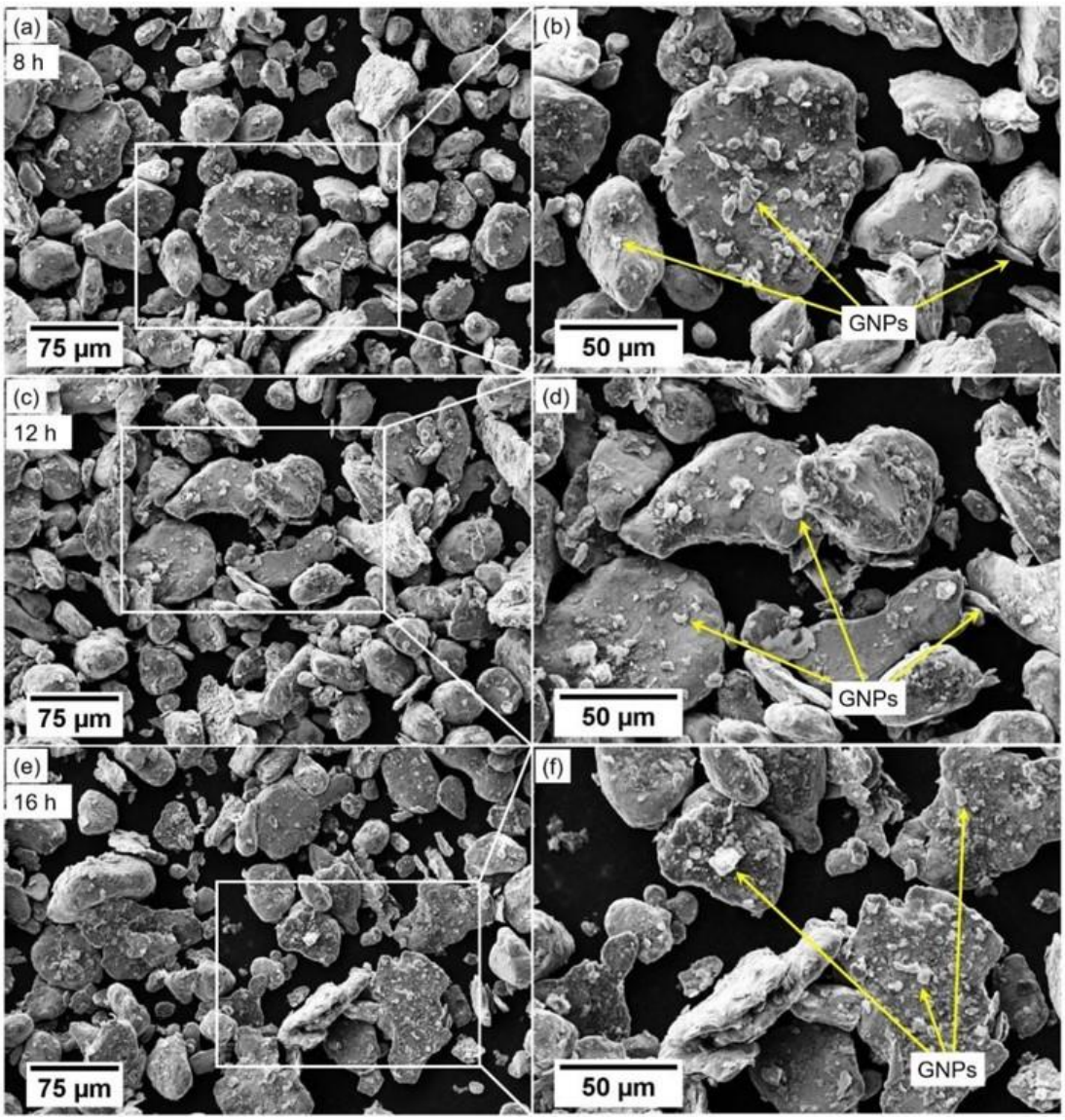

Figure 5.12: SEM images showing the morphological alteration of powders and the dispersion of agglomerated GNPs in the milled alloys from 8 to 16 hr.

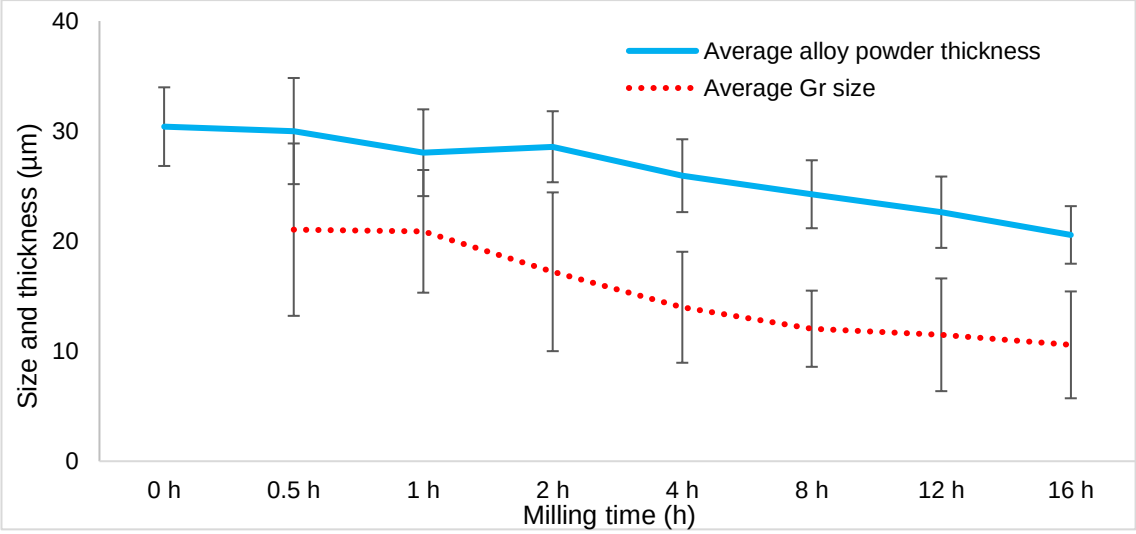

Figure 5.13: Average particle thickness of the raw alloy and milled composite powder.

5.2.2.3. Microhardness Analysis

OM images of the raw alloy, 4 and 16 hr milled powders, mounted in resin sample holders are shown in Figure 5.14. The raw and milled powders were embedded into resin in order to conduct the microhardness test. The evolution of powder morphology to flat with increasing milling time can be seen in the OM images as well as SEM images. Some powders were removed during the grinding and polishing process, creating small gaps on the observed surfaces.

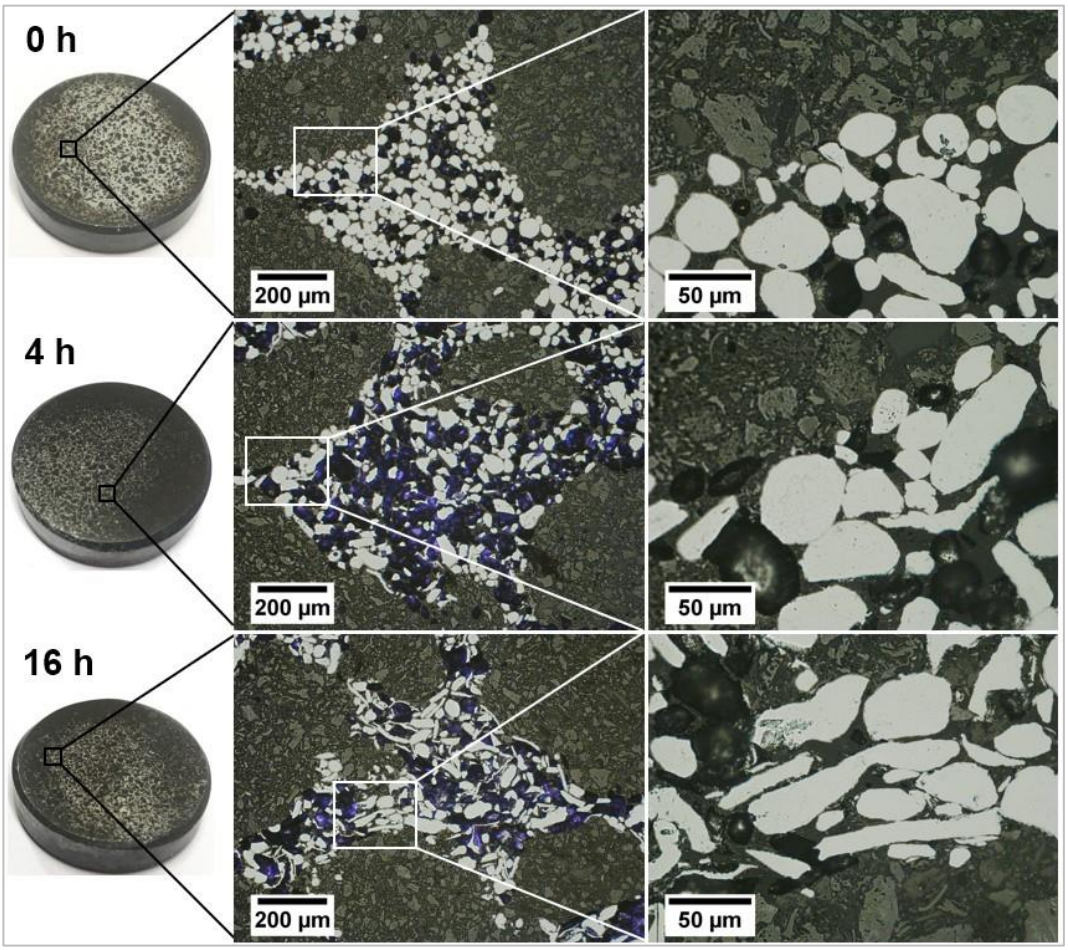

Figure 5.14: OM images of raw alloy, 4 and 16 hr milled powders.

The Vickers microhardness (HV) test results (under 100 g load and 10 seconds dwell time) for raw alloy, 4 and 16 hr milled powders are given in Figure 5.15. This test has been conducted on the raw and milled powders in order to demonstrate the evolution of the powders under different milling times. To provide more precise results, the measurements were gathered from horizontally and

vertically different locations. The microhardness of the raw alloy powder increased from 98.9 to 101.8 $HV_{0.1}$ at 16 hr milling. This small variation illustrates that low ball milling has no significant effect on the microhardness of the milled powder. Along with this, it is important to mention that progressively rise in the hardness and reduction in crystallite size of the XRD result suggest that increased dislocation density inside the particles at longer milling times creates more refined crystallite and internal crystallite strain (microhardness) improved (Bera et al. 2013; Han et al. 2016). This also substantiates that a large number of crystallite boundaries causes an increase in the internal strain and restricts the movement of the crystallite proportionally to the milling time (Zuhailawati and Mahani 2009; Rahman et al. 2019). Hence, the hardness of the particles starts to improve progressively.

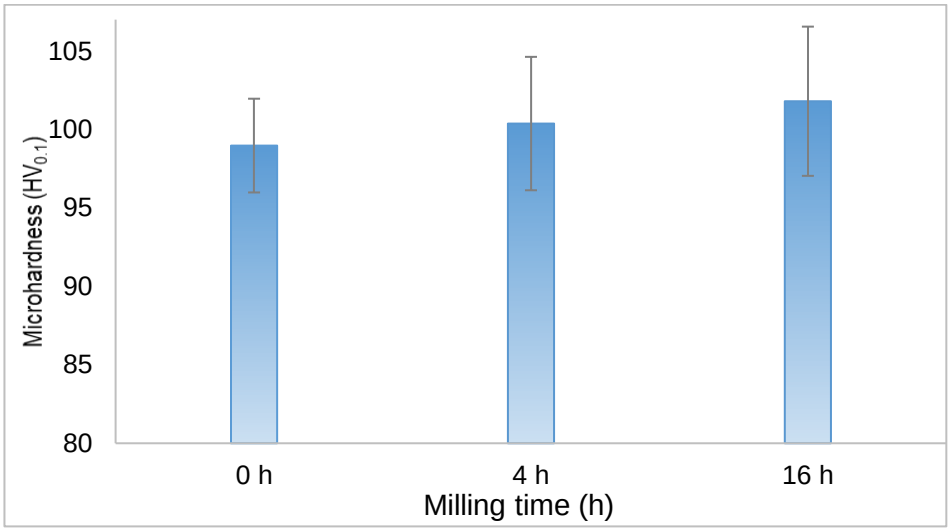

Figure 5.15: Microhardness results of raw alloy, 4 and 16 hr milled powders.

5.2.2.4. Calibration of Surface Energy and Morphology Volume

In the first step of the calibration of the parameters, the DEM simulation was driven with three different raw alloy particle morphologies (obtained from SEM images of real particles) under different surface energy values in order to calibrate the powder-to-powder surface energy (see Figure 5.16). Increasing particle surface energy (from 0 to 2 mJ/m^2) results in a higher angle of repose (from 7.1°

to 36.5°), which means that the flowability of the powder becomes poor at higher surface energy values (Meier et al. 2019). The closest angle of repose to the experimental result of the raw alloy (27.4°, see Figure 5.21a) was achieved with a surface energy of 1.4 mJ/m^2 (28.5°, see Figure 5.16c). A similar approach has been followed in other studies to determine the surface energy from the angle of repose achieved from physical funnel experiments (Chen et al. 2017; Meier et al. 2019). Raw alloy powder was used to calibrate the surface energy value and volume differentiation. The surface energy of 1.4 mJ/m^2 was adopted for the rest of the study. Intensive work in order to determine the surface energy has been done with three particles because more particles result in a longer simulation time. While each three-particle simulation takes 2-3 days, each ten-particle simulation takes 7-10 days to complete.

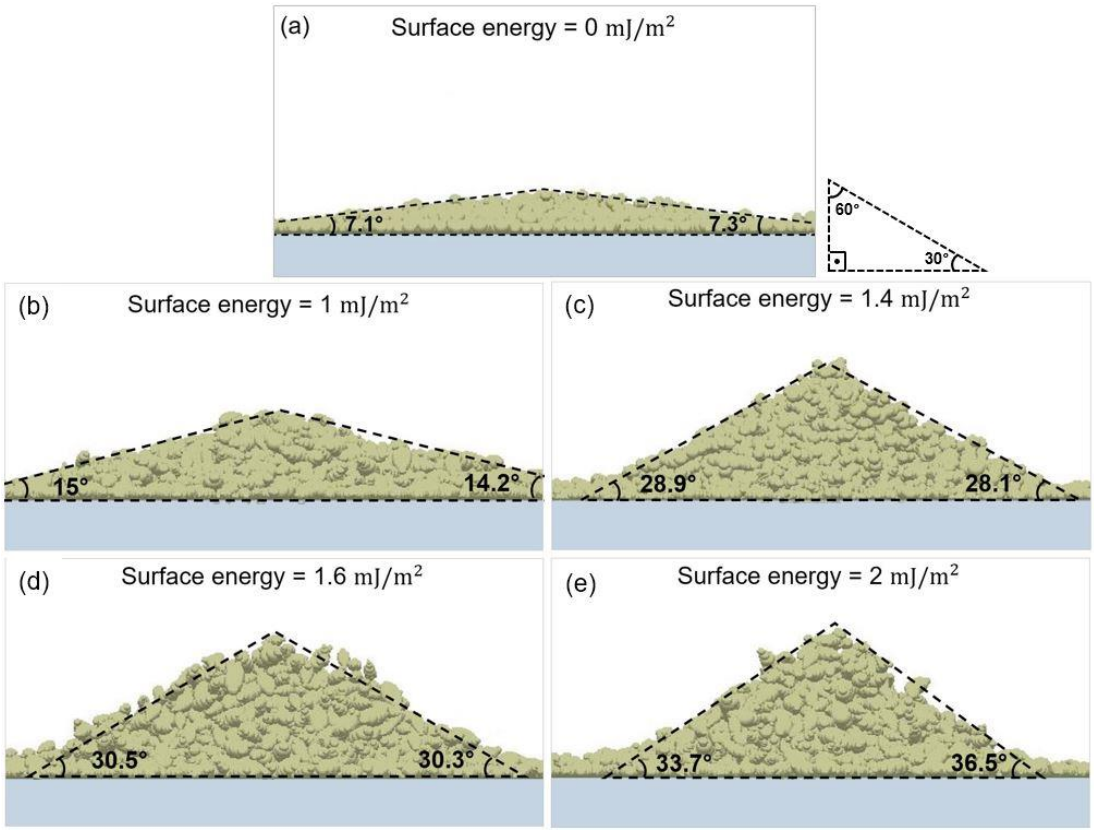

Figure 5.16: Angle of repose of the raw alloy powder under different surface energy values.

In the second step of the calibration, obtained surface energy (1.4 mJ/m^2) from three different particle morphologies (Type 2a-c) were verified with six (Type 2a-f) and ten (Type 2a-j) particle morphologies (see Figure 5.17). Both six and ten different particle morphologies from SEM are nearly identical with three different particles, and all of them are in the experimental result region. Extended particle morphology results in less deviation from experimental results. However, when the long simulation time and extensive preparation period for a large variety of powder morphologies in the simulation powder pool were considered, three was the most representative particle from the SEM images as it gives adequate results in comparison to the six and ten morphologies.

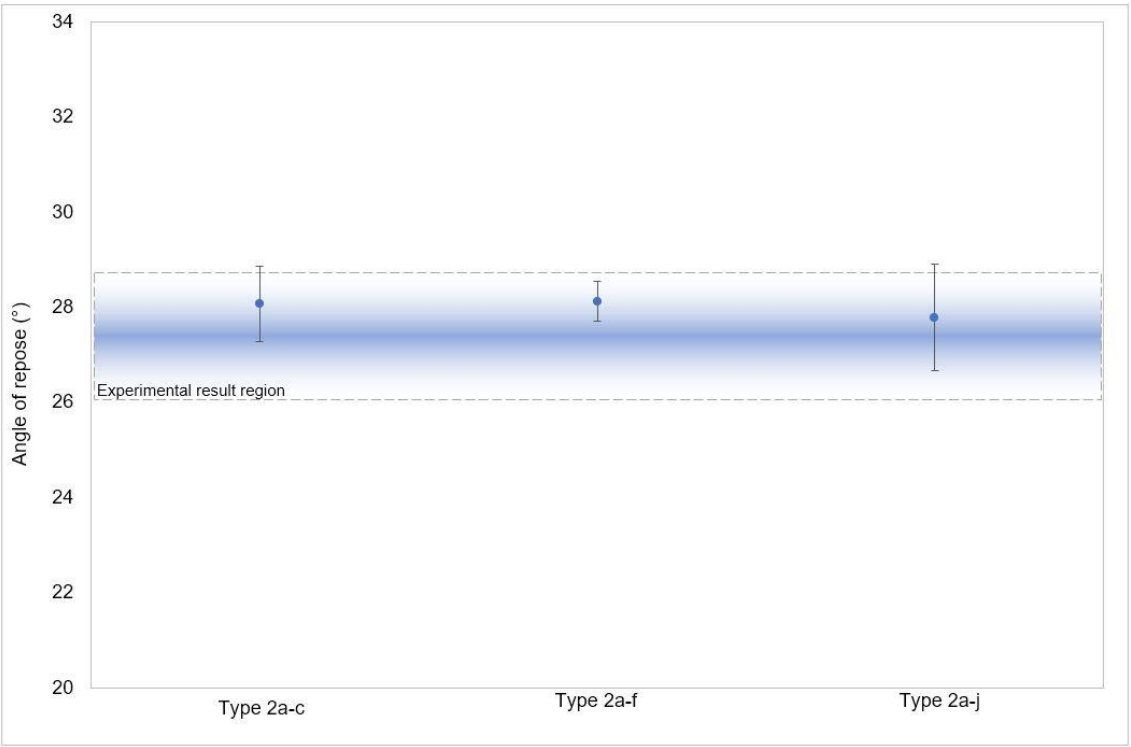

Figure 5.17: Angle of repose of three, six, and ten powder morphology obtained from SEM images of real particles.

The suitability of the commonly used particles for DEM simulations of AA2024 powder was tested in the next step of the calibration (see Figure 5.18). First, single spherical and five different multi-spherical particles were simulated individually, and then all particles were simulated in a powder pool with equal

percentages (16.6%). Even though the angle of repose for most of the particles is lower than the experimental result, Type 1e has a higher value than experimental work owing to the flat powder morphology. Additionally, an equal combination of the series in the simulation powder pool resulted in a higher value than the experimental work. As a consequence of this, none of the Type 1 series particles and combination of the series is representative of the DEM simulation of AA2024. In order to have an accurate result for the alloy, SEM images of the real particles need to be utilised.

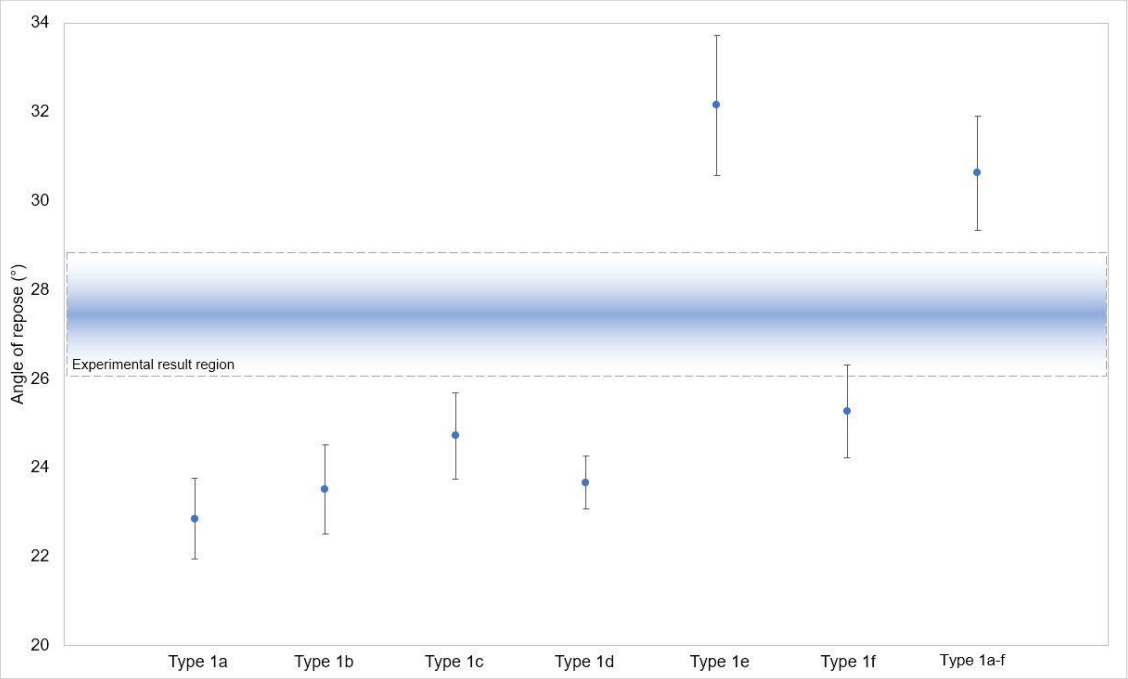

Figure 5.18: Angle of repose of commonly used particles in literature.

The percentages of three different particle morphologies in the powder pool of the DEM simulation varied from 20 to 50% in order to estimate the effect of the volume of different particle morphologies on the angle of repose. The results are shown in Figure 5.19. Dominant particles in the powder pool exhibit identical pattern, such as the similarities of both Type 2a and Type 2b (50%). Moreover, it shows that a multi-shape particle with varying percentages in the powder pool is not strongly influential on the angle of repose. To this end, an equal volume (33.3%) for each particle in powder pools was used in the rest of the study.

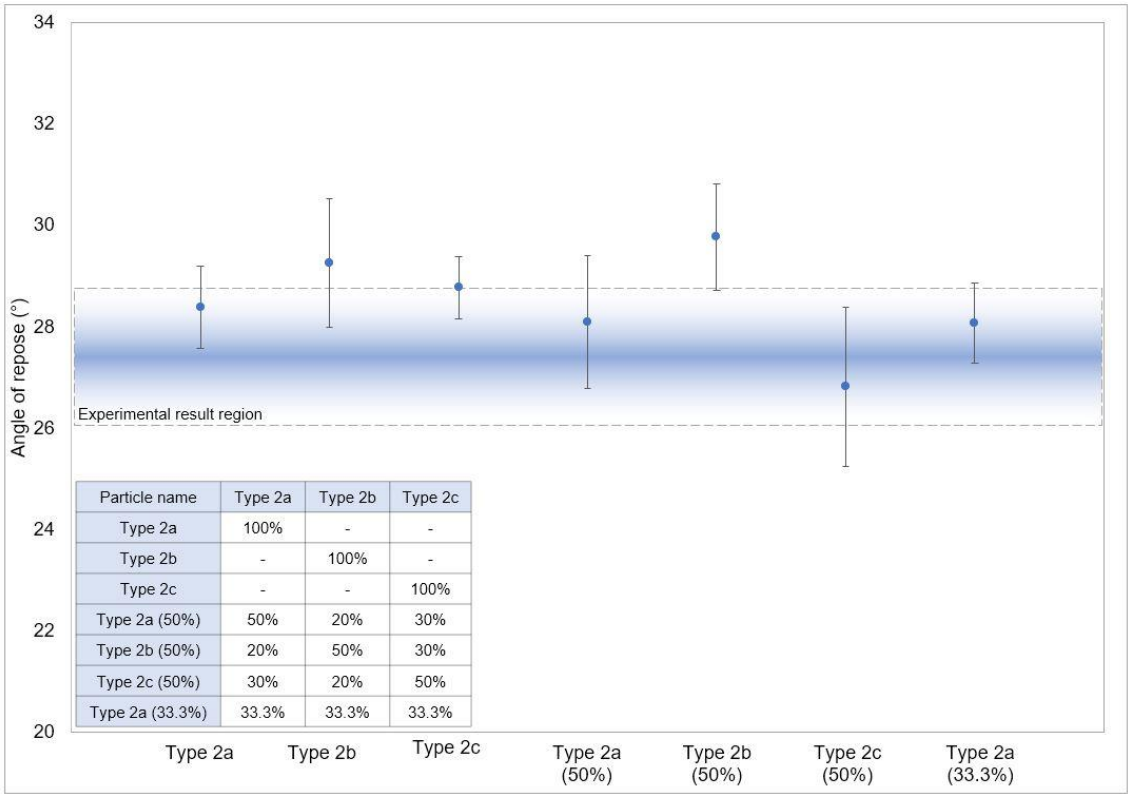

Figure 5.19: Angle of repose for different percentages of powder morphologies in simulation powder pool.

5.2.2.5. Flowability Analysis

Figure 5.20 shows the angle of repose of raw and GNPs-reinforced alloy under different milling times (0.5 to 16 hr). A narrower angle of repose represents better flowability of the powder. Experimental results show that raw alloy has the narrowest angle of repose (27.4°) compared to the milled powders' angle. Milled alloys have an angle of repose between 31° and 36.4°; thus, milled alloys are less flowable than raw alloy powder. First, the angle of repose of the milled alloys in the experiment slightly reduces from 33.7° to 31.1° with increasing milling time from 0.5 to 4 hr. After 4 hr, the angle of repose started to increase up to 35.8°. On the basis of the above observation, it can be deduced that reinforced Gr which has a poor flowability (see Figure 5.21g) negatively affects the flowability of the raw alloy owing to the accumulated large Gr particles in the powder bed at the beginning. However, at further millings, the large and accumulated GNPs are

disintegrated and adhered to the powder surface, thus becoming less effective at the angle of repose. Additionally, morphological evaluation of the powder from nearly-spherical to nearly-flat could be the other reason. Similar observations and findings have been achieved from multi-layer Gr reinforced Ti-based MMC under different milling times (Lin et al. 2021). The contrast between the experiment and simulation (which was created from real particle shapes) did not provide a significant difference in flowability. However, the simulation results of longer milling times (in which separated Gr particles are less effective on flowability) are more comparable to experimental results. These findings lead us to the following conclusion that the flowability of the composite more depends on powder morphology than accumulated Gr. The low weight ratio of the Gr (0.2%) in the composite is the other reason for the ineffectiveness of the Gr. The effect of Gr percentages on the flowability of Gr/Inconel 718 composite has been studied experimentally and reported that 0.25% and 1% of Gr negatively affect the flowability of 2.2% and 9%, respectively (Xiao et al. 2018). On the other hand, 30° is the border between excellent-flow (<30°) and free-flow (30° - 38°) characteristics. Some measured angles at short milling times (up to 4 hr) therefore tend to cross between flow categories because their angle of repose is close to the border. Another reason for crossing between flow categories is long error bars owing to the variation in the experimental results.

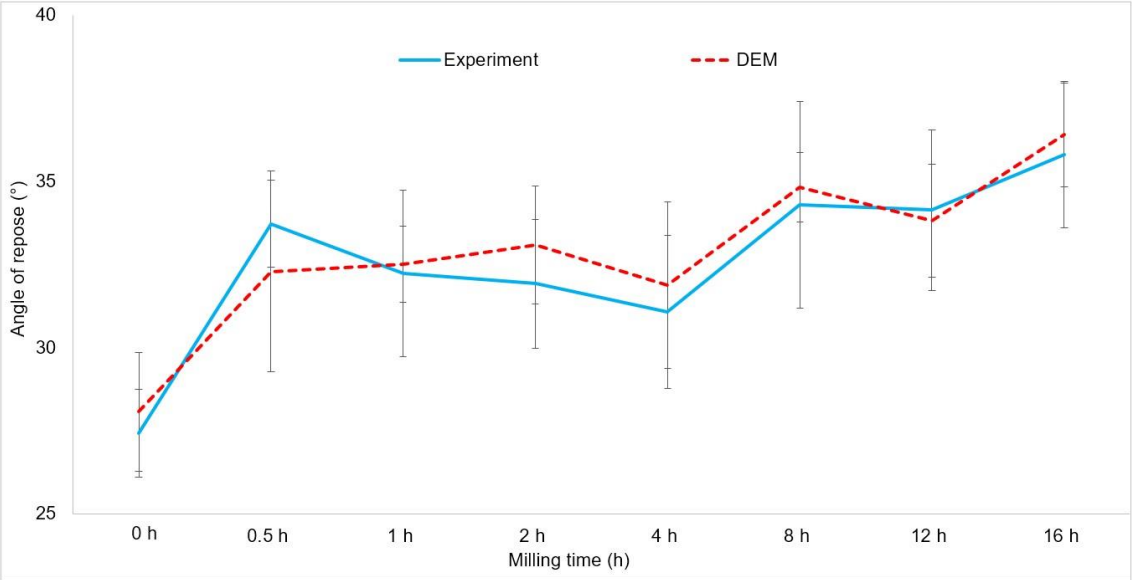

Figure 5.20: Angle of repose of the raw alloy and milled Gr/AA2024 obtained from experimental work and DEM simulation.

Meanwhile, continuously applied impact energy on powder inside the milling bowls gradually changes the particle morphology to flat. The SEM images (see Figure 5.11 and Figure 5.12) corroborate this hypothesis. Nevertheless, after 4 hr, the angle of repose starts to increase up to 35.8° due to a dramatic change of the particle shape at this point, from spherical to flat, which reduces the flowability characteristic of the powders. Similarly, GO nanosheets have been studied as reinforcement material for Cu, and it was reported that the addition of GO to the matrix material results in an accumulation of GO at a low milling time (1 hr). However, further milling (up to 5 hr) dispersed the GO and the smaller particles adhered to the matrix material's surface, which then becomes less effective on the powder flowability (Yue et al. 2017).

The experimental and simulation results show excellent correlation at high milling hours. This can be explained as further milling separates the Gr particles (which are excluded from the simulation) and adheres them to the alloy powders. It makes the Gr less effective on the angle of repose. However, small fluctuations between the simulation result and the experimental work can be seen at low

milling times, owing to the fact that the unrepresented GNPs in the DEM results create a discrepancy at low milling times. While 4 hr milled powder in the experimental results has the narrowest angle of repose (among the milled powders), a similar angle of repose can be seen for 0.5, 1, and 4 hr milled powder in the simulation results. Consequently, 4 hr milling time produces the best flowability in both experimental and DEM simulation results. By using this method (not only for these materials but also for some other matrix and reinforcement materials), the number of experimental works can be reduced, and time and powder material will not be wasted in order to see the difference in flowability characteristics of reinforced composite and matrix elements at different milling times.

Flowability characteristics, in relation to the angle of repose, Carr's index, and the Hausner ratio are given in Table 5.1. The measured angle of repose of the powders indicates that while raw alloy powder (27.4°) has excellent-flow characteristics, milled powders (ranging from 31° to 36.4°) are in the free-flow characteristic. Carr's index and the Hausner ratio again show the excellent-flow characteristic of the raw alloy. However, milled powders lie between free-flow and poor-flow characteristics.

Table 5.1: Flowability characteristics in relation to the angle of repose, Carr's classification, and the Hausner ratio (Beakawi Al-Hashemi and Baghabra Al-Amoudi 2018; Kaleem et al. 2020).

Flow characteristics	Response angle	Carr's index	Hausner ratio
Excellent-flow	< 30°	< 10%	1 – 1.11
Free-flow	30 - 38°	11 – 15%	1.12 – 1.18
Fair-flow	38 - 45°	16 – 20%	1.19 – 1.25
Poor-flow	45 - 55°	21 – 25%	1.26 – 1.34
Very poor-flow	> 55°	>26%	>1.35

Some illustrative images of the angle of repose from experimental work (left side of Figure 5.21) and simulation (right side of Figure 5.21) are given for comparison. The excellent-flow characteristic (27.4°) of the raw alloy and the poor-flow characteristic (46.3°) of the GNPs are shown in Figure 5.21a and Figure 5.21g. The borderline-excellent flowability of 4 hr milled alloy (31°) and borderline-fair flowability of 16 hr milled alloy (36°) are presented in Figure 5.21c-f.

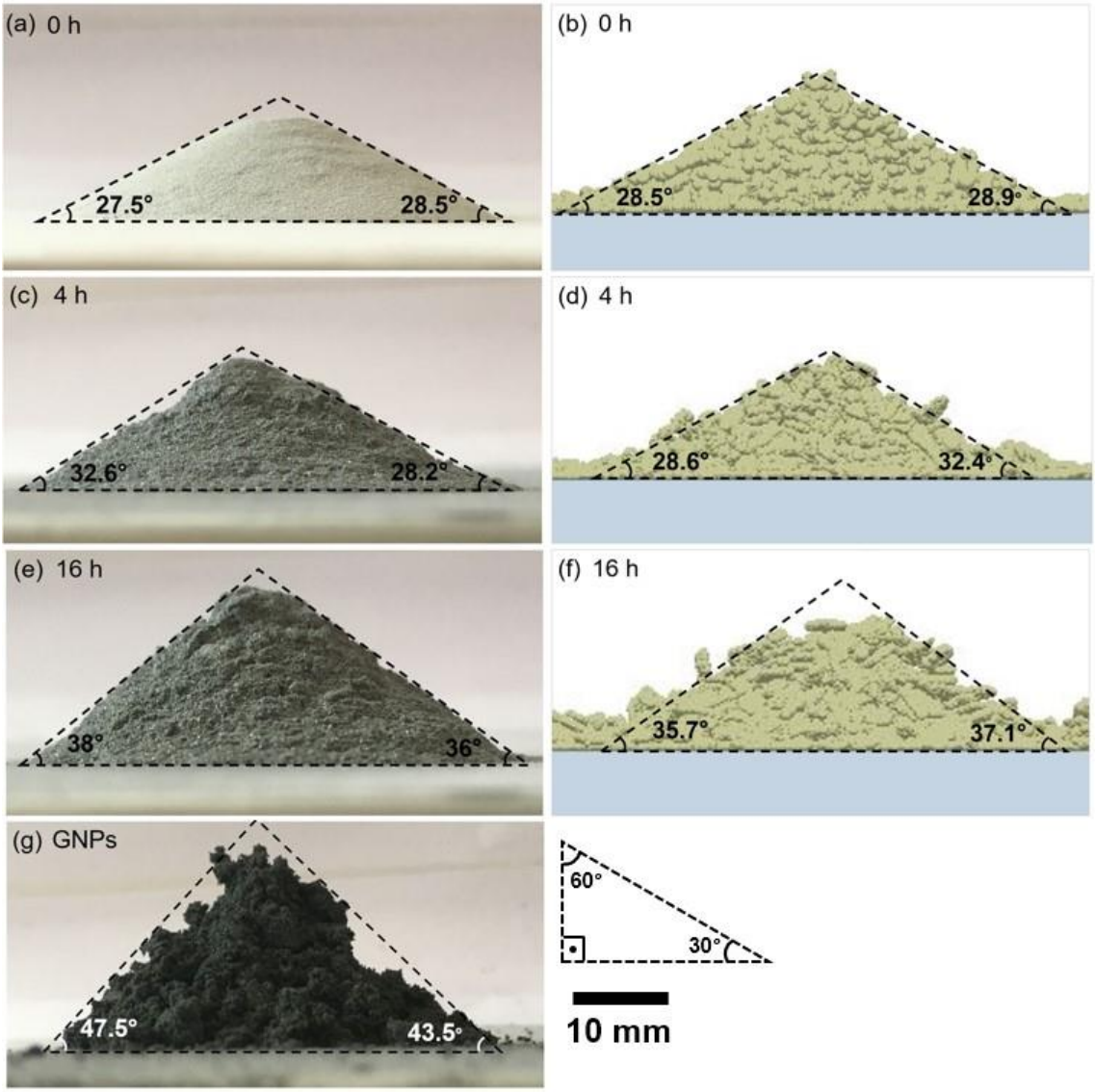

Figure 5.21: Reposed powder, showing Raw alloy, GNPs, 4 and 16 hr milled alloy from (a-c-e-g) experimental work and (b-d-f) DEM simulation.

Compaction results for the raw and milled alloys are given in Figure 5.22. Both Carr's index and the Hausner ratio of the powders depict that milled powders are more compressible than raw alloy. While the flow characteristic of the raw alloy

is excellent, 1 and 4 hr milled powder have free-flow characteristics. However, the compressibility of the 12 and 16 hr milled alloys shows poor-flow characteristics due to the flat powder shapes. Both the angle of repose curves (see Figure 5.20) and compaction characteristic curves (see Figure 5.22) are nearly identical, showing similar development of the powder with milling time.

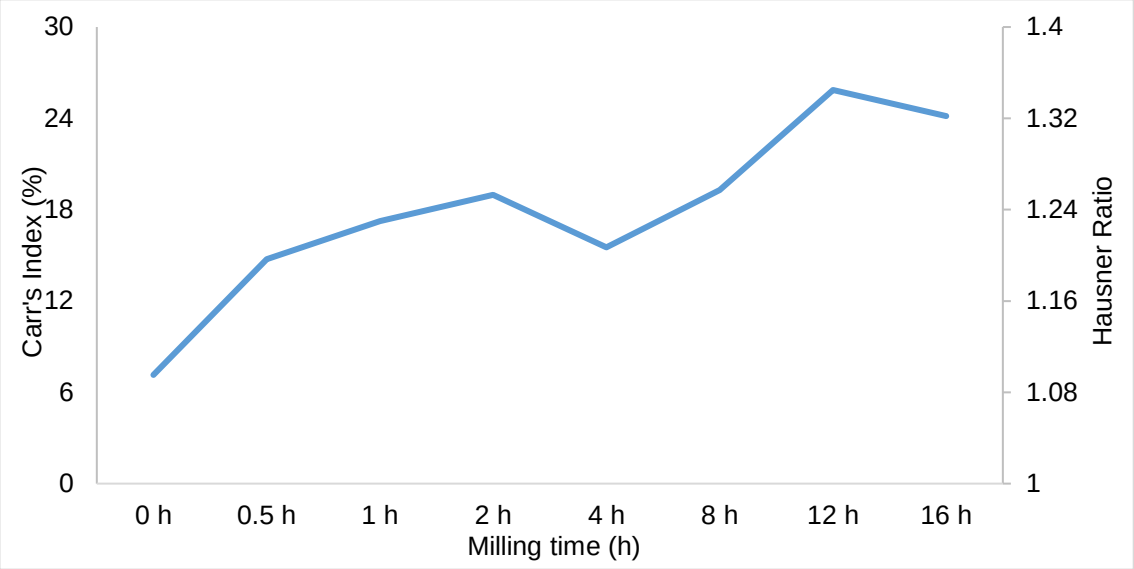

Figure 5.22: Carr's index and the Hausner ratio of the composites at different milling times.

5.2.2.6. Effect of Gr Concentration on Flowability

Figure 5.23 depicts the comparison of the angle of repose with different percentages of Gr reinforcement in the composite powder at 4 hr milling. Additionally, the angle of repose from the DEM simulations is presented for comparison. There is a trend in the angle of repose, depending on the concentration of Gr in the composite powder. While 0.1% of the Gr-reinforced composite has the poorest flowability, 1% of the Gr-reinforced composite has the best flowability. This improvement in flowability with more Gr concentration from 0.1 to 1% provides grounds to hypothesise that more Gr in the composite consumes more energy in order to break the strong bonds between Gr sheets; however, the energy generated during the milling with a low percentage of Gr

present (i.e., 0.1%) will be used to change the morphology of the powder to flat. Even though slightly flattened powder, corresponding to the reduction in the Gr percentage, affects the angle of repose of the composite at a low percentage of Gr, the powder remains in the free-flow region.

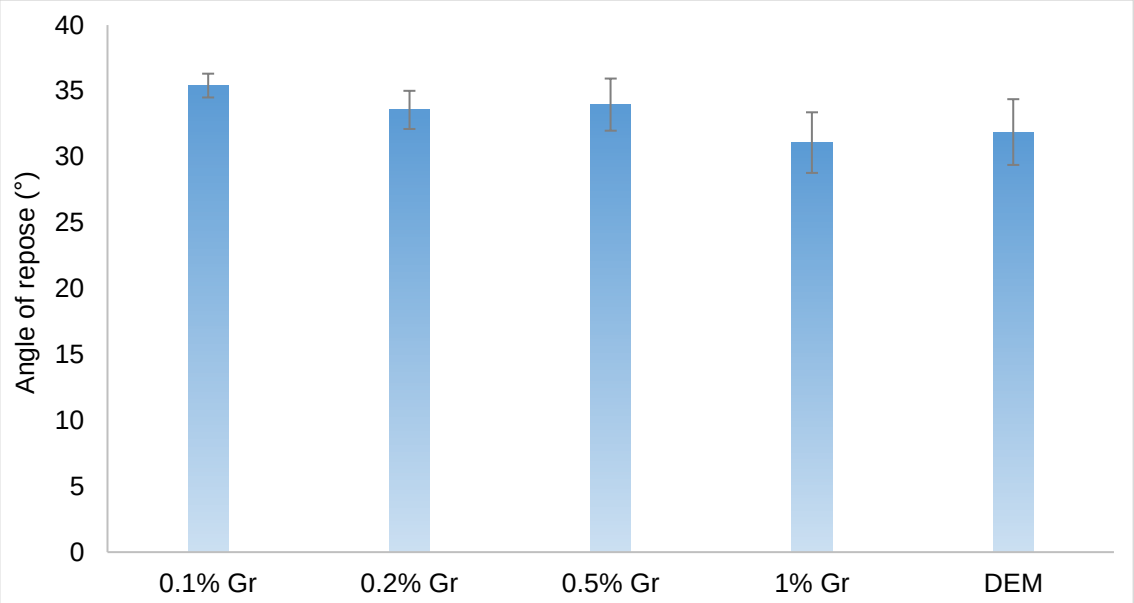

Figure 5.23: Angle of repose of 4 hr milled powder with different percentages of Gr (0.1, 0.2, 0.5, and 1 wt.%) and DEM.

5.3. Discussion

The PSD of milled powders represents that small powder particles tend to weld first because of the compressive force of the milling equipment, especially after 4 hr of milling time (Benjamin 1976). Hence, curves gradually sift to right. A similar approach had been observed for Al-nitride and Si-nitride reinforced AA6061 (Fogagnolo et al. 2003). Moreover, powder morphology also significantly affects the median particle size and volume density. In addition, accumulated Gr particles at short milling times under low-energy ball milling create a laminar structure because of the insufficient compressive energy to break the interlayer van der Waals forces of GNPs. This laminar structure can cause fluctuation in powder size and volume density due to the angle between the particle and laser beam of

the analyser (Fogagnolo et al. 2003). However, when the impact energy is continuously applied to the powder over 2 hr, GNPs become disintegrated into small particles (the laminar structure dissolves in the powder pool) and cover the surface of alloy powder gradually. The shear force created by the collusion of milling balls has the potential to exfoliate Gr layers from graphite, as well as change the morphology of milled powders into flake-like shapes (which can also give additional dispersion sites for GNPs) (Li et al. 2015b; Yi and Shen 2015). As a result, the distribution of Gr became increasingly uniform on the milled powder. Coated powders with disintegrated Gr flakes can be seen in Figure 5.12. Nonetheless, longer milling more than 8 hr results in flat powder morphology which negatively affects the flowability of the powder. The gradual morphological alteration of the milled powder and Gr particles can be seen in Figure 5.11 and Figure 5.12 shows that powder morphology changes from spherical to flat and that agglomerated Gr particles dispersed progressively. When the Gr dispersion and powder morphology are considered for optimum parameters, 4 hr of milling meets the requirements. More importantly, SEM images, PSD, XRD results, microhardness images, experimental flowability test of the milled powder, and DEM results show excellent compatibility with each other.

Additionally, the continuously applied impact energy generated by compressing force of milling balls mainly consequences in the localisation of plastic deformation which is a form of shear bands (Han et al. 2017a; Xu et al. 2017). Additionally, powder flattening accelerated in direct proportion to milling time. The micro-forge mechanism generated by milling balls was responsible for the increasing flattening of mixed powders (Yu et al. 2019). As a result of this deformation, 20% more new crystallites in the milled powder formed and thus accelerating the grain refinement process. Hence, the microhardness of the

milled powder improved by 3% because of dislocation movement. Furthermore, the work-hardening of powders owing to continuously applying high energy at a longer milling time also causes a microstructural evolution (Toozandehjani et al. 2017). The microhardness test of milled powders gives identical results to the microhardness of as-fabricated AA2024 samples in a previous study (Pekok et al. 2020).

The slow compressing force inside the milling bowl allowed the GNP aggregates to progressively break apart and equally distribute across the surface of the alloy particles prior to the particles becoming flattened. Similar morphological evaluations of powder have been observed for CNT and GNPs reinforced Al composites milled under low ball milling parameters (Xu et al. 2017; Yu et al. 2019). While the Gr concentration in the composite powder is high, the flowability of 4 hr milled powder decreases (Figure 5.23). The hypothesis behind this reduction is that the energy created inside the milling bowls was firstly used to break strong van der Waals forces between layers and disperse the accumulated large amount of Gr particles present when 1% Gr is included in the composite prior to morphological evaluation of the powder. However, a small amount of Gr (0.1%) in composite required less energy to disperse the Gr into the composite. The remaining energy for the 0.1% Gr-reinforced composite was therefore used to deform the powder morphology of the matrix material. Therewith, more flattened powder negatively affects the flowability of the powder. Nevertheless, the overall effect of Gr content on flowability is reasonably small, when varied between 0.1 to 1%.

AA2024 powders have their unique and non-spherical powder morphology. Type 1 particle shapes prove that commonly used particle morphologies in DEM simulations are not representative of the alloy powder. In order to obtain more

accurate results, several powders from SEM images of the real powder (Type 2) need to be used. In the literature, a similar method has been commonly employed for non-spherical particles (Barrios et al. 2013; Haeri 2017; Nan and Ghadiri 2019; Tan et al. 2021). It is perceptible from Figure 5.17 that more variety in powder morphology based on SEM images provides more accurate findings; however, longer simulation running time and preparation period of the model with more powders need to be considered. Furthermore, the percentage of each powder morphology in the simulation powder pool is not significantly affecting the flowability.

Since flow characteristics are highly dependent on powder morphology and the weight ratio of reinforced Gr (0.2 %) in the composite is quite low, the flowability of the composite can be estimated by DEM without Gr nanoparticles under these conditions. On the other hand, the contrast of experimental study with Gr reinforcement and DEM simulation without Gr gives an opportunity to understand the effect of Gr on flowability. DEM simulation calibrated with as-received alloy without milling and Gr reinforcement. Further experimental contrasting discloses the effect of Gr in the composite. This contrast demonstrates that short milling times have more fluctuation than long milling times in comparison to experimental results. The hypothesis behind this fluctuation is that accumulated large Gr particles under 2 hr milling are able to change flowability. It is a well-known fact that while near-spherical particles give better flowability, near-flat morphology reduces the flowability of the powder (Nguyen et al. 2018). The accumulated and folded Gr particles in the composite at short milling times reduce the flowability of the composite because Gr acts as a flat particle in the composite. However, when the Gr particles were disintegrated into small flakes and adhered to the composite powder, the direct effect of the Gr in the composite was gradually reduced and

even disappeared. Thus, the composite powder starts to react in the same way as Al powder without Gr. In the meantime, flattened powder at longer millings deteriorated the flowability of the milled powder. The balance between better dispersed Gr (longer than 2 hr) and less affected morphology (shorter than 8 hr) is settled at 4 hr milling for 100 rpm milling speed. The contrasting experiment and simulation can result that this modelling approach can be applied for GNPs reinforced MMCs under particular conditions in order to predict the flowability for further studies.

5.4. Summary

This chapter focuses on the effect of milling speed and time on GNPs-reinforced AA2024 powder for use in LPBF. Moreover, agglomeration of the Gr nanoplatelets in MMCs with different milling times has been studied. A wide range of milling times, from 0.5 to 16 hr, was examined with two milling speeds (100 and 250 rpm). In addition to this, DEM simulations for each milling time were modelled without GNPs, in order to understand the effect of Gr particles on the flowability of the milled alloy powder. The importance of this study is that both experimental work and DEM simulation are in excellent harmony when the simulation is modelled under the right conditions. The contrast of experimental results and the simulation with near-shape particles modelled using SEM images reveal the effect of GNPs in composite to flowability. The following findings are drawn from experimental and simulation results:

1) The volume density of powder under 10 μm decreases when increasing the milling speed from 100 to 250 rpm, owing to the fact that high impact energy accumulates the particles and small Gr sheets are stuck onto the surface of the powder.

2) The powder shape at slow milling speed remains nearly identical to the shape of the raw alloy powder, due to the low collision energy of the milling balls; however, the powders form a flake shape at high milling speeds due to the higher impact energy. Additionally, slow milling speeds create insufficient impact energy to stick the Gr sheets onto the powder. Increasing the milling speed to 250 rpm creates flattened powder particles, which are not convenient for AM processing, as non-spherical powders may lead to uneven layer thicknesses.

3) Short milling time (0.5 to 2 hr) provided insufficient impact energy inside the milling bowls to break the strong van der Waals forces. Hence, agglomerated Gr particles were observed at short milling times. However, long milling times (8 to 16 hr) notably changed the powder morphology. While the raw alloy powder particles had a rounded shape, flat powder morphology was observed after 8 hr milling. Additionally, plastic deformation on powder becomes more obvious in direct proportion to milling time. Furthermore, GNPs were better separated and adhered to the Al powder surface at longer milling times.

4) The average crystallite size of the powder declined from 35.75 to 27.14 nm during ball milling up to 16 hr due to dislocation movement. As a result of the refined microstructural dislocation and work-hardening, the powder's microhardness was improved by 3% by ball milling up to 16 hr.

5) The surface energy of the alloy was calculated as 1.4 mJ/m^2, based on the angle of repose obtained from experimental work. Even though some common DEM particles (Type 1) in literature were tested, several near-shape SEM particles obtained from real powders are more representative. More variety in morphology results in sensitive results; however, the

running time of the simulation and preparation of more particles is extensive.

6) The contrast of the experimental work and simulation results regarding the flowability test show excellent correlation at long milling times. However, simulation results at short milling times show differentiation from the experimental results. The reason behind this is that separated Gr particles, achieved at long milling times, become less effective on the angle of repose.

7) While the Gr concentration in the composite powder is high, the flowability of 4 hr milled powder decreases. The hypothesis behind this reduction is that the energy created inside the milling bowls was used to break and disperse the accumulated large amount of Gr particles present when 1% Gr is included in the composite. However, a small amount of Gr (0.1%) in composite required less energy to disperse the Gr into the composite. The remaining energy for the 0.1% Gr-reinforced composite was therefore used to deform the powder morphology of the matrix material. Therewith, more flattened powder negatively affects the flowability of the powder. Nevertheless, the overall effect of Gr content on flowability is reasonably small, when varied between 0.1 to 1%.

6. Chapter: Fabrication of GNPs/AA2024 Composite

The third research objective of this thesis is provided in this chapter. The effect of various percentages of GNPs (0.1, 0.2 and 0.5 wt.%) on the composite is studied in this chapter. Microstructural, mechanical properties and wear performance of the as-fabricated composite are investigated. Basically, this chapter is divided into four main sections. The research hypothesis is given in Section 6.1. Then, experimental results are provided in Section 6.2. Phase indentation, various density measurement results, microhardness, nano and macro wear behaviour, surface roughness and tensile properties of the composites are supplied in this section. Finally, discussion and conclusion of the chapter is presented in Section 6.3 and 6.4.

6.1. Research Hypothesis

The following are some of the research hypotheses:

- Determination of optimum percentage of Gr in composite will crucially affect the density of the fabricated specimens.
- Using the optimum amount of Gr may consistently generates the greatest results in all microstructural and mechanical parameters.
- The composites' wear behaviours might be consistent at both macro and nano scales.

6.2. Results

6.2.1. Phase Identification

XRD patterns of raw alloy powder and 4 hr milled powder, in addition to raw alloy sample and Gr-reinforced composites (under 200 W laser power, 195 mm/s scanning speed and 80 μm hatch spacing), have been shown in Figure 6.1. The machine identified only the Al element. Neither carbon element nor iron (as a contamination element from the milling equipment) was detected. The reason for the lack of iron element can be that 2 wt.% stearic acid is sufficient to protect the powder from contamination from the milling equipment. The other reason for this can be the lower volume percentage of iron and carbon in the composite than their detectable levels in the XRD machine. Additionally, the patterns exhibit that milling time in the powder preparation process and the addition of Gr in as-fabricated samples result in a reduction of intensity. Furthermore, the major difference between powders and as-fabricated composites can be seen in the earlier 2θ values. The highest peak (at 38°) for the powders was shifted to 45° for as-fabricated samples due to the lattice defects.

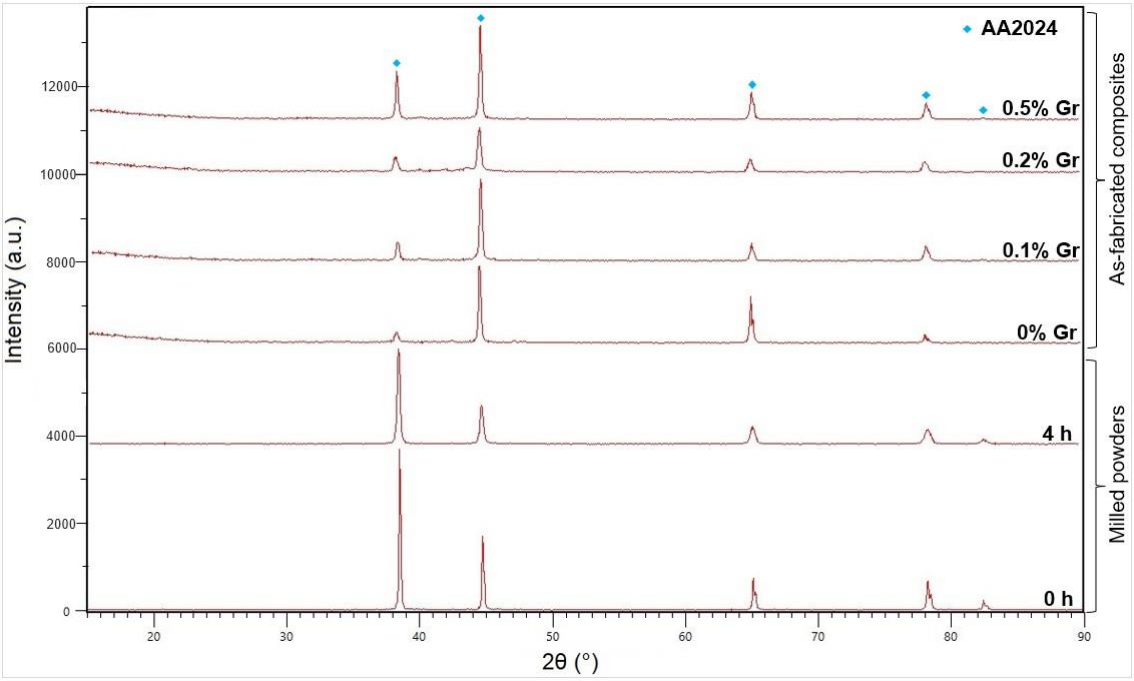

Figure 6.1: XRD of raw alloy, 4 hr milled powders, and Gr-reinforced composites.

The calculated average crystallite size of the powders and as-fabricated composites is shown in Figure 6.2. While continuous impact energy results in the reduction of crystallite size in milled powder, the addition of Gr also causes finer crystallite size. Previous research also demonstrates that longer milling times result in finer crystallite size. Additionally, as-fabricated composites show gradual reduction with higher percentages of Gr (see Figure 6.2) because the addition of Gr improves thermal conductivity and increases the dislocation density, which results in fine-grain microstructure.

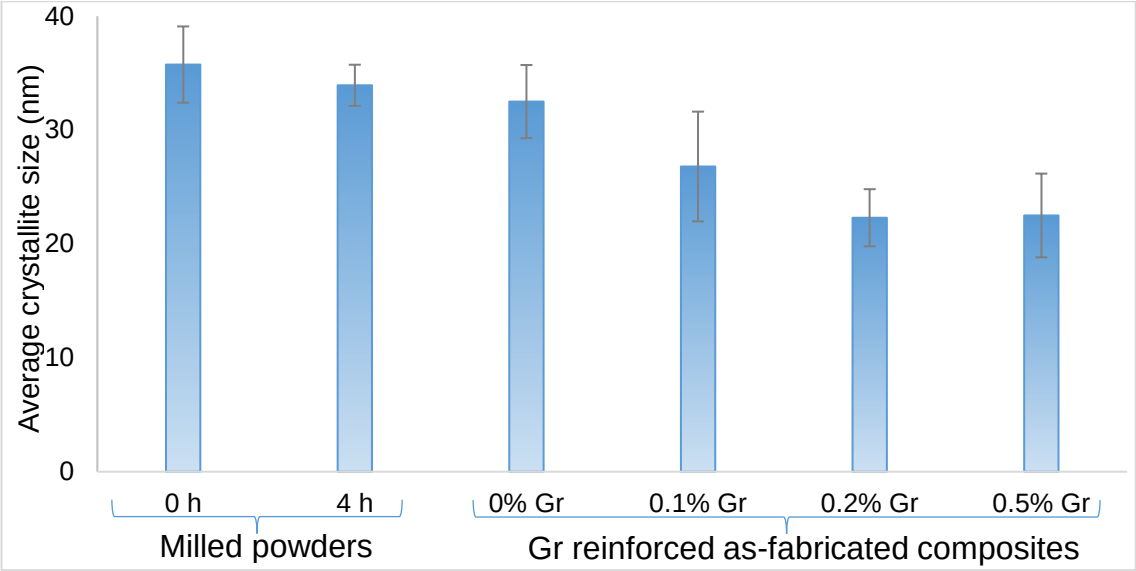

Figure 6.2: The average crystallite size of the powders and Gr-reinforced as-fabricated composites, obtained from XRD results.

6.2.2. Porosity and Densities

OM images of as-fabricated composites with relation to Gr concentration from 0.1 to 0.5 wt.% and laser speed from 195 to 727 mm/s are shown in Figure 6.3. Experimental results demonstrate that while Gr percentage has a positive effect on porosity at slow scanning speeds (in the green line, below 10%), higher Gr concentration generates additional porosity at faster scanning speeds (in the red line, over 20%). The best (Figure 6.3 a-3) and the worst result (Figure 6.3 d-3) among the applied parameters are achieved from 0.5 wt.% Gr-reinforced composites depending on scanning speed.

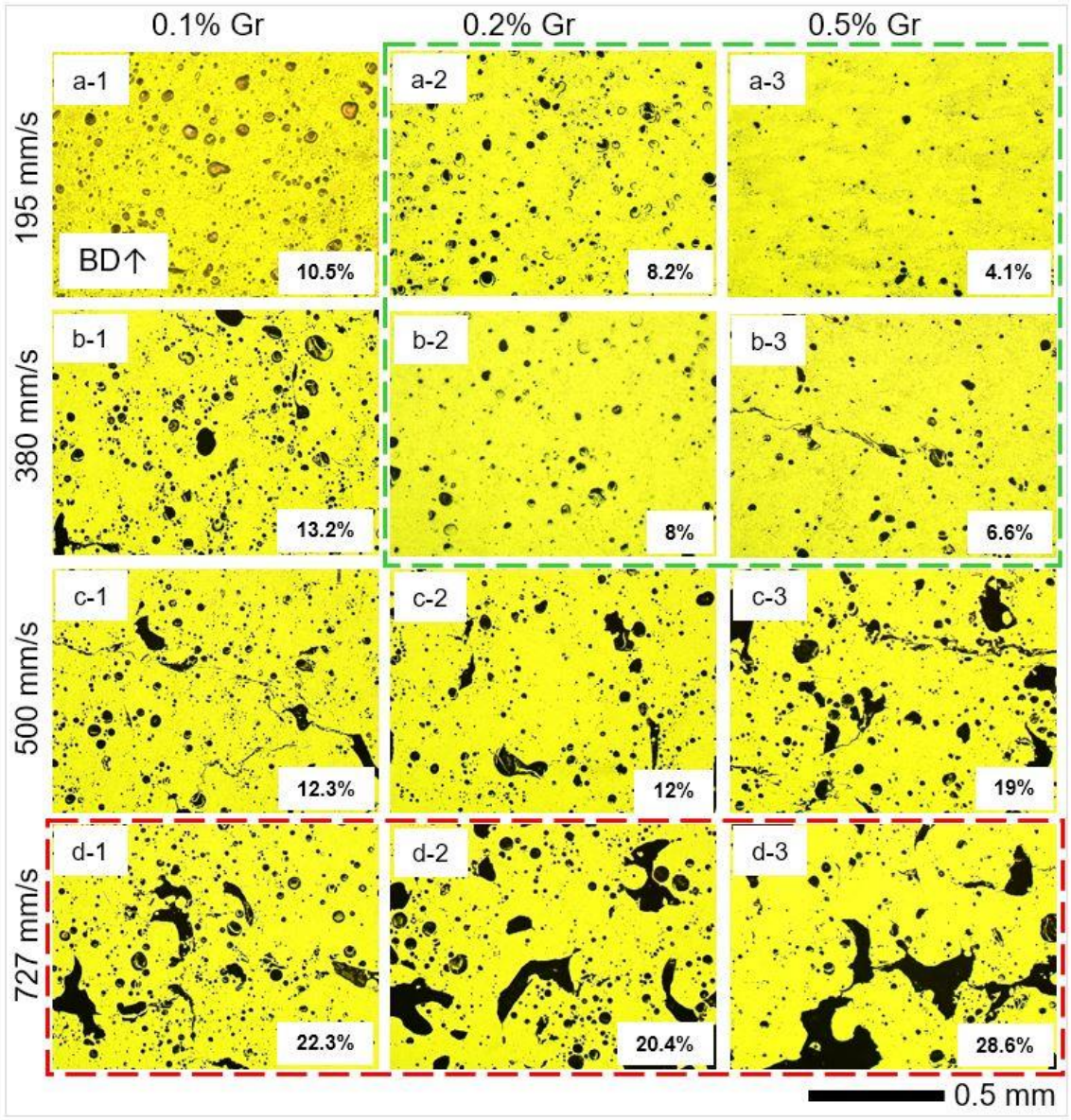

Figure 6.3: OM images showing the porosity of GNPs-reinforced composites plotted against laser speed (195 to 727 mm/s) and GNPs concentration (0.1 to 0.5 wt.%).

Figure 6.4 and Figure 6.5 show the relative and Archimedes' densities of as-fabricated composites, respectively. A comparison of the as-received alloy without Gr (0% Gr) and Gr-reinforced composites illustrates that the addition of Gr dramatically reduces the density of the as-fabricated composites. Additionally, the destructive effect of Gr on relative density is more obvious at faster scanning speeds (Figure 6.4). In addition, Archimedes' density results show that the 0.2 wt.% Gr-reinforced composite has the best results among the other percentages across all applied scanning speeds (Figure 6.5). On the other hand, Gr addition

caused a severe reduction in Archimedes' densities (between 8.8% and 17.4%) in comparison to raw alloy due to the lesser density of the Gr.

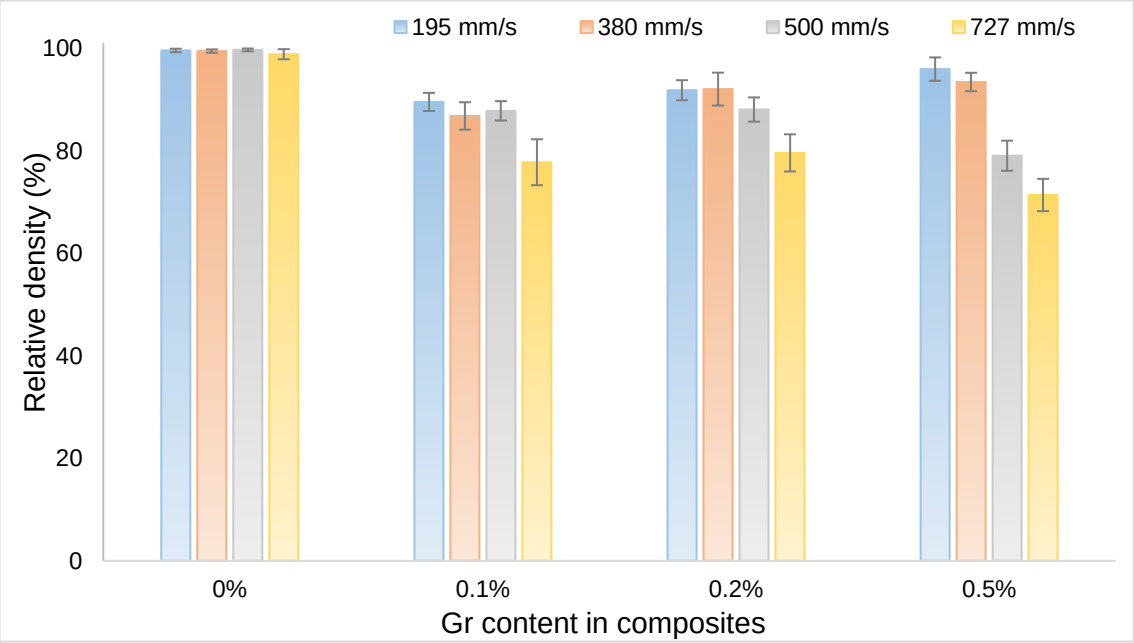

Figure 6.4: Relative density of the composites in relation to Gr percentage and scanning speed.

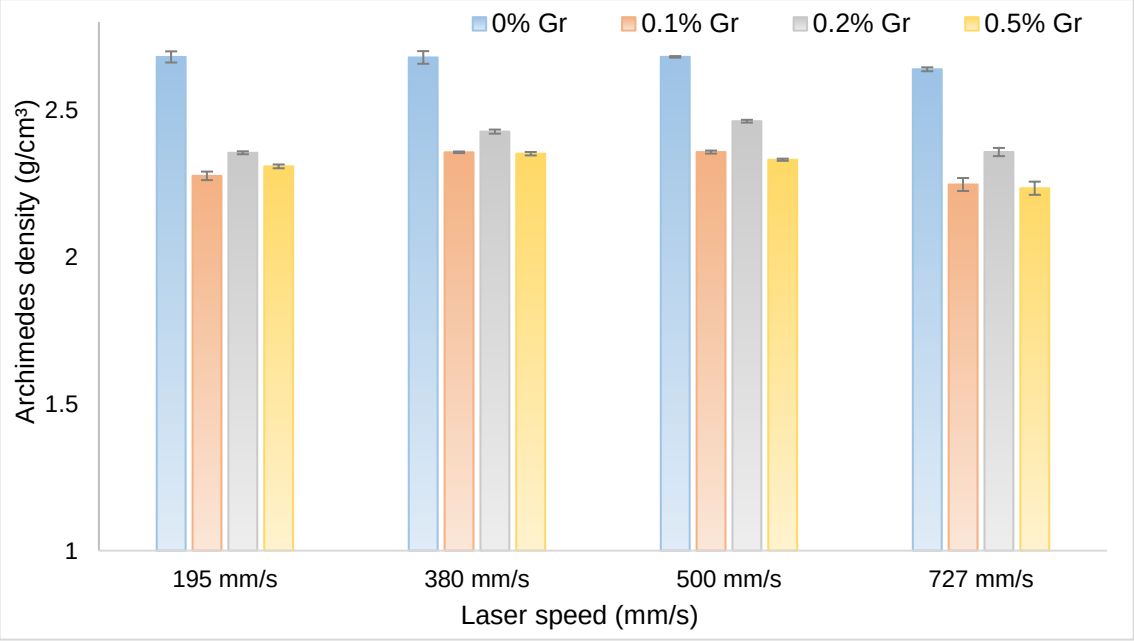

Figure 6.5: Archimedes' density of the composites in relation to scanning speed and Gr percentage.

Archimedes', theoretical and relative densities of as-fabricated composites were compared in Figure 6.6. All determined and calculated densities show a resemblance to the raw alloy. These results are consistent with others (Lava

Kumar et al. 2022) who reported that the addition of Gr decreases the relative density of the composites. However, the estimated theoretical density shows a small difference at 0.1 and 0.2 wt.% because the error margin of the theoretical density estimation at high porosity is increasing. Furthermore, the different determination techniques may also cause this difference.

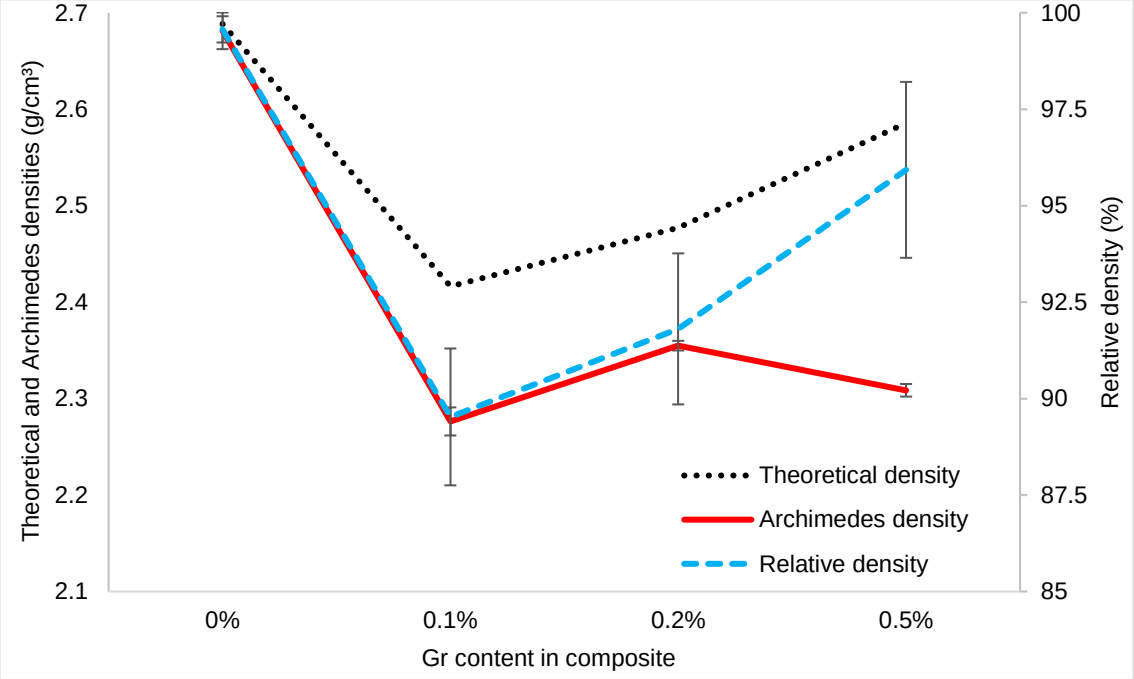

Figure 6.6: Comparison of theoretical, Archimedes', and relative densities of fabricated composites.

6.2.3. Microstructure

SEM images and distribution of Al and C (as a representative of GNPs) are shown in Figure 6.7 for different Gr percentages. The EDS does not give sensitive results for detecting the Carbon and Oxygen value of the milled powder; however, the measured values are given for only qualitative comparison. Figure 6.7(abc-3) reveals that when the Gr percentage is increased, the distribution of Gr is more homogeneous. The distribution of Gr in prepared powder shown in Figure 6.7a prior to the LPBF has been detailly discussed in a previous study. All detected elements are the alloying and reinforcement elements of the composite, which indicates that contamination prior to and during the fabrication is successfully

prevented. On the other hand, Gr accumulated on the pores area of 0.1 wt. % Gr reinforced composite, suggests that Gr has a negative influence on density. Due to the proportion of Gr, accumulation of Gr can occur often on 0.5 wt. % Gr reinforced composites.

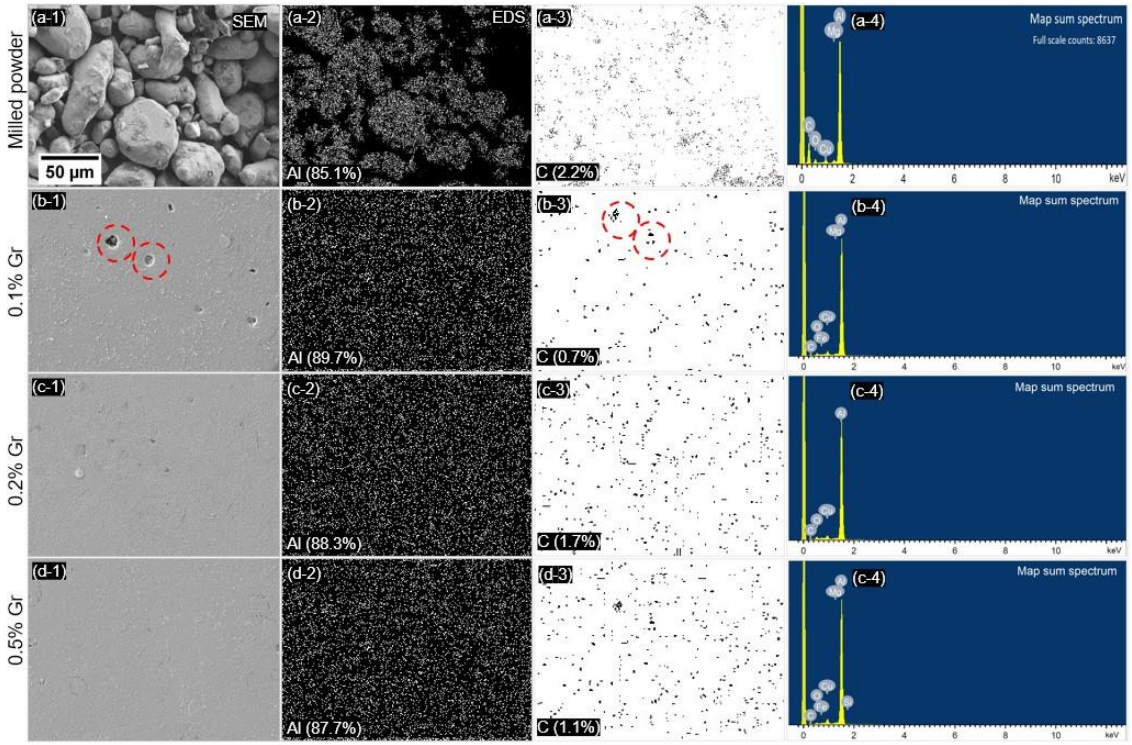

Figure 6.7: SEM images and distribution of Al and C elements via EDS and map sum spectrum of Gr reinforced milled powder (a) and composites (b-d)

The microstructures of the as-fabricated composites are shown in Figure 6.8 and Figure 6.9. Non-uniform formation of microstructure was obtained due to the re-melting process. Both coarse-grain and fine-grain microstructures were formed at the melt-pool. Some melt-pools were surrounded by HAZ due to the re-melting and high laser energy. Additionally, microcracks were formed from the bottom to the top of the melt-pool because of the dendrite orientation during the cooling time. Both defects and pores are visible in OM (Figure 6.8) and SEM (Figure 6.9) images. Moreover, microvoids were accumulated near solidification boundaries. Furthermore, a high cooling rate (as a result of high laser ED) caused the trapping

of non-uniform gas bubbles in the melt-pool and created pores, which is unavoidable for laser-based AM technologies (Tiwari et al. 2020).

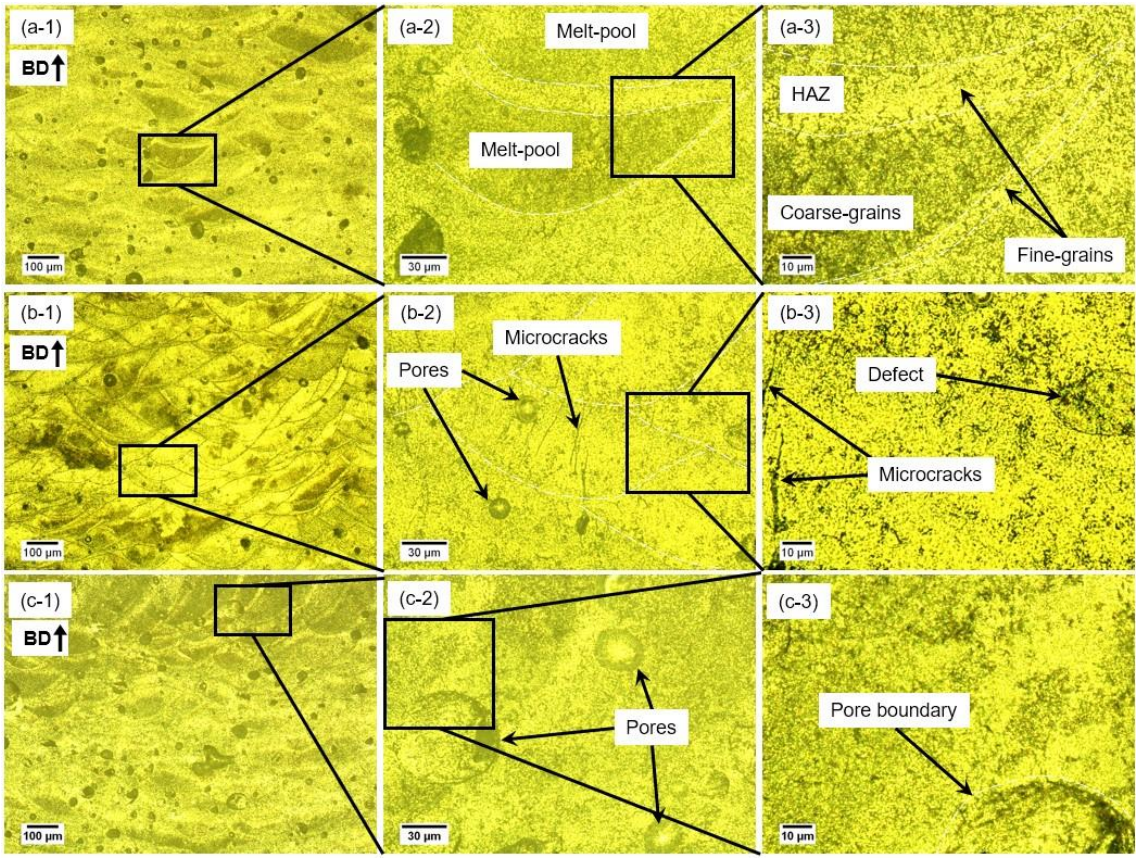

Figure 6.8: OM images showing microstructure, pores, and microcracks of Gr-reinforced composites.

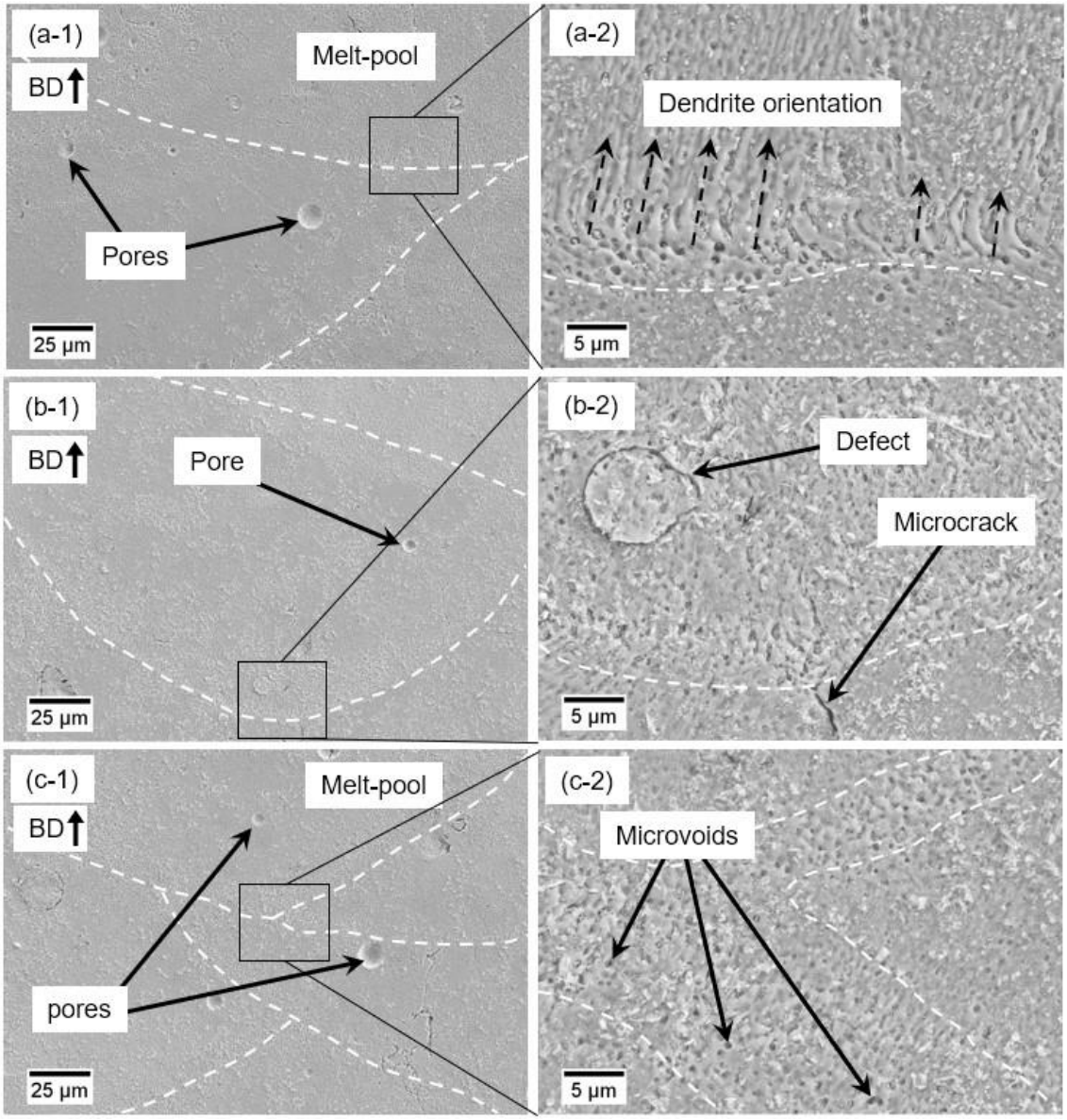

Figure 6.9: SEM images showing dendrite orientation, pores, and microvoids of Gr-reinforced composites.

6.2.4. Microhardness

Figure 6.10 shows that a higher Gr content in the composite leads to a harder microsized material. In comparison to the raw alloy, the addition of Gr improved the hardness from 27.8% to 44.3%. The highest results are achieved in the 0.2 wt.% Gr-reinforced composite at all scanning speeds. This result proves the uniform distribution of Gr and its effective participation in composites. After the peak point (0.2 wt.%), further addition of Gr (0.5 wt.%) caused a 14% reduction at every scanning speed. This finding was also supported by the XRD results

(Figure 6.2), showing that the smaller crystallite size improves hardness as a result of restricted dislocation movement. In addition, this finding is also supported by the literature (Tiwari et al. 2020), where a 30% improvement in microhardness has also been observed in the 0.2% Gr-reinforced AlSi10Mg alloy.

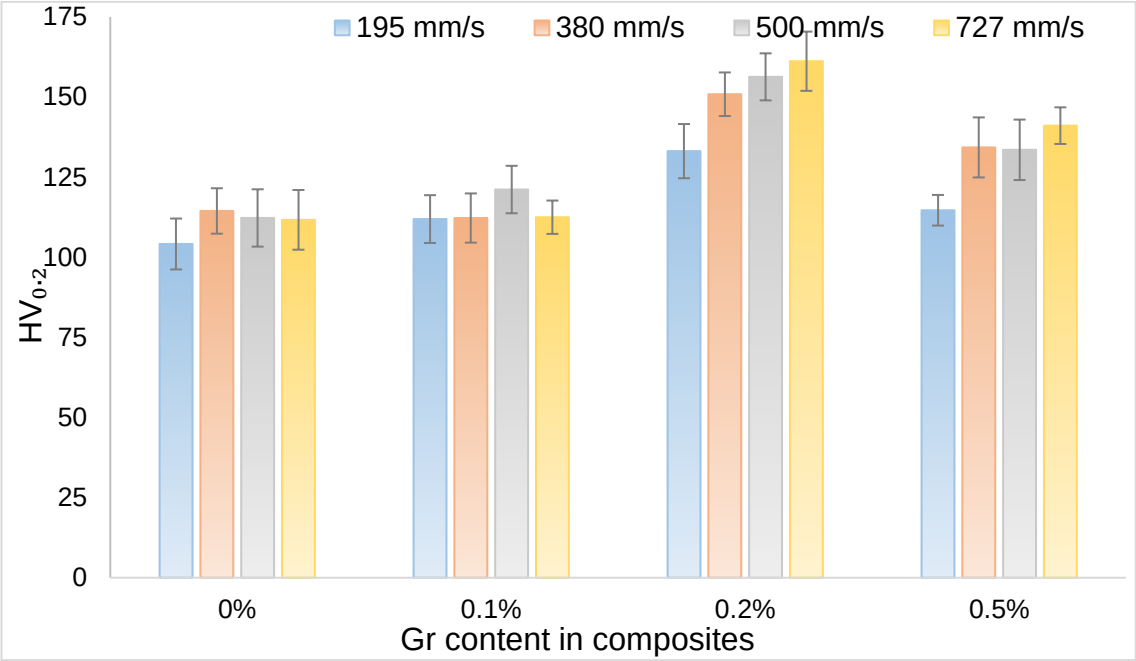

Figure 6.10: Microhardness results in raw alloy and Gr-reinforced composites.

Traces of microhardness indentation toll on the observed surfaces and depth properties in the alloy and composites are shown in Figure 6.11. Even though the diagonal angle of the indentation tool was 136°, the penetration angle on the observed surface was less than that due to the bounce back caused by elastic deformation after the indentation tool was removed (Mukhopadhyay et al. 2001). More details on the finite element analysis of elastic/plastic deformation during and after indentation may be found elsewhere (Giannakopoulos and Suresh 1999). According to the Orowan looping mechanism, reinforced Gr in the composites reacts as an interstitial atom, which restricts the dislocation movement and improves the hardness (Raj et al. 2021). Consequently, a higher percentage of Gr in composite results in a wider penetration angle because of the reduced ductility of the composite. Similarly, a narrower penetration angle in

comparison to the indentation tool dimensions has been reported in another literature study (Mukhopadhyay et al. 2001).

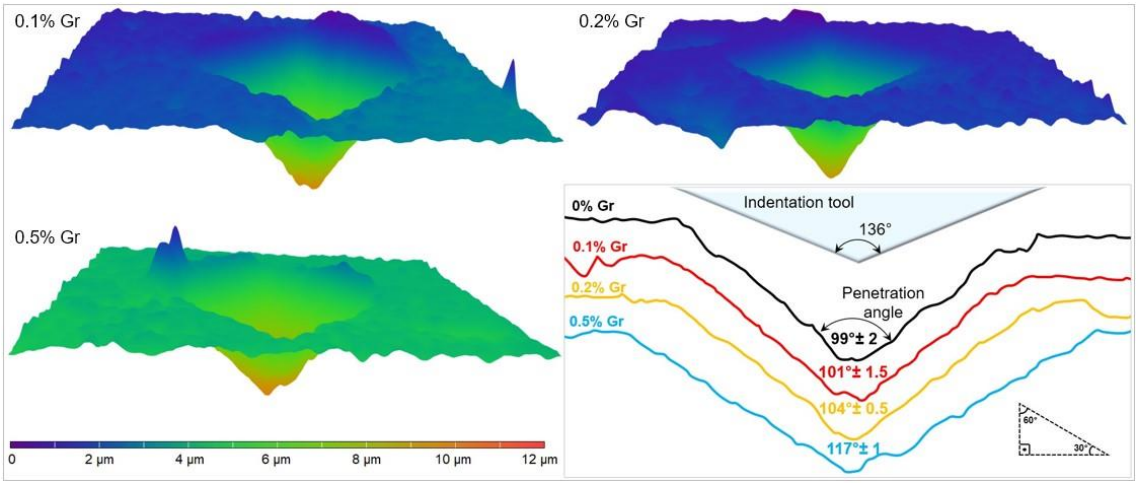

Figure 6.11: OM images showing the microhardness indentation tool trace and penetration angles of Gr-reinforced composites on the surface.

6.2.5. Macro Wear Behaviour

Friction coefficients of raw alloy and Gr-reinforced composites (obtained by tribology test under 1 kg load for half an hour of sliding) are shown in Figure 6.12. Despite the presence of large fluctuations at the beginning due to the vibration, nearly stable coefficient signals were observed afterwards. Relatively similar friction coefficient patterns for the composites have been observed. In comparison to the average friction coefficient of the raw alloy, Gr-reinforced composites offered 60% improvement, which could be explained by a uniform distribution of Gr in the composite. Furthermore, the trend lines of the mid-points tend to plot upstream lines for the alloy and composites (except 0.5 wt.%) due to the local hardening at the friction regions. Another reason is that the highest contact has been achieved after the 13th second as a result of the deep grooves between the specimen and the wearing ball (Yu et al. 2021).

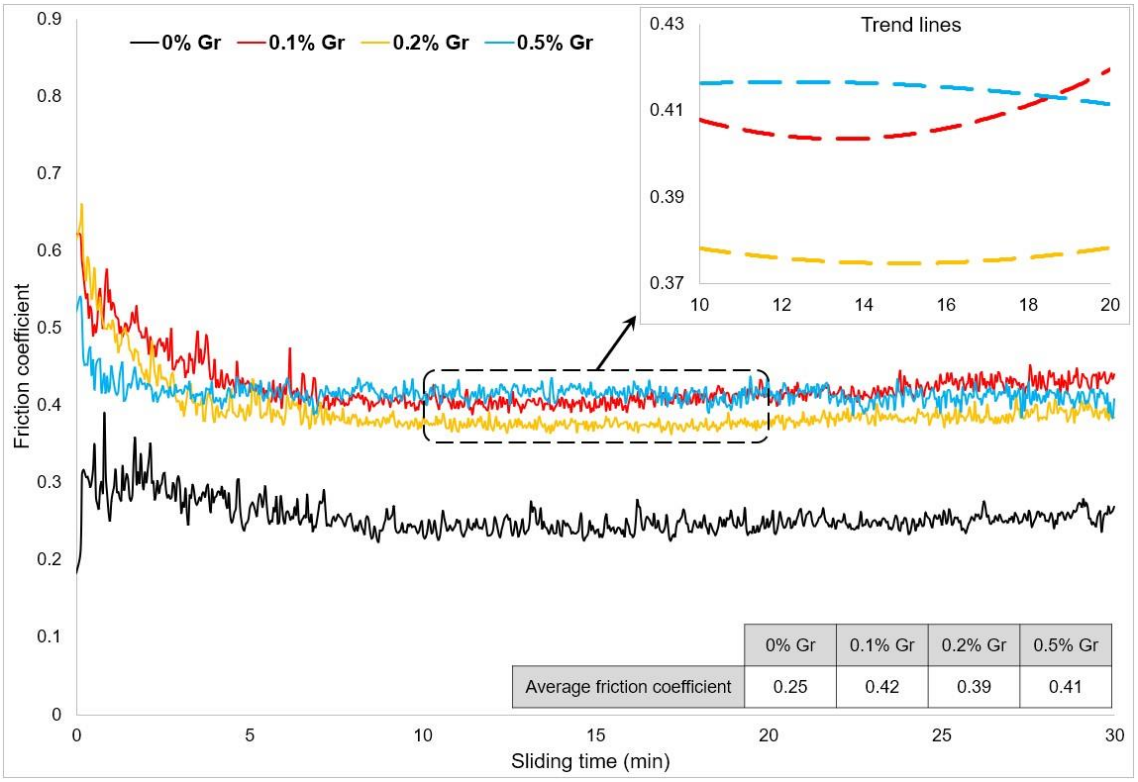

	0% Gr	0.1% Gr	0.2% Gr	0.5% Gr
Average friction coefficient	0.25	0.42	0.39	0.41

Figure 6.12: Friction coefficient variation, the trend line of mid-point, and the average friction coefficient of the raw alloy and composites.

Wear rates of the raw alloy and composites (calculated using Eq. 3) are shown in Figure 6.13. In comparison to the raw alloy, the composites demonstrate better performance, with a proven positive effect of the composite's Gr on the wear behaviour. While one of the reasons for this could be a uniform distribution of the reinforcement material in composite, the other reason is that improved microhardness allows for a significant reduction in the wear rate (Naik H R et al. 2021). Additionally, the 0.2 wt.% Gr-reinforced composite has the best performance among the others. However, the wear performance is reducing at the further point (0.5 wt.%). This could be explained by the 0.2 wt.% of Gr in AA2024 depicting the peak point, and beyond that, the structure starts to fail due to the surpassing of the carbon amount in the composite.

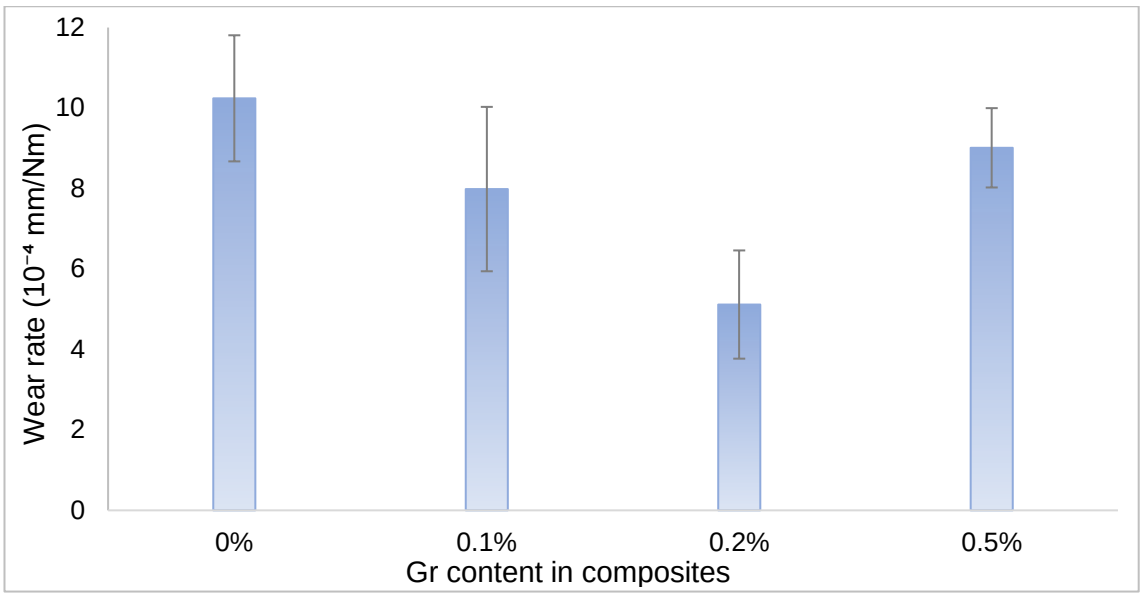

Figure 6.13: Wear rates of the raw alloy and the Gr-reinforced composites.

6.2.6. Nano Wear Behaviour

The lateral output voltage signal of the Position Sensitive Photo Detector (PSPD) built into the AFM instrument was used to detect the friction force of the AFM tip during the scratching time. Therefore, the friction coefficient was calculated from the lateral signal using Eq. 4. It can be observed from Figure 6.14 that, while the lateral voltage output of the raw alloy and the 0.1 wt.% Gr-reinforced composite display similar patterns, the other composites have substantially higher voltage owing to the hardness of the composites. The reason why the alloy and the 0.1 wt.% Gr composite has similar values is that Gr distribution of the 0.1 wt.% Gr may not be homogeneous enough to make a difference at the nanoscale. It is important to note that the composites that have higher microhardness, have higher friction coefficients, similar to the pin-on-disc results. While raw alloy and the 0.1 wt.% have lower friction coefficients in comparison to the pin-on-disc results, the other composites exhibit similarities. In addition, the highest output was obtained from the 0.2 wt.% Gr-reinforced composite.

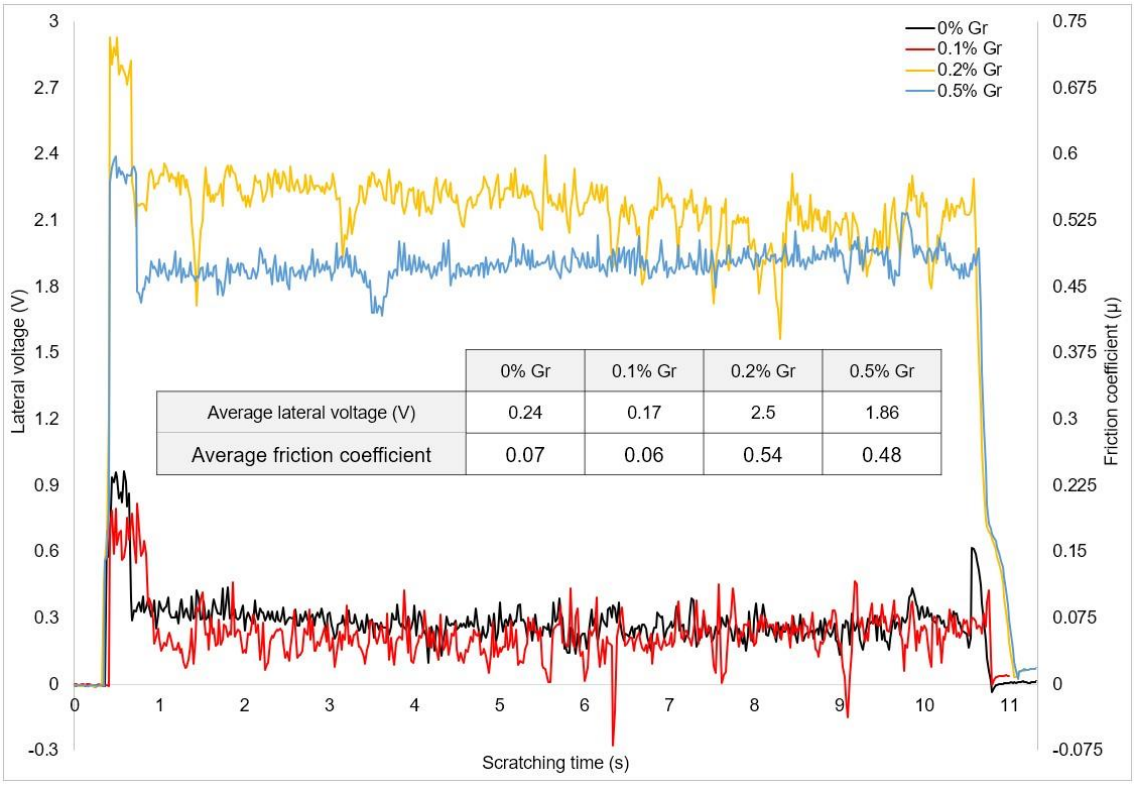

	0% Gr	0.1% Gr	0.2% Gr	0.5% Gr
Average lateral voltage (V)	0.24	0.17	2.5	1.86
Average friction coefficient	0.07	0.06	0.54	0.48

Figure 6.14: Lateral voltage outputs and average lateral signals of raw alloy and the composites.

The top view of the AFM tip and the scratches can be seen in Figure 6.15. All lines are parallel to each other, and each line is 20 μm in length. The experiment has been conducted in a 20x35 μm^2 area. Removed debris particles during the stretching time by the AFM tip can also be seen at the end of the lines in Figure 6.15b. As shown in Figure 6.14, at the beginning of the scratch (0 to 0.5 seconds), the AFM tip is subjected to large fluctuations until the instruments adjust the required force (10 μN). After this point, the line is smoother until the end (10^{th} second).

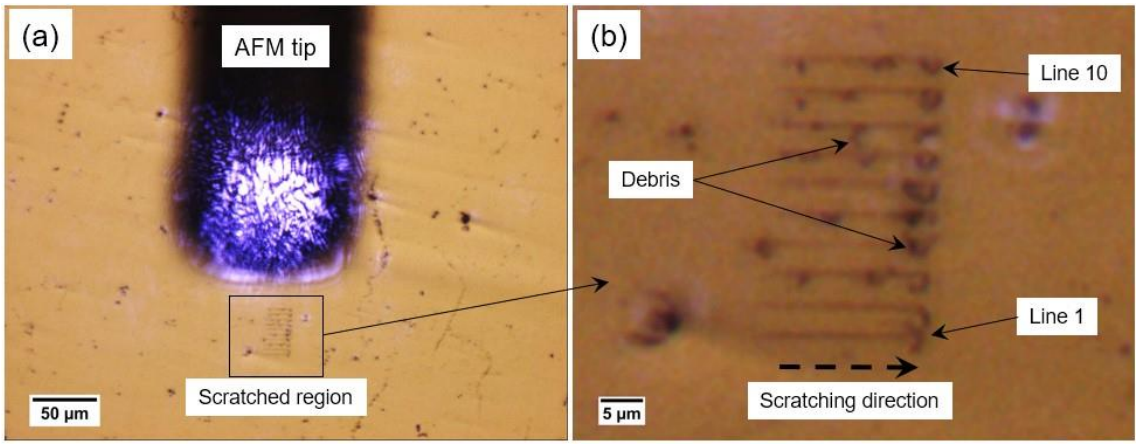

Figure 6.15: AFM images showing the top view of the tip and the scratches.

6.2.7. Surface Roughness (Ra)

Surface roughness measurements of the as-fabricated and polished specimens are shown in Figure 6.16 (AFM) and Figure 6.18 (optical profilometer). Different equipment results with different surface roughness values are explained by the limitation of the scanned area. While AFM examines a 20x20 µm2 area, an optical profilometer identifies the 1.4x1.7 mm2 (for as-fabricated) and 700x850 µm2 (for polished) surface area. The surface roughness (Ra) of the as-fabricated specimens exhibits fluctuations when the Gr percentage is increased up to 0.2 wt.% Gr reinforced composite (Figure 6.18). On the other hand, even though the same grinding and polishing equipment and order have been used, Gr-reinforced composites increased surface roughness in comparison to the raw alloy due to the greater porosity and defect on the observed surface (Figure 6.18). The negative effect of the Gr on porosity can be clearly seen from both as-fabricated and polished samples. The porosities and cracks (which were created inside the sample) become more apparent after being polished, as can be seen from Figure 6.8 and Figure 6.9.

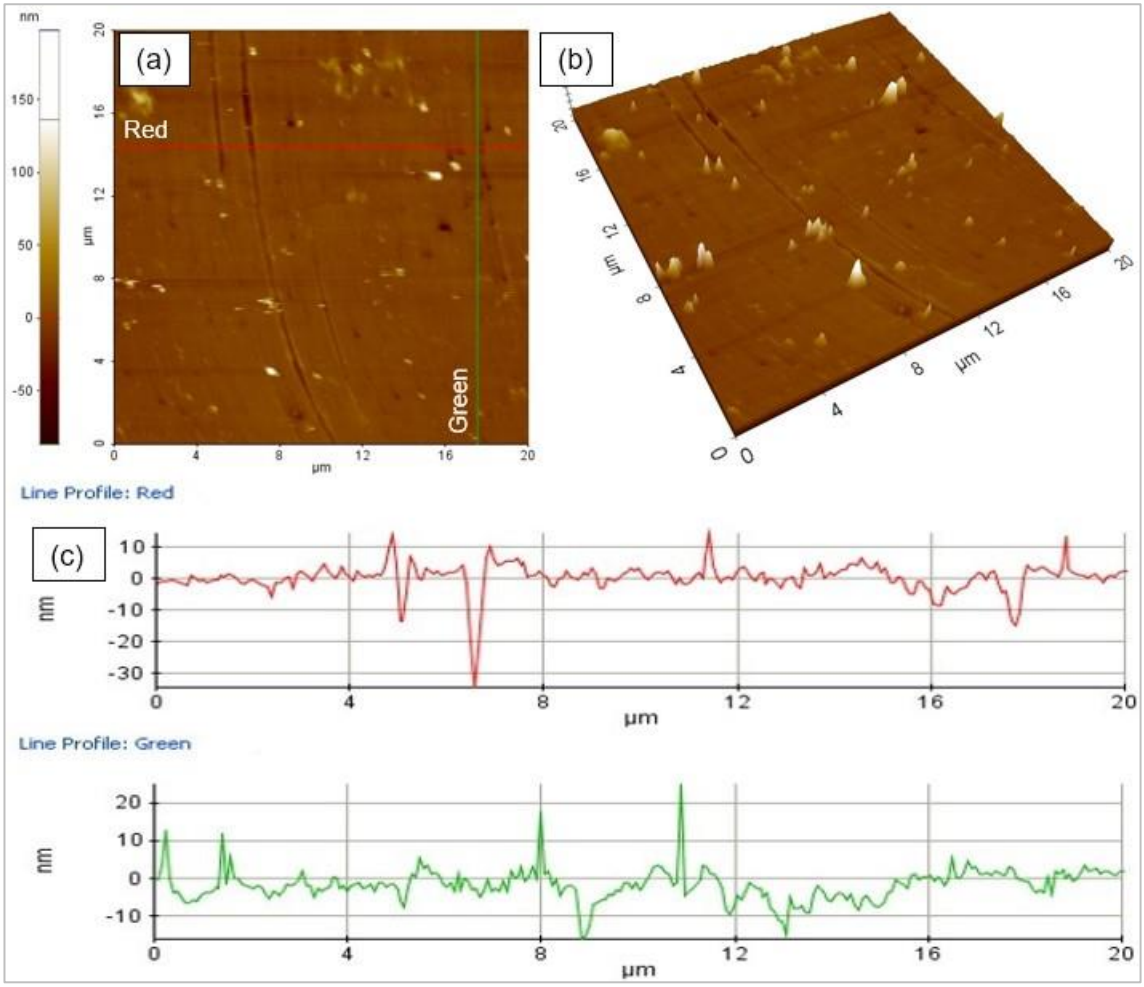

Figure 6.16 AFM images of the 0.2 wt.% Gr-reinforced composite showing (a) 2D surface roughness, (b) 3D surface roughness, and (c) topography of selected lines that are perpendicular to each other.

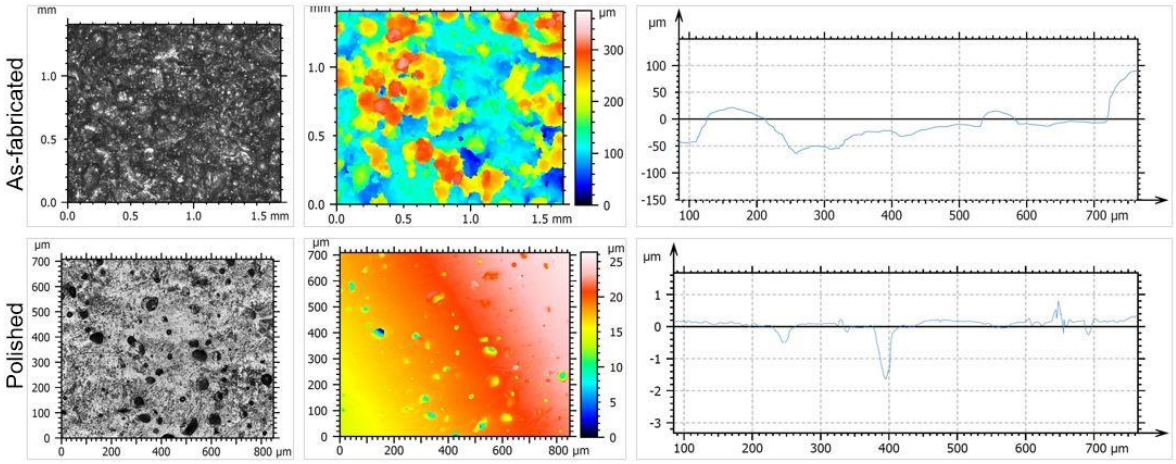

Figure 6.17 Image of observed surface, the topography of all layers and selected lines for 0.2% Gr reinforced as-fabricated and polished samples obtained from optical profilometer.

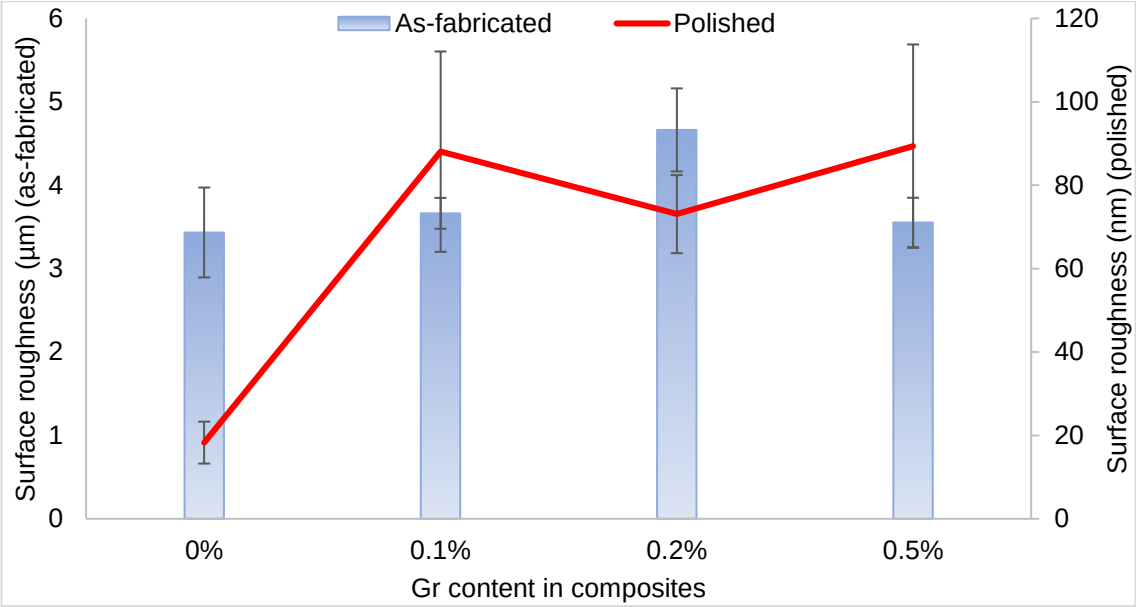

Figure 6.18 Surface roughness measurement of the as-fabricated and polished specimens using an optical profilometer.

6.2.8. Tensile Strength

The tensile properties of the raw alloy and Gr-reinforced composites are shown in Figure 6.19. While the 0.2 wt.% Gr-added composite depicts slight improvement (6.2%), 0.1% and 0.5 wt.% Gr-reinforced composites resulted in a reduction (4% and 50%, respectively) of UTS in comparison to the raw alloy. It is important to note that despite the severe reduction in density (8%) of the composite from the raw alloy to the 0.2 wt.%, the tensile strength showed improvement. The higher and the lower percentages of Gr than 0.2 wt.% results in a reduction. This may be due to the fact that the adequate percentage of Gr in the composite leads to improved mechanical properties of the composite. In addition, the uniform distribution of the Gr in the composite could be another reason that positively affects the tensile property. On the other hand, despite the lesser reduction (4%) of density between the raw alloy and the 0.5 wt.% Gr-reinforced composite, tensile strength showed dramatic reduction (50%) due to the exceeding concentration of the carbon element.

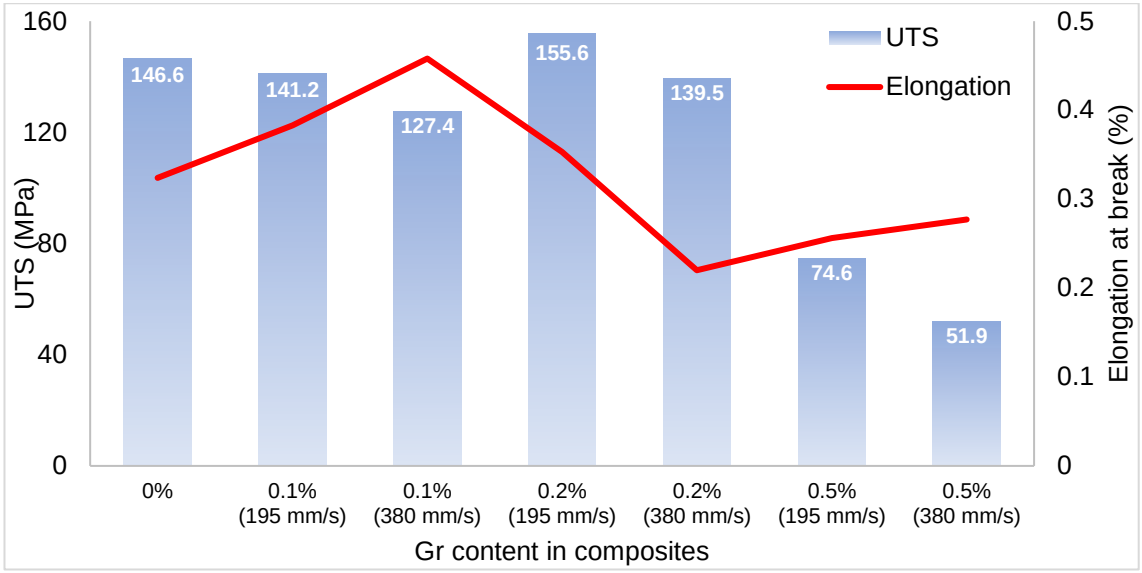

Figure 6.19: UTS of the raw alloy and the Gr-reinforced composites.

SEM images of the fracture surface of the composites fabricated under 195 mm/s scanning speed and 200 W laser power are shown in Figure 6.20. Similar fracture microstructure on the observed surfaces can be seen for the composites. Porosities and inner cracks that cause an early failure of the sample in the tensile tests are highlighted with arrows. Even though high laser energy was used during the fabrication process, several unmelted powders and powder holes (porosities) on the observed surface can still be seen in Figure 6.20 (which suggests that a higher laser power than 200 W might be required for the composites to reduce unmelted powder in the structure). Additionally, dimple structure and cleavage can be seen locally. Zoomed SEM images of the 0.2 wt.% Gr-reinforced composite is shown in Figure 6.21 in order to see the dimple structure. Very fine dimple structures (dimple size: 2 to 0.1 µm), which also implied ductile behaviour, have been observed from the fracture surface (Han et al. 2018a; Han et al. 2018b).

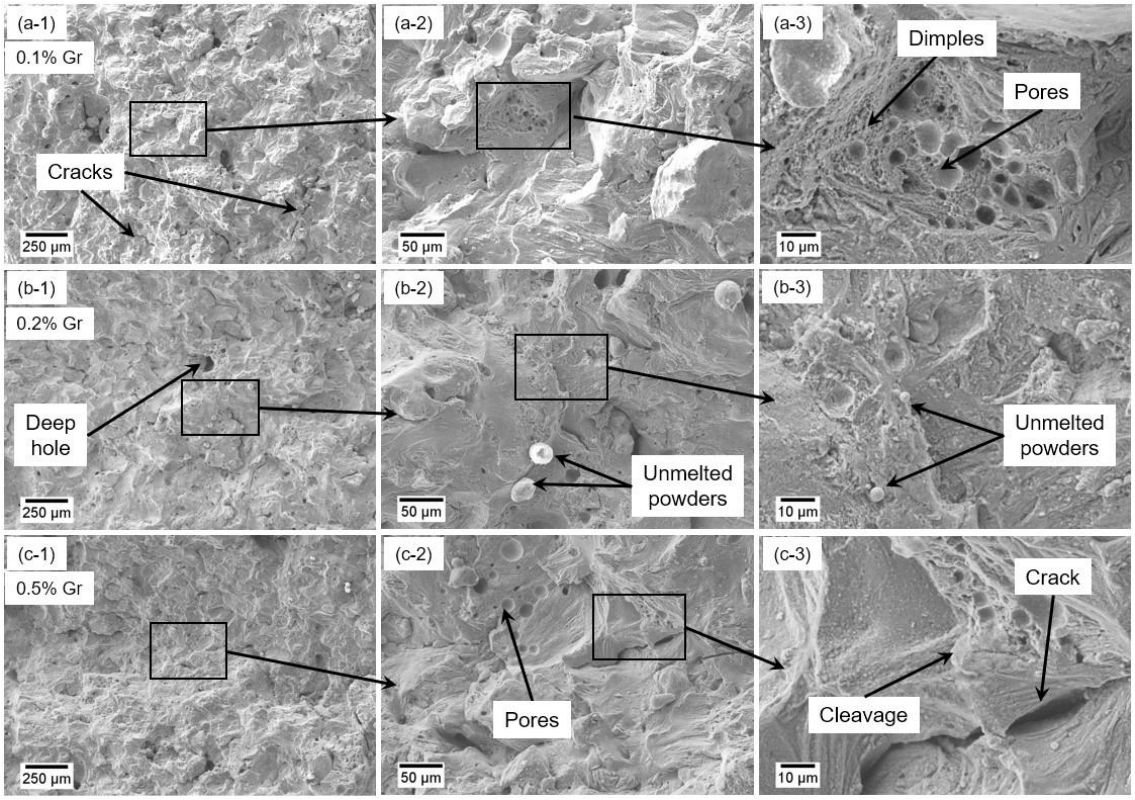

Figure 6.20: SEM images of the fracture surface showing porosity, cracks, and unmelted powders.

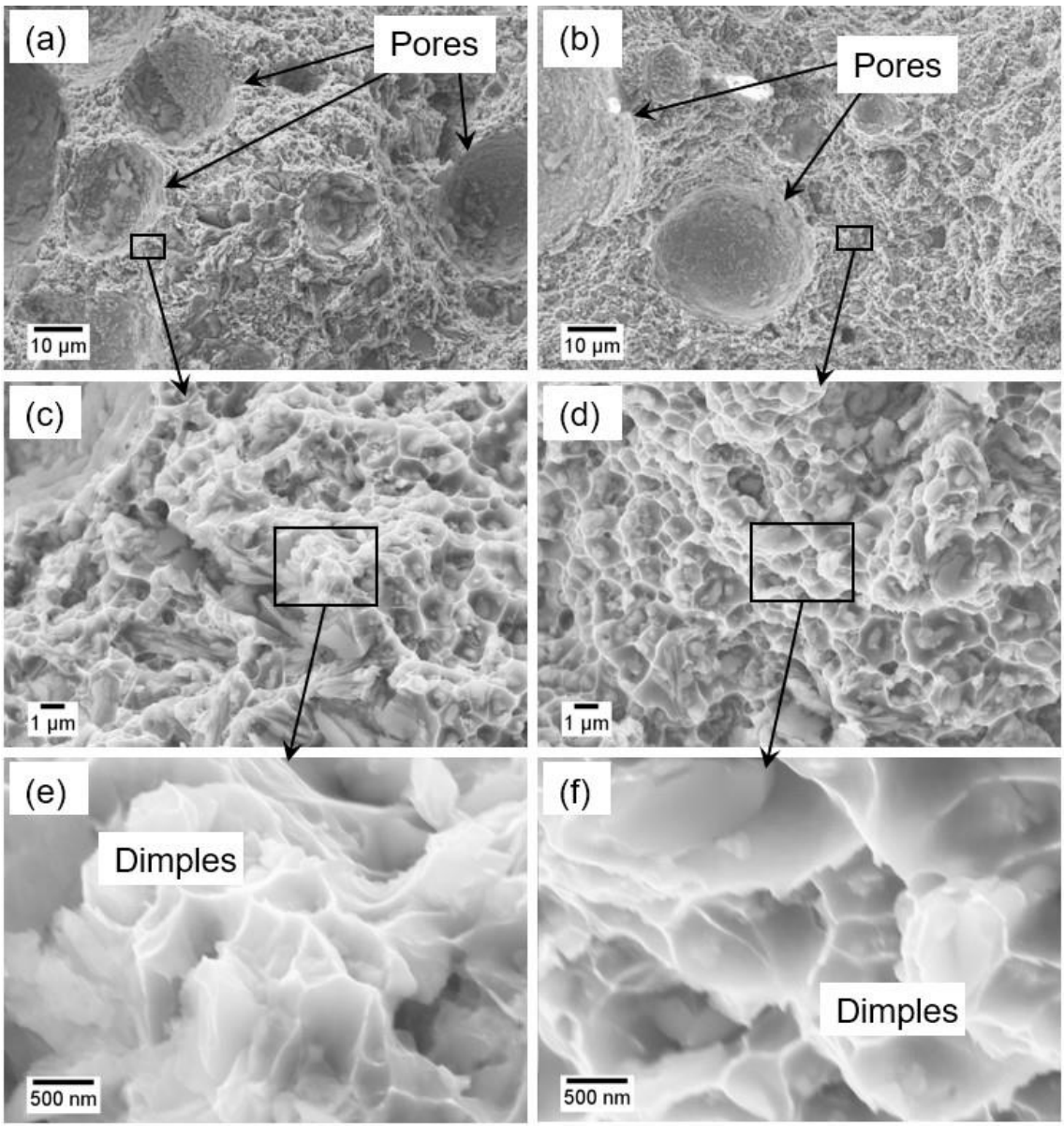

Figure 6.21: Fracture surface of the 0.2 wt.% Gr-reinforced composite showing dimples in nanoscale.

6.3. Discussion

Milling time and addition of Gr have a direct proportion on the crystallite refinement. The effect of the milling time on the phase identification was investigated in the previous study, and it had been reported that continuous impact energy in the milling bowl causes more lattice defects in powder as a consequence of severe cold-working and plastic deformation. On the other hand, the effect of Gr on the crystallite refinement is presented in Figure 6.2, which shows that a higher amount of Gr improves the crystallite density. This is due to

the contribution of Gr subsequent to the fabrication in the pinning of the displacements, which produces further strain in the matrix (Tiwari et al. 2020). The peak shift and broadenings following the fabrication can also be explained by the incredibly high cooling rate and the existence of a Gr-related increase in the dislocation density as a result of induced lattice strain (Mandal et al. 2020).

Therewith, the finer grain and crystallite size results in a higher number of grain and crystallite boundaries, which improve the mechanical properties by restricting the movement of dislocations and causing dislocation pileup (Nieto et al. 2017). Additionally, better heat distribution of the Gr-reinforced composites has been reported due to the elevated thermal conductivity of Gr (5000 W/mK (Dorri Moghadam et al. 2015)), which is substantially higher than of AA2024 (194 W/mK) (Chen et al. 2021). The presence of Gr in the composite enhances the thermal conductivity and cooling rate of the composite due to the excellent thermal conductivity of the Gr. Hence, the higher cooling rates trigger greater dislocation density, resulting in the finer crystallite size, seen in the as-fabricated composites in Figure 6.2.

The relative density and Archimedes' density show a similar pattern until the 0.2 wt.% (Figure 6.6), which can be explained by the uniformity of the layers. While Archimedes' density quantifies the density of a cube for each parameter, the relative density is obtained from the three separate layers of each specimen utilising OM images and ImageJ software. Similarly, the big difference between Archimedes' density and the relative density at 0.5 wt.% can also be explained as the non-uniformity of the layers. On the other hand, in comparison with Archimedes' density of the raw alloy and the as-fabricated composites, Gr reinforcement results in a severe reduction (Figure 6.5) for two reasons. First, more pores are formed in composites with the addition of Gr, and thus

Archimedes' density results are reduced. A similar effect of Gr on Al alloys was also shown in other studies (Liu et al. 2019; Tiwari et al. 2020; Naik H R et al. 2021). The other reason is that the addition of lighter reinforcement material naturally reduces the density of the composites. The combination of these two effects generates a difference between the raw alloy and the composites. Furthermore, different measurement and estimation techniques (such as relative, theoretical, and Archimedes' densities) may also cause different patterns.

The addition of Gr improved the microhardness of the as-fabricated composites by 45% (at 0.2 wt.%) (Figure 6.10). The latter suggests the uniform distribution of Gr and its efficient contribution to grain refinements (see Figure 6.2) (Tiwari et al. 2020). However, the high porosity intensity at 0.5 wt.% reduced the microhardness of the as-fabricated sample (Bai et al. 2019). Similarly, the negative effect of the high percentage of Gr on microhardness has been previously reported in another study (Azar et al. 2019). Additionally, while the raw alloy and the 0.1 wt.% Gr-reinforced specimens were almost unaffected by scanning speed, the positive effect of the scanning speed on the microhardness can be seen after 0.2 wt.%. The reason for this improvement in fast scanning speed can be attributed to the solidification rate. Slow scanning speeds cause an increase in solidification time, which results in a coarser microstructure (Zhang et al. 2019). Contrary to this, fast scanning speeds reduce the solidification time and form a finer microstructure that restricts the dislocation movement (Larimian et al. 2020). Hence, lesser dislocation movement improves the microhardness of the composites.

Tribology (pin-on-disc) testing demonstrates that the addition of Gr improves the wear performance of the composites (Figure 6.12 and Figure 6.13). The friction output voltage was increased depending on hardness (Yu et al. 2021). Parallel to

microhardness results, 0.2 wt.% Gr-added composite provides 56% higher output voltage. Additionally, trend lines of the mid-points demonstrate that the output voltage gradually improves after a certain point. The reason for this change on the trend lines is that the milling ball creates deeper grooves in the process, which increases the surface contact and generates additional temperature at the friction region. Higher temperature results in local hardening, and thus friction coefficient starts to increase slightly (Yu et al. 2021). Similarly, wear rates of the composites have better performance in comparison to the raw alloy due to the hardness, which means that the removed volume from the harder specimens is less than from the softer ones, as expected.

A comparison of the AFM and the pin-on-disc tests demonstrates that while AFM friction coefficients of 0.2% and 0.5 wt.% show similarities, values of the other composites are lower in the AFM results. AFM tests have been conducted in a 20x35 μm^2 area (which is a relatively small area). At this sale, nano cracks and nanopores (see Figure 6.8 and Figure 6.9) may strongly influence the outcome of the AFM test. This might be the explanation for why the raw alloy and the 0.1 wt.% are lower than the pin-on-disc results.

On the other hand, severe reduction in the tensile testing recordings of 0.1% and 0.5 wt.% Gr-reinforced composites illustrate the significant effect of the porosity and cracks in comparison to the raw alloy. However, the 0.2 wt.% composites show that a certain amount of Gr can improve the mechanical properties of the composite.

6.4. Summary

The present study investigated the effect of laser scanning speed and Gr concentration on microstructure and mechanical characteristics of the

GNPs/AA2024 composites fabricated using LPBF. The effect of crack and porosity formation on the mechanical properties was also identified, and the following key findings were drawn from the experimental data:

1) Not only milling the powder but also adding the Gr decreases the crystallite size due to the enhanced thermal conductivity of the composite with the addition of Gr. The addition of 0.2 wt.% Gr resulted in a 37.6% reduction in crystallite size compared to the raw alloy. The higher conductivity and cooling rate results in the formation of the finer microstructure, which restricts the dislocation movements.
2) The Microhardness of the as-fabricated composites was improved up to 45% parallel to the Gr concentration. This indicates that Gr is distributed evenly throughout the structure. Additionally, the faster scanning speed is another positive effect on the improvement of the microhardness due to the high solidification rate resulting in a finer microstructure.
3) Due to the greater laser power requirements of the new composites, the addition of Gr causes an increase in the porosity of the composites. The best density (95.6%) has been achieved from 195 mm/s scanning speed and 0.5 wt.% Gr-reinforced composite. Even though the porosity of the sample has risen, the UTS for 0.2 wt.% Gr was marginally enhanced (7%).
4) Both macro (pin-on-disc) and nano (AFM) wear performance of the composites improved gradually with the addition of Gr. The 0.2 wt.% Gr had a 50% and 56% superior wear rate and average friction coefficient (μ) performance than the raw alloy due to uniform distribution and improved hardness of the composite.

7. Chapter: Contributions, Conclusions and Future Work

The study covered in this thesis comes to a close in this chapter. The fundamental aspects of this study are highlighted in Section 7.1. The conclusions are stated in Section 7.2, while the suggestions for further study are addressed in Section 7.3.

7.1. Contributions

The following are the most important contributions of this research:

i. A systematic method for as-received AA2024 has been developed in order to optimise the LPBF parameters and characterise the fabricated samples. Three significant parameters (laser power, scanning speed and hatch distance) have been studied and the effect of these parameters on the mechanical and microstructural characteristics of as-fabricated samples are uncovered. The binary parameter method was adopted in this study to find the best LPBF settings. First laser power and scanning speed were examined (Experiment-1), and then hatch spacing and scanning speed were discussed (Experiment-2) using the optimum laser power from the previous experiment. It has been discovered that the high reflectivity of the alloy powder can be compensated with high laser power and slow scanning speed. Additionally, the relationship between ED, processing parameters and the achieved results in the as-fabricated specimens is another in-depth understanding of this research.

ii. A method was developed for ball milling in order to explore the characteristics of the different percentages of Gr (0.1, 0.2 and 0.5%) reinforced composite powder under different milling parameters. An

interrelation between milling parameters, powder morphology and agglomeration of the reinforced particles in the composite has been discovered and found that while short milling times create insufficient impact energy to break strong van der Waals bonds of the Gr, long milling time significantly affects the powder morphology.

iii. A simulation model has been developed to estimate the flowability of the powder from both common (Type 1) and realistic (Type 2) particle morphologies. Additionally, the effect of single and multiple (3, 6, and 10) particles and different volumes of the multiple particles in the powder pool is discovered which is impossible to examine through experimental work. Simulated realistic particles outperformed typical particle morphology as a consequence of a comprehensive understanding of the powder's flowability.

iv. Finally, this study addresses the knowledge gap in this area by investigating the wear performance, microstructural, and mechanical properties of different weight ratios (0.1 to 0.5 wt.%) of GNPs-reinforced AA2024 composite fabricated using LPBF. The effect of various scanning speeds (195 to 727 mm/s) and weight ratios of Gr in composite on microstructure, microhardness, density, wear performance, and tensile properties of the composites were explored. Additionally, the main contribution of this research is developing an in-depth understanding of the relationship between the applied processing parameters of LPBF, Gr concentration in the composites, and the obtained results. Moreover, a comparison of macroscale (pin-on-disc test) and nanoscale (AFM, nano-scratching) wear performance of the composites is presented. Besides,

the present work offers some practical recommendations for fabrication parameters and concentration of the reinforced element.

7.2. Conclusions

The aim of this study is to investigate the effect of GNPs on AA2024 using ball milling and LPBF techniques. In order to achieve this aim, three main objectives have been followed. The first objective is to explore the microstructure and mechanical characteristics of as-fabricated specimens using the LPBF technique of raw AA2024 in order to find the optimal working parameters for fabricating nearly full dense specimens and to utilize the optimum parameters as a benchmark in all following investigations. Secondly, ball milling of advanced composite powder (GNPs/AA2024) will be investigated in order to incorporate homogeneously distributed Gr nanoparticles in MMCs. The final objective is to investigate the advanced composite's LPBF process in order to determine the influence of the reinforced material on the composite.

In light of the aim and objectives, the following conclusion has been drawn.

i. The processing parameters, especially laser power, hatch spacing and scanning speed of the LPBF process have a substantial effect on the properties of the as-fabricated specimens. A 98 mm/s scanning speed, 80 µm hatch spacing and 150 W laser power were used to obtain the maximum relative density (99.9%). However, with a 40 µm hatch spacing, the maximum Archimedes' density (99.7%) was reached using the highest laser power (200 W) and the slowest scanning speed (98 mm/s). When using EDs less than 130 J/mm^3, the most common adverse effects are unmelted powder and significant fractures appearing inside the structure owing to insufficient fusion. Microcracks and small gas pores (due to air

existing between the prepared powder particles) within the melt-pool during the melting process are the most significant concern for EDs greater than 300 J/mm^3. Solidification cracking has a considerable influence on the strength of larger pieces fabricated from these alloys, according to tensile testing findings and fracture surface analyses. The tensile test specimen produced with 150 W laser power and 98 mm/s scanning speed at 80 µm hatch spacing had a maximum UTS of 145 MPa. In contrast to the findings obtained from the 6x6x7 mm^3 specimens, SEM photos reveal unmelted powder on the worn surfaces of the tensile test specimen. As a result of the presented study, 60 and 80 µm hatch spacing and 98 mm/s scanning speed under 200 W laser power and 25 µm layer thickness are recommended for the fabrication of small components. Nevertheless, solidification cracking creates some limitations in producing larger parts from this alloy.

ii. The milling times and speeds of ball milling have a significant impact on MMC. When the milling speed is increased (from 100 to 250 rpm), the volume density of powder under 10 µm drops because strong impact energy gathers the particles and small Gr platelets stick on the powder's surface. It is concluded that a high milling speed has some positive effects (for instance the Gr sheets are stuck onto the Al powder particles); however, flattened powders are not convenient for AM processing. On the other hand, slow milling speed allows does not affect the form of the powder shape, but the Gr platelets are not homogeneously dispersed inside the MMC.

iii. Inadequate impact energy within the milling bowls due to the short milling period (0.5 to 2 hr) was insufficient to break the strong van der Waals

bonds. However, long milling periods (8 to 16 hr) significantly altered the powder morphology. After 8 hr of milling, the raw alloy powder particles had a flat morphology, whereas the raw alloy powder particles had a spherical form. Furthermore, as milling time increases, plastic deformation on powder becomes much more visible. Longer milling periods also resulted in greater separation and adhesion of GNPs to the Al powder surface. The homogeneous distribution of Gr was obtained above 4 hr milled alloy. The best flowability among the milled powders was obtained from 4 hr milled powder, based on the angle of repose and compaction tests. The flowability test results demonstrate great correlation when contrasting experimental and simulation findings at longer milling times. Theoretical findings for short milling times, on the other hand, diverge from experimental data. This is because dispersed Gr nanoparticles, which are obtained by extensive milling durations, are less effective on the angle of repose. When the flowability and compressibility test of the milled powders, microstructural analysis, and DEM simulation results are considered, it is concluded that 4 hr milled GNPs/AA2024 powder at 100 rpm milling speed satisfies the LPBF process requirements to obtain better-deposited layers and uniform composite.

iv. Adding Gr to a composite fabricated using LPBF increases porosity and causes more cracks; however, a certain amount of Gr reinforcement can result in higher mechanical attributes (microstructure, wear performance, and tensile strength). Due to the increased thermal conductivity of the nanocomposite with the addition of Gr, not only milling the powder but also adding the Gr reduces the crystallite size. In comparison to the raw alloy, the addition of 0.2 wt.% Gr resulted in a 37.6% reduction in crystallite size.

Because of the higher conductivity and cooling rate, a fine-grained microstructure forms, which inhibits the movement of dislocations. Corresponding to the Gr intensity, the microhardness of the as-fabricated composites was enhanced by up to 45% which shows that Gr is uniformly distributed throughout the structure. Furthermore, due to the increased solidification rate resulting in a fine-grained microstructure, the fast scanning speed has a beneficial influence on the enhancement of microhardness. The incorporation of Gr increases the porosity of the composites due to the higher laser power requirements of the new composites. The highest density (95.6%) was attained with a scanning speed of 195 mm/s and 0.5 wt.% Gr-reinforced composite. Despite the increased porosity of the specimen, the UTS for 0.2 wt.% Gr was only slightly improved (7%). With the inclusion of Gr, the composites' macro (pin-on-disc) and nano (AFM) wear performance steadily improved. Because of the homogeneous distribution and enhanced hardness of the composite, the 0.2 wt.% Gr had a 50% and 56% better wear rate and average friction coefficient performance than the raw alloy. In consideration of the mechanical performance, 0.2 wt.% Gr-reinforced AA2024 composite has been recommended for LPBF under the applied fabrication parameters.

7.3. Future Work

The following are examples of possible future projects that might be considered:

- Further study might be required in order to investigate whether further improvements to the mechanical properties of the alloy can be achieved with various reinforcing elements, multiple materials structures, and

different AM fabrication techniques (i.e., laser-directed energy deposition). Some materials (i.e., Al_2O_3, SiC, TiN, BN, WC, B_4C and some other carbon-based allotropes) might improve the mechanical properties of the alloy combination with Gr.

- With the aid of mechanical improvement, the new advanced composite might be preferred by the companies for their applications. For instance, landing gears and breaks of aerospace vehicles, sports equipment, piston combustion faces and rings of diesel engines can be made using the new composite due to its excellent wear resistance, high thermal conductivity, high strength, and low density. This assumption might be addressed in future studies, demonstrating the suitability of the advanced composite for new applications in engineering sectors.
- The deposited material layer plays a significant role in milled powder on the quality of the fabricated samples. A clockwise rolling recorder might be developed and examined in order to minimize short-feeding and achieve a well-packed layer of powder.

Apendix A

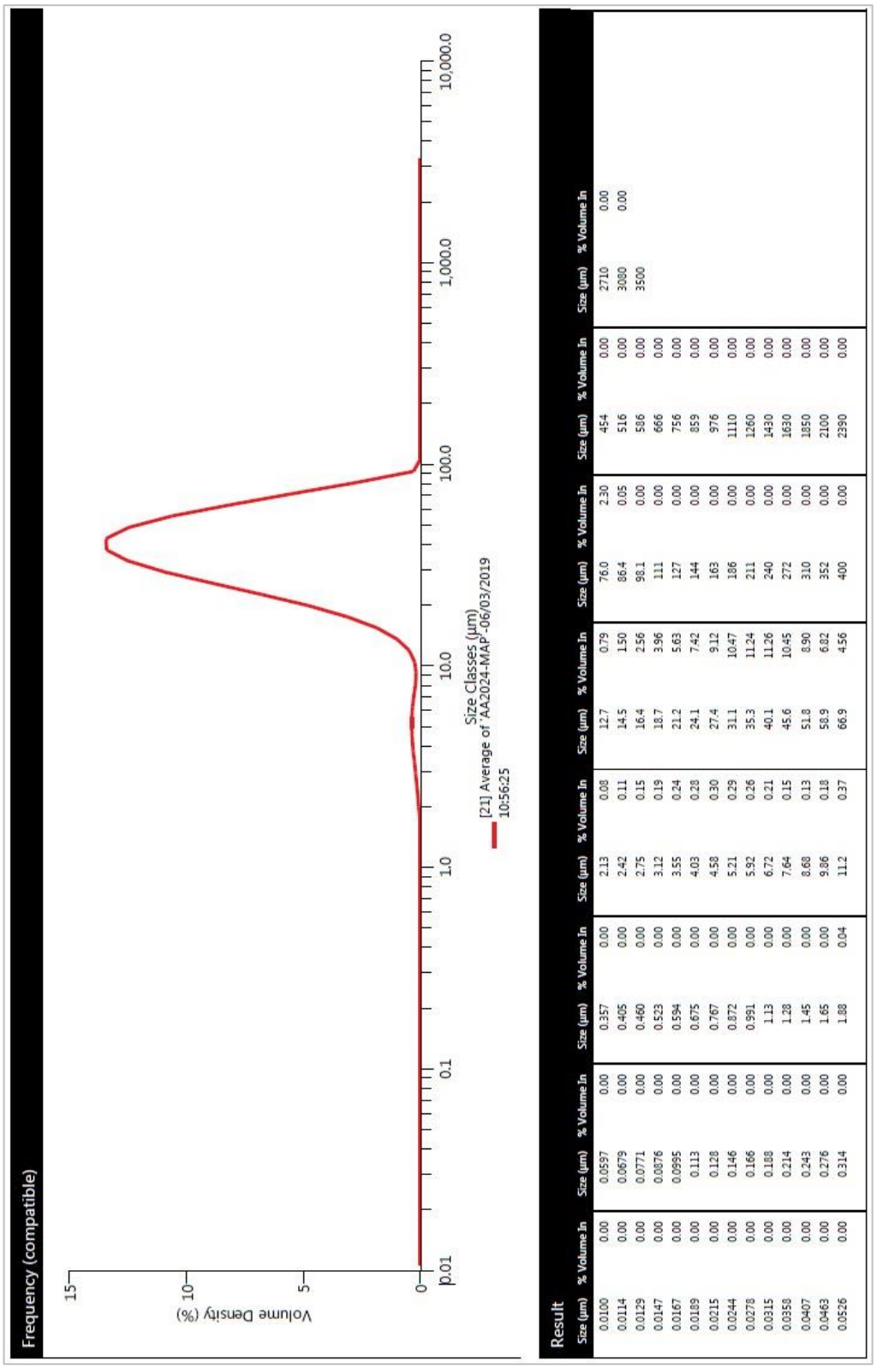

Result

Size (µm)	% Volume In	Size (µm)	% Volume In	Size (µm)	% Volume In	Size (µm)	% Volume In	Size (µm)	% Volume In	Size (µm)	% Volume In	Size (µm)	% Volume In	Size (µm)	% Volume In
0.0100	0.00	0.0597	0.00	0.357	0.00	2.13	0.08	12.7	0.79	76.0	2.30	454	0.00	2710	0.00
0.0114	0.00	0.0679	0.00	0.405	0.00	2.42	0.11	14.5	1.50	86.4	0.05	516	0.00	3080	0.00
0.0129	0.00	0.0771	0.00	0.460	0.00	2.75	0.15	16.4	2.56	98.1	0.00	586	0.00	3500	
0.0147	0.00	0.0876	0.00	0.523	0.00	3.12	0.19	18.7	3.96	111	0.00	666	0.00		
0.0167	0.00	0.0995	0.00	0.594	0.00	3.55	0.24	21.2	5.63	127	0.00	756	0.00		
0.0189	0.00	0.113	0.00	0.675	0.00	4.03	0.28	24.1	7.42	144	0.00	859	0.00		
0.0215	0.00	0.128	0.00	0.767	0.00	4.58	0.30	27.4	9.12	163	0.00	976	0.00		
0.0244	0.00	0.146	0.00	0.872	0.00	5.21	0.29	31.1	10.47	186	0.00	1110	0.00		
0.0278	0.00	0.166	0.00	0.991	0.00	5.92	0.26	35.3	11.24	211	0.00	1260	0.00		
0.0315	0.00	0.188	0.00	1.13	0.00	6.72	0.21	40.1	11.26	240	0.00	1430	0.00		
0.0358	0.00	0.214	0.00	1.28	0.00	7.64	0.15	45.6	10.45	272	0.00	1630	0.00		
0.0407	0.00	0.243	0.00	1.45	0.00	8.68	0.13	51.8	8.90	310	0.00	1850	0.00		
0.0463	0.00	0.276	0.00	1.65	0.00	9.86	0.18	58.9	6.82	352	0.00	2100	0.00		
0.0526	0.00	0.314	0.00	1.88	0.04	11.2	0.37	66.9	4.56	400	0.00	2390	0.00		

Figure A.1: PSD of raw AA2024.

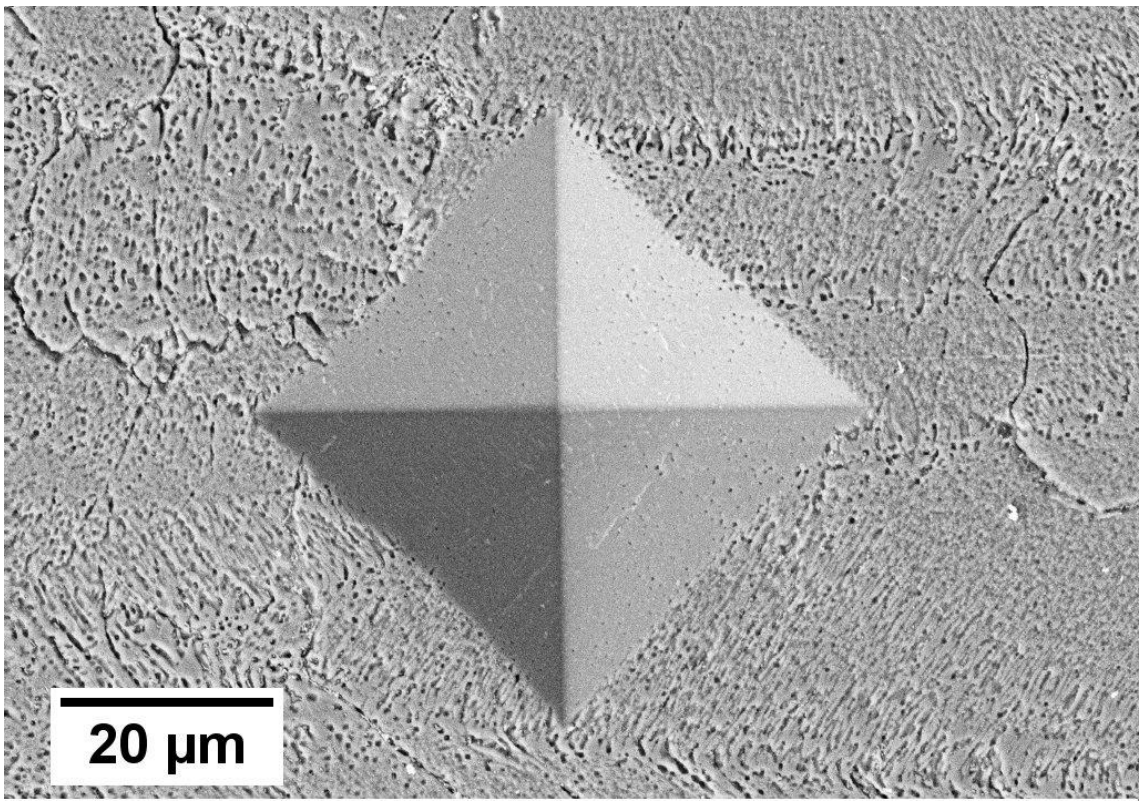

Figure A.2: SEM images showing microhardness indentation tool trace on specimen.

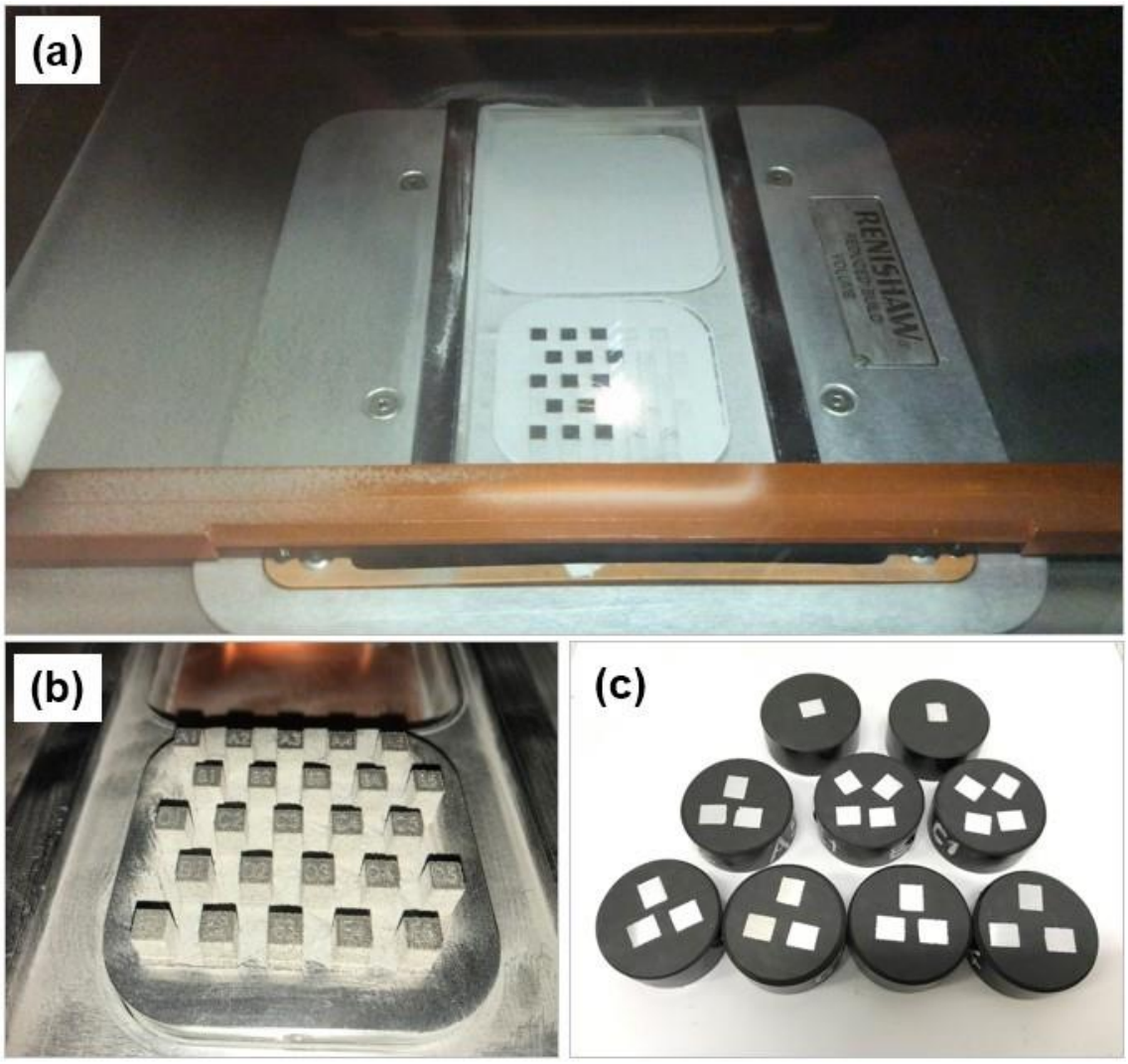

Figure A.3: LPBF process of cubic specimens for raw alloy (a) during and (b) after fabrication, and (c) samples in sample holders

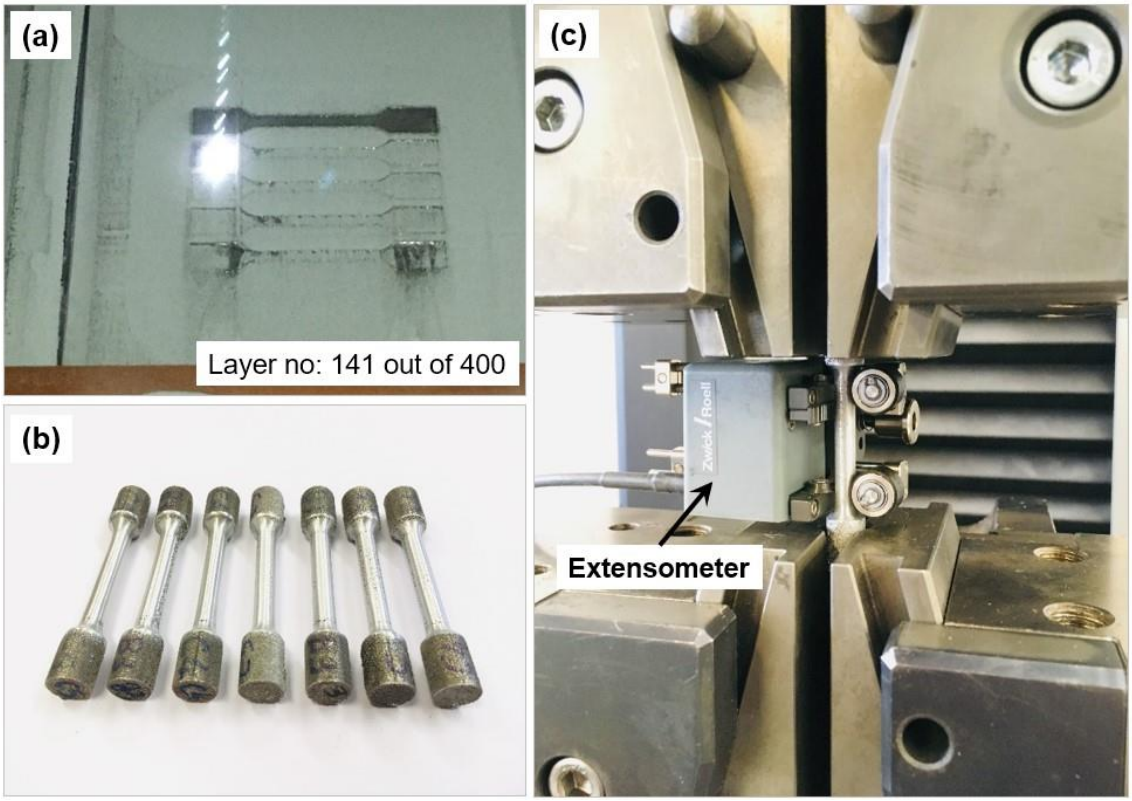

Figure A.4: LPBF process of tensile specimens (a) during and (b) after fabrication, and tensile test process.

Apendix B

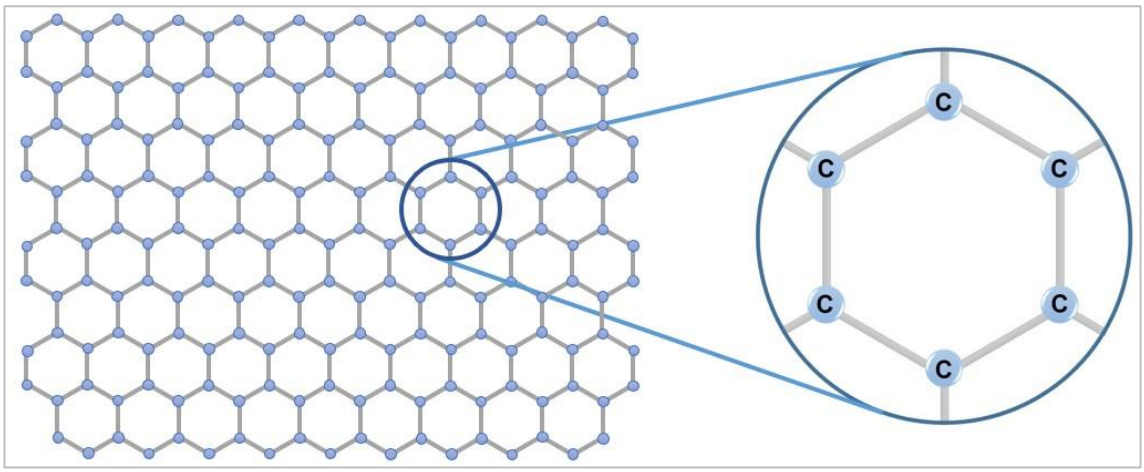

Figure B.1: Schematic of atomic structure of Gr.

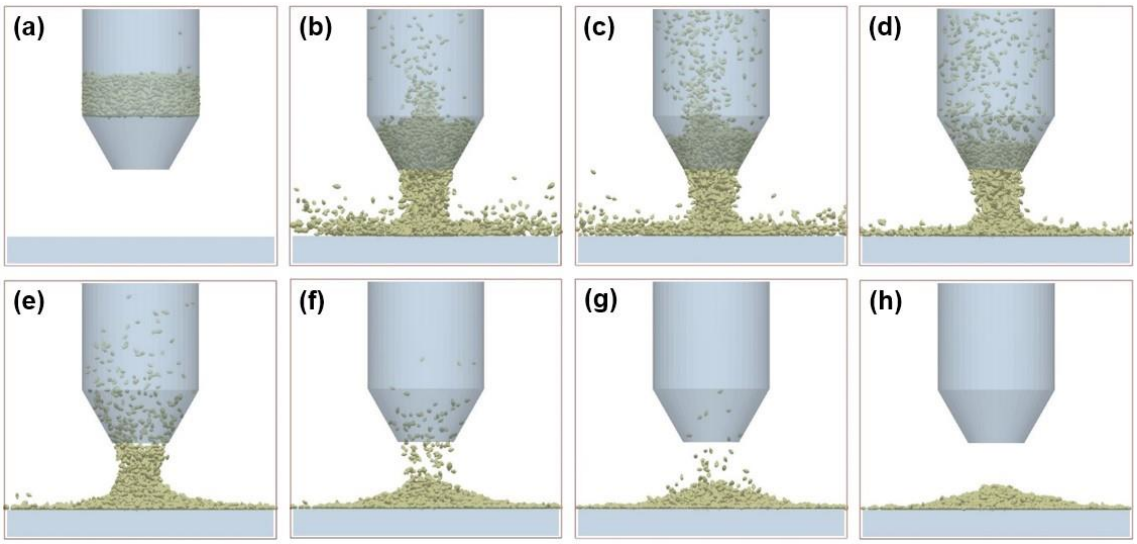

Figure B.2: Powder flow process of the DEM from (a) to (h).

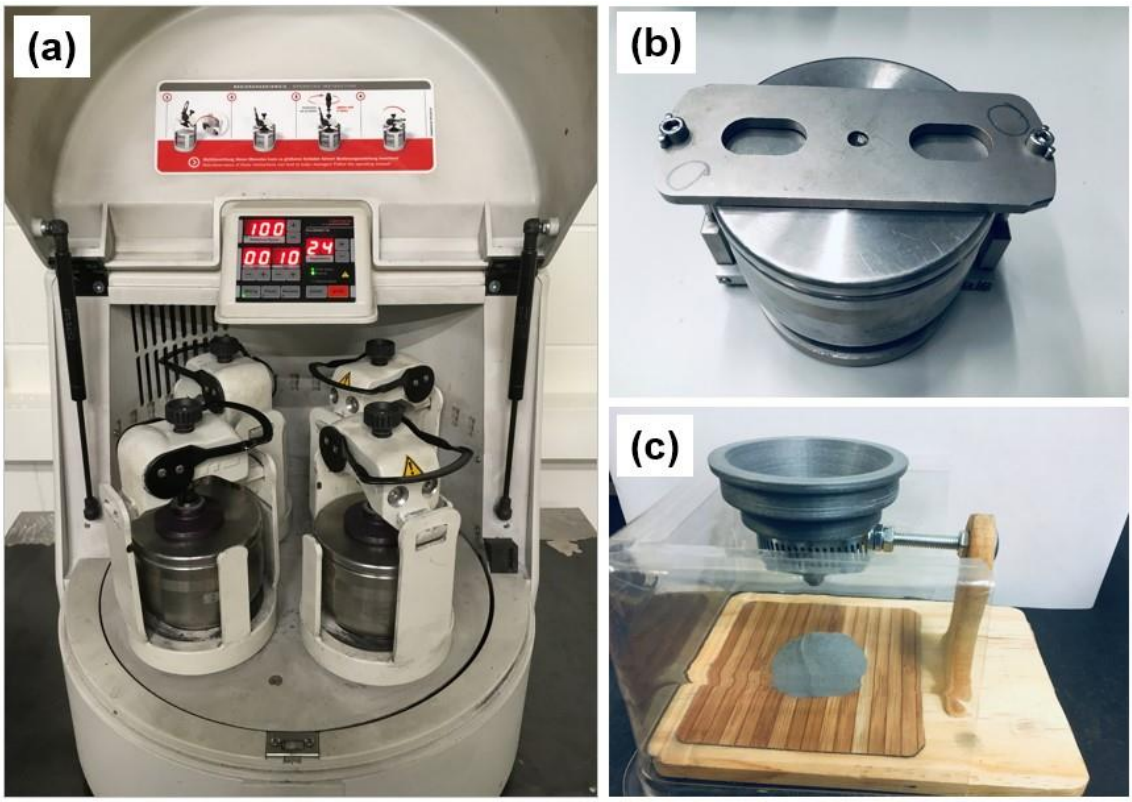

Figure B.3: Powder preparation process showing (a) the milling speed, circle and period time of the ball milling machine, (b) milling bowls with safety clamp, and (c) flowability test kit.

Apendix C

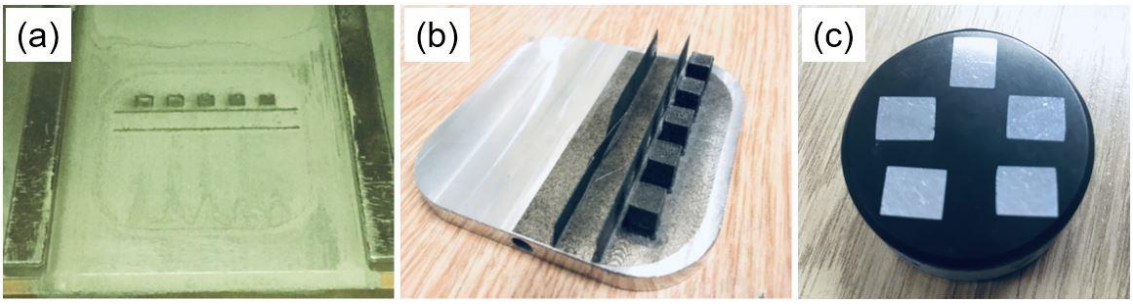

Figure C.1: LPBF process of cubic specimens for GNPs/AA2024 (a) during and (b) after fabrication, and (c) samples in sample holders

References

Abdel-Aziem, W. et al. 2022. On the current research progress of metallic materials fabricated by laser powder bed fusion process: A review. *Journal of Materials Research and Technology* . Available at: https://linkinghub.elsevier.com/retrieve/pii/S2238785422011243.

Aboulkhair, N.T. et al. 2019. 3D printing of aluminium alloys: Additive manufacturing of aluminium alloys using selective laser melting. *Progress in Materials Science* 106(July), p. 100578. doi: 10.1016/j.pmatsci.2019.100578.

Ahamed, H. and Senthilkumar, V. 2010. Role of nano-size reinforcement and milling on the synthesis of nano-crystalline aluminium alloy composites by mechanical alloying. *Journal of Alloys and Compounds* 505(2), pp. 772–782. doi: 10.1016/j.jallcom.2010.06.139.

Ahmad, S.I. et al. 2020. Graphene-reinforced bulk metal matrix composites: Synthesis, microstructure, and properties. *Reviews on Advanced Materials Science* 59(1), pp. 67–114. doi: 10.1515/rams-2020-0007.

Amidon, G.E. et al. 2017. Particle, powder, and compact characterization. In: *Developing Solid Oral Dosage Forms*. Elsevier, pp. 271–293. doi: 10.1016/B978-0-12-802447-8.00010-8.

Anthony Xavior, M. et al. 2018. Tribological studies on AA2024-graphene/CNT nanocomposites processed through powder metallurgy. *Materials Today: Proceedings* 5(2), pp. 6588–6596. doi: 10.1016/j.matpr.2017.11.314.

Anwar, A. Bin and Pham, Q.C. 2017. Selective laser melting of AlSi10Mg: Effects of scan direction, part placement and inert gas flow velocity on tensile strength. *Journal of Materials Processing Technology* 240, pp. 388–396. doi: 10.1016/j.jmatprotec.2016.10.015.

Ascari, A. et al. 2012. The influence of process parameters on porosity formation in hybrid LASER-GMA welding of AA6082 aluminum alloy. *Optics & Laser Technology* 44(5), pp. 1485–1490. doi: 10.1016/j.optlastec.2011.12.014.

Azar, M.H. et al. 2019. Investigating the microstructure and mechanical properties of aluminum-matrix reinforced- graphene nanosheet composites fabricated by mechanical milling and equal-channel angular pressing. *Nanomaterials* 9(8), pp. 1–17. doi: 10.3390/nano9081070.

Bai, P. et al. 2019. Microstructure and tribological behavior of graphene/Al composites produced by selective laser melting. *Materials Research Express* 6(10). doi: 10.1088/2053-1591/ab3ef5.

Baláž, P. 2008. Mechanochemistry in minerals engineering. In: *Mechanochemistry in Nanoscience and Minerals Engineering*. Berlin, Heidelberg: Springer Berlin Heidelberg, pp. 257–296. doi: 10.1007/978-3-540-74855-7_5.

Banhart, F. et al. 2011. Structural defects in graphene. *ACS Nano* 5(1), pp. 26–41. doi: 10.1021/nn102598m.

Barrios, G.K.P. et al. 2013. Contact parameter estimation for DEM simulation of iron ore pellet handling. *Powder Technology* 248, pp. 84–93. doi: 10.1016/j.powtec.2013.01.063.

Bartolucci, S.F. et al. 2011. Graphene-aluminum nanocomposites. *Materials Science and Engineering A* 528(27), pp. 7933–7937. doi: 10.1016/j.msea.2011.07.043.

Beakawi Al-Hashemi, H.M. and Baghabra Al-Amoudi, O.S. 2018. A review on the angle of repose of granular materials. *Powder Technology* 330, pp. 397–417. doi: 10.1016/j.powtec.2018.02.003.

Benjamin, J.S. 1976. Mechanical alloying. *Scientific American* 234(5), pp. 40–

49.

Bera, S. et al. 2013. Mechanical properties of Al7075 alloy with nano-ceramic oxide dispersion synthesized by mechanical milling and consolidated by equal channel angular pressing. *Journal of Alloys and Compounds* 548, pp. 257–265. doi: 10.1016/j.jallcom.2012.09.007.

Biffi, C.A. et al. 2018. Continuous wave vs pulsed wave laser emission in selective laser melting of AlSi10Mg parts with industrial optimized process parameters: Microstructure and mechanical behaviour. *Additive Manufacturing* 24, pp. 639–646. doi: 10.1016/j.addma.2018.10.021.

Boland, M.J. et al. 2018. Graphene used as a lateral force microscopy calibration material in the low-load non-linear regime. *Review of Scientific Instruments* 89(11), p. 113902. doi: 10.1063/1.5044727.

Brandl, E. et al. 2012. Additive manufactured AlSi10Mg samples using selective laser melting (SLM): Microstructure, high cycle fatigue, and fracture behavior. *Materials & Design* 34, pp. 159–169. doi: 10.1016/j.matdes.2011.07.067.

Brock, H. 2001. *Aluminium industry vision sustainable solutions*. Washington D.C.

Broitman, E. 2017. Indentation hardness measurements at macro-, micro-, and nanoscale: A critical overview. *Tribology letters* 65(1), pp. 1–18. doi: 10.1007/s11249-016-0805-5.

Cabeza, M. et al. 2017. Effect of high energy ball milling on the morphology, microstructure and properties of nano-sized TiC particle-reinforced 6005A aluminium alloy matrix composite. *Powder Technology* 321, pp. 31–43. doi: 10.1016/j.powtec.2017.07.089.

Cao, X. et al. 2003. Research and progress in laser welding of wrought aluminum alloys. II. metallurgical microstructures, defects, and mechanical

properties. *Materials and Manufacturing Processes* 18(1), pp. 23–49. doi: 10.1081/AMP-120017587.

Caprio, L. et al. 2019. Influence of pulsed and continuous wave emission on melting efficiency in selective laser melting. *Journal of Materials Processing Technology* 266, pp. 429–441. doi: 10.1016/j.jmatprotec.2018.11.019.

Ch, S.R. et al. 2019. Influence of working environment and built orientation on the tensile properties of selective laser melted AlSi10Mg alloy. *Materials Science and Engineering A* 750(October 2018), pp. 141–151. doi: 10.1016/j.msea.2019.01.103.

Chen, F. et al. 2018. Graphene-reinforced aluminum matrix composites: A review of synthesis methods and properties. *Jom* 70(6), pp. 837–845. doi: 10.1007/s11837-018-2810-7.

Chen, H. et al. 2017. Flow behavior of powder particles in layering process of selective laser melting: Numerical modeling and experimental verification based on discrete element method. *International Journal of Machine Tools and Manufacture* 123(July), pp. 146–159. doi: 10.1016/j.ijmachtools.2017.08.004.

Chen, L.-Y. et al. 2012. Novel nanoprocessing route for bulk graphene nanoplatelets reinforced metal matrix nanocomposites. *Scripta Materialia* 67(1), pp. 29–32. doi: 10.1016/j.scriptamat.2012.03.013.

Chen, L. et al. 2021. Enhanced mechanical properties and thermal conductivity for GNPs/Al2024 composites with in situ SiC nanorods. *Metals and Materials International* 27(10), pp. 4263–4270. doi: 10.1007/s12540-020-00803-9.

Chu, K. and Jia, C. 2014. Enhanced strength in bulk graphene-copper composites. *physica status solidi (a)* 211(1), pp. 184–190. doi: 10.1002/pssa.201330051.

Coetzee, C.J. 2019. Particle upscaling: Calibration and validation of the discrete

element method. *Powder Technology* 344, pp. 487–503. doi: 10.1016/j.powtec.2018.12.022.

Collur, M.M. et al. 1987. Mechanism of alloying element vaporization during laser welding. *Metallurgical Transactions B* 18(4), pp. 733–740. doi: 10.1007/BF02672891.

Cree, D. and Pugh, M. 2010. Production and characterization of a three-dimensional cellular metal-filled ceramic composite. *Journal of Materials Processing Technology* 210(14), pp. 1905–1917. doi: 10.1016/j.jmatprotec.2010.07.002.

Crowell, N. and Shivkumar, S. 1995. Solution treatment effects in cast Al–Si–Cu alloys. *AFS Trans* 107, pp. 721–726.

Cullity, B.D. 2001. Elements of X-ray Diffraction. Third. Prentice Hall, London

Dadbakhsh, S. et al. 2019. Selective laser melting to manufacture “in situ” metal matrix composites: A review. *Advanced Engineering Materials* 21(3), pp. 1–18. doi: 10.1002/adem.201801244.

Davis, J.R. 2001. *Aluminum and aluminum alloys*. Ohio: ASM International. doi: 10.1361/autb2001p351.

Demir, A.G. et al. 2017. From pulsed to continuous wave emission in SLM with contemporary fiber laser sources: effect of temporal and spatial pulse overlap in part quality. *The International Journal of Advanced Manufacturing Technology* 91(5–8), pp. 2701–2714. Available at: http://link.springer.com/10.1007/s00170-016-9948-7.

Dorri Moghadam, A. et al. 2015. Mechanical and tribological properties of self-lubricating metal matrix nanocomposites reinforced by carbon nanotubes (CNTs) and graphene - A review. *Composites Part B: Engineering* 77, pp. 402–420. doi: 10.1016/j.compositesb.2015.03.014.

Du, L. et al. 2021. Influence of processing parameters of selective laser melting on high-cycle and very-high-cycle fatigue behaviour of Ti-6Al-4V. *Fatigue & Fracture of Engineering Materials & Structures* 44(1), pp. 240–256. doi: 10.1111/ffe.13361.

Dutkiewicz, J. et al. 2015. Microstructure and properties of bulk copper matrix composites strengthened with various kinds of graphene nanoplatelets. *Materials Science and Engineering: A* 628, pp. 124–134. doi: 10.1016/j.msea.2015.01.018.

Dutt, A.K. et al. 2022. Optimization of selective laser melting (SLM) additive manufacturing process parameters of 316L austenitic stainless steel. *Transactions of the Indian Institute of Metals* . doi: 10.1007/s12666-022-02687-2.

Eldesouky, A. et al. 2014. Effect of grain size reduction of AA2124 aluminum alloy powder compacted by spark plasma sintering. *Journal of Alloys and Compounds* 609, pp. 215–221. doi: 10.1016/j.jallcom.2014.04.136.

Emery, E. et al. 2009. Flowability of moist pharmaceutical powders. *Powder Technology* 189(3), pp. 409–415. doi: 10.1016/j.powtec.2008.06.017.

Esawi, A.M.K. et al. 2009. Fabrication and properties of dispersed carbon nanotube–aluminum composites. *Materials Science and Engineering: A* 508(1–2), pp. 167–173. doi: 10.1016/j.msea.2009.01.002.

Etsion, I. and Amit, M. 1993. The effect of small normal loads on the static friction coefficient for very smooth surfaces. *Journal of Tribology* 115(3), pp. 406–411. doi: 10.1115/1.2921651.

Fathy, A. et al. 2014. Effect of mechanical milling on the morphology and structural evaluation of Al-Al2O3 nanocomposite powders. *International Journal of Engineering, Transactions A: Basics* 27(4), pp. 625–632. doi:

10.5829/idosi.ije.2014.27.04a.14.

Fiocchi, J. et al. 2021. Heat treatment of aluminium alloys produced by laser powder bed fusion: A review. *Materials & Design* 204, p. 109651. doi: 10.1016/j.matdes.2021.109651.

Fogagnolo, J.. et al. 2003. Effect of mechanical alloying on the morphology, microstructure and properties of aluminium matrix composite powders. *Materials Science and Engineering: A* 342(1–2), pp. 131–143. doi: 10.1016/S0921-5093(02)00246-0.

Galy, C. et al. 2018. Main defects observed in aluminum alloy parts produced by SLM: From causes to consequences. *Additive Manufacturing* 22(February), pp. 165–175. doi: 10.1016/j.addma.2018.05.005.

Gariépy, A. et al. 2011. Shot peening and peen forming finite element modelling-towards a quantitative method. *International Journal of Solids and Structures* 48(20), pp. 2859–2877. doi: 10.1016/j.ijsolstr.2011.06.003.

Geim, A.K. and Novoselov, K.S. 2007. The rise of graphene. *Nature Materials* 6(3), pp. 183–191. doi: 10.1038/nmat1849.

Giannakopoulos, A.E. and Suresh, S. 1999. Determination of elastoplastic properties by instrumented sharp indentation. *Scripta Materialia* 40(10), pp. 1191–1198. doi: 10.1016/S1359-6462(99)00011-1.

Girisha and Sharma 2012. Effect of magnesium on strength and microstructure of aluminium copper magnesium alloy. *International Journal of Scientific & Engineering Research* 3(2), pp. 3–6.

Gotor, F.J. et al. 2013. Influence of the milling parameters on the mechanical work intensity in planetary mills. *Powder Technology* 233, pp. 1–7. doi: 10.1016/j.powtec.2012.08.031.

Govindaraj, P. et al. 2019. A review on graphene polymer nanocomposites in

harsh operating conditions. *Industrial and Engineering Chemistry Research* 58(37), pp. 17106–17129. doi: 10.1021/acs.iecr.9b01183.

Goyal, A. et al. 2015. Development and physico-chemical characterization of microencapsulated flaxseed oil powder: A functional ingredient for omega-3 fortification. *Powder Technology* 286, pp. 527–537. doi: 10.1016/j.powtec.2015.08.050.

Gu, D. et al. 2015. Selective laser melting additive manufacturing of novel aluminum based composites with multiple reinforcing phases. *Journal of Manufacturing Science and Engineering, Transactions of the ASME* 137(2), pp. 1–11. doi: 10.1115/1.4028925.

Gu, D.D. et al. 2012. Laser additive manufacturing of metallic components: Materials, processes and mechanisms. *International Materials Reviews* 57(3), pp. 133–164. doi: 10.1179/1743280411Y.0000000014.

Gu, J. et al. 2018. Design and cracking susceptibility of additively manufactured Al-Cu-Mg alloys with tandem wires and pulsed arc. *Journal of Materials Processing Technology* 262(June), pp. 210–220. doi: 10.1016/j.jmatprotec.2018.06.030.

Güler, Ö. and Bağcı, N. 2020. A short review on mechanical properties of graphene reinforced metal matrix composites. *Journal of Materials Research and Technology* 9(3), pp. 6808–6833. doi: 10.1016/j.jmrt.2020.01.077.

Gupta, R.K. et al. 2017. High-energy ball milling parameters in production of nanocrystalline Al alloys., pp. 7–28. doi: 10.1007/978-3-319-57031-0_2.

Gusev, V.G. et al. 2019. Simulation of the energy–force parameters of planetary ball mill processing and estimation of their influence on the particle size in an AMg2 alloy/graphite composite powder. *Russian Metallurgy (Metally)* 2019(1), pp. 24–30. doi: 10.1134/S0036029519010063.

Haeri, S. 2017. Optimisation of blade type spreaders for powder bed preparation in additive manufacturing using DEM simulations. *Powder Technology* 321, pp. 94–104. doi: 10.1016/j.powtec.2017.08.011.

Han, Q. et al. 2016. Synthesis and characterisation of advanced ball-milled Al-Al2O3 nanocomposites for selective laser melting. *Powder Technology* 297, pp. 183–192. doi: 10.1016/j.powtec.2016.04.015.

Han, Q. et al. 2017a. Characterisation and milling time optimisation of nanocrystalline aluminium powder for selective laser melting. *International Journal of Advanced Manufacturing Technology* 88(5–8), pp. 1429–1438. doi: 10.1007/s00170-016-8866-z.

Han, Q. et al. 2017b. Macro and nanoscale wear behaviour of Al-Al2O3 nanocomposites fabricated by selective laser melting. *Composites Part B: Engineering* 127, pp. 26–35. doi: 10.1016/j.compositesb.2017.06.026.

Han, Q. et al. 2017c. Selective laser melting of advanced Al-Al2O3 nanocomposites: Simulation, microstructure and mechanical properties. *Materials Science and Engineering A* 698(May), pp. 162–173. doi: 10.1016/j.msea.2017.05.061.

Han, Q. et al. 2018a. Laser powder bed fusion of Hastelloy X: Effects of hot isostatic pressing and the hot cracking mechanism. *Materials Science and Engineering A* 732(July), pp. 228–239. doi: 10.1016/j.msea.2018.07.008.

Han, Q. et al. 2018b. Manufacturability of AlSi10Mg overhang structures fabricated by laser powder bed fusion. *Materials and Design* 160, pp. 1080–1095. doi: 10.1016/j.matdes.2018.10.043.

Han, Q. et al. 2019. Discrete element simulation of powder layer thickness in laser additive manufacturing. *Powder Technology* 352, pp. 91–102. doi: 10.1016/j.powtec.2019.04.057.

Han, Q. and Jiao, Y. 2019. Effect of heat treatment and laser surface remelting on AlSi10Mg alloy fabricated by selective laser melting. *International Journal of Advanced Manufacturing Technology* 102(9–12), pp. 3315–3324. doi: 10.1007/s00170-018-03272-y.

Hanzl, P. et al. 2015. The influence of processing parameters on the mechanical properties of SLM parts. *Procedia Engineering* 100(January), pp. 1405–1413. doi: 10.1016/j.proeng.2015.01.510.

Hassanpour, A. et al. 2011. Analysis of particle motion in a paddle mixer using discrete element method (DEM). *Powder Technology* 206(1–2), pp. 189–194. doi: 10.1016/j.powtec.2010.07.025.

He, L. et al. 2014. Microstructure and wear properties of Al2O3-CeO2/Ni-base alloy composite coatings on aluminum alloys by plasma spray. *Applied Surface Science* 314(2), pp. 760–767. doi: 10.1016/j.apsusc.2014.07.047.

Hu, Z. et al. 2016a. Laser sintered graphene nickel nanocomposites. *Journal of Materials Processing Technology* 231, pp. 143–150. doi: 10.1016/j.jmatprotec.2015.12.022.

Hu, Z. et al. 2016b. Laser sintered single layer graphene oxide reinforced titanium matrix nanocomposites. *Composites Part B: Engineering* 93, pp. 352–359. doi: 10.1016/j.compositesb.2016.03.043.

Hu, Z. et al. 2018. 3D printing graphene-aluminum nanocomposites. *Journal of Alloys and Compounds* 746, pp. 269–276. doi: 10.1016/j.jallcom.2018.02.272.

Hu, Z. et al. 2019. Microstructure, mechanical properties and strengthening mechanisms of AlCu5MnCdVA aluminum alloy fabricated by selective laser melting. *Materials Science and Engineering A* 759(May), pp. 154–166. doi: 10.1016/j.msea.2019.04.114.

Huang, C. yang et al. 2019. Influence of rolling temperature on the interfaces

and mechanical performance of graphene-reinforced aluminum-matrix composites. *International Journal of Minerals, Metallurgy and Materials* 26(6), pp. 752–759. doi: 10.1007/s12613-019-1780-2.

Ion, J.C. et al. 1992. Diagrams for laser materials processing. *Acta Metallurgica et Materialia* 40(7), pp. 1539–1551. doi: 10.1016/0956-7151(92)90097-X.

Ion, J.C. 2005. *Laser processing of engineering materials: Principles, procedure and industrial application*. United Kingdom: El Sevier.

Jiang, J. et al. 2018. Support structures for additive manufacturing: A review. *Journal of Manufacturing and Materials Processing* 2(4), p. 64. doi: 10.3390/jmmp2040064.

Jiang, J. and Ma, Y. 2020. Path planning strategies to optimize accuracy, quality, build time and material use in additive manufacturing: A review. *Micromachines* 11(7). doi: 10.3390/MI11070633.

Jung, H.J. et al. 2015. Physicochemical properties of ball milled boron particles: Dry vs. wet ball milling process. *Powder Technology* 269, pp. 548–553. doi: 10.1016/j.powtec.2014.03.058.

Kaleem, M.A. et al. 2020. An experimental investigation on accuracy of Hausner Ratio and Carr Index of powders in additive manufacturing processes. *Metal Powder Report* xxx(xx), pp. 1–5. doi: 10.1016/j.mprp.2020.06.061.

Kalpakjian, S. et al. 2014. *Manufacturing engineering and technology*. Seventh ed. Singapore: Pearson Education South Asia Pte Ltd.

Karg, M. et al. 2014. Processability of high strength aluminium-copper alloys AW-2022 and 2024 by laser beam melting in powder bed. *25th Annual International Solid Freeform Fabrication Symposium; An Additive Manufacturing Conference, SFF 2014* , pp. 420–436. doi: http://dx.doi.org/10.26153/tsw/15696.

Khodir, S.A. and Shibayanagi, T. 2007. Microstructure and mechanical

properties of friction stir welded dissimilar aluminum joints of AA2024-T3 and AA7075-T6. *Materials Transactions* 48(7), pp. 1928–1937. doi: 10.2320/matertrans.MRA2007042.

Kim, J. et al. 2018. A review: Melt pool analysis for selective laser melting with continuous wave and pulse width modulated lasers. *Applied Science and Convergence Technology* 27(6), pp. 113–119. doi: 10.5757/ASCT.2018.27.6.113.

Kim, W.J. et al. 2014. Multi-layer graphene/copper composites: Preparation using high-ratio differential speed rolling, microstructure and mechanical properties. *Carbon* 69, pp. 55–65. doi: 10.1016/j.carbon.2013.11.058.

Kimura, T. and Nakamoto, T. 2016. Microstructures and mechanical properties of A356 (AlSi7Mg0.3) aluminum alloy fabricated by selective laser melting. *Materials and Design* 89, pp. 1294–1301. doi: 10.1016/j.matdes.2015.10.065.

Kotadia, H.R. et al. 2021. A review of laser powder bed fusion additive manufacturing of aluminium alloys: Microstructure and properties. *Additive Manufacturing* 46, p. 102155. Available at: https://linkinghub.elsevier.com/retrieve/pii/S2214860421003195.

Koutny, D. et al. 2018. Influence of scanning strategies on processing of aluminum alloy EN AW 2618 using selective laser melting. *Materials* 11(2). doi: 10.3390/ma11020298.

Kumar, N.M. et al. 2022. A critical review on heat treatment of aluminium alloys. *Materials Today: Proceedings* 58, pp. 71–79. doi: 10.1016/j.matpr.2021.12.586.

Kumar, P.S. et al. 2021. Significance of continuous wave and pulsed wave laser in direct metal deposition. *Materials Today: Proceedings* 46, pp. 8086–8096. doi: 10.1016/j.matpr.2021.03.041.

Kumar, S. 2014. *Selective laser sintering/melting*. Elsevier. doi: 10.1016/B978-

0-08-096532-1.01003-7.

Kumar, V. et al. 2015. Effect of silicon content on the mechanical properties of aluminum alloy. *International Research Journal of Engineering and Technology* 2(4), pp. 1326–1330.

Larimian, T. et al. 2020. Effect of energy density and scanning strategy on densification, microstructure and mechanical properties of 316L stainless steel processed via selective laser melting. *Materials Science and Engineering A* 770(September 2019), p. 138455. doi: 10.1016/j.msea.2019.138455.

Lathabai, S. 2018. Additive manufacturing of aluminium-based alloys and composites. In: *Fundamentals of Aluminium Metallurgy*. Elsevier, pp. 47–92. doi: 10.1016/b978-0-08-102063-0.00002-3.

Lava Kumar, P. et al. 2022. Recent advances in aluminium matrix composites reinforced with graphene-based nanomaterial: A critical review. *Progress in Materials Science* 128, p. 100948. doi: 10.1016/j.pmatsci.2022.100948.

Lee, W.H. et al. 2017. Discrete element modeling of powder flow and laser heating in direct metal laser sintering process. *Powder Technology* 315, pp. 300–308. doi: 10.1016/j.powtec.2017.04.002.

Lei, Z. et al. 2019. Effect of energy density on formability, microstructure and micro-hardness of selective laser melted Sc- and Zr- modified 7075 aluminum alloy. *Powder Technology* 356, pp. 594–606. doi: 10.1016/j.powtec.2019.08.082.

Li, G. et al. 2022. Investigation into the effect of energy density on densification, surface roughness and loss of alloying elements of 7075 aluminium alloy processed by laser powder bed fusion. *Optics & Laser Technology* 147, p. 107621. doi: 10.1016/j.optlastec.2021.107621.

Li, J.L. et al. 2015a. Microstructure and tensile properties of bulk nanostructured

aluminum/graphene composites prepared via cryomilling. *Materials Science and Engineering A* 626, pp. 400–405. doi: 10.1016/j.msea.2014.12.102.

Li, M. et al. 2014. Highly enhanced mechanical properties in Cu matrix composites reinforced with graphene decorated metallic nanoparticles. *Journal of Materials Science* 49(10), pp. 3725–3731. doi: 10.1007/s10853-014-8082-x.

Li, Z. et al. 2015b. Synergistic strengthening effect of graphene-carbon nanotube hybrid structure in aluminum matrix composites. *Carbon* 95, pp. 419–427. doi: 10.1016/j.carbon.2015.08.014.

Lin, K. et al. 2021. Selective laser melting of graphene reinforced titanium matrix composites: Powder preparation and its formability. *Advanced Powder Technology* 32(5), pp. 1426–1437. doi: 10.1016/j.apt.2021.03.003.

Liu, R. et al. 2006. Solidification crack susceptibility of aluminum alloy weld metals. *Transactions of Nonferrous Metals Society of China* 16(1), pp. 110–116. doi: 10.1016/S1003-6326(06)60019-8.

Liu, X. et al. 2019. CNT-reinforced AlSi10Mg composite by selective laser melting: microstructural and mechanical properties. *Materials Science and Technology (United Kingdom)* 35(9), pp. 1038–1045. doi: 10.1080/02670836.2019.1603899.

Louvis, E. et al. 2011. Selective laser melting of aluminium components. *Journal of Materials Processing Technology* 211(2), pp. 275–284. doi: 10.1016/j.jmatprotec.2010.09.019.

Lupo, M. et al. 2021. Calibration of DEM for cohesive particles in the SLS powder spreading process. *Processes* 9(10), p. 1715. doi: 10.3390/pr9101715.

Maamoun, A.H. et al. 2018. The effect of selective laser melting process parameters on the microstructure and mechanical properties of Al6061 and AlSi10Mg alloys. *Materials* 12(1). doi: 10.3390/ma12010012.

Mahamood, R.M. et al. 2013. Characterizing the effect of laser power density on microstructure, microhardness, and surface finish of laser deposited titanium alloy. *Journal of Manufacturing Science and Engineering, Transactions of the ASME* 135(6), pp. 1–4. doi: 10.1115/1.4025737.

Majimel, J. et al. 2004. High-resolution transmission electron microscopy and tomographic atom probe studies of the hardening precipitation in an Al–Cu–Mg alloy. *Philosophical Magazine* 84(30), pp. 3263–3280. doi: 10.1080/14786430412331283983.

Malekipour, E. and El-Mounayri, H. 2018. Common defects and contributing parameters in powder bed fusion AM process and their classification for online monitoring and control: a review. *International Journal of Advanced Manufacturing Technology* 95(1–4), pp. 527–550. doi: 10.1007/s00170-017-1172-6.

Mandal, A. et al. 2020. Microstructural and mechanical properties evaluation of graphene reinforced stainless steel composite produced via selective laser melting. *Materials Science and Engineering A* 774(May 2019), p. 138936. doi: 10.1016/j.msea.2020.138936.

Mathers, G. 2002. *The welding of aluminium and its alloys*. First. Cambridge: Woodhead Publishing.

Meier, C. et al. 2019. Modeling and characterization of cohesion in fine metal powders with a focus on additive manufacturing process simulations. *Powder Technology* 343, pp. 855–866. doi: 10.1016/j.powtec.2018.11.072.

Mirzaei, M. et al. 2015. Microstructure and mechanical properties relation in cold rolled Al 2024 alloy determined by X-ray line profile analysis. *Materials Science and Engineering: A* 620, pp. 44–49. doi: 10.1016/j.msea.2014.09.110.

Modi, Y.K. and Sahu, K.K. 2021. Process parameter optimization for porosity

and compressive strength of calcium sulfate based 3D printed porous bone scaffolds. *Rapid Prototyping Journal* 27(2), pp. 245–255. doi: 10.1108/RPJ-04-2020-0083.

Moustafa, M.A. et al. 2003. Effect of solution heat treatment and additives on the microstructure of Al-Si (A413.1) automotive alloys. *Journal of Materials Science* 38, pp. 4507–4522.

Mukhopadhyay, N.K. et al. 2001. An analysis of microhardness of single-quasicrystals in the Al-CU-Co-Si system. *Materials Science and Engineering A* 315(1–2), pp. 202–210. doi: 10.1016/S0921-5093(01)01186-8.

Nafsin, N. and Rashed, H.M.M.A. 2013. Effects of copper and magnesium on microstructure and hardness of Al-Cu-Mg alloys. *International Journal of Engineering and Advanced Technology* 2(5), pp. 533–536.

Naik H R, M. et al. 2021. Effect of microstructure, mechanical and wear on Al-CNTs/graphene hybrid MMC'S. *Advances in Materials and Processing Technologies* 00(00), pp. 1–14. doi: 10.1080/2374068X.2021.1927646.

Nan, W. and Ghadiri, M. 2019. Numerical simulation of powder flow during spreading in additive manufacturing. *Powder Technology* 342, pp. 801–807. doi: 10.1016/j.powtec.2018.10.056.

Narasimharaju, S.R. et al. 2022. A comprehensive review on laser powder bed fusion of steels: Processing, microstructure, defects and control methods, mechanical properties, current challenges and future trends. *Journal of Manufacturing Processes* 75, pp. 375–414. doi: 10.1016/j.jmapro.2021.12.033.

Ngo, T.D. et al. 2018. Additive manufacturing (3D printing): A review of materials, methods, applications and challenges. *Composites Part B: Engineering* 143, pp. 172–196. doi: 10.1016/j.compositesb.2018.02.012.

Nguyen, Q.B. et al. 2018. The role of powder layer thickness on the quality of

SLM printed parts. *Archives of Civil and Mechanical Engineering* 18(3), pp. 948–955. doi: 10.1016/j.acme.2018.01.015.

Nieto, A. et al. 2017. Graphene reinforced metal and ceramic matrix composites: a review. *International Materials Reviews* 62(5), pp. 241–302. doi: 10.1080/09506608.2016.1219481.

Niu, X. et al. 2019. Review of materials used in laser-aided additive manufacturing processes to produce metallic products. *Frontiers of Mechanical Engineering* 14(3), pp. 282–298. doi: 10.1007/s11465-019-0526-1.

Nouri, A. et al. 2010. Effect of process control agent on the porous structure and mechanical properties of a biomedical Ti–Sn–Nb alloy produced by powder metallurgy. *Acta Biomaterialia* 6(4), pp. 1630–1639. doi: 10.1016/j.actbio.2009.10.005.

Olakanmi, E.O. 2013. Selective laser sintering/melting (SLS/SLM) of pure Al, Al-Mg, and Al-Si powders: Effect of processing conditions and powder properties. *Journal of Materials Processing Technology* 213(8), pp. 1387–1405. doi: 10.1016/j.jmatprotec.2013.03.009.

Olakanmi, E.O. et al. 2015. A review on selective laser sintering/melting (SLS/SLM) of aluminium alloy powders: Processing, microstructure, and properties. *Progress in Materials Science* 74, pp. 401–477. doi: 10.1016/j.pmatsci.2015.03.002.

Pastor, M. et al. 1999. Porosity, underfill and magnesium loss during continuous wave Nd:YAG laser welding of thin plates of aluminum alloys 5182 and 5754. *Welding Journal* 78(6), pp. 207–216.

Patel, S. and Vlasea, M. 2020. Melting modes in laser powder bed fusion. *Materialia* 9, p. 100591. doi: 10.1016/j.mtla.2020.100591.

Pekok, M. et al. 2021. Effect of milling speed and time on graphene-reinforced

AA2024 powder. In: *Smart Innovation, Systems and Technologies*., pp. 215–225. doi: 10.1007/978-981-15-8131-1_20.

Pekok, M.A. et al. 2020. Effect of process parameters on the microstructure and mechanical properties of AA2024 fabricated using selective laser melting. *International Journal of Advanced Manufacturing Technology* . doi: 10.1007/s00170-020-06346-y.

Pérez-Bustamante, R. et al. 2015. Microstructural and hardness behavior of graphene-nanoplatelets/aluminum composites synthesized by mechanical alloying. *Journal of Alloys and Compounds* 615(S1), pp. S578–S582. doi: 10.1016/j.jallcom.2014.01.225.

Pourmand, N.S. and Asgharzadeh, H. 2020. Aluminum matrix composites reinforced with graphene: A review on production, microstructure, and properties. *Critical Reviews in Solid State and Materials Sciences* 45(4), pp. 289–337. doi: 10.1080/10408436.2019.1632792.

Prasad, N.E. and Wanhill, R.J.H. 2017. *Aerospace materials and material technologies*. Prasad, N. E. and Wanhill, R. J. H. eds. Singapore: Springer Singapore. doi: 10.1007/978-981-10-2134-3.

Prasad, S. V. and Asthana, R. 2004. Aluminum metal-matrix composites for automotive applications: Tribological considerations. *Tribology Letters* 17(3), pp. 445–453. doi: 10.1023/B:TRIL.0000044492.91991.f3.

Prosser, M. et al. 2022. Primary aluminium production. Available at: www.world-aluminium.org.

Radeke, C.A. et al. 2010. Large-scale powder mixer simulations using massively parallel GPUarchitectures. *Chemical Engineering Science* 65(24), pp. 6435–6442. Available at: https://linkinghub.elsevier.com/retrieve/pii/S0009250910005737.

Rahman, M.A. et al. 2019. Effect of milling time on the density, hardness and corrosion behavior of Al 7150 alloy produced by high energy ball milling. *Materials Research Express* 6(7), p. 076566. doi: 10.1088/2053-1591/ab1749.

Rahmati, Z. et al. 2021. Effects of pre-heat treatment of the consumable rod on the microstructural and mechanical properties of the friction surfaced Al-Cu-Mg alloy over pure aluminum. *Surface and Coatings Technology* 410, p. 126954. doi: 10.1016/j.surfcoat.2021.126954.

Rai, R. et al. 2007. A computationally efficient model of convective heat transfer and solidification characteristics during keyhole mode laser welding. *Journal of Applied Physics* 101(5), p. 054909. doi: 10.1063/1.2537587.

Raj, R.R. et al. 2021. Effect of graphene addition on the mechanical characteristics of AA7075 aluminium nanocomposites. *Carbon Letters* 31(1), pp. 125–136. doi: 10.1007/s42823-020-00157-7.

Ramezani, M. and Neitzert, T. 2012. Mechanical milling of aluminum powder using planetary ball milling process. *Journal of Achievements in Materials and Manufacturing Engineering* 55(2), pp. 790–798.

Rana, R.S. et al. 2012. Reviews on the influences of alloying elements on the microstructure and mechanical properties of aluminum alloys and aluminum alloy composites. *Internation Journal of Scientific and Research Publications* 2(6), pp. 1–7.

Rashad, M. et al. 2014. Powder metallurgy of Mg–1%Al–1%Sn alloy reinforced with low content of graphene nanoplatelets (GNPs). *Journal of Industrial and Engineering Chemistry* 20(6), pp. 4250–4255. doi: 10.1016/j.jiec.2014.01.028.

Rashad, M. et al. 2015. Enhanced tensile properties of magnesium composites reinforced with graphene nanoplatelets. *Materials Science and Engineering A* 630, pp. 36–44. doi: 10.1016/j.msea.2015.02.002.

Raviathul Basariya, M. et al. 2014. Microstructural characteristics and mechanical properties of carbon nanotube reinforced aluminum alloy composites produced by ball milling. *Materials & Design* 64, pp. 542–549. doi: 10.1016/j.matdes.2014.08.019.

Read, N. et al. 2015. Selective laser melting of AlSi10Mg alloy: Process optimisation and mechanical properties development. *Materials and Design* 65, pp. 417–424. doi: 10.1016/j.matdes.2014.09.044.

Revie, R.W. 2011. *Uhlig's corrosion handbook*. Third. Revie, R. W. ed. Hoboken, NJ, USA: John Wiley & Sons, Inc. doi: 10.1002/9780470872864.

Revie, R.W. and Uhlig, H.H. 2008. *Corrosion and corrosion control: An introduction to corrosion science and engineering*.

Rometsch, P.A. et al. 2022. Review of high-strength aluminium alloys for additive manufacturing by laser powder bed fusion. *Materials & Design* 219, p. 110779. doi: 10.1016/j.matdes.2022.110779.

Ruiz-Angulo, A. and Hunt, M.L. 2010. Measurements of the coefficient of restitution for particle collisions with ductile surfaces in a liquid. *Granular Matter* 12(2), pp. 185–191. doi: 10.1007/s10035-010-0166-y.

Saboori, A. et al. 2018. An overview of key challenges in the fabrication of metal matrix nanocomposites reinforced by graphene nanoplatelets. *Metals* 8(3), p. 172. doi: 10.3390/met8030172.

Sampath, K. 2009. Transverse-weld tensile properties of a new al-4cu-2si alloy as filler metal. *Journal of Materials Engineering and Performance* 18(9), pp. 1218–1225. doi: 10.1007/s11665-009-9371-4.

Schuster, M. et al. 2021. Precipitation in a 2xxx series Al-Cu-Mg-Zr alloy fabricated by laser powder bed fusion. *Materials & Design* 211, p. 110131. doi: 10.1016/j.matdes.2021.110131.

Sercombe, T.B. and Li, X. 2016. Selective laser melting of aluminium and aluminium metal matrix composites: Review. *Materials Technology* 31(2), pp. 77–85. doi: 10.1179/1753555715Y.0000000078.

Shah, R.K. and Dey, P.P. 2019. Process parameter optimization of dmls process to produce AlSi10Mg components. *Journal of Physics: Conference Series* 1240(1). doi: 10.1088/1742-6596/1240/1/012011.

Shehadeh, L.M. and Jalham, I.S. 2016. The effect of adding different percentages of manganese (Mn) and copper (Cu) on the mechanical behavior of aluminum. *Jordan Journal of Mechanical and Industrial Engineering* 10(1), pp. 19–26.

Shi, J. and Wang, Y. 2020. Development of metal matrix composites by laser-assisted additive manufacturing technologies: a review. *Journal of Materials Science* 55(23), pp. 9883–9917. doi: 10.1007/s10853-020-04730-3.

Shim, D. 2021. Effects of process parameters on additive manufacturing of aluminum porous materials and their optimization using response surface method. *Journal of Materials Research and Technology* 15, pp. 119–134. doi: 10.1016/j.jmrt.2021.08.010.

Shin, S.E. et al. 2016. Mechanical and thermal properties of nanocarbon-reinforced aluminum matrix composites at elevated temperatures. *Composites Part B: Engineering* 106, pp. 66–73. doi: 10.1016/j.compositesb.2016.09.017.

Shin, S.E. and Bae, D.H. 2015. Deformation behavior of aluminum alloy matrix composites reinforced with few-layer graphene. *Composites Part A: Applied Science and Manufacturing* 78, pp. 42–47. doi: 10.1016/j.compositesa.2015.08.001.

Singh, P. et al. 2019. Effect of milling time on powder characteristics and mechanical performance of Ti4wt%Al alloy. *Powder Technology* 342, pp. 275–

287. doi: 10.1016/j.powtec.2018.09.075.

Sjölander, E. and Seifeddine, S. 2010. The Heat Treatment of Al–Si–Cu–Mg Casting Alloys. *Journal of Materials Processing Technology* 210(10), pp. 1249–1259. doi: 10.1016/j.jmatprotec.2010.03.020.

Sopicka-lizer, M. 2010. Introduction to mechanochemical processing. *High-Energy Ball Milling* , pp. 1–5. doi: 10.1533/9781845699444.1.

Su, J. and Teng, J. 2021. Recent progress in graphene-reinforced aluminum matrix composites. *Frontiers of Materials Science* 15(1), pp. 79–97. doi: 10.1007/s11706-021-0541-0.

Suryanarayana, C. 2001. Mechanical alloying and milling. *Progress in Materials Science* 46(1–2), pp. 1–184. doi: 10.1016/S0079-6425(99)00010-9.

Tailor, S. 2011. Study the effects of mechanically alloying on 2024Al with SiCp and on plasma sprayed coatings. In: *Proceedings of EURO PM2011*., pp. 91–96.

Takacs, L. and Pardavi-Horvath, M. 1994. Nanocomposite formation in the Fe 3 O 4 -Zn system by reaction milling. *Journal of Applied Physics* 75(10), pp. 5864–5866. doi: 10.1063/1.355543.

Tan, P. et al. 2021. A numerical study on the packing quality of fibre/polymer composite powder for powder bed fusion additive manufacturing. *Virtual and Physical Prototyping* 16(sup1), pp. S1–S18. doi: 10.1080/17452759.2021.1922965.

Tang, Y. et al. 2014. Enhancement of the mechanical properties of graphene–copper composites with graphene–nickel hybrids. *Materials Science and Engineering: A* 599, pp. 247–254. doi: 10.1016/j.msea.2014.01.061.

Taylor, J. a 2004. The effect of iron in Al-Si casting alloys. *35th Australian Foundry Institute National Conference* (October 2004), pp. 148–157.

Thakur, S.C. et al. 2016. Scaling of discrete element model parameters for cohesionless and cohesive solid. *Powder Technology* 293, pp. 130–137. doi: 10.1016/j.powtec.2015.05.051.

Thompson, S.M. et al. 2015. An overview of direct laser deposition for additive manufacturing; Part I: Transport phenomena, modeling and diagnostics. *Additive Manufacturing* 8, pp. 36–62. doi: 10.1016/j.addma.2015.07.001.

Tiwari, J.K. et al. 2020. Investigation of porosity, microstructure and mechanical properties of additively manufactured graphene reinforced AlSi10Mg composite. *Additive Manufacturing* 33, pp. 1–12. doi: 10.1016/j.addma.2020.101095.

Toozandehjani, M. et al. 2017. Effect of milling time on the microstructure, physical and mechanical properties of Al-Al2O3 nanocomposite synthesized by ball milling and powder metallurgy. *Materials* 10(11). doi: 10.3390/ma10111232.

Varia, H. and Goyal, B. 2017. A Review on effect of process parameters on surface quality and properties of parts realized by selective laser sintering process. 5(6), pp. 45–51. Available at: http://www.ijritcc.org.

Wang, H. and Gee, M.L. 2014. AFM lateral force calibration for an integrated probe using a calibration grating. *Ultramicroscopy* 136, pp. 193–200. doi: 10.1016/j.ultramic.2013.10.012.

Wang, L. et al. 2018a. An approach to predict the residual stress and distortion during the selective laser melting of AlSi10Mg parts. *International Journal of Advanced Manufacturing Technology* 97(9–12), pp. 3535–3546. doi: 10.1007/s00170-018-2207-3.

Wang, P. et al. 2018b. Microstructure and mechanical properties of a heat-treatable Al-3.5Cu-1.5Mg-1Si alloy produced by selective laser melting. *Materials Science and Engineering A* 711(October 2017), pp. 562–570. doi: 10.1016/j.msea.2017.11.063.

Wang, P. et al. 2020. A review of particulate-reinforced aluminum matrix composites fabricated by selective laser melting. *Transactions of Nonferrous Metals Society of China* 30(8), pp. 2001–2034. doi: 10.1016/S1003-6326(20)65357-2.

Wang, Y. et al. 2018c. Investigation of porosity and mechanical properties of graphene nanoplatelets-reinforced AlSi10 Mg by selective laser melting. *Journal of Micro and Nano-Manufacturing* 6(1), pp. 1–7. doi: 10.1115/1.4038454.

Wei, P. et al. 2017. The AlSi10Mg samples produced by selective laser melting: single track, densification, microstructure and mechanical behavior. *Applied Surface Science* 408, pp. 38–50. doi: 10.1016/j.apsusc.2017.02.215.

Wilkening, M. et al. 2017. Structure and ion dynamics of mechanosynthesized oxides and fluorides. *Zeitschrift fur Kristallographie - Crystalline Materials* 232(1–3), pp. 107–127. doi: 10.1515/zkri-2016-1963.

Williams, C. 1997. CO2 laser processing – an overview. *Aircraft Engineering and Aerospace Technology* 69(1), pp. 43–52.

Wong, K. V. and Hernandez, A. 2012. A review of additive manufacturing. *ISRN Mechanical Engineering* 2012, pp. 1–10. doi: 10.5402/2012/208760.

Wood, L. 2018. *High strength aluminum alloys market by end-use industry type (automotive & transportation, aerospace & defense, marine), alloy type (cast, and wrought), strength type (high, and ultra-high strength), and region - global forecast to 2023*.

Wu, H. et al. 2020. Effect of processing parameters on forming defects during selective laser melting of AlSi10Mg powder. *Rapid Prototyping Journal* 26(5), pp. 871–879. doi: 10.1108/RPJ-07-2018-0184.

Wu, X. et al. 2013. Accelerated precipitation due to mechanical milling of two-phase B2/L21 Fe30Ni20Mn20Al30. *Journal of Alloys and Compounds* 559, pp.

97–100. doi: 10.1016/j.jallcom.2013.01.083.

Xiao, W. et al. 2018. Mechanical and tribological behaviors of graphene/Inconel 718 composites. *Transactions of Nonferrous Metals Society of China* 28(10), pp. 1958–1969. doi: 10.1016/S1003-6326(18)64841-1.

Xie, H. et al. 2012. *Atomic force microscopy based nanorobotics*. Berlin, Heidelberg: Springer Berlin Heidelberg. doi: 10.1007/978-3-642-20329-9.

Xu, R. et al. 2017. Balanced strength and ductility in CNT/Al composites achieved by flake powder metallurgy via shift-speed ball milling. *Composites Part A: Applied Science and Manufacturing* 96, pp. 57–66. Available at: https://linkinghub.elsevier.com/retrieve/pii/S1359835X17300659.

Yahaya, S.N. et al. 2020. An overview on forming process and heat treatments for heat treatable aluminium alloy. *Journal of Advanced Research in Fluid Mechanics and Thermal Sciences* 70(1), pp. 112–124. doi: 10.37934/arfmts.70.1.112124.

Yan, S.J. et al. 2014. Investigating aluminum alloy reinforced by graphene nanoflakes. *Materials Science and Engineering A* 612, pp. 440–444. doi: 10.1016/j.msea.2014.06.077.

Yefimov, N.A. 2019. Powders with quasicrystalline structure. In: *Handbook of Non-Ferrous Metal Powders*. Elsevier, pp. 313–321. doi: 10.1016/B978-0-08-100543-9.00010-5.

Yeom, S.B. et al. 2019. Application of the discrete element method for manufacturing process simulation in the pharmaceutical industry. *Pharmaceutics* 11(8), p. 414. doi: 10.3390/pharmaceutics11080414.

Yi, M. and Shen, Z. 2015. A review on mechanical exfoliation for the scalable production of graphene. *Journal of Materials Chemistry A* 3(22), pp. 11700–11715. doi: 10.1039/C5TA00252D.

Yu, T. et al. 2021. Microstructure and wear characterization of carbon nanotubes (CNTs) reinforced aluminum matrix nanocomposites manufactured using selective laser melting. *Wear* 476(September 2020). doi: 10.1016/j.wear.2020.203581.

Yu, Z. et al. 2019. Effect of ball milling time on graphene nanosheets reinforced Al6063 composite fabricated by pressure infiltration method. *Carbon* 141, pp. 25–39. doi: 10.1016/j.carbon.2018.09.041.

Yue, H. et al. 2017. Effect of ball-milling and graphene contents on the mechanical properties and fracture mechanisms of graphene nanosheets reinforced copper matrix composites. *Journal of Alloys and Compounds* 691, pp. 755–762. doi: 10.1016/j.jallcom.2016.08.303.

Yusuf, S. et al. 2017. Investigation on porosity and microhardness of 316L stainless steel fabricated by selective laser melting. *Metals* 7(2), p. 64. doi: 10.3390/met7020064.

Zakeri, M. and Vakili-Ahrarirudi, A. 2012. Effect of milling speed and shaping method on mechanical properties of nanostructure bulked aluminum. *Materials and Design* 37, pp. 487–490. doi: 10.1016/j.matdes.2012.01.033.

Zhang, B. et al. 2017. Defect formation mechanisms in selective laser melting: A review. *Chinese Journal of Mechanical Engineering (English Edition)* 30(3), pp. 515–527. doi: 10.1007/s10033-017-0121-5.

Zhang, H. et al. 2016. Selective laser melting of high strength Al-Cu-Mg alloys: Processing, microstructure and mechanical properties. *Materials Science and Engineering A* 656, pp. 47–54. doi: 10.1016/j.msea.2015.12.101.

Zhang, J. et al. 2019. A review of selective laser melting of aluminum alloys: Processing, microstructure, property and developing trends. *Journal of Materials Science and Technology* 35(2), pp. 270–284. doi:

10.1016/j.jmst.2018.09.004.

Zhang, Y.F. et al. 1999. Prediction of the amount of PCA for mechanical milling. *Journal of Materials Processing Technology* 89–90, pp. 260–265. doi: 10.1016/S0924-0136(99)00042-4.

Zhao, H. and Debroy, T. 2001. Weld metal composition change during conduction mode laser welding of aluminum alloy 5182. *Metallurgical and Materials Transactions B* 32(1), pp. 163–172. doi: 10.1007/s11663-001-0018-6.

Zhao, X. et al. 2016. Selective laser melting of carbon/AlSi10Mg composites: Microstructure, mechanical and electronical properties. *Journal of Alloys and Compounds* 665, pp. 271–281. doi: 10.1016/j.jallcom.2015.12.126.

Zuhailawati, H. and Mahani, Y. 2009. Effects of milling time on hardness and electrical conductivity of in situ Cu-NbC composite produced by mechanical alloying. *Journal of Alloys and Compounds* 476(1–2), pp. 142–146. doi: 10.1016/j.jallcom.2008.09.018.